

**Multimessenger Astronomy with Low-Latency
Searches for Transient Gravitational Waves**

by

Jameson Graef Rollins

Submitted in partial fulfillment of the
requirements for the degree of

Doctor of Philosophy in Physics

in the Graduate School of Arts and Sciences

COLUMBIA UNIVERSITY

2011

© 2011
Jameson Graef Rollins
All Rights Reserved

Abstract

Multimessenger Astronomy with Low-Latency Searches for Transient Gravitational Waves

by

Jameson Graef Rollins

The Laser Interferometer Gravitational-wave Observatory (LIGO) and the Virgo Gravitational-wave Observatory have just completed the S6/VSR2 science run in which three long-baseline, geographically-separated detectors of similar sensitivity operated in coincidence. This new network of detectors allowed for the first time the reconstruction of the source location in the sky of candidate gravitational-wave events with unprecedented accuracy and precision. This new position-reconstruction capability further allowed for the possibility of observing electromagnetic counterparts to gravitational-wave events. This thesis describes the first gravitational-wave search to take advantage of these capabilities by analyzing the network data with very low-latency, reconstructing the source location of candidate events with a new coherent Bayesian algorithm, and sending this information to electromagnetic telescopes for follow-up observation.

Contents

Contents	i
List of Figures	vi
List of Tables	xii
Glossary	xiii
Acknowledgments	xvi
1 Introduction	1
2 Gravitational Radiation	7
2.1 Theory	7
2.2 Effect on local spacetime structure	11
2.3 Generation of gravitational waves	14
2.4 Observational evidence of gravitational radiation	17
3 Detection of Gravitational Waves with Interferometric Detectors	19
3.1 Overview of current detectors	21
3.2 Detector description	23
3.2.1 Interferometer configuration	23
3.2.2 Interferometer readout and control	25
3.2.3 Light source	28
3.2.4 Vacuum system	28

3.2.5	Optics and test masses	29
3.2.6	Thermal compensation	29
3.2.7	Suspensions and seismic isolation	30
3.2.8	Environmental monitoring	31
3.3	Interferometer response	32
3.4	Noise sources	35
3.4.1	Seismic noise	35
3.4.2	Thermal noise	37
3.4.3	Actuator noise	39
3.4.4	Auxiliary DOF noise	39
3.4.5	Shot noise	40
3.4.6	Other sensing noises	41
3.4.7	Excess noise	41
3.5	Detector improvements and future detectors	42
4	Transient Multimessenger Astronomy with Gravitational Waves	45
4.1	Triggered multimessenger searches	46
4.1.1	Electromagnetic \rightarrow Gravitational triggering (“ExtTrig”)	47
4.1.2	Gravitational \rightarrow Electromagnetic triggering (“LookUp”)	48
4.2	Transient multimessenger sources	49
4.2.1	Compact binary coalescence	50
4.2.2	Core-collapse supernovae	56
4.2.3	Neutron stars disruptions	60
5	Bayesian Network Analysis	64
5.1	Basics of network analysis	66
5.2	Null stream analysis	68
5.3	Formulation of the Bayesian analysis	71
5.3.1	Marginalization	72
5.3.2	The gravitational wave search problem	73
5.4	Noise model	73

5.5	Signal model	75
5.6	Glitch model	77
6	A Low-Latency Transient Search Pipeline for Gravitational Waves	80
6.1	The Omega transient search pipeline	81
6.1.1	Structure of the pipeline	82
6.1.2	Single detector analysis	83
6.1.3	Coincidence and candidate selection	88
6.1.4	Coherent follow-ups	88
6.2	The Omega-Pipeline Rapid Online Analysis	93
6.2.1	Structure of the online pipeline	94
6.2.2	Data discovery	97
6.2.3	Core analysis	97
6.2.4	Rapid significance estimation	98
6.2.5	Vetos, thresholds, post-processing, and notification	98
6.3	Characterizing the search algorithm	99
6.3.1	Preparing the data	100
6.3.2	Understanding the background	100
6.3.3	Monte Carlo simulations	103
6.3.4	Characterizing position reconstruction	110
7	Results from the S6 Search	115
7.1	The S6 low-latency/EM follow-up search	115
7.1.1	The full pipeline	117
7.1.2	The EM follow-up processors	118
7.1.3	The EM observatories	120
7.2	Preliminary results from the S6 online search	120
7.2.1	Event 970159718	120
7.3	Recent improvements to Ω -Pipeline candidate selection	126
7.4	Results from an offline search of S6b	130

8	Conclusion	133
8.1	Success of the S6 low-latency search	133
8.2	Low-latency searches in the advanced detector era	136
8.2.1	Challenges	137
A	S6b/VSR2 Monte Carlo Characterization Plots	142
A.1	Gaussian injections	143
A.1.1	GA0d1 injections	146
A.1.2	GA1d0 injections	149
A.1.3	GA2d5 injections	152
A.1.4	GA4d0 injections	155
A.2	Sine-Gaussian, Q 3 injections	158
A.2.1	SG70Q3 injections	161
A.2.2	SG235Q3 injections	164
A.2.3	SG849Q3 injections	167
A.2.4	SG1615Q3 injections	170
A.3	Sine-Gaussian, Q 9 injections	173
A.3.1	SG70Q8d9 injections	176
A.3.2	SG100Q8d9 injections	179
A.3.3	SG153Q8d9 injections	182
A.3.4	SG235Q8d9 injections	185
A.3.5	SG361Q8d9 injections	188
A.3.6	SG554Q8d9 injections	191
A.3.7	SG849Q8d9 injections	194
A.3.8	SG1053Q9 injections	197
A.3.9	SG1304Q9 injections	200
A.3.10	SG1615Q9 injections	203
A.3.11	SG2000Q9 injections	206
A.4	Sine-Gaussian, Q 100 injections	209
A.4.1	SG70Q100 injections	212

A.4.2	SG235Q100 injections	215
A.4.3	SG849Q100 injections	218
A.4.4	SG1615Q100 injections	221
A.5	White noise burst injections	224
A.5.1	WNB_1000_1000_0d01 injections	227
A.5.2	WNB_1000_1000_0d1 injections	230
A.5.3	WNB_1000_10_0d1 injections	233
A.5.4	WNB_100_100_0d1 injections	236
A.5.5	WNB_250_100_0d1 injections	239
B	Sky Position Coordinate Transformation	242
	Bibliography	244

List of Figures

1-1	The LIGO and Virgo observatories	2
2-1	Polarizations of gravitational waves	14
2-2	PSR B1913+16 orbital decay	18
3-1	Schematic of LIGO/Virgo interferometers	24
3-2	Schematic of PDH cavity control	26
3-3	LIGO vacuum system	29
3-4	Interferometric detector antenna response	33
3-5	LIGO and Virgo strain sensitivities during S6/VSR2	34
3-6	LIGO H1 noise sources during S5	36
3-7	LIGO H1 noise distribution during S5	43
4-1	GRB X-ray afterglows	54
4-2	Radiation emission times from CBC	55
4-3	CCSN light curves	57
4-4	LGRB afterglow light curves	61
4-5	Radiation emission times from CCSNe	62
4-6	SGR 1806-20 light curve	63
5-1	Network null stream construction	69
6-1	Flowchart of Omega search algorithm	84
6-2	Omega spectrograms	86
6-3	Omega selected Q tiles	87

6-4	Omega clustered Q tiles	87
6-5	Determination of cluster coincidence	88
6-6	Omega Bayesian sky map	91
6-7	Block diagram of the Omega Rapid Online Analysis pipeline	95
6-8	Cumulative background of Omega triggers	102
6-9	Omega injection event scatter plots	106
6-10	Omega injection event histograms	107
6-11	Omega detection efficiency	109
6-12	Omega ROC plots	111
6-13	Omega ROC plots, by injection scale	112
6-14	Position reconstruction angle error	113
6-15	Position reconstruction confidence	114
7-1	Timeline of S6 online analysis runs.	116
7-2	Low-latency analysis and EM follow-up pipeline	117
7-3	OROA event latencies	119
7-4	Ω -Pipeline sky map for event 970159718	124
7-5	LUMIN Pi of the Sky tiling for event 970159718	125
7-6	Liverpool Telescope image of NGC1507 from event 970159718	126
7-7	SkyMapper images from event 970159718	127
7-8	QUEST images from event 970159718	128
7-9	Selection of coincident triggers	129
7-10	Final event distributions with Ω -Pipeline	131
7-11	Sky map, largest event in vSCGR foreground	132
A-1	GA injections scatter plot	143
A-2	GA injections histograms	144
A-3	GA ROC plots	145
A-4	GA0d1 injections scatter plot	146
A-5	GA0d1 injections histograms	147
A-6	GA0d1 ROC plots	148

A-7	GA1d0 injections scatter plot	149
A-8	GA1d0 injections histograms	150
A-9	GA1d0 ROC plots	151
A-10	GA2d5 injections scatter plot	152
A-11	GA2d5 injections histograms	153
A-12	GA2d5 ROC plots	154
A-13	GA4d0 injections scatter plot	155
A-14	GA4d0 injections histograms	156
A-15	GA4d0 ROC plots	157
A-16	SGQ3 injections scatter plot	158
A-17	SGQ3 injections histograms	159
A-18	SGQ3 ROC plots	160
A-19	SG70Q3 injections scatter plot	161
A-20	SG70Q3 injections histograms	162
A-21	SG70Q3 ROC plots	163
A-22	SG235Q3 injections scatter plot	164
A-23	SG235Q3 injections histograms	165
A-24	SG235Q3 ROC plots	166
A-25	SG849Q3 injections scatter plot	167
A-26	SG849Q3 injections histograms	168
A-27	SG849Q3 ROC plots	169
A-28	SG1615Q3 injections scatter plot	170
A-29	SG1615Q3 injections histograms	171
A-30	SG1615Q3 ROC plots	172
A-31	SGQ9 injections scatter plot	173
A-32	SGQ9 injections histograms	174
A-33	SGQ9 ROC plots	175
A-34	SG70Q8d9 injections scatter plot	176
A-35	SG70Q8d9 injections histograms	177
A-36	SG70Q8d9 ROC plots	178

A-37 SG100Q8d9 injections scatter plot	179
A-38 SG100Q8d9 injections histograms	180
A-39 SG100Q8d9 ROC plots	181
A-40 SG153Q8d9 injections scatter plot	182
A-41 SG153Q8d9 injections histograms	183
A-42 SG153Q8d9 ROC plots	184
A-43 SG235Q8d9 injections scatter plot	185
A-44 SG235Q8d9 injections histograms	186
A-45 SG235Q8d9 ROC plots	187
A-46 SG361Q8d9 injections scatter plot	188
A-47 SG361Q8d9 injections histograms	189
A-48 SG361Q8d9 ROC plots	190
A-49 SG554Q8d9 injections scatter plot	191
A-50 SG554Q8d9 injections histograms	192
A-51 SG554Q8d9 ROC plots	193
A-52 SG849Q8d9 injections scatter plot	194
A-53 SG849Q8d9 injections histograms	195
A-54 SG849Q8d9 ROC plots	196
A-55 SG1053Q9 injections scatter plot	197
A-56 SG1053Q9 injections histograms	198
A-57 SG1053Q9 ROC plots	199
A-58 SG1304Q9 injections scatter plot	200
A-59 SG1304Q9 injections histograms	201
A-60 SG1304Q9 ROC plots	202
A-61 SG1615Q9 injections scatter plot	203
A-62 SG1615Q9 injections histograms	204
A-63 SG1615Q9 ROC plots	205
A-64 SG2000Q9 injections scatter plot	206
A-65 SG2000Q9 injections histograms	207
A-66 SG2000Q9 ROC plots	208

A-67 SGQ100 injections scatter plot	209
A-68 SGQ100 injections histograms	210
A-69 SGQ100 ROC plots	211
A-70 SG70Q100 injections scatter plot	212
A-71 SG70Q100 injections histograms	213
A-72 SG70Q100 ROC plots	214
A-73 SG235Q100 injections scatter plot	215
A-74 SG235Q100 injections histograms	216
A-75 SG235Q100 ROC plots	217
A-76 SG849Q100 injections scatter plot	218
A-77 SG849Q100 injections histograms	219
A-78 SG849Q100 ROC plots	220
A-79 SG1615Q100 injections scatter plot	221
A-80 SG1615Q100 injections histograms	222
A-81 SG1615Q100 ROC plots	223
A-82 WNB injections scatter plot	224
A-83 WNB injections histograms	225
A-84 WNB ROC plots	226
A-85 WNB_1000_1000_0d01 injections scatter plot	227
A-86 WNB_1000_1000_0d01 injections histograms	228
A-87 WNB_1000_1000_0d01 ROC plots	229
A-88 WNB_1000_1000_0d1 injections scatter plot	230
A-89 WNB_1000_1000_0d1 injections histograms	231
A-90 WNB_1000_1000_0d1 ROC plots	232
A-91 WNB_1000_10_0d1 injections scatter plot	233
A-92 WNB_1000_10_0d1 injections histograms	234
A-93 WNB_1000_10_0d1 ROC plots	235
A-94 WNB_100_100_0d1 injections scatter plot	236
A-95 WNB_100_100_0d1 injections histograms	237
A-96 WNB_100_100_0d1 ROC plots	238

A-97 WNB_250_100_0d1 injections scatter plot	239
A-98 WNB_250_100_0d1 injections histograms	240
A-99 WNB_250_100_0d1 ROC plots	241

List of Tables

3.1	Current and proposed interferometric detectors	22
6.1	Time slides used in the background analysis	103
6.2	Simulation waveform parameters	104
7.1	Telescopes used in the S6 EM follow-up search	121
7.2	Online events reported during S6d/VSR3	122
7.3	Omega reconstructed event parameters for the 970159718 event.	123
7.4	Omega significance of the 970159718 event.	123
7.5	S6b offline foreground and background events	130

Glossary

γ	gamma-rays
ν	neutrinos
Ω	Ω -Pipeline or OROA
BH	black hole
AS	anti-symmetric port
BS	beam splitter
Caltech	California Institute of Technology
CBC	compact binary coalescence
CCSN(e)	core-collapse supernova(e)
cWB	Coherent WaveBurst analysis pipeline
DECIGO	Deci-hertz Interferometer Gravitational-Wave Observatory
EM	electromagnetic
ETM	end test mass
GCN	Gamma-ray burst Coordinates Network
GraceDB	Gravitational-Wave Candidate Event Database
GRB	gamma-ray burst
GW	gravitational wave
H1	LIGO Hanford 4km detector
HE	high energy
IPN3	Third Interplanetary Network
IR	infrared radiation
ITM	input test mass

L1	LIGO Livingston 4km detector
LCGT	Large-Scale Cryogenic Gravitational-Wave Telescope
LE	low energy
LIGO	Laser Interferometer Gravitational-Wave Observatory
LISA	Laser Interferometer Satellite Array
LHO	LIGO Hanford Observatory
LLO	LIGO Livingston Observatory
LSST	Large Synoptic Survey Telescope
MBTA	MBTA online analysis pipeline
MDC	mock data challenge
NS	neutron star
OMC	output mode cleaner
OROA	Ω -Pipeline Rapid Online Analysis
PD	photo-detector
PSL	pre-stabilized laser
PTF	Palomar Transient Factory
Q	quality factor
QPO	quasi-periodic oscillation
RCD	real-time calibrated data
REF	reflection port
RM	recycling mirror
S6	LIGO's 6th science run
S6b	LIGO's 6th science run, segment B
SG	sine-Gaussian
SGR	soft gamma repeater
SN(e)	supernova(e)
SNR	signal-to-noise ratio
SRD	science requirement document
UV	ultraviolet radiation
V1	Virgo 3km detector

Virgo	Virgo gravitational-wave observatory
VSR2/VSR3	Virgo's 2nd/3rd science runs
WNB	white noise burst
WGDN	world-wide gravitational-wave detector network
X	X-rays

Acknowledgments

It's been a long time coming...

First and foremost, I thank Rebecca Bureau. Her love, support, caring, and patience over the last nine years have pulled me through the toughest times and helped me finally see this thing to completion.

My adviser Szabolcs Márka has been incredibly steadfast. His passion, creativity, and unwavering confidence in me were an immense source of inspiration. He took a chance on me and I can only hope I am able to repay him for what he has given to me.

Szabi was not the first to take a chance on me. My previous advisors Keith Riles and Rainer Weiss also went out on limbs for me. If it was not for them I would not be here today.

I have had the pleasure and luck to work closely with many incredible people. Antony Searle, my closest collaborator, has been a patient teacher, and a good friend. Brennan Hughey, Jonah Kanner, and Patrick Sutton have been wonderful teammates whose help was invaluable. The LIGO and Virgo reviewers of the EM followup program, led by Ben Owen, did a great and thorough job of making sure our harried efforts were focused on the right science. Stan Whitcomb, the “S6 Run Czar”, also deserves particular thanks for holding my feet to the fire and always expecting the best. Nick Smith and Mike Landry made long nights working on the detector fun again. My office mate Imre Bartos was a reliable source of knowledge and entertainment. I look forward to continuing to work with all of them.

My family has been a constant source of comfort and support. Jim, Stefan, Julie, Bob, Monique, David, Lynn: I love you all.

Finally, I want to thank all of my good friends, without whom I would have surely finished this project much much sooner: the Monkeys, Gost Trio, the Poker Nuts, Recess, the Farmers, Unlockedgroove. Michael Haskell deserves particular thanks, since his editorializing, both for this thesis and in life, helped birth this gigantic baby physicist.

The author gratefully acknowledges the support of the United States National Science Foundation (Awards–0457528, 0757982, 0847182 and 0856691) and Columbia University in the City of New York.

The author also gratefully acknowledge the support of the United States National Science Foundation for the construction and operation of the LIGO Laboratory and the Science and Technology Facilities Council of the United Kingdom, the Max-Planck-Society, and the State of Niedersachsen/Germany for support of the construction and operation of the GEO600 detector. The authors also gratefully acknowledge the support of the research by these agencies and by the Australian Research Council, the Council of Scientific and Industrial Research of India, the Istituto Nazionale di Fisica Nucleare of Italy, the Spanish Ministerio de Educación y Ciencia, the Conselleria d’Economia, Hisenda i Innovació of the Govern de les Illes Balears, the Royal Society, the Scottish Funding Council, the Scottish Universities Physics Alliance, The National Aeronautics and Space Administration, the Carnegie Trust, the Leverhulme Trust, the David and Lucile Packard Foundation, the Research Corporation, and the Alfred P. Sloan Foundation.

This document has been assigned LIGO DCC number P1100009.

For Stefanie

Chapter 1

Introduction

The *Laser Interferometer Gravitational-Wave Observatory*, otherwise known as LIGO, operates the world's largest and most sensitive gravitational-wave detectors [1, 2, 3, 4]. The goal of the LIGO project is to directly detect gravitational waves of astronomical and cosmological origin incident on the Earth. While to date there has been no direct observation of gravitational waves, the project has made enormous strides towards first detection.

LIGO has just completed its sixth science run (known as “S6”). During this period, the two LIGO detectors, one in Hanford, WA, and the other in Livingston Parish, LA, operated with unprecedented sensitivity, routinely achieving peak strain sensitivities of nearly $10^{-23}/\sqrt{\text{Hz}}$ at 200 Hz. At these levels, some sources are thought to be detectable at rates of about once per year of observation. Analysis of the data collected during S6 is ongoing. Meanwhile, construction of the advanced LIGO detectors is already well underway.

More important than the sensitivity of the individual LIGO detectors is the fact that they are now operating as part of a *worldwide gravitational-wave detector network* (WGDN). The European *Virgo* Gravitational-wave Observatory operates a detector of similar sensitivity to LIGO's near Pisa, Italy. Other detectors in Germany and Japan have made recent contributions, while new more sensitive detectors in Japan



Figure 1-1: The two LIGO observatories (Hanford left, Livingston center) and the Virgo observatory (right).

and possibly Australia may be on the way soon. We may even see sensitive detectors in space in the coming decades.

While a single interferometric detector can now be made sufficiently sensitive to detect the strain amplitudes that we believe the universe is generating, it is unlikely that observations from just a single detector will be sufficient to claim a first detection. We do not have a good enough understanding of the sources we hope to observe to know with absolute certainty what waveforms they will produce. Even if we did, we would still have a difficult time distinguishing true signals from the instrumental artifacts known as “glitches,” which manifest as transient noise non-stationarities that tend to look unfortunately similar to the signals we hope to detect. All of this means that coincident observations from multiple detectors will likely be required for a confident first detection.

The benefit of a network of detectors is further revealed when considering its astronomical impact. A network of three or more non-co-located detectors can be used to accurately reconstruct the source location in the sky of a gravitational-wave event candidate. This is an extremely significant extra piece of information which allows us to perform searches that were previously impossible. Most intriguingly, source position reconstruction brings the prospect of simultaneously observing the source of a gravitational-wave event with other astronomical observatories. The observation of an astronomical event via multiple forms of radiation, so called *multimessenger*

astronomy, is a very powerful tool for understanding the nature of the universe. Each “messenger”, be they photons, neutrinos, or gravitational waves, tells us something different about the nature of the source, probing different stages, regions, or scales of the physical processes. The coincident observation of these different messengers gives us a much clearer picture of the whole of what is actually happening, and the whole is certainly greater than the sum of its parts.

Multimessenger astronomy can, however, be quite challenging. Transient events tend to fade quickly from view. This means that observation of an event by one observatory must be quickly communicated to other observatories so that it can be further observed before it disappears. This requires tightly coordinated efforts. The challenges are well worth the effort, though, since the scientific pay-off can be enormous.

A perfect example of the need for source position reconstruction and quick observational turnaround was the first observation of X-ray and optical afterglows from gamma-ray burst (GRB) events. GRBs, while powerful, can last for mere fractions of a second, making it difficult to learn anything about them. They were initially a mystery, but astronomers knew that if the GRBs had afterglows that could be observed, the mystery might be revealed. This in fact turned out to be the case when the Beppo-SAX telescope first observed X-ray afterglow of GRB 970228 in 1997 [5].

The scientific benefit of similar electromagnetic followup searches based on gravitational-wave event candidates is clear:

- We can increase detection confidence, by requiring coincident observation by other observatories.
- We can increase the sensitivity of the searches by accepting higher false alarm rates.
- We can significantly increase the amount of information we learn about the source, such as host galaxy and more accurate position, distance, composition,

etc.

- We can potentially catch events that might be otherwise missed by non-gravitational-wave observatories, such as observing off-axis of “choked” GRBs.

What made Beppo-SAX successful was its ability to do two things: localize the source of the GRB, and do it quickly so that it could make further observations of the source before it disappeared. Similarly, the new WGDN of the S6 science run allowed for the possibility of reconstructing the sky location of our potential sources. What was needed to do real multimessenger astronomy with this network—to make it possible for other observatories to make follow-up observations of gravitational-wave triggers—was to identify event candidates and their likely source locations quickly.

To this end, during S6, data from the WGDN was for the first time made available for analysis with very low latency (e.g. on time scales of minutes). The first analyses to take full advantage of this low-latency data availability were the transient, or “burst”, pipelines that look for short-lived gravitational-wave transients that are well localized in time, usually to much less than one second, and are therefore well-suited to low-latency analysis. Before the run began these burst pipelines were enhanced with new source position reconstruction algorithms and adapted to run in very low-latency modes, producing event candidates on time scales of minutes. The results from these analyses were promptly communicated to electromagnetic follow-up observatories that opportunistically made observations of the most probable source locations of the events.

In this thesis, I will describe the first ever low-latency search for transient gravitational waves from a world-wide network of detectors. I will describe in detail one of the principle data analysis pipelines that was modified to run in a low-latency mode and produce position reconstruction sky maps. The triggers from this search were promptly communicated to multiple electromagnetic follow-up observatories that made follow-up observations of the gravitational-wave event candidates. The analysis

of the results from the electromagnetic follow-up observations based on this search is on-going.

This thesis is organized as follows:

Chapter 2 gives a brief overview of the theory of gravitational radiation, including the generation of gravitational waves and their effect on local spacetime.

Chapter 3 describes the detection of gravitational waves with interferometric detectors, covering the basic principle of their operation and the major sources of noise that limit their sensitivity.

Chapter 4 is a general discussion of multimessenger astronomy, with a focus on electromagnetic emissions that might follow gravitational-wave bursts. The goal of this chapter is to motivate low-latency searches by noting the myriad of interesting physical phenomena that could be observed by electromagnetic follow-up observations of gravitational-wave events. I also discuss previous work on multimessenger astronomy with gravitational waves, which to date has been exclusively based on electromagnetic triggers guiding look-back searches in pre-recorded gravitational-wave data.

Chapter 5 is a description of a pioneering new Bayesian coherent detection algorithm for transient gravitational-wave signals in a network of detectors that is capable of quickly generating full probability distribution maps of source location on the sky. This algorithm incorporates a new model for detector glitches that is capable of effectively rejecting glitches as event candidates.

Chapter 6 is a description of one of the transient search pipelines used in the S6 low-latency search. The Ω -Pipeline, which is based on a pre-existing search pipeline, was modified to include the coherent Bayesian detection algorithm described in chapter 5, as well as to run in a robust low-latency mode. I describe these modifications, as well as extensive characterizations of the pipeline performed to demonstrate its suitability in the search.

Chapter 7 is a description of the full low-latency search that was performed during

the S6 science run, including the EM follow-up projects that made follow-up observations of gravitational-wave event candidates found by the low-latency search pipelines. Included is preliminary results from an Ω -Pipeline event on October 3, 2010. I also present results from an offline Ω -Pipeline analysis of segment B of the S6 run (S6b).

Chapter 8 is concluding remarks on the success to-date of the S6 low-latency search and electromagnetic follow-up program. This chapter also includes a discussion on the challenges that were faced in developing low-latency analyses, and how they may be addressed in the advanced detector era.

Chapter 2

Gravitational Radiation

2.1 Theory

The culmination of Einstein's general theory of relativity is embodied in a single equation, known as the Einstein field equation:

$$\mathbf{G} = \frac{8\pi G}{c^4} \mathbf{T}. \quad (2.1)$$

This tensor equation describes the curvature of spacetime, \mathbf{G} (the Einstein tensor), as the product of a constant times the stress-energy tensor, \mathbf{T} , which is a description of the mass and energy content of spacetime. The Einstein tensor is derived from the spacetime metric tensor, $g_{\alpha\beta}$, which, when acting on differential line elements, expresses the fundamental interval between two neighboring points in the spacetime,

$$ds^2 = g_{\alpha\beta} dx^\alpha dx^\beta. \quad (2.2)$$

The idea that spacetime can be curved implies that it is an “elastic” medium that could, theoretically, sustain waves. But the nature of the curvature tensor and the extremely small constant of proportionality, $8\pi G/c^4$, mean that spacetime is extremely stiff and rigid. Enormous amounts of energy are required to produce even

very small curvatures or, as we are concerned with here, very low amplitude waves.

Einstein's field equation is highly nonlinear. Normally this nonlinearity would prevent a precise separation of the spacetime curvature into background and gravitational wave contributions. However, the extreme stiffness of spacetime means that in general the background curvature is very small. This allows for what is known as the *weak field* approximation to the field equations. In this weak field limit, the field equations become linear and, with the right choice of gauge, can be easily solved.

In the absence of any gravitational source, spacetime is completely flat and described by the Minkowski metric of special relativity:

$$g_{\alpha\beta} = \eta_{\alpha\beta} \equiv \begin{pmatrix} -1 & 0 & 0 & 0 \\ 0 & 1 & 0 & 0 \\ 0 & 0 & 1 & 0 \\ 0 & 0 & 0 & 1 \end{pmatrix}. \quad (2.3)$$

When sources are present, the spacetime becomes curved and the metric acquires off-diagonal elements. At reasonable distances from the sources, though, spacetime is nearly flat and the weak field approximation allows us to separate the metric into the flat Minkowski metric and a very small perturbation term,

$$g_{\alpha\beta} = \eta_{\alpha\beta} + h_{\alpha\beta} \quad (2.4)$$

$$|h_{\alpha\beta}| \ll 1.$$

In this weak field approximation, the Einstein tensor can be written [6]:

$$G_{\alpha\beta} = -\frac{1}{2}(\partial_\sigma\partial_\beta h^\sigma_\alpha + \partial_\sigma\partial_\alpha h^\sigma_\beta - \partial_\alpha\partial_\beta h - \square h_{\alpha\beta} - \eta_{\alpha\beta}\partial_\rho\partial_\lambda h^{\rho\lambda} + \eta_{\alpha\beta}\square h), \quad (2.5)$$

where $\square \equiv -\frac{1}{c^2}\partial_t^2 + \partial_x^2 + \partial_y^2 + \partial_z^2$ is the shorthand d'Alembertian operator.

Let us now define a tensor called the *trace reverse* of $h_{\alpha\beta}$ [7],

$$\bar{h}_{\alpha\beta} = h_{\alpha\beta} - \frac{1}{2}\eta_{\alpha\beta}h, \quad (2.6)$$

where

$$h \equiv h_{\alpha}{}^{\alpha} \quad (2.7)$$

is the *trace* of $h_{\alpha\beta}$. If we choose to work in the *Lorenz gauge* by requiring that $\bar{h}_{\alpha\beta}$ be divergence-free, i.e.,

$$\partial_{\alpha}\bar{h}^{\alpha\beta} = 0, \quad (2.8)$$

we can reduce the Einstein tensor to:

$$G_{\alpha\beta} = -\frac{1}{2}\square\bar{h}_{\alpha\beta}. \quad (2.9)$$

Combining equations 2.1 and 2.9, the weak field Einstein field equation becomes:

$$\square\bar{h}_{\alpha\beta} = -\frac{16\pi G}{c^4}T_{\alpha\beta}, \quad (2.10)$$

or in more generic tensor notation:

$$\square\bar{\mathbf{h}} = -\frac{16\pi G}{c^4}\mathbf{T}. \quad (2.11)$$

With these weak field approximations we have reduced the field equation to an inhomogeneous wave equation with the stress-energy tensor as the source. Equation (2.11) has analytical solutions for some values of \mathbf{T} .

In the vacuum of spacetime, where the stress-energy tensor is essentially zero, equation 2.10 reduces to

$$\square\bar{h}_{\alpha\beta} = 0, \quad (2.12)$$

which is simply the three-dimensional homogeneous wave equation in \bar{h} . If we fur-

then restrict ourselves to consideration of only plane waves, the general solution to equation 2.12 is of the form

$$\bar{h}_{\alpha\beta} = A_{\alpha\beta} e^{\pm i k^\mu x_\mu} = A_{\alpha\beta} e^{\mp i(2\pi f t - k^m x_m)}, \quad (2.13)$$

where $A_{\alpha\beta}$ is the wave amplitude, k^m is the wave vector, and $f = k^0 c / 2\pi$ is the frequency [8]. Equation 2.13 now describes plane waves in the perturbation component of the metric, traveling at the speed of light, c ; otherwise known as *gravitational waves*.

If we impose two further gauge constraints on $\bar{h}_{\alpha\beta}$ similar to those imposed in equation 2.8, namely that

$$\bar{h}_{\alpha 0} = 0 \quad (2.14)$$

$$\bar{h}_\alpha{}^\alpha = 0, \quad (2.15)$$

we then have what is known as the *transverse-traceless (TT) gauge* and $\bar{h}_{\alpha\beta}$ becomes a transverse-traceless tensor,

$$\bar{h}_{\alpha\beta} \Rightarrow h_{\alpha\beta}^{\text{TT}}. \quad (2.16)$$

It is transverse because it is purely spatial (2.14) and traceless because the trace vanishes (2.15). In this gauge (assuming that the waves are traveling along the \hat{z} -axis), the metric perturbation simplifies to:

$$h_{\alpha\beta}^{\text{TT}} = \begin{pmatrix} 0 & 0 & 0 & 0 \\ 0 & a & b & 0 \\ 0 & b & -a & 0 \\ 0 & 0 & 0 & 0 \end{pmatrix}. \quad (2.17)$$

We can then look at equation 2.17 as the sum of two components,

$$h_{\alpha\beta}^{\text{TT}} = a \hat{h}_+ + b \hat{h}_\times, \quad (2.18)$$

where \hat{h}_+ and \hat{h}_\times are the two *basis tensors*,

$$\hat{h}_+ \equiv \begin{pmatrix} 0 & 0 & 0 & 0 \\ 0 & 1 & 0 & 0 \\ 0 & 0 & -1 & 0 \\ 0 & 0 & 0 & 0 \end{pmatrix}, \quad \hat{h}_\times \equiv \begin{pmatrix} 0 & 0 & 0 & 0 \\ 0 & 0 & 1 & 0 \\ 0 & 1 & 0 & 0 \\ 0 & 0 & 0 & 0 \end{pmatrix}, \quad (2.19)$$

which describe two orthogonal polarizations of the gravitational wave, each rotated 45° relative to the other.

It is interesting to note that if gravitational waves are quantizable, which may be required for consistency with the Standard Model, the quantum of gravity, referred to as the *graviton*, would be a spin-2 particle. This can be seen in (2.19) where a rotation through 90° would take each of these tensors into itself with a sign change.

2.2 Effect on local spacetime structure

In order to have any chance of detecting gravitational radiation, we must first understand the effect that a gravitational wave should have on a locally Lorentzian spacetime, such as the one in which we currently reside. The best way to do this is to look directly at what happens to freely falling test particles affected by a gravitational wave.

The spacetime interval in the weak field approximation is

$$\begin{aligned} ds^2 &= g_{\alpha\beta} dx^\alpha dx^\beta \\ &= (\eta_{\alpha\beta} + h_{\alpha\beta}^{\text{TT}}) dx^\alpha dx^\beta. \end{aligned} \quad (2.20)$$

Consider two freely falling test masses lying on the \hat{x} -axis, one at the origin and the other at $x = L$, $y = z = 0$. In the TT gauge, the proper distance between them is then

$$\bar{L} = \int ds \tag{2.21}$$

$$= \int_0^L |g_{xx}|^{1/2} dx. \tag{2.22}$$

Noting from equation 2.3 that $\eta_{xx} = 1$, this gives

$$g_{xx} = 1 + h_{xx}^{\text{TT}}, \tag{2.23}$$

so the proper separation becomes

$$\begin{aligned} \bar{L} &= \int_0^L |1 + h_{xx}^{\text{TT}}|^{1/2} dx \\ &\approx \int_0^L \left(1 + \frac{1}{2} |h_{xx}^{\text{TT}}| \right) dx. \end{aligned} \tag{2.24}$$

We can now solve this explicitly using the solution to the homogeneous gravitational wave equation 2.13. The transverse-traceless solutions are

$$h_{\alpha\beta}^{\text{TT}} = A_{\alpha\beta}^{\text{TT}} e^{i(2\pi ft - k^n x_n)} \tag{2.25}$$

where

$$A_{\alpha\beta}^{\text{TT}} = \begin{pmatrix} 0 & 0 & 0 & 0 \\ 0 & A_+ & A_\times & 0 \\ 0 & A_\times & -A_+ & 0 \\ 0 & 0 & 0 & 0 \end{pmatrix} \tag{2.26}$$

$$= A_+ \hat{h}_+ + A_\times \hat{h}_\times. \tag{2.27}$$

If we consider only a purely \hat{h}_+ polarized gravitational wave traveling down the \hat{z} -axis ($k^1 = k^2 = 0$) we see that solution is then

$$h_{xx}^{\text{TT}} = A_+ e^{i(2\pi ft - k^z z)}. \quad (2.28)$$

Plugging this into equation 2.24, and looking at just the real part, we get:

$$\begin{aligned} \bar{L} &\approx \int_0^L \left(1 + \frac{1}{2} A_+ \cos(2\pi ft - k^z z) \right) dx \\ &= \left(1 + \frac{1}{2} A_+ \cos(2\pi ft - k^z z) \right) \int_0^L dx \\ &= \left(1 + \frac{1}{2} A_+ \cos(2\pi ft - k^z z) \right) L. \end{aligned} \quad (2.29)$$

As equation 2.29 shows, the proper distance between the two masses oscillates back and forth around the coordinate distance with a frequency equal to the frequency of the gravitational wave. We can repeat this same procedure for particles lying on the \hat{y} axis, where we note the result differs only in the phase of the oscillating term due to the fact that $h_{yy}^{\text{TT}} = -h_{xx}^{\text{TT}}$:

$$\bar{L} = \left(1 - \frac{1}{2} A_+ \cos(2\pi ft - k^z z) \right) L. \quad (2.30)$$

A similar procedure can also be done for \hat{h}_\times -polarized waves.

Note that equations (2.29) and (2.30) can be simply rewritten as:

$$\bar{L} \approx \left(1 - \frac{h}{2} \right) L, \quad (2.31)$$

which leads to

$$h \propto \frac{L - \bar{L}}{L} = \frac{\Delta L}{L}. \quad (2.32)$$

The perturbation h manifests as a change in length per unit length, or in other words a *strain* in the local spacetime. h is therefore generally referred to as the gravitational-

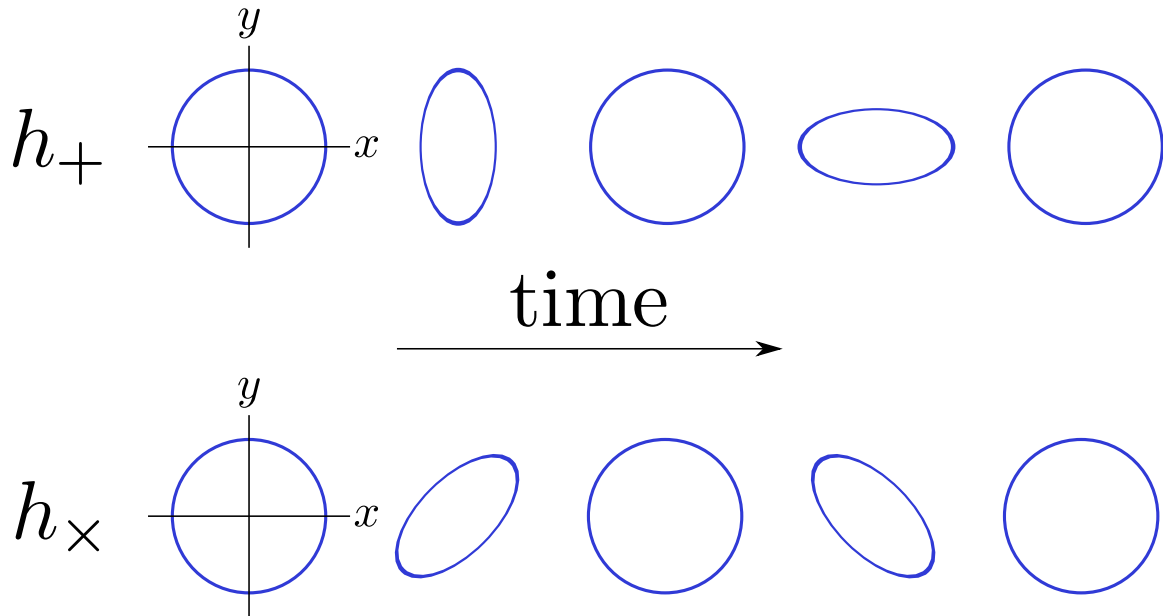


Figure 2-1: The effect of the two wave polarizations on a ring test mass lying in the $x-y$ plane (wave traveling in \hat{z} -direction).

wave *strain*.

If we generalize the above results to a ring of test masses lying in the $x-y$ plane, we see that the \hat{h}_+ polarization would have the effect of compressing distances in x while simultaneously expanding those in y . Half a wavelength later, the opposite happens, expanding in x while compressing in y . For \hat{h}_\times the same thing happens but instead along axes rotated 45° relative to those for \hat{h}_+ . This effect is illustrated in figure 2-1.

2.3 Generation of gravitational waves

Before we begin the search for gravitational waves, we must first try to understand what, if anything, might actually emit them. This is most easily done by making use of analogies to electromagnetism.

We can begin by noting that equation (2.11), the inhomogeneous wave equation for the strain \mathbf{h} , is very similar to the electromagnetic inhomogeneous wave equation:

$$\square \mathbf{A} = 4\pi \mathbf{J}, \quad (2.33)$$

where instead of waves in the electromagnetic potential tensor, \mathbf{A} , we have waves in the metric perturbation, \mathbf{h} , and instead of the source being the 4-current tensor, \mathbf{J} , we have the gravitational stress-energy tensor, \mathbf{T} .

A good approximation to the potential of an electromagnetic source is made through the use of a finite multipole expansion. Since accelerating charges or, more explicitly, time-varying potentials give rise to electromagnetic radiation, and each term in the multipole expansion is a function of a term dependent on the charge distribution, or charge *moment*, electromagnetic radiation is a function of these time-varying moments. Conservation of charge dictates that the monopole moment cannot vary with time so the dominant contribution to electromagnetic radiation is from the varying dipole charge distribution, or dipole moment.

Equivalently, for gravitation, we can look at a multipole expansion of the “gravitational potential,” \mathbf{h} , to determine what time varying mass moments will contribute to the production of gravitational radiation. There are two crucial differences between electromagnetism and gravitation that will influence further interpretation of our analogy. First, there are two possible signs of electric charge and only one of gravitational “charge” (i.e. mass). Second, the gravitational mass is, by the Principle of Equivalence, the same as the inertial mass. These differences mean that more conservation laws affect the radiative process of gravity.

Conservation of energy, the gravitational equivalent to conservation of charge, says that we will not have a time-varying gravitational radiation monopole term. Conservation of linear and angular momentum dictates that there will be no dipole terms either. The first nonzero multipole term for gravitational radiation is therefore the quadrupole term.

In reduced form, the quadrupole moment is given by [6]:

$$I_{ab} = \int y^a y^b T^{00} d^3y. \quad (2.34)$$

The T^{00} element of the stress-energy tensor is the energy density ρ . The gravitational radiation source must then be proportional to the time-varying quadrupole moment. In 1918, Einstein developed a formula for \mathbf{h} as a function of the second time derivative of the quadrupole moment:

$$\bar{h}_{ab} = \frac{2G}{c^4 R} \frac{d^2}{dt^2} I_{ab}, \quad (2.35)$$

or

$$\mathbf{h} = \frac{2G}{c^4 R} \ddot{\mathbf{I}}, \quad (2.36)$$

where R is the distance from the source [6]. Although this derivation was for non-self-gravitating sources moving much slower than the speed of light, it is still a good approximation for most sources as long as the gravitational radiation wavelength, $\lambda/2\pi$, is much longer than the source. While this is the case for some sources, it does not include many of the strongest and most interesting. Regardless, it is still a useful approximation for giving us some idea of what geometries to look for in our sources.

It is important to look at what equation 2.36 means practically. Do *any* sources exist that could produce detectable waves? As discussed previously, the factor G/c^4 is extremely small ($\sim 10^{-44} \text{ kg}^{-1} \text{ m}^{-1} \text{ s}^2$). Current interferometric detectors (see chapter 3) have maximum strain sensitivities of the order 10^{-23} . A terrestrial source even one meter away would have to have a \ddot{I} on the order of $10^{21} \text{ kg m}^2 \text{ s}^{-2}$ to be detectable, which is clearly impossible (this mass of the entire earth is only $\sim 6 \times 10^{24} \text{ kg}$). However, astrophysical sources can easily achieve huge \ddot{I} , large enough to overcome the minuscule pre-factor even at large astronomical distances.

It is clear that a nonzero quadrupole moment requires a non-spherically symmetric mass distribution. The challenge, then, is to identify astronomical entities lacking spherical symmetry yet still massive enough and rotating fast enough to produce

gravitational waves strong enough to be detected on or near the earth. This is, of course, not trivial since massive bodies have a propensity for spherical symmetry. There are, however, quite a few good candidates, the most important of which is the compact binary star system. These and other candidates have been discussed extensively in the literature, but we will be discussing some of them in the context of multimessenger astronomy in chapter 4.

2.4 Observational evidence of gravitational radiation

To date, there have been no direct observations of gravitational waves (although chapter 3 will discuss many of the ongoing searches). There is, however, conclusive indirect evidence. In 1974, Russell A. Hulse and Joseph H. Taylor Jr. made the first discovery of a binary pulsar, known as PSR 1913+16 using the 300-m Arecibo radio telescope [9, 10]. This unique system provided a powerful measure of the effects of general relativity. By 1989 they had gathered enough observations of the pulsar to show conclusively that the period of the binary orbit was decreasing at a rate exactly predicted by general relativity [11, 12]. The orbital decay is entirely attributable to the emission of gravitational radiation from the system. Figure 2-2 shows the measured shift in periastron of PSR 1913+16 from 1978 to 2005 and its agreement to the predictions of general relativity. This system will continue to emit gravitational radiation and decay until it merges as a compact binary coalescence (see section 4.2.1) in roughly 3×10^8 years.

For their discovery of the pulsar, and for the subsequent GR investigations, Hulse and Taylor were awarded the 1993 Nobel Prize in Physics.

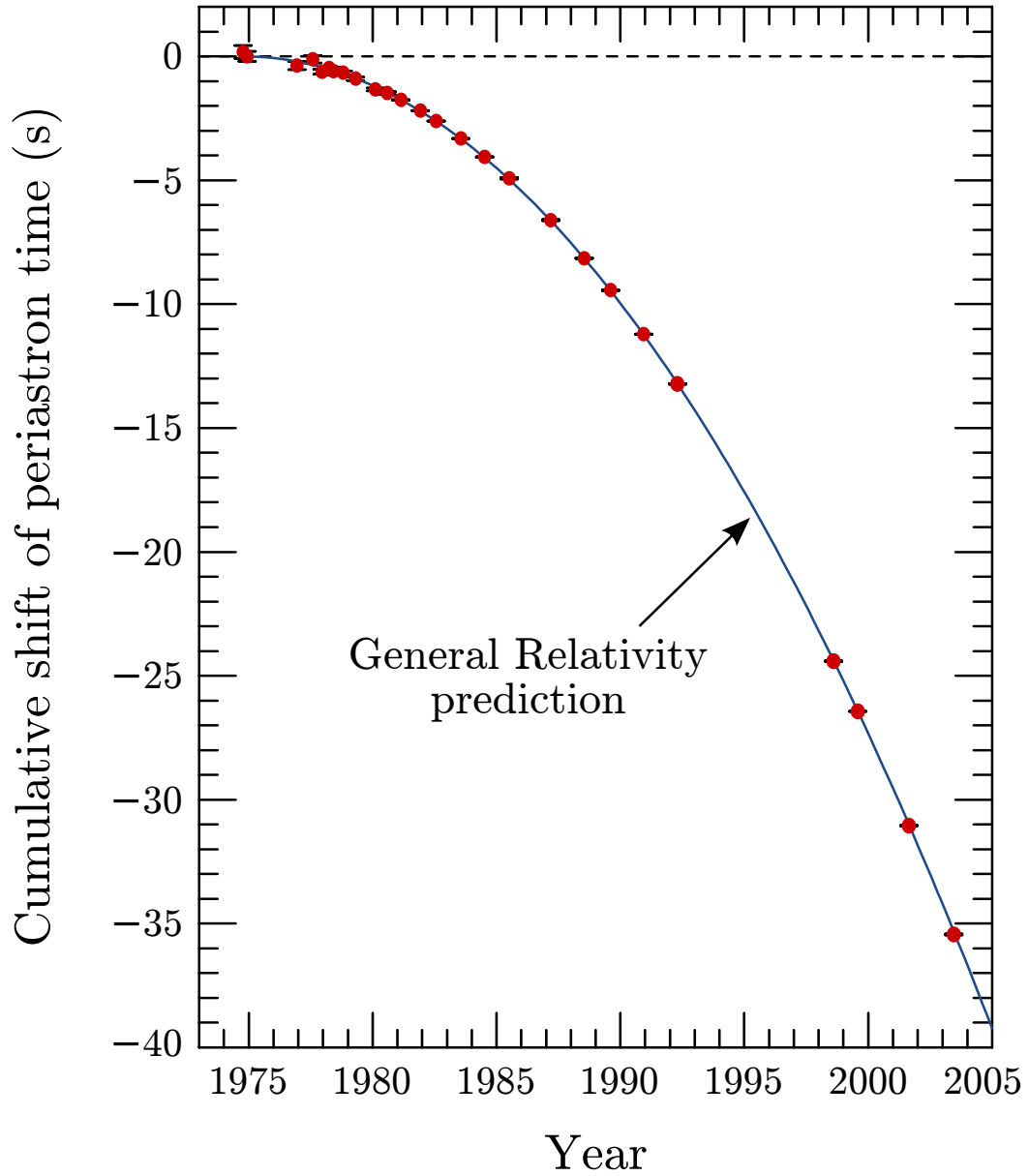


Figure 2-2: Orbital decay of PSR B1913+16. The data points indicate the observed change in the epoch of periastron with date while the parabola illustrates the theoretically expected change in epoch for a system emitting gravitational radiation, according to general relativity (adapted from [13]).

Chapter 3

Detection of Gravitational Waves with Interferometric Detectors

The search for gravitational waves has had an interesting and colorful history. The field was essentially founded by the pioneer experimentalist Joseph Weber, who first attempted searches using resonant bar detectors in the 1960s. These detectors were made of giant solid metal cylinders that were finely tuned to be resonant at particular frequencies where gravitational waves were thought to be present.

In the 1970s, scientists began experimenting with the idea of using optical interferometers as gravitational wave detectors [14]. A significant benefit that interferometric detectors have over bar detectors is their *broadband* nature. Interferometers can be made sensitive to very wide ranges of frequencies, and therefore many more sources of gravitational waves. Already by the 1980s experiments with broadband detectors had begun, and by the late 1990s they had eclipsed bar detectors to become the primary type of detector used in experiments and searches.

The idea of using interferometers to measure metric perturbations was not new. A. A. Michelson invented what has become known as the *Michelson interferometer* to measure, with Edward Morley in 1887, the motion of the earth relative to a hypothetical *luminiferous aether*. This motion was famously not seen and led directly to

the advent of the special and general theories of relativity.

A Michelson-type interferometer generally consists of two arms at right angles to each other. Light is obliquely incident on one side of a beam splitter which splits the light down the two perpendicular arms. At the end of the arms are mirrors that redirect the light back to the beam splitter, where it is recombined. Whether the light exits at the port it entered, the so-called *symmetric* port, or the opposite port, the *antisymmetric* port, depends on the interference condition at the beam splitter, which is directly related to the relative lengths of the two arms. Antisymmetric length changes in the arms produce light level changes at the antisymmetric port, thus the name.

Michelson's idea was to use this device to measure the relative speed of light in the two perpendicular arms. However, even a cursory glance at the effect of a gravitational wave on local spacetime, as seen in figure 2-1, makes it apparent that this same principle could be applied equally well to the detection of gravitational waves.¹ Imagine a Michelson interferometer placed at the origin of the coordinate system in figure 2-1, with one arm lying on the x axis and the other lying on the y axis. If the mirrors are effectively isolated from the ground then they can act as *test masses* in a locally inertial reference frame. The effect of a gravitational wave passing through this configuration would be a differential motion of the mirrors at the ends of the arms, thereby producing an oscillating interference condition at the beam splitter. The Michelson interferometer has become a gravitational wave detector.

Actually creating an interferometer capable of taking advantage of this effect is far from trivial. The greatest challenge, as discussed previously, is the very small strains that we're dealing with. Even the strongest sources are expected to produce strains of only 10^{-22} . This means that a strain sensor with a length of one kilometer would need to be sensitive to distance perturbations of a mere 10^{-19} meters. It is difficult to even grasp how astronomically small this number is. The diameter of a

¹See [15, 16] for interesting discussions about why this is true in current detector designs.

proton is generally thought to be of the order 10^{-15} meters. This means that the length perturbations we are looking for are *four orders of magnitude smaller* than a proton. Most impressively, that these strain sensitivities are actually being achieved in modern detectors.

3.1 Overview of current detectors

The current field of experimental gravitational wave physics is dominated by two large collaborations: the LIGO Scientific Collaboration [1], based in the United States, and the Virgo Collaboration [17], which is mainly a joint effort between France and Italy. LIGO operates two 4 km-baseline detectors in the United States: one in Hanford, WA (“H1”) and one in Livingston Parish, LA (“L1”). Virgo operates a single 3 km-baseline detector in Cascina, Italy (“V1”). In 2007 the LIGO and Virgo collaborations entered into a cooperative data-sharing agreement and formed the joint LIGO/Virgo Collaboration.

There are a couple of other international collaborations that have been pursuing research into large-scale interferometric detectors. The German/British GEO Collaboration [18] operates a 600 m-baseline detector in Hannover, Germany. This detector has a different configuration than the LIGO/Virgo detectors and is less sensitive in the important low-frequency range where signals are more plausible. However, this detector is being used as a test platform for advanced quantum readout methods that may be used in future detectors. The Japanese TAMA Collaboration [19] operates a 300 m-baseline detector in Tokyo, Japan.

Table 3.1 is an overview of the current detectors and some proposed detectors, some of which have secured funding for development.

	detector	location	baseline (m)
1st generation	LIGO (H1) [1]	Hanford, USA	4000
	LIGO (L1) [1]	Livingston, USA	4000
	Virgo (V1) [17]	Pisa, Italy	3000
	GEO600 (G1) [18]	Hanover, Germany	600
	TAMA300 (T1) [19]	Tokyo, Japan	300
2nd generation	Adv. LIGO (H1) [1]	Hanford, USA	4000
	Adv. LIGO (L1) [1]	Livingston, USA	4000
	Adv. LIGO (H2) [1] †	Hanford, USA	4000
	AIGO (A1) [20] †	Perth, Australia	4000
	Adv. Virgo (V1) [17]	Pisa, Italy	4000
	GEO HF (G1) [18]	Hanover, Germany	600
	LCGT (C1) [21]	Kamioka mine, Japan	3000
3rd generation	Einstein Telescope [22]	Europe(?)	?
space	DECIGO [23]	space	1×10^6
	LISA [24]	space	5×10^9
	Big Bang Observer	space	?

Table 3.1: Active (“1st generation”) and proposed interferometric detectors. The 1st generation detectors were all constructed and are either currently operational or being decommissioned. The 2nd generation detectors are all being constructed, or have secured funding and will begin construction soon. Beyond 2nd generation is still speculative. †: while the current Advanced LIGO baseline design calls for a second full-scale interferometer co-located with H1 at Hanford (H2), there is a proposal currently under review to move this interferometer to a new facility in Australia (A1). In either case, there will be three Advanced LIGO-like detectors.

3.2 Detector description

In this section we describe the LIGO and Virgo detectors, since these were used for the searches described herein. The LIGO and Virgo detectors are quite similar, and the two LIGO detectors are essentially identical. LIGO and Virgo use similar interferometer configurations and generally have similar design principles and detection strategies. They also face many of the same technical challenges.

3.2.1 Interferometer configuration

Figure 3-1 is a schematic diagram of the interferometer configuration used by the three current LIGO/Virgo detectors. The basic Michelson topology is created by the beam splitter (BS) and the two end test masses (ETM). The field has advanced significantly in the last couple of decades, and the modern LIGO/Virgo interferometers have improved on the basic configuration in a number of ways to increase considerably the interferometer sensitivity.

The primary improvement over the simple Michelson topology is to replace the interferometer arms with Fabry-Pérot cavities. This is done by placing partially transmitting mirrors (input test masses [ITM]) at the entrances to the arms. The ITM/ETM then form resonant cavities which trap the light and increase the number of round trips that the photons make in the arms, effectively increasing the length of the arms by the same factor. This can have a very large effect when the cavity gains are large.

In interferometer operation, the interference condition at the beam splitter is such that the antisymmetric port of the Michelson interferometer is *dark*, i.e., very little of the input light leaves through the antisymmetric port. (Because of this, the antisymmetric port is sometimes referred to as the “dark port.”) This means, by conservation of energy, that all the remaining light must be redirected back toward the input symmetric port. Another major improvement is then to place another

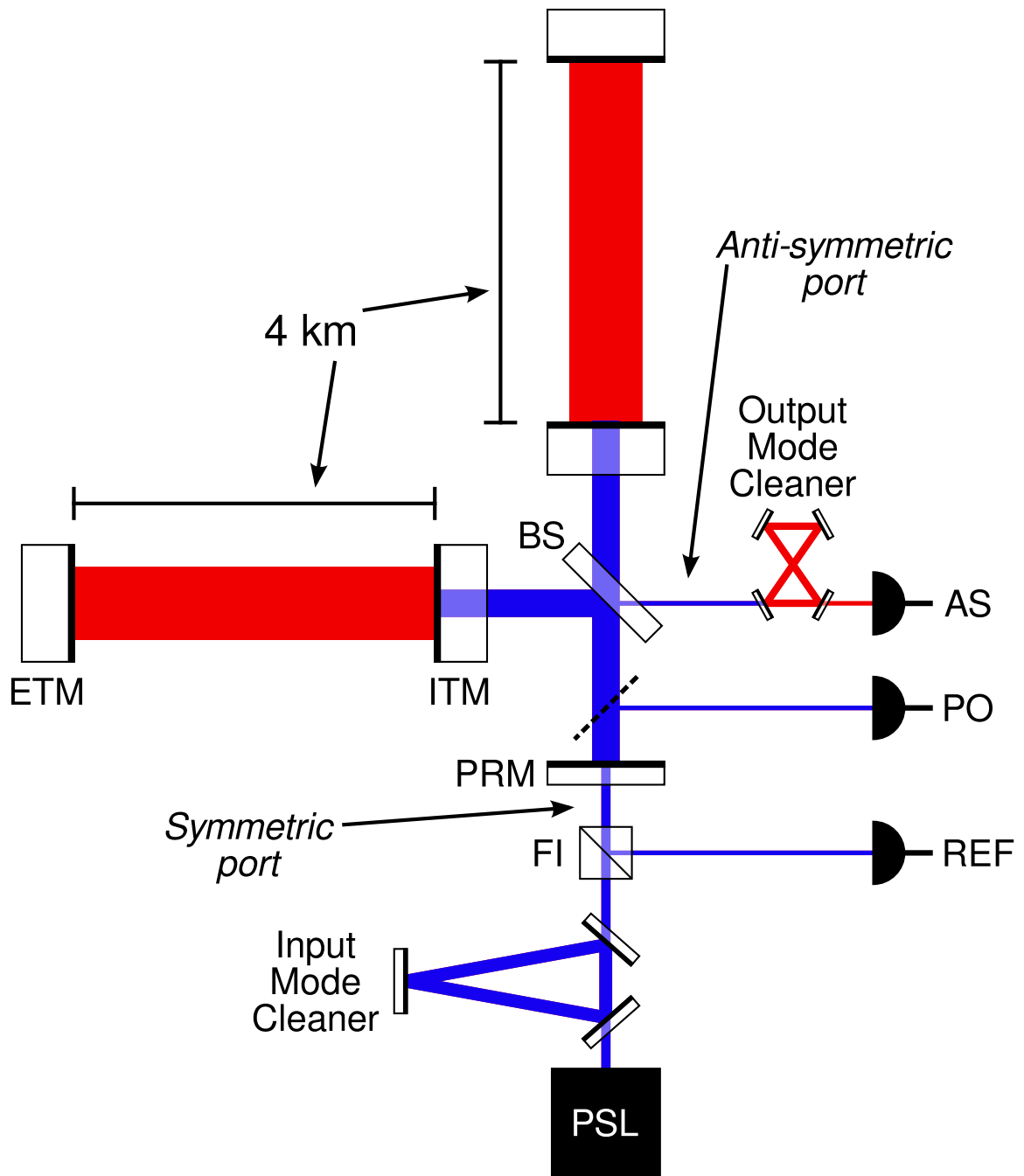


Figure 3-1: Schematic diagram of the LIGO/Virgo interferometric gravitational wave detectors in their current *power-recycled Fabry-Pérot Michelson* configurations. The red beams indicate the presence of just the carrier fields, whereas the blue beams indicate the presence of carrier and sideband fields. Definitions: PSL: pre-stabilized laser; FI: Faraday isolator; PRM: power recycling mirror; BS: beam splitter; ITM: input test mass; ETM: end test mass; REF: reflection port; PO: pick-off port; AS: antisymmetric port.

partially transmitting mirror at the symmetric port to redirect this exiting light back into the interferometer. This mirror is known as the *power recycling mirror* (PRM), and the new cavity formed by the PRM and the two input test masses is known as the *power recycling cavity* (PRC). The effect of the PRC is to increase the amount of power at the beam splitter, which therefore increases the shot-noise-limited phase sensitivity.

The combined configuration is referred to as a *power-recycled Fabry-Pérot Michelson* (PRFPM). In LIGO, the combined effect of both of these improvements is an optical power gain of about 8,000 in the arms. This translates to a circulating power in the arm cavities of up to 20 kilowatts for Initial LIGO [4], and even more for the current configurations with increased input laser power.

3.2.2 Interferometer readout and control

Resonant optical cavities are very nonlinear devices. The resonance conditions are narrow, offering only a limited range over which linearity can be achieved and the signal can be read out. Furthermore, the test masses must reside in inertial space and be free to move relative to each other. This means that the resonance conditions of various cavities must be actively maintained by use of positive feedback control systems.

Feedback control systems, sometimes referred to as *servo-mechanisms* (or just “servos”), are commonly used in many applications to maintain a system in a desired state. In interferometric detectors, the primary method used for feedback control of the optical cavities is a generalized version of a technique known as *Pound-Drever-Hall* (PDH) *locking* [25] (see figure 3-2 for a basic description). This technique was notably invented by gravitational wave physicists working on early interferometric detectors. In this technique, an error signal is derived from the beating of the main *carrier* light, which is resonant in all cavities, with RF *sidebands*, which are added to the main beam via phase modulation and which are resonant in only the power recycling

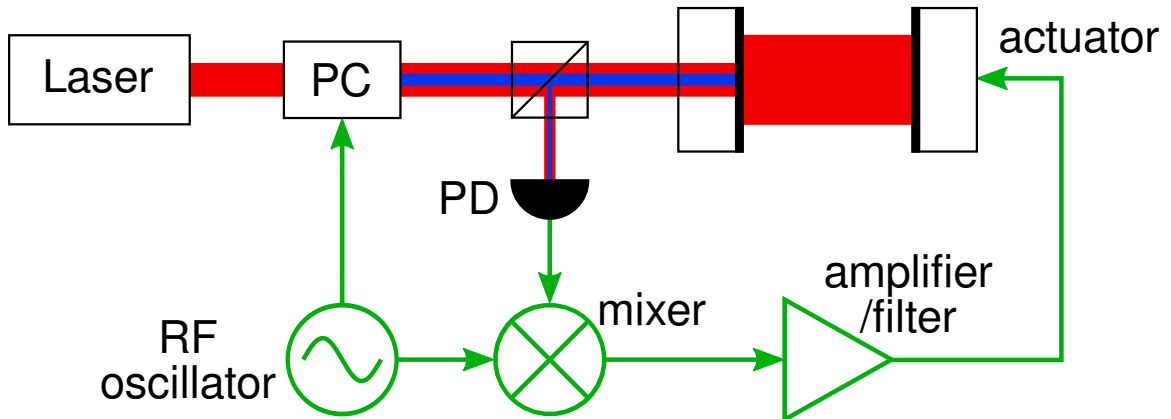


Figure 3-2: Schematic diagram of the Pound-Drever-Hall cavity locking technique [25]. The light from the laser (the “carrier,” red beam) is passed through a *Pockels cell* (PC) which adds RF sidebands to the light via phase modulation (blue beam). The RF sidebands are not resonant in the cavity and are reflected back from the cavity input mirror. The carrier and the RF sidebands mix at the photo detector (PD). The output of the PD is demodulated at the original RF frequency to produce an error signal that is then amplified and fed to actuators that push on the mirrors to maintain the resonance condition.

cavity. When the cavity deviates from resonance, the phase of the carrier field shifts relative to the (relatively) static field of the sideband, changing the amplitude of the beat frequency at the output. This technique is also known as *heterodyne detection* since it involves the combining of differing light fields that are present in different parts of the interferometer. The error signal is filtered and amplified, and the product is used to actuate directly on the test masses via electromagnetic actuators affixed to the them.

There are four main length degrees of freedom (DOF) in the PRFPM interferometer configuration: the three cavity lengths and the relative arm phase of the Michelson PRC. These four DOF can be translated into a basis more relevant to the full interferometer: the differential and common DOF of the full arms, L_- and L_+ , and the differential and common DOF of the Michelson PRC, l_- and l_+ . The signals needed to control these DOF can be derived from detection of the light at the antisymmetric port and the reflected (symmetric) port, and from an intra-cavity pick-off mirror in

the power recycling cavity (see figure (3-1)). A good description of how the error signals needed to control the various DOF can be derived from various sensing ports can be found in [26].

The most critical DOF is L_- , since that is the degree of freedom upon which the gravitational wave acts. The error signal for the L_- DOF is derived from the beam that exits through the interferometer antisymmetric port. This differential length control error signal is the gravitational wave signal readout for the detector.

In Initial LIGO, the PDH signal was derived from the sideband and carrier light that leaks out the antisymmetric port. In Enhanced LIGO, a new technique was used called *DC readout* or *homodyne detection*. In this technique, the error signal is derived from direct measurement of the intensity of the carrier beam at the antisymmetric port. It was pursued as a way to eliminate the noise associated with intensity fluctuations of the RF sidebands. For this technique a new transmissive ring cavity was inserted into the sensing beam leaving through the antisymmetric port. This cavity suppresses the RF sidebands that would otherwise dominate the signal and is known as the *output mode cleaner* (OMC).

In addition to the length degrees of freedom, all of the interferometer's 16 angular degrees of freedom must also be controlled to maintain proper alignment. This is needed to maintain the full light power build-up needed to achieve maximum sensitivity. Misalignment of the interferometer can be measured through the use of specialized photo-detectors that can measure the relative alignment of the wavefronts of the carrier and sideband fields.

The primary length and angular control systems are implemented digitally. This provides the flexibility essential for realizing stable operation. Acquisition of the locked state of the interferometer also requires filters and gain levels that can be changed quickly, which is more easily accomplished with digital computer control. In LIGO, the sample rate is 2^{14} samples/second, while in Virgo it is 2×10^4 samples/second.

3.2.3 Light source

The light sources for the interferometers are very stable, single-frequency, continuous wave lasers that operate at a wavelength of 1064 nm. The Initial LIGO laser power was 10 watts, and this was increased to more than 30 watts for Enhanced LIGO. The laser light goes through multiple stages of power and frequency stabilization before being injected into the interferometer. Frequency stabilization is handled by a stable reference cavity, as well as a transmissive ring cavity known as a *pre-mode cleaner*. The mode cleaner suppresses high-frequency frequency noise, as well as any light not in the fundamental Hermite-Gaussian spatial transverse electromagnetic mode (TEM₀₀). This entire system is known as the *pre-stabilized laser* (PSL).

Another important function that the PSL serves is to add the radio frequency side bands to the laser beam that are used for the Pound-Drever-Hall locking of the arm and power cycling cavities. The side bands are the product of RF phase modulation on the main laser beam.

3.2.4 Vacuum system

After leaving the PSL, the beam enters the vacuum system. The interferometers must be isolated in ultra-high vacuum to provide both acoustic isolation and elimination of phase fluctuations from index of refraction modulation of the air. All of the core optics are housed in large chambers, which are connected via 1.2 meter diameter stainless steel *beam tubes*, through which the interferometer beams pass. The beam tubes are lined with hundreds of *baffles* designed to absorb scattered light from the vacuum chamber walls. Scattered light is an important concern since the vibrational motion of the tube walls is typically more than 10 orders of magnitude larger than the motions of the test mass surfaces. The residual gas pressure of the vacuums is $< 10^{-8}$ torr, making the LIGO/Virgo vacuum systems the largest ultra-high vacuum systems in the world.



Figure 3-3: Photo of the L1 vacuum system vertex in the LIGO Livingston Observatory corner station (Courtesy LIGO Laboratory).

3.2.5 Optics and test masses

The interferometer optics, including the test masses, are made of fused-silica substrates with multilayer dielectric coatings. They are designed to have very low absorption and scattering. The absorption levels in the test mass coatings are generally less than a few parts per million (ppm), and the total scattering losses are less than 70 ppm. The test masses themselves are 25 cm in diameter and 10 cm thick, weighing 10.7 kg, with highly polished spherical surfaces.

3.2.6 Thermal compensation

When operating at full power, the ITM can absorb up to 60 mW. This absorption produces a thermal lens in the ITM. While this lensing does not have much of an effect on the carrier mode resonant in the arm cavities, it can have a strong effect on the resonance condition in the power cycling cavity, and therefore on the resonance of the RF sidebands. To counteract this effect, a thermal compensation system is used

to heat the ITM faces in an inverse pattern to the central heating pattern from the main beam, thereby counteracting the thermal lens.

3.2.7 Suspensions and seismic isolation

In order for the interferometer to actually probe the properties of the local spacetime metric, the test mass mirrors must reside in inertial space and must be isolated from the ground. This is achieved through multiple layers of vibration isolation that act to mechanically decouple the test masses from their surroundings. The suspensions and seismic isolation systems are the most complicated mechanical subsystems in the detectors.

The basic idea of mechanical isolation is to use the unique frequency response properties of a damped mechanical resonator. Above the mechanical resonance frequency, the frequency response of a damped mechanical resonator falls off as f^{-2} . The lower the resonant frequency, the greater the isolation. Furthermore, this effect is multiplicative, such that multiple resonator stages in series will each add an additional power of -2 of isolation per stage.

Gravitational wave interferometers take advantage of this by using multiple mechanical resonators in series to isolate the test masses from the ground. The resonators are designed to have resonance frequencies as low as possible below the signal band. The actual implementation of these principles is slightly different in LIGO and Virgo.

In LIGO, the masses are suspended as simple pendula. The pendulum provides an isolation of 2×10^4 at 100 Hz. Most of the isolation, though, comes from hanging the pendula from passive mass-spring vibration isolation platforms. There are four stages in the isolation stacks, providing f^{-8} isolation above 10 Hz. The combined effect of these two isolation systems is greater than 10^{12} suppression of ground motion at 100 Hz.

Virgo, on the other hand, uses a large system known as the “superattenuator” [27]. The 8m-tall superattenuator consists of 7 seismic filters, each hung from the other

by cantilevered blade springs. The blade springs provide vertical isolation while the pendula provide horizontal isolation. The entire structure hangs from an actively controlled seismic isolation table. Overall, the system provides more than 7 orders of magnitude of horizontal and vertical isolation at ~ 4 Hz.

For Enhanced LIGO, a new active seismic isolation table was installed under the output mode cleaner. This new system is identical to what will be used in Advanced LIGO and was installed primarily to test the new system.

3.2.8 Environmental monitoring

An important part of the LIGO experiment is making thorough measurements of the ambient local detector environment. Excess noise in the local environment can couple into the gravitational wave readout channel and mask potential signals. Understanding environmental couplings is crucial for mitigating them. In the event that they can't be fully mitigated, the information about the coupling can be used to create data quality vetoes that mark times where known excess environmental noise has adversely affected the quality of the data. Some of the environmental monitors are:

- Seismometers and accelerometers that measure vibrations of the ground and various interferometer components
- Microphones that measure acoustic noises
- Magnetometers that monitor magnetic fields that could couple to the test mass actuators or control electronics
- Radio receivers that monitor spurious RF fields that could couple into the readout electronics

3.3 Interferometer response

Figure 2-1 showed the effect of a gravitational wave passing perpendicularly through a mass ring lying in the $x - y$ plane. The response of a real interferometric detector aligned with the $x - y$ axes to the same wave is as you might expect: it is maximally sensitive to the h_+ polarization and has zero sensitivity to the h_\times polarization, which would move both arms exactly in phase. This then indicates that the interferometer has a response that varies with the polarization and wave vector of the incoming gravitational wave.

The response of the interferometer to the incoming h_+ and h_\times wave polarizations as a function of relative angle of incidence, given by the angles θ and ϕ , and relative polarization angle, ψ , is given by the interferometer *response functions*, F^+ and F^\times :

$$\begin{aligned} F^+(\theta, \phi, \psi) &= \frac{1}{2} \cos 2\psi (1 + \cos^2 \theta) \cos 2\phi - \sin 2\psi \cos \theta \sin 2\phi \\ F^\times(\theta, \phi, \psi) &= -\frac{1}{2} \sin 2\psi (1 + \cos^2 \theta) \cos 2\phi - \cos 2\psi \cos \theta \sin 2\phi. \end{aligned} \quad (3.1)$$

The measured strain is then the linear combination of the response of the interferometer to the h_+ and h_\times polarizations:

$$h(t) = F^+(\theta, \phi, \psi)h_+(t) + F^\times(\theta, \phi, \psi)h_\times(t). \quad (3.2)$$

Figure 3-4 shows this antenna response function for various wave polarizations over all θ and ϕ . The result is the interferometer *antenna pattern*.

Interferometric detectors also have a slight frequency dependence [28, 29, 30]. The response can be represented by a single-pole transfer function:

$$R(f) \propto \frac{1}{1 + if/f_p}, \quad (3.3)$$

where f_p is the frequency of the cavity pole, which is related to the light storage time

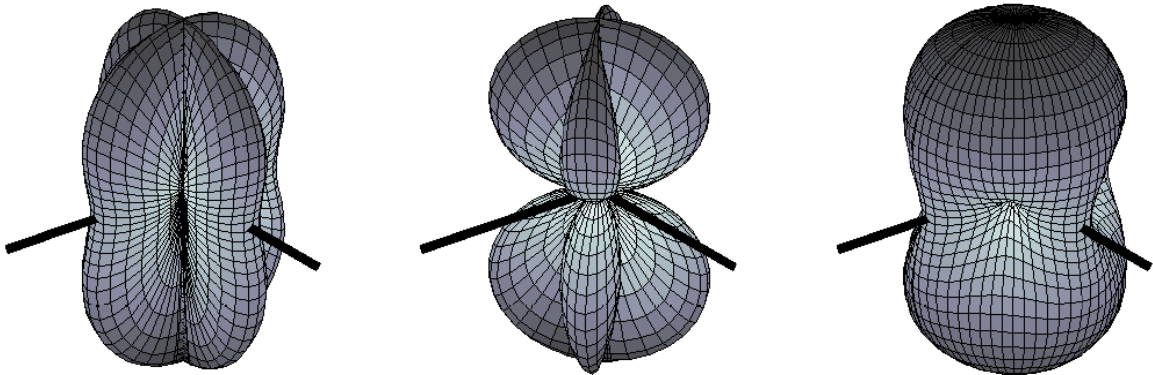


Figure 3-4: Antenna response pattern for a interferometric gravitational wave detector, in the long-wavelength approximation. The interferometer beamsplitter is located at the center of each pattern, and the thick black lines indicate the orientation of the interferometer arms. The distance from a point of the plot surface to the center of the pattern is a measure of the gravitational wave sensitivity in this direction. The pattern on the left is for $+$ polarization, the middle pattern is for \times polarization, and the right-most one is for unpolarized waves. (Courtesy [4])

in the arm cavities, τ_s , by $f_p = 1/4\pi\tau_s$. At frequencies above the cavity pole, the response falls off as f^{-1} . In LIGO the cavity pole is at about 85 Hz.

Figure 3-4 and equations (3.2) and (3.3) are analytic representations of the theoretical detector response. They actually say very little about the capability of the detector to measure strain. The actual limits of strain detectability are largely encapsulated in what is arguably the most important figure of merit for interferometric detectors: the detector *strain sensitivity*. Strain sensitivity plots, frequently referred to as simply *spectra*, are a measure of the broadband residual noise amplitude spectral density of the detector, in units of $1/\sqrt{\text{Hz}}$. The amplitude spectral density is the square root of the noise power spectrum and gives the strain per square root measurement bandwidth.

Figure 3-5 is a plot of the most recently measured and calibrated strain sensitivities of the LIGO and Virgo interferometers during the S6 and VSR3 science runs.

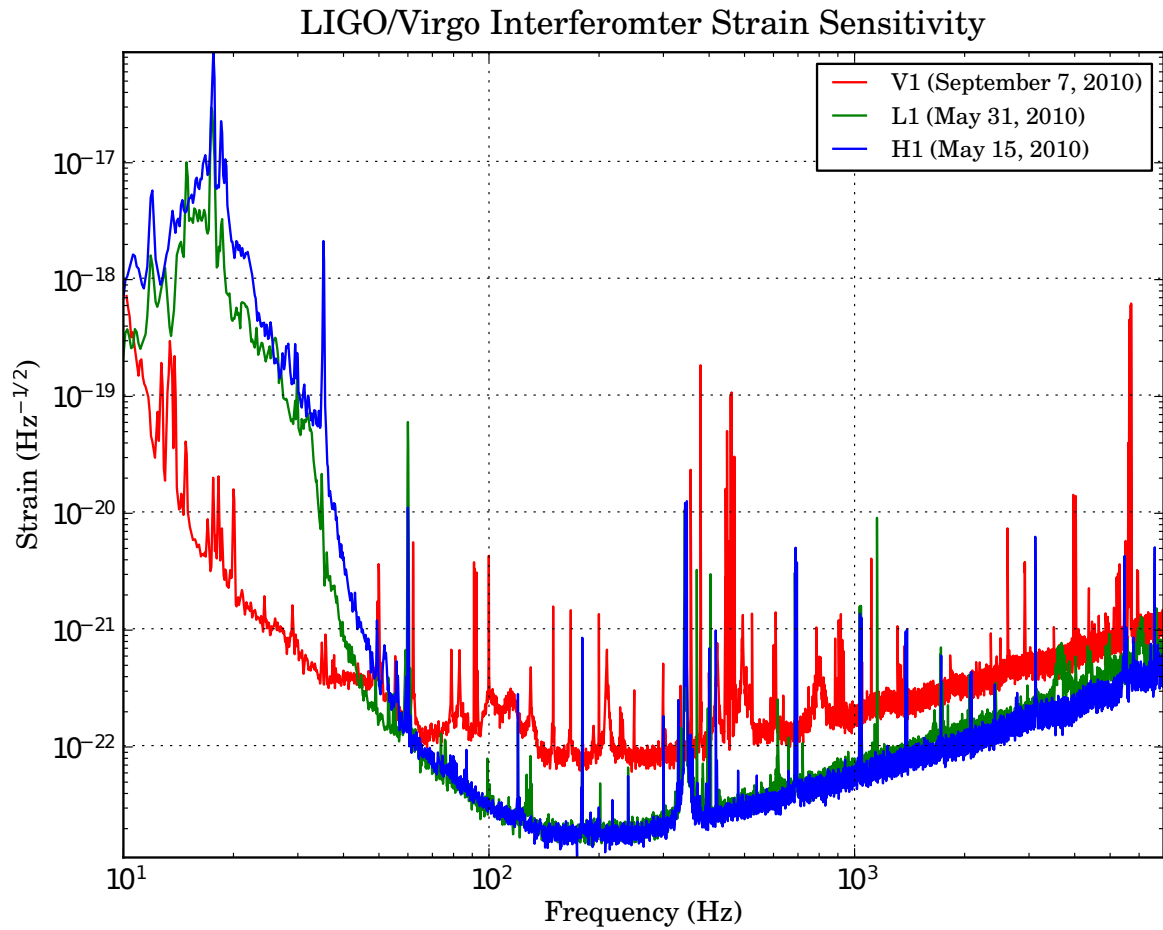


Figure 3-5: Strain sensitivity of the LIGO and Virgo detectors during the S6/VSR3 joint science run.

3.4 Noise sources

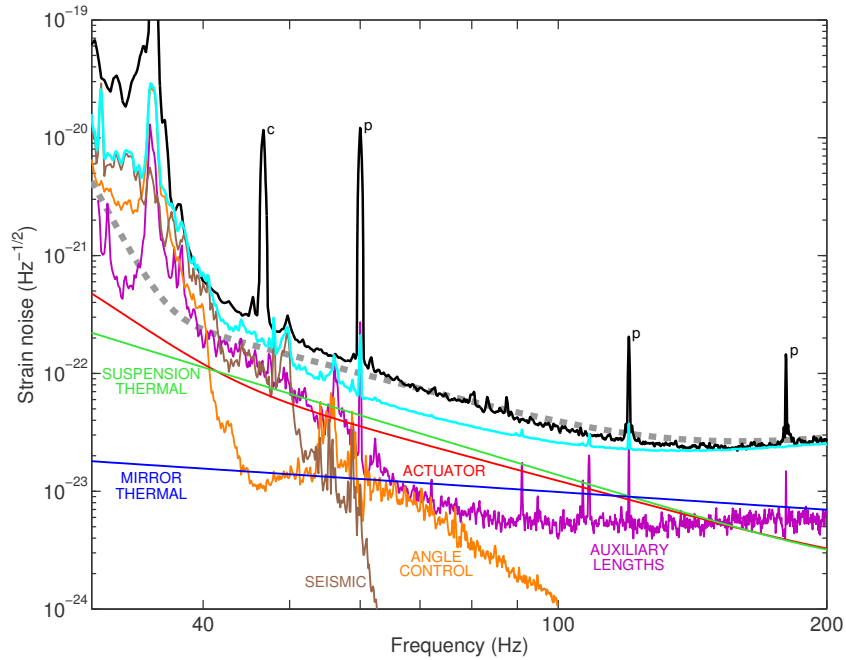
There are two main types of noise sources that contribute to the distinct shape of the strain spectra curves in figure 3-5. At the low frequency end of the sensitivity curve, below 200 Hz, interferometric detectors are dominated by *displacement noise* sources. Displacement noises directly cause motion of the test masses or mirror surfaces. On the high frequency end, above 100 Hz or so, detector sensitivity is typically dominated by *sensing noise* which obscures the test mass motions and limits the ability to detect them. Both of these types of noise sources are illustrated in figure 3-6, which shows the noise budget for the LIGO H1 detector during Initial LIGO.

The displacement noise levels in Enhanced LIGO are not notably improved over those in Initial LIGO. Enhanced LIGO did however significantly improve the shot noise performance by increasing the circulating power in the interferometers, therefore lowering the overall effect of sensing noise. This will be discussed further in section 3.4.5.

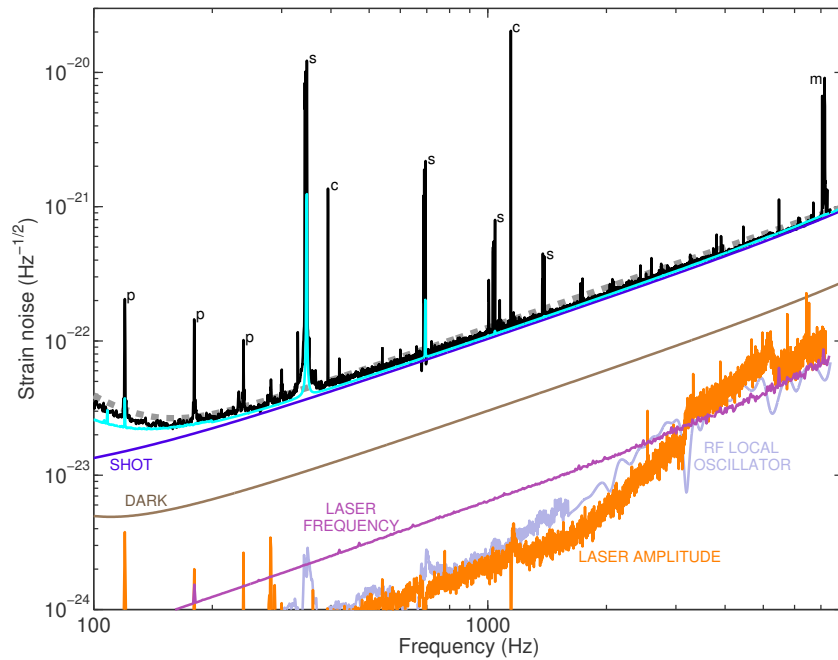
3.4.1 Seismic noise

The largest single noise source affecting the interferometers and dominating the strain sensitivity at low frequencies is seismic noise. The seismic noise peaks at a couple of millihertz in what is known as the “microseism,” caused largely by ocean waves. In the 0.5 to 10 Hz range, the seismic noise is mostly man-made, from sources such as nearby construction and automobile traffic. Above 10 Hz, the noise comes from acoustic and vibrational noises from the observatory site facilities themselves, such as the building HVAC systems. Problematically, most of these sources are non stationary, meaning that they have large variation over various time scales. The anthropogenic sources, for instance, have strong daily variation. Earthquakes and other transient sources are important as well.

Estimating the seismic contribution to the noise budget involves first measuring



(a) displacement noise sources



(b) sensing noise sources

Figure 3-6: List of known noise sources contributing to the H1 strain sensitivity during Initial LIGO. The top plot shows the displacement noise sources that dominate at low frequencies up to 200 Hz. The bottom plot shows the sensing noise sources that dominate at high frequencies above 100 Hz. The black curve is the measured strain sensitivity, the gray dashed curve is the design goal, and the cyan curve is root-square-sum of all the known noise contributors. The labeled peaks are: *c*: calibration line; *p*: power lines harmonics; *s*: suspension wire vibrational modes; *m*: test mass vibrational mode. (Courtesy [4])

the actual ground motion with seismometers and accelerometers (see section 3.2.8). A rough estimate of the displacement noise above 0.1 Hz at a quiet site is:

$$x(f) = \left(\frac{10^{-8}}{f^2} \right) \frac{\text{m}}{\sqrt{\text{Hz}}}, \quad f > 0.1\text{Hz}. \quad (3.4)$$

This noise is then attenuated by the suspensions and seismic isolation systems described in section 3.2.7.

For LIGO, the result is a “seismic wall” at roughly 40 Hz. However, the situation below 40 Hz in LIGO is actually significantly worse than what is predicted from seismic noise alone. This can be seen in figure 3-6a as the discrepancy between the measured noise (black curve) and the predicted noise (cyan curve) below 40 Hz. As of this writing, it is still unclear what the source of this excess noise is.

Because of their multi stage suspension systems, the seismic noise situation in Virgo is significantly better. As can be seen in figure 3-5, the performance of the Virgo interferometer (V1) is nearly 3 orders of magnitude better than H1 at 20 Hz.

3.4.2 Thermal noise

In the most sensitive region of the strain spectrum, from 50 to 200 Hz, the sensitivity of the interferometers is dominated by thermal excitations of the test masses and their suspensions. Thermal noise is a fundamental noise source in any high-precision mechanical experiment and is one of the trickiest noise sources to understand and mitigate.

As dictated by the fluctuation-dissipation theorem, dissipative mechanisms in a mechanical system leach energy from coherent primary oscillatory modes of the system into other disordered thermal modes [31]. This theory was applied to measurements of test mass surfaces in [32] and again in [33] to produce the following formula for the

spectral density of fluctuations in a readout variable x :

$$S_x(f) = \frac{2k_B T W_{diss}}{\pi^2 f^2 F_0^2}, \quad (3.5)$$

where k_B is Boltzmann's constant, T is the temperature, W_{diss} is the time-averaged power dissipated in the system, and F_0 is the thermal driving force. In the case of gravitational wave interferometers the driving force is actually the light pressure on the test mass surface.

The important point to note about (3.5) is that the fluctuations increase with increased dissipation, which leads to dampening of a mechanical resonator. Dampening is inversely proportional to mechanical quality factor, Q . Mechanical systems with very high quality factor, and therefore low loss, will have less thermal noise. Another way to think about this is that for systems with high Q , excitations will be strongly absorbed by the primary vibrational modes, rather than being thermally dissipated broadly across all frequencies. The goal is to create mechanical systems with very low loss and very high quality factor. If the primary resonant modes can also be tuned to be outside the measurement band, then the effect of thermal noise in the instrument can be greatly reduced.

Thermal noise manifests in interferometric detectors in two important ways. The first is via the test mass suspension wires (*suspension thermal noise*). Dissipation in a suspension wire tends to come from the end of the wire where the wire flexes or rubs against its clamp. The second source is in the thin-film dielectric optical coatings on the test masses themselves (*mirror thermal noise*). While the test mass substrates have very low mechanical losses, the coatings have fairly high mechanical loss and are therefore a large source of thermal noise. These two noise sources dominate between 50 and 200 Hz.

It is very difficult to measure the broadband thermal noise in situ. The suspension and mirror thermal noise traces in figure 3-6a are derived from finite element models

of the mechanical properties of the test masses and their coatings and substrates.

3.4.3 Actuator noise

The test mass actuators pose a particularly difficult technical challenge. The actuator electronics chain, from the digital-to-analog converters (DACs) to the analog current amplifiers that ultimately drive the test masses, must have the largest dynamic range of all electronics in the system. It must be powerful enough to overcome the large seismic-induced motions of the test masses, particularly during times of high seismic noise (storms, earthquakes, etc.), which can require coil currents of tens of mAmps. However, the current noise must also be small enough to not cause excessive displacement noise on the test masses. The requirement on current noise turns out to be no more than a couple of pA/ $\sqrt{\text{Hz}}$ in order to remain below the thermal noise sources. While actuator noise is not a fundamental noise source, it is a real technical challenge to meet the requirements. This noise is only really reduced through clever electronics design, including the use of multiple paths that can be switched in situ, between high-gain modes of operation needed for locking the interferometer and low-noise modes needed for high sensitivity operation.

3.4.4 Auxiliary DOF noise

Another major technical challenge involves the reduction of noise associated with coupling between the primary differential length degree of freedom and the other length and angular degrees of freedom. There are two main problems. The first is that noise in the l_- and l_+ degrees of freedom in the PRC cavity can show up in L_- (*auxiliary length noise*). This PRC length coupling is mitigated by digitally subtracting the PRC error signals from the L_- control path. The second major contributor is spurious angular motions of the test masses (*angular control noise*). These angular fluctuations can cause the beam to displace from the cavity axis, producing a phase

shift that mimics a length shift in the cavity. Imbalances in the test mass actuators can also produce torques that cross-couple into piston motions of the masses. The angular couplings are mitigated by carefully balancing the test masses and their actuators, as well as through severe filtering of the angular control loops.

3.4.5 Shot noise

Above 100 Hz, interferometer strain sensitivity is entirely dominated by sensing noise in the form of *shot noise*. Shot noise comes directly from the fundamental quantum particle-like nature of photons. A light beam detected by a photo detector is not a continuous wave, but is instead ultimately a rain of individual photons, each impacting the photo detector at random times governed by Poisson counting statistics.

The expression for the phase noise at the detector is [34]:

$$\delta\phi(f) = \sqrt{\frac{4\pi\hbar c}{\eta P_{\text{BS}}\lambda} \frac{\text{rad}}{\sqrt{\text{Hz}}}}, \quad (3.6)$$

where \hbar is the reduced Plank's constant, c is the speed of light, λ is the light wavelength, η is the quantum efficiency of the photo detector, and P_{BS} is the light power at the beam splitter. There are two things worth noting about equation (3.6). The first is that the noise is *inversely* proportional to square root of the optical power at the beam splitter. This means that increasing the power at the beam splitter reduces the shot noise, which motivates the use of power recycling. The second thing to note is that there is no frequency dependence on the right side of (3.6); this noise has a completely flat, or “white,” frequency spectrum. The apparent increase in shot noise with frequency seen in figures 3-5 and 3-6b is not actually a property of the noise itself but is instead attributable to the inherent frequency response of the interferometer, as noted in equation (3.3).

Shot noise can also come from “junk” light on the photo detector, such as scattered light or carrier light not in the primary TEM₀₀ mode, that can not be used to read

out the GW signal.

Another important thing to note about equation (3.6) is that the shot noise level is inversely proportional to the square root of the laser power. This means that increasing laser power decreases the shot noise level. This motivates a desire for increased laser power. There is a limit to the benefit of increased laser power, though. As the laser power is increased this same shot noise effect begins to manifest as a random fluctuation force on the test masses known as *quantum radiation pressure*. This effect does not become apparent until the laser power is significantly higher than the levels currently in use, and it can be mitigated by increasing the mass of the test masses.

3.4.6 Other sensing noises

Other than shot noise, there are a couple of other sensing noise sources that are worth noting, even though they don't actually impact the current detector sensitivity. *Dark noise* is noise inherent in the photo detectors used to detect light at the anti-symmetric port. It is generally not too difficult to keep this noise below the shot noise level by careful design of the photo detectors and readout electronics. Laser frequency and amplitude noise are also technical noise sources that can couple into the differential degree of freedom, typically via imperfections in the optics in the two arms. These noises can be suppressed by careful design of the PSL (see section 3.2.3). Finally, noise in the RF oscillator used to impress the RF sidebands on the main carrier laser beam can also couple into the differential DOF. Noise in the amplitude of the RF oscillator can cause amplitude fluctuations in the side bands, while noise in the RF phase can couple in if the RF signal paths are not well tuned.

3.4.7 Excess noise

A notable feature of figure 3-6, specifically in the low-frequency displacement noise plot of figure 3-6a, is that the sum of all known noise sources (cyan curve) does *not*

match the measured strain sensitivity (black curve). This is particularly notable in the region below 35 Hz and in the region from 40 to 150 Hz. The low-frequency excess is presumably caused by higher-than-expected seismic noise coupling. More worrying, though, is the unidentified excess noise at the lowest point in the strain spectrum. The two best hypotheses to account for this excess are electric charge build-up on the test masses, and nonlinear up-conversion of low-frequency actuator coil currents occurring in the actuator magnets [4]. Both of these sources will need to be addressed in advanced detectors.

Other issues of particular importance to the analyses are non-Gaussianity, non-stationarity, and “glitchiness” in the noise. These are problems are faced by all interferometers, and they adversely affect the sensitivity of the searches (see chapter 5). High glitch rates and non-stationarity are particularly important because overcoming them incurs large computational costs. Figure 3-7 shows a sample of measured noise distribution for the H1 detector and indicates their deviations from the Gaussian ideal.

3.5 Detector improvements and future detectors

The field of gravitational wave physics has been growing rapidly. Work has already begun on the next generation detectors, and plans are being made for the so-called *third* generation and beyond. Table 3.1 includes some information on these future detectors.

As of October 20, 2010, construction has begun on the Advanced LIGO [35] detectors at the Hanford and Livingston facilities. A third Advanced LIGO detector will also be built, but at this time it is still unclear where. The initial proposal was to make the third detector co-located with H1, occupying the same vacuum system. There has recently appeared the possibility that this third detector could be built instead in a new facility in western Australia. As of this writing, the proposal is still

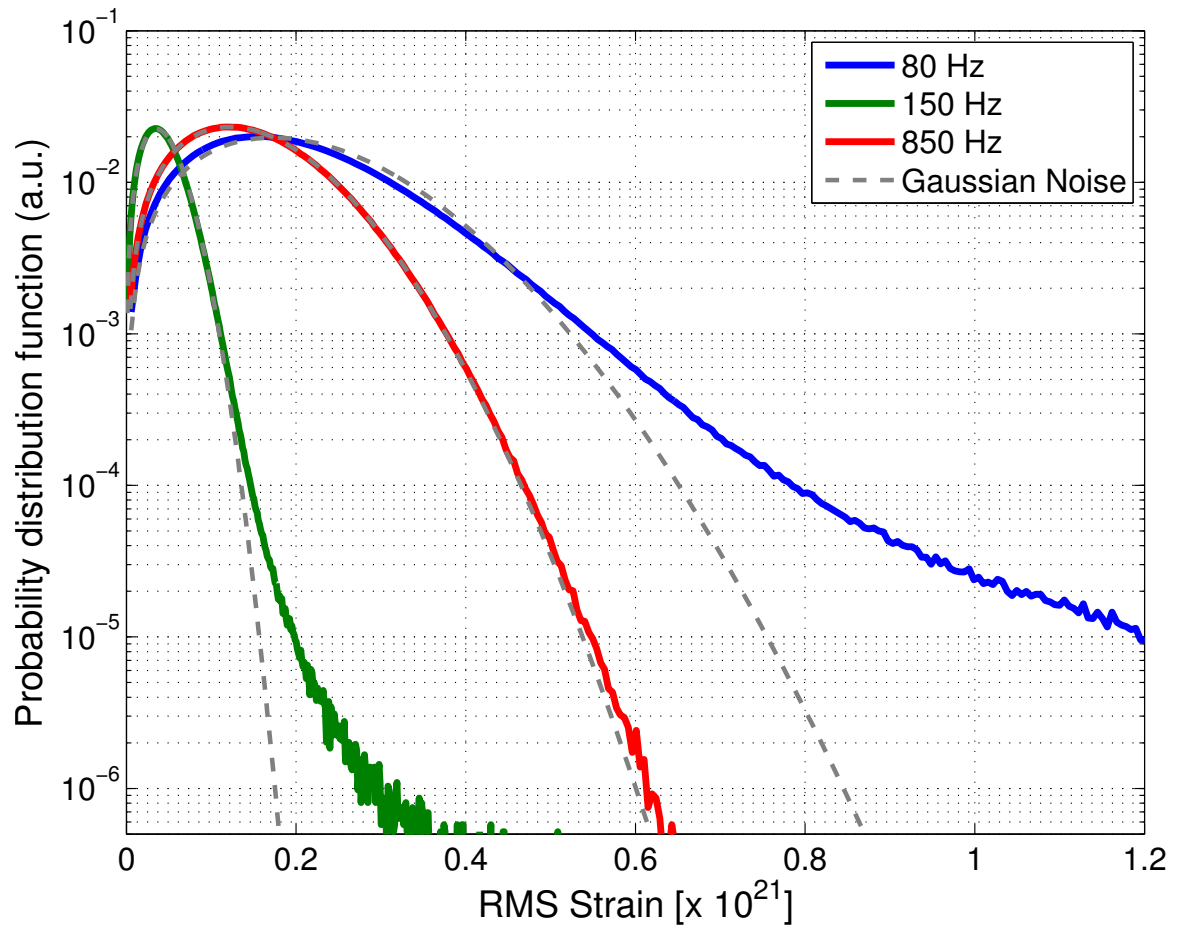


Figure 3-7: Distributions of strain noise amplitude at three frequencies in the measurement band of the H1 detector. Each curve is a histogram of noise spectral amplitude. The dashed lines indicate the Rayleigh distributions as expected for Gaussian white noise. (Courtesy [4])

under review. Work has also already begun on the Advanced Virgo [36] detector.

The Advanced LIGO and Virgo detectors will be debuting considerable technological advancements:

- The addition of signal recycling to the interferometer configuration
- A more powerful laser to decrease shot noise
- More massive test masses to reduce test mass thermal noise
- Multistage pendula and active isolation stacks to reduce seismic noise

There is also the possibility of injecting squeezed light into the anti-symmetric port to achieve further reduction of shot noise

Construction should soon start on the Japanese Large-scale Cryogenic Gravitational wave Telescope (LCGT) [21]. The LCGT facility will be in a mine to further reduce seismic noise. LCGT will also employ radiative cryogenic cooling of the test masses and suspensions.

Multiple space-based interferometers have been proposed to search for gravitational waves at much lower frequencies than are accessible by ground-based detectors. The Laser Interferometer Space Antenna (LISA) [24] would probe the millihertz range, and the Deci-hertz Interferometer Gravitational-wave Observatory (DECIGO) [23] would obviously be targeting the decihertz band.

Path-finding work has also begun on a third-generation detector known as the Einstein Telescope [22] that hopes to push sensitivities even further.

Chapter 4

Transient Multimessenger Astronomy with Gravitational Waves

Multimessenger astronomy, the coincident observation of an event with multiple forms of radiation, can provide significantly more information about a source than could be gathered from observations from only a single messenger alone. The physical processes that produce neutrinos, for instance, are quite different from those that produce visible light. Each messenger can provide different pieces to the puzzle of what is the source of the event, the nature of the progenitor, composition, envelope, distance, host galaxy, etc. Understanding when those emissions happen relative to each other and how they vary in time can give invaluable information about how the underlying physical processes interact.

This is all particularly compelling when it comes to observations of gravitational radiation emissions [37, 38]. Gravitational waves tell us about the bulk dynamics of matter, something that we have only been able to roughly infer from traditional observations. Furthermore, observation of a non-gravitational wave counterparts to a prospective gravitational wave observation can greatly bolster confidence in grav-

itational wave detection. This is an extremely important motivation in this current pre-detection era, and in the early low-SNR detection era.

Of particular interest here are transient sources that emit gravitational radiation *bursts* that are well localized in time. These short-lived sources tend to be associated with very energetic explosions that should emit messengers of all forms. Furthermore, sources that are well localized in time also tend to be well localized in space, and spatial localization helps further target our multimessenger search efforts.

Localization in time and space are both important for triggered searches for gravitational waves. The basic detection algorithms for transient events are well established in gravitational wave search efforts. Temporal and spatial localization also allow for more efficient use of coherent detection algorithms, described in chapter 5, that are more computationally expensive but can look deeper into the noise. Recent improvements to the transient search algorithms have also significantly increased our ability to reconstruct the sky positions of transient sources, which I will discuss in chapters 5 and 6. Position reconstruction is particularly important for the “LookUp” searches described in the next section.

4.1 Triggered multimessenger searches

As gravitational waves have not yet been directly observed, gravitational wave multimessenger astronomy has been used to aid first detection efforts, as well as help put upper limits on possible GW emissions. Traditional astronomical observations are being used in an attempt to increase detection confidence of gravitational wave searches. In lieu of detection, it’s possible to put more stringent upper limits on current theories. Joint observations can also be used to increase the sensitivity of gravitational wave searches by requiring coincidence and consistency. Traditional untriggered searches require very low false alarm rates in order to be sure that a detection candidate is real. If external observations are available that can constrain the

parameters of a search, much higher false alarm rates may be acceptable, and higher false alarm rates usually translate into increased sensitivity.

There are currently two main types of multimessenger gravitational wave searches being pursued. The first uses traditional observations of transient astronomical events to focus the parameters of a gravitational wave search. These are known as “ExtTrig” searches [39], since they use external triggers to point to where in the gravitational wave data we should look. The second type, known as “LookUp,” [40] use the inverse procedure, whereby gravitational wave triggers prompt electromagnetic observations.

4.1.1 Electromagnetic \rightarrow Gravitational triggering (“ExtTrig”)

Before December 2009, all multimessenger gravitational wave searches were of the ExtTrig variety. ExtTrig searches typically involve the analysis of data that has already been gathered and archived. These searches use triggers from traditional astronomical observations (usually electromagnetic) to prompt further analysis of data previously collected by whatever gravitational wave detectors were active at the time. Because the electromagnetic triggers are often well localized in both time and sky location, they are also amenable to coherent analysis methods (discussed in detail in chapter 5), which are more sensitive than incoherent methods.

Gamma-ray bursts (GRBs) are very attractive targets, as I discuss in section 4.2.1. GRB triggers are readily available (most prominently from the *Swift* observatory [41] and IPN 3 network [42]), and therefore most published results of triggered searches have involved GRB triggers. The first extensive GRB-triggered search looked for short duration gravitational wave bursts associated with GRB 030329 [43]. A triggered follow-up of GRB 070201 was able to exclude a binary neutron star merger progenitor from the M31 galaxy [44]. Ensemble searches have since looked for gravitational wave bursts associated with large classes of GRBs [45, 46]. Matched filter “inspiral” algorithms have also been used to look for gravitational waves associated with short GRBs [47].

Other searches have looked for gravitational waves associated with soft gamma repeaters [48, 49, 50]. One search has also focused on looking for gravitational waves associated with quasi-periodic oscillations in the X-ray tail of SGR 1806-20 [51].

There are also still many promising ExtTrig searches to be done. Optical and other lower-energy EM transients have not been used as triggers. Optical supernovae are an obvious target. Searches are also underway for gravitational waves associated with high-energy neutrino events, in collaboration with the ANTARES [52] and IceCube [53] detectors.

4.1.2 Gravitational \rightarrow Electromagnetic triggering (“LookUp”)

LookUp searches are the newest form of multimessenger gravitational wave search, aiming to observe electromagnetic counterparts to gravitational wave triggers. Data from the full gravitational wave detector network is analyzed in *real time* to produce triggers with very low latency. The triggers must include reconstructed sky location information that can be used to point telescopes to the likely source location on the sky. As soon as the triggers are generated, they are passed to electromagnetic observatories that make opportunistic observations of the reconstructed source locations.

LookUp searches are very ambitious, and more technically challenging and resource intensive than off-line ExtTrig searches. Triggers must be identified with very low latency since the phenomena that we hope to observe is inherently transient and will fade from view if not observed in time. The need for accurate position reconstruction further adds to the difficulty because of the extra computational cost involved. Real-time analysis requires that data from the entire worldwide network of detectors must be quickly transferred to a central analysis location. Large computer resources must be continuously available to analyze backgrounds and determine event significance within the necessary time window. Close coordination and communication with the follow-up observatories must also be achieved for these searches to be successful.

The potential scientific payoff from successful LookUp searches is commensurate

with their difficulty. Electromagnetic afterglows can provide a wealth of information that is difficult to ascertain otherwise. From the afterglows it is possible to determine properties such as precise location, redshift, host galaxy, energy scale, composition, etc., all of which are invaluable for understanding the source. A LookUp search may also lead to an observation that would otherwise be impossible (or at least extremely unlikely). This includes observing the shock breakout from a supernova, or the optical or X-ray afterglow from an off-axis or choked GRB.

This thesis describes the first LookUp search for electromagnetic counterparts to gravitational wave event candidates.

4.2 Transient multimessenger sources

In this section I will take a closer look at some of the most prominent transient multimessenger sources that will likely emit gravitational radiation. I will focus on the physical objects themselves and the specific types and timescales of radiation they may emit. In particular, I will be discussing:

- Coalescence of binary systems of compact stellar-mass objects
- Core-collapse supernovae
- Neutron star disruptions

These three classes are some of the most studied potential sources, and they have all been extensively observed in many non-GW bands. The point here is to build up a picture of what we might expect to see if we “look up” immediately after identifying a gravitational wave burst candidate, and to explore what those observations might tell us about the nature of the physical phenomena. I examine time scales that range from seconds to weeks after the initial gravitational wave burst, for all messengers that are currently being monitored by astronomical observatories.

4.2.1 Compact binary coalescence

The coalescence of a compact binary star system is thought to be one of the strongest emitters of gravitational radiation. Compact binaries consist of two very compact objects, such as neutron stars (NS) and black holes (BH). Such systems have large time-varying quadrupole moments, particularly during the final stages of inspiral and merger, and should be efficient emitters of gravitational radiation (see section 2.3).

Estimates of the rate of compact binary coalescence (CBC) in our galaxy are based largely on only a handful of observations of radio pulsar binaries and tend to be in the range of roughly 10^{-6} yr^{-1} up to maybe 10^{-4} yr^{-1} [54, 55, 56, 57, 58]. If the merger rate is proportional to blue stellar luminosity [55], then this local rate corresponds to a cosmological rate of $10^{-8} - 10^{-6} \text{ Mpc}^{-3} \text{ yr}^{-1}$ [55]. This rate is quite favorable for detection by second-generation detectors which are expected to have sensitivity to these kinds of systems out to distances of hundreds of mega-parsecs [59]. The result is an expected detection rate for Initial LIGO of $2 \times 10^{-4} - 0.2$ per year, and between 0.4 and 400 per year for Advanced LIGO [59].

The relative simplicity of the geometry of CBCs means that their gravitational wave signatures have been extensively modeled (at least for the most simple cases without spin). During the early stages of the inspiral, the waveforms are well approximated by analytical solutions [60, 61, 62]. In the later stages, post-Newtonian expansions are able to provide better waveform predictions [63]. Only recently have computationally intensive numerical relativity simulations been able to suggest what might be expected for the merger phase, where the gravitational emissions should peak [64, 65].

These factors have directed much of the gravitational wave search effort to date, which have focused specifically on looking for the gravitational wave signatures from CBCs [66, 67, 68, 69, 70, 71, 72, 73, 74, 75, 76, 47]

The mechanisms for non-gravitational wave emission from CBCs are equally complicated. Black holes are purely gravitational objects that may or may not have

envelopes of accreting matter that would support non-gravitational emissions when disrupted. Neutron stars, on the other hand, consist of highly dense nuclear matter that certainly should emit copious amounts of radiation when disturbed.

The Gammy-ray burst connection

Gamma-ray bursts are some of the most energetic and enigmatic events in the universe. The sources of these short bursts of gamma radiation appear to be isotropically distributed in the sky, indicating that they are almost certainly cosmological in origin. The duration of observed GRBs is bimodal, indicating that GRBs come from two distinct source distributions [77]. The two classes have become known as *short* and *long* gamma ray bursts, with durations less than and greater than ~ 2 seconds respectively.

While the long GRBs (LGRBs) are widely believed to be associated with core-collapse supernovae (see section 4.2.2), the origin of short GRBs (SRGB) is less clear. That said, the hypothesis that SGRBs are a result of the formation of a black hole from the coalescence of compact objects, most likely binaries of two neutron stars (NS-NS) or a neutron star and a black hole (NS-BH), is becoming more widely accepted [78, 79, 80, 81].

GRBs, both the long and short varieties, are probably the result of highly relativistic jets emitted during the rapid formation of a spinning compact object, likely as stellar-mass black hole, fed by an accretion disk of very dense nuclear matter [81, 80]. The remnant black hole and accretion disk should constitute an efficient power source for driving highly relativistic jets and other high-energy emissions. The total amount of energy available is largely gravitational and is set by the total available mass [81]:

$$E_{\text{GW}} \approx \frac{GM_{\text{BH}}M_{\text{disk}}}{R_{\text{disk}}} \approx \left(\frac{M_{\text{BH}}}{3M_{\odot}}\right) \left(\frac{M_{\text{disk}}}{0.1M_{\odot}}\right) \left(\frac{10^7\text{cm}}{R_{\text{disk}}}\right) 10^{52} \text{ ergs.} \quad (4.1)$$

Key to understanding GRBs is understanding the relativistic jets that are likely

driving the gamma emissions. The current hypothesis is that, as nuclear matter from the disk falls into the remnant, neutrinos are emitted that escape and act to cool the accretion inflow, a process referred to as “neutrino cooled accretion flow” [80]. The energy dissipation from the neutrino cooling acts to heat electrons, accelerating them to highly relativistic velocities and causing them to radiate in the presence of various electromagnetic fields (via synchrotron and inverse Compton scattering) to produce the relativistic jets of radiation [81]. These jets are highly collimated and beamed along the rotational axis, and if the beaming happens to be pointed toward the earth, this is what is observed as the initial gamma ray burst. The GW emission should also be maximum along this axis, but will be far less beamed than the jet (meaning that it should be possible to observe GW emission even if the jet is not visible). These processes happen on very short timescales, leading to sharp bursts of radiation that disappear quickly.

It was the observation of fading X-ray and optical afterglows, starting with the observation of GRB 970228 in 1997 by the *Beppo-SAX* satellite [5], that really started to shed light (so to speak) on the underlying nature of GRBs. Little information can be discerned from the gamma ray burst itself; the signals are too short and the energy is too high to make useful measurements of things like their redshift or composition. The afterglows, on the other hand, are a boon, providing redshifts, energy scales, and so on.

GRB 970228 was, however, a long GRB. The first observation of the afterglow from a short GRB was not made until 2005, when the *Swift* satellite observatory made observations of the quickly decaying X-ray afterglow of GRB 050509b [82]. This was notable because it provided some of the earliest evidence that short GRBs may be the result of compact binary coalescence [83].

Afterglows are generally believed to arise from highly magnetized relativistic particle winds interacting with the ambient warm gas in the envelope around the object [80]. These afterglows can last for many days, even more than a week. This

can be seen in figure 4-1, which shows the X-ray afterglows of three notable SGRBs. While no optical or radio afterglows were observed in GRB 050509b, follow-up observations of GRBs 050709 and 050724 revealed optical, near infrared, and radio afterglows [84, 85]. The optical emissions are thought to come from the radioactive decay of newly formed heavy elements in the ejecta from the merger [86]. Some models also predict detectable radio afterglows in the seconds and minutes after the burst [87]. Figure 4-2 is an overview of these various emission products from a compact binary coalescence, relative to the time of the peak gravitational wave burst.

One of the more interesting prospects for LookUp searches is the possibility of observing off-axis GRBs. Since GRBs are most likely the result of highly collimated and beamed relativistic jets, we probably see only a fraction of the actual number. The rest would be pointed away from us and not observable. The afterglows would probably still be observable, though, if we knew where to look. The gravitational wave emissions from CBCs, on the other hand, should be much more uniformly distributed. Observations based on gravitational wave triggers might catch the afterglow of a CBC *without* observing the actual GRB itself. This would be strong confirmation of jet-like nature of the burst and would help refine the estimates of event rates.

Naked BH-BH binaries

It is interesting to note that BH-BH binaries are thought by some to constitute a class of strong GW sources that may in fact *not* be accompanied by any non-gravitational emissions. Many binary black hole systems are suspected of being “naked,” i.e. not surrounded by other forms of non-exotic matter [88]. These naked BH-BH binaries could have either accreted or blown off any extra matter that could have been present when the black holes or binary were formed. If such objects do exist, they might constitute a stronger and more pervasive source than binaries that include neutron stars.

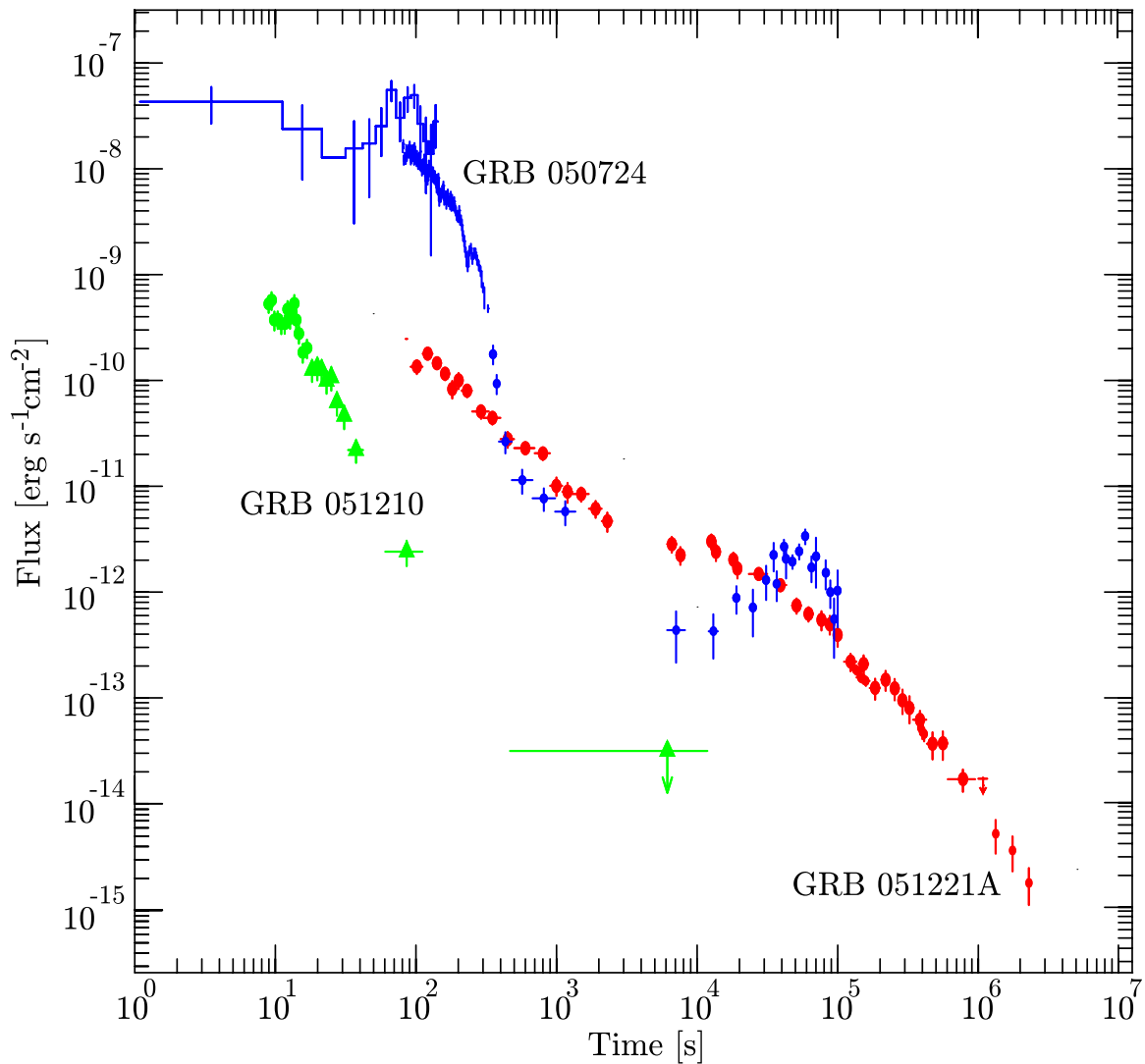


Figure 4-1: Lightcurves of soft X-ray afterglows from three short gamma ray bursts observed by the *Swift* satellite observatory: GRB 050724, GRB 051210, and GRB 051221A. The y axis is the flux of photons in the 2-10 keV range, and the x axis is time in seconds since the initially detected gamma ray burst. (Courtesy [81])

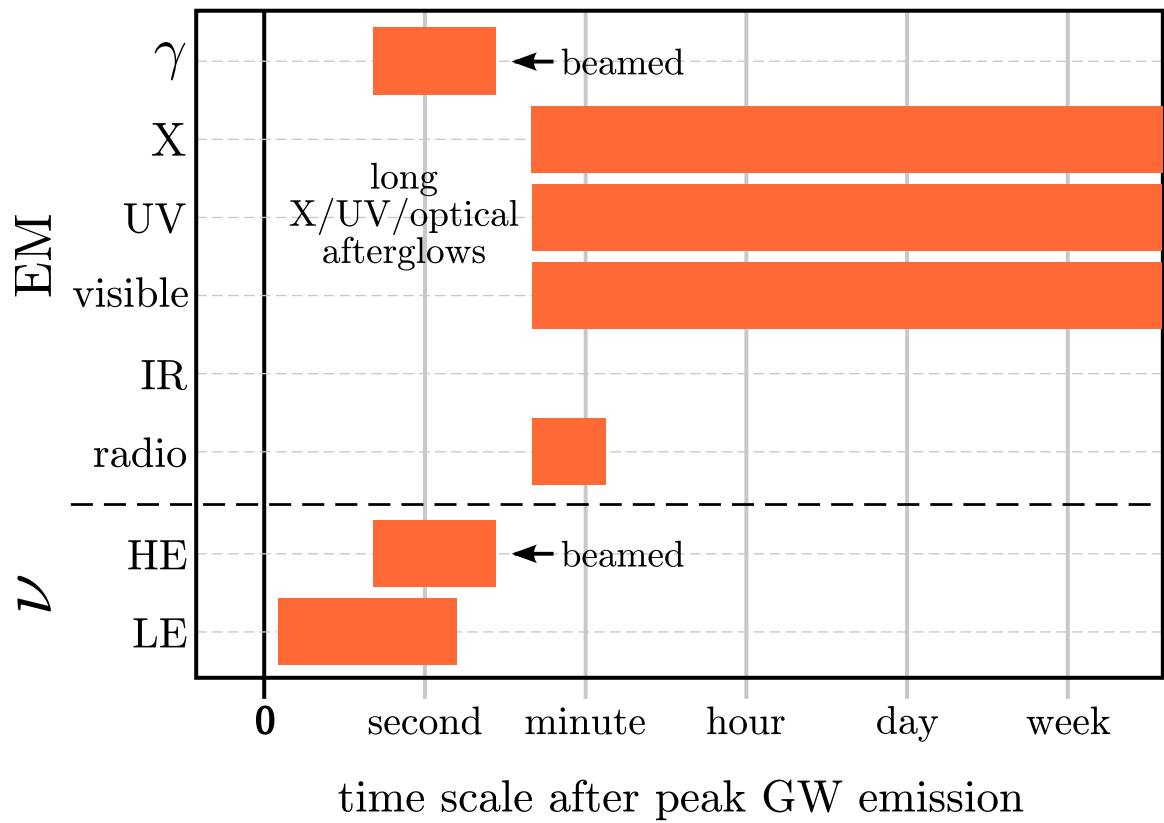


Figure 4-2: Relative arrival time of various emissions from NS-NS and NS-BH binary coalescence. Times are measured from from peak gravitational wave emissions.

4.2.2 Core-collapse supernovae

Core-collapse supernovae (CCSNe), the result of explosions of massive stars that undergo gravitational collapse at the end of their lifetimes, also look to be another promising gravitational wave multimessenger source. Core-collapse supernovae are well known emitters of both electromagnetic radiation and neutrinos, and models suggest they are likely emitters of gravitational radiation as well.

Supernovae have been observed broadly throughout the EM spectrum for many years (thousands, actually). Their emissions are incredibly bright and distinct, and the most notable events have been observable with the naked eye. Their afterglows span the EM spectrum and can last for weeks (e.g. figure 4-3). A credible explanation of their origin as stars undergoing gravitational collapse into neutron stars was first published in 1934 by Baade and Zwicky [89]. While it is now known that not all supernovae involve core-collapse, the ones that do are the most massive and therefore likely to produce the most brilliant explosions, typically releasing upwards of 10^{51} ergs.¹

Certainly the most famous supernova ever observed was SN1987A. SN1987A was also the first and *only* extrasolar object ever observed via neutrinos [91, 92]. The neutrino observations actually *preceded* electromagnetic observations by roughly three hours, indicating the actual explosion time and providing important evidence for the theory of supernova shock breakout [93].

Current estimates put the CCSNe rate in our galaxy at $0.7 - 2$ per century [94]. Using the same proportionality to blue stellar luminosity as in section 4.2.1 [55] leads to a local cosmological rate of $0.7 - 2 \times 10^{-4} \text{ Mpc}^{-3} \text{ yr}^{-1}$. However, unlike compact binary coalescence, the gravitational wave signals from CCSNe are expected to be quite weak, and the corresponding sensitivity for advanced detectors is much lower.

¹This unit of energy, 10^{51} ergs, is now known as 1 *bethe*, in honor of Hans Bethe, a pioneer in the theory of supernova physics.

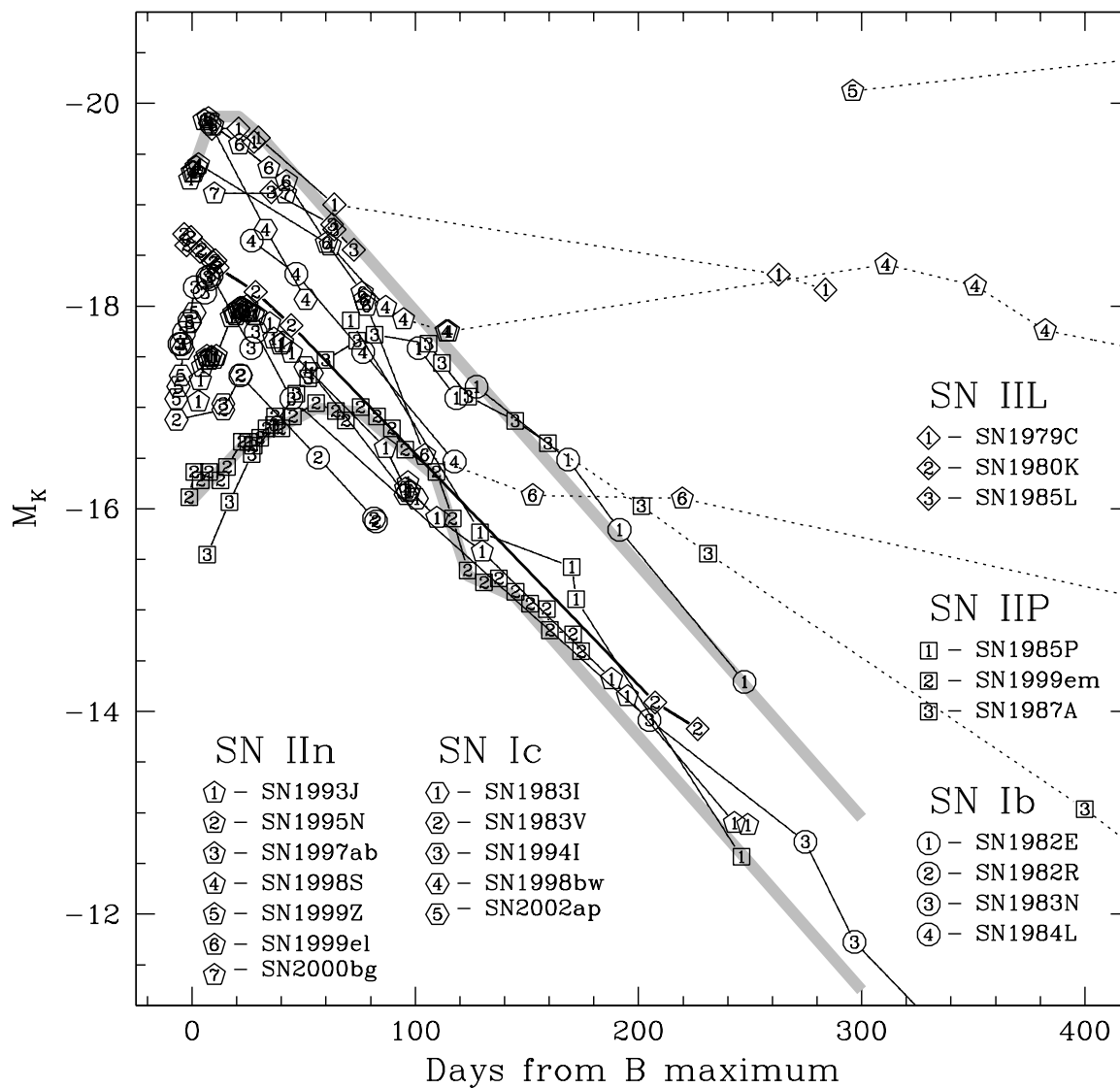


Figure 4-3: K-band (near-infrared) light curves from a large selection of core-collapse supernovae. (Courtesy [90])

The explosion mechanism

In 1990, inspired by the fervor surrounding SN1987A, Hans Bethe published a seminal paper outlining the most up-to-date theory of core collapse [95]. More recently Kotake et al. [96] and Ott [97] have also covered current theories of gravitational wave emission from CCSN. As a star runs out of nuclear fuel, it begins to undergo gravitational collapse. The collapse is eventually halted (after only a tenth of a second or so) when the core reaches nuclear densities. This sudden halt of the collapse leads to a “bounce” and an outward propagating shock wave. When the shock wave finally escapes the core, known as *shock breakout*, it blows out the less dense stellar envelope, leading to the tremendous EM emissions that we observe as the supernovae.

Unfortunately, simple models and computer simulations fail to endow this “prompt shock” with enough energy to keep it from stalling before reaching the surface of the iron core [95, 96, 98]. Consequently these models fail to account for the supernova explosion itself. A hope in reviving the shock has been the copious amounts of low-energy neutrinos produced from electron capture in the core collapse. These neutrinos are initially trapped in the collapsing core, but are released almost immediately as the shock expands outward. Some models suggest that these neutrinos could deposit the needed energy in the shock front to revive, but only with small cores or low density envelopes [98]. The explosion mechanism for massive progenitors remains a mystery.

Various models for gravitational wave emission from CCSN have been studied and each should produce unique gravitational wave signatures [99, 97, 100, 101, 102]. Other than the neutrino mechanism, other mechanisms include magnetorotational instabilities in rapidly rotating progenitors with strongly magnetized cores [103], and acoustic oscillations of the remnant proto-neutron star [104]. The most energetic of these mechanisms is expected to produce strains detectable by advanced detectors at distances of about 100 kpc or so [99].

Shock breakout and EM emission

One of the other big unknowns in supernova theory is the nature of the shock breakout itself. We have very little understanding of when the shock breakout happens relative to the core collapse time or how long it takes to escape the stellar envelope. These things are intimately related to the size, makeup, and geometry of the progenitor. The problem is that it has been very difficult to know when exactly the core collapse has taken place. Neutrino emissions begin almost immediately after the collapse [105, 98], but to date there has only been a single observation of neutrinos from SN (1987A). Since gravitational waves are emitted directly by the core collapse they would provide a precise time of collapse. Subsequent observations of the EM emissions from the supernova itself would teach us much about the nature of the progenitor.

Observations of the actual shock breakout have also been few and far between. We know that the initial breakout produces a bright flash of UV and X-ray radiation [106, 107, 95], but these bursts have been only rarely observed. LGRB 060218 showed a time-varying thermal component in its X-ray emissions that indicated the possible observation of the shock breakout [108, 109, 110]. In 2008, astronomers serendipitously observed an X-ray burst during another scheduled observation that ended up being the first observations of SN2008D [111].

Long gamma ray bursts

As mentioned in section 4.2.1, the observations of X-ray afterglows have provided substantial evidence to indicate that most LGRBs are associated with Type Ic CC-SNe [78]. Multiple models have been proposed for the origin of LGRBs, each predicting different afterglow behavior that should be observationally distinguishable. The progenitors are thought to be very massive Wolf-Rayet stars [112]. In the *collapsar* model the core collapses immediately into a $\sim 3M_{\odot}$ black hole [113], which would centrifugally support an accretion disk that could supply long afterglows [114]. In the *supernova* model a “hypermassive” neutron star is formed, supported by high ro-

tational velocity, which might have quickly decaying or absent afterglows [115]. The production of a rapidly spinning Kerr black hole could also produce long-duration radio emissions [116]. Figure 4-4 shows the visible light curves of afterglows for many of the observed LGRBs, collected in [117].

As with SGRB, LGRB jets would also be beamed, meaning gravitational wave triggers would provide the same unique opportunity to view the afterglow from an off-axis LGRB as they would for SGRB. Because LGRB occur in the cores of stars surrounded by dense circumstellar matter, there is also the interesting possibility that the GRB would be “choked” and not actually make it out of the star [118]. Gravitational wave triggers could therefore allow for the observation of afterglows from these choked GRBs.

4.2.3 Neutron stars disruptions

Supernovae are not the only form of stellar instability that are suspected of emitting gravitational radiation. In fact, any relativistic star that undergoes a significant mass/energy reconfiguration could, in principle, release gravitational radiation. Some of the most extreme of these are neutron stars with very strong magnetic fields: *magnetars*. Magnetars were first posited to explain the intense bursts of gamma and X-ray radiation coming from *soft gamma repeaters* (SGR) and *anomalous X-ray pulsars* (AXP) [119, 120, 121, 122, 123, 124].

Magnetars are neutron stars that are thought to possess magnetic fields up to and possibly greater than 10^{15} Gauss [122]. They are possibly remnants of compact binary coalescence [125] with strong magnetic fields. While the energy densities, rotational motions, and stochastic reconfigurations of magnetars would suggest gravitational wave emission, there is unfortunately little theoretical understanding of how the emission might actually occur. The current speculation is that SGRs are the product of global rearrangements of the magnetar’s magnetic fields [126]. These rearrangements can release energy upwards of 10^{45} erg, causing violent reconfigurations of the

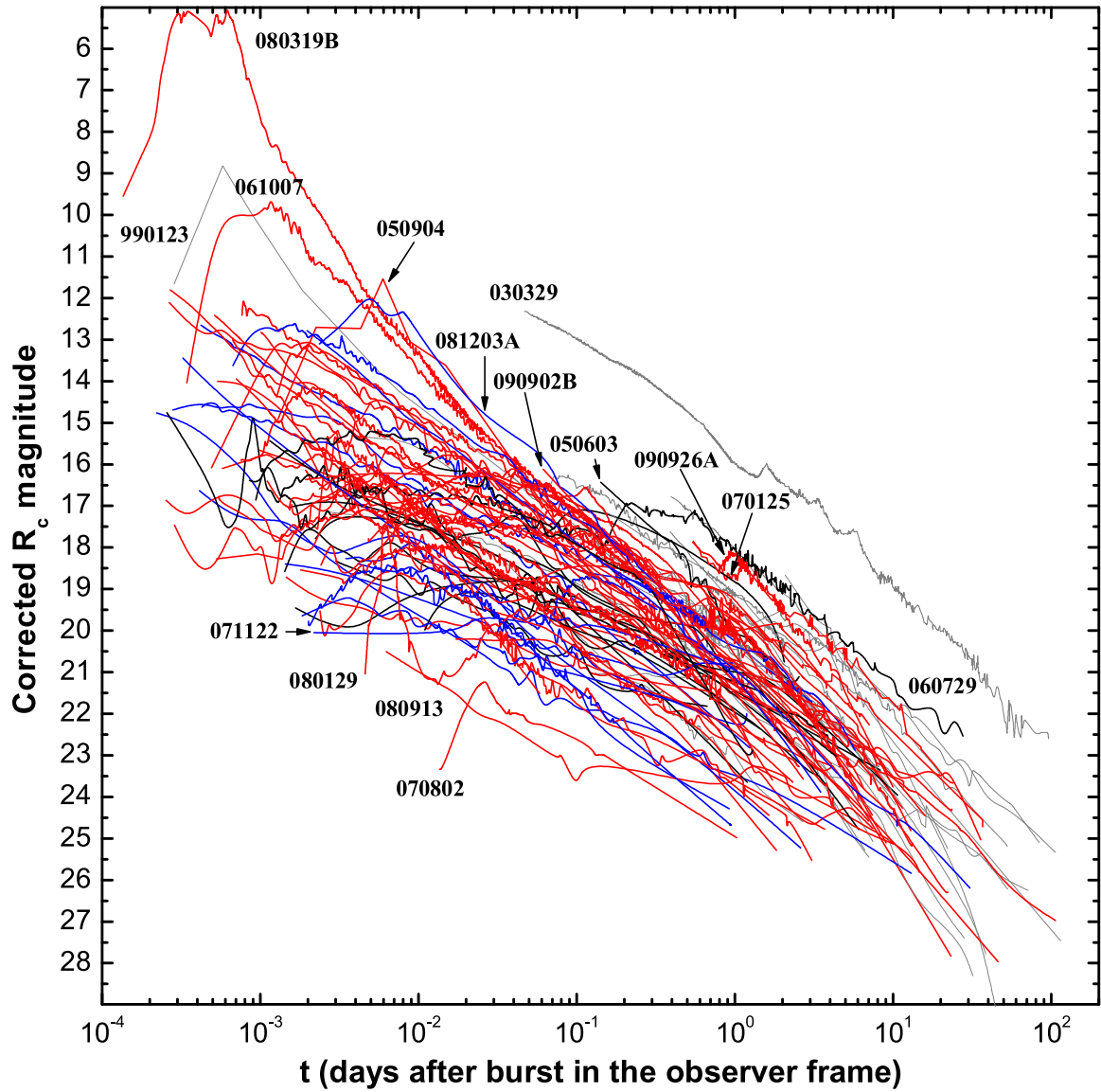


Figure 4-4: Visible (R_c band) afterglows for a large number of long gamma-ray bursts, corrected for Galactic extinction (Courtesy [117])

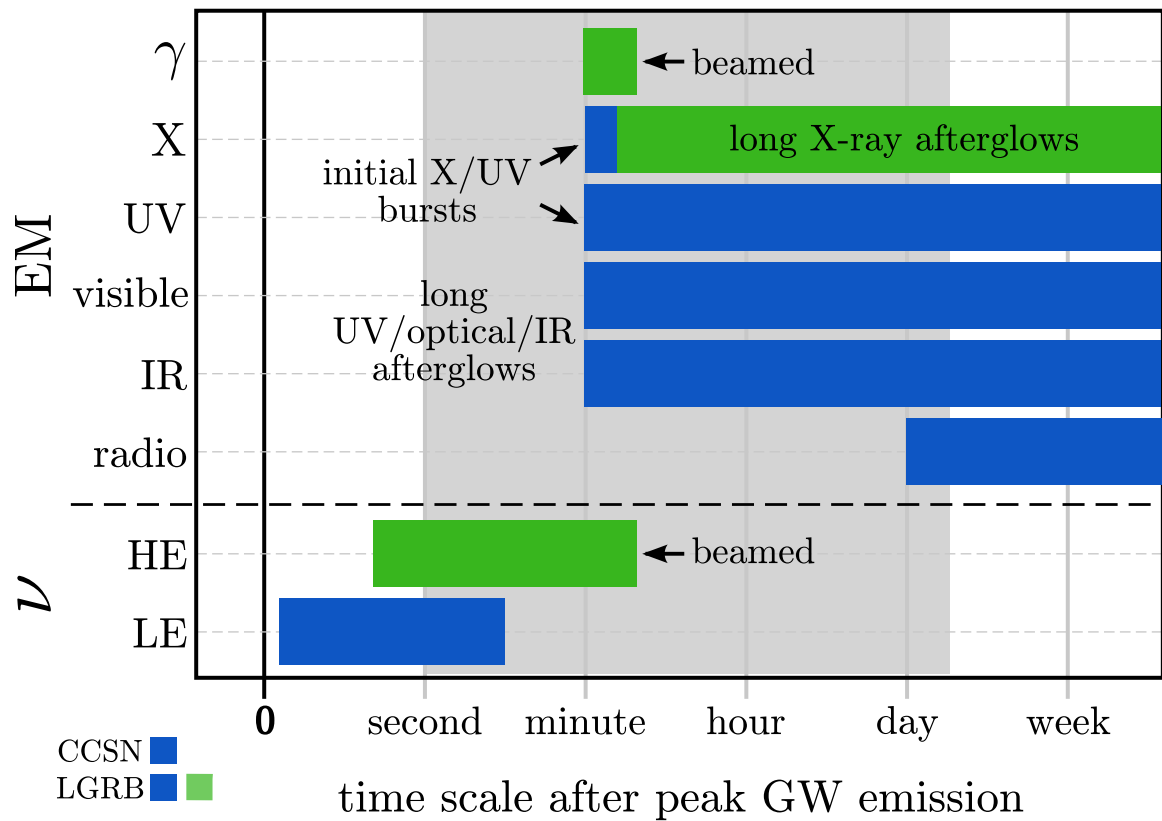


Figure 4-5: Relative arrival time of various emissions from core-collapse supernovae, as a function of time relative to peak gravitational emissions.

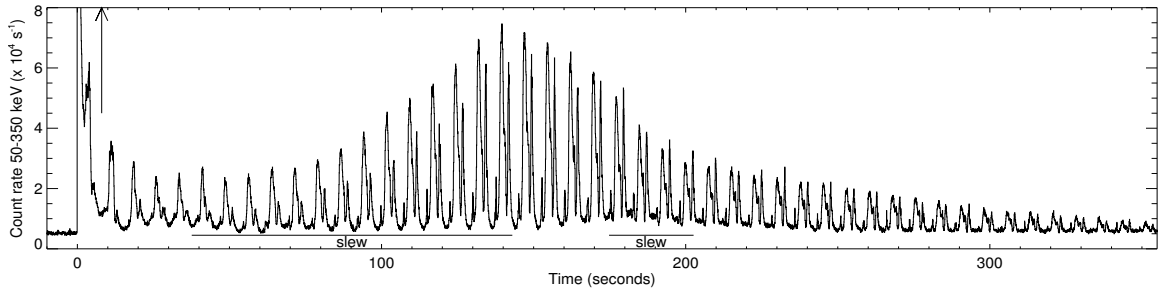


Figure 4-6: Light curve of the SGR 1806-20 giant flare, as observed by the Burst Alert Telescope (BAT) on the *Swift* observatory. The apparent increase in counts at 140 s was due to a preplanned spacecraft reorientation. (Courtesy [133])

neutron star crust, so called *crustquakes*. These crustquakes might excite nonradial modes of oscillation, such as spherical f and r modes, that should emit gravitational radiation [127, 128, 129]. This theory is supported by, among other things, the observation of *quasi-periodic oscillations* (QPOs) in the tails of SGR giant flares [130, 131] that are coincident with the observed SGR spin rates.

Soft gamma repeaters sporadically emit intense but brief bursts of soft (i.e., low energy) gamma rays. These bursts commonly reach peak luminosities of up to 10^{42} erg/s lasting for around 0.1 s [124]. Some SGRs occasionally emit giant flares, such as the SGR 1806-20 giant flare, which reached a peak isotropic energy of 10^{46} erg and was followed by a prolonged pulsating tail [132, 133] (see figure 4-6). SGRs are also known to have persistent X-ray [122] and neutrino [134] emissions.

Chapter 5

Bayesian Network Analysis

Multiple detectors are useful for more than just increasing detection confidence. While gravitational waves have two independent polarizations, a single interferometric detector is only sensitive to a linear combination of them (section 3.3). A *network* of three or more detectors, on the other hand, overdetermines the waveform (at least in the large SNR limit). This allows for the reconstruction of the waveform and its various parameters. The most important of these parameters for gravitational wave astronomy, and for this thesis in particular, is the direction of the signal.

Waveform reconstruction is known as the *inverse problem*. Gürsel and Tinto were the first to work out this problem in detail for a network of three interferometers [135]. They were also the first to describe the construction of network *null streams* (described in section 5.2) as an effective tool for signal discrimination [135]. The null stream was later shown to be effective at signal discrimination in the presence of non-Gaussian and non-stationary noise distributions [136, 137], as well as for discriminating signals from instrumental noise glitches [138].

Algorithms that use the full network to reconstruct waveform parameters and null streams are known as *coherent* algorithms, as opposed to *incoherent* algorithms that analyze each detector stream independently. One of the first real uses of coherent techniques was in searches directed at particular sky locations. If a target source

location is known, the coherent null stream technique can be applied to that single sky location with great effect. This is the basis of almost all of the ExtTrig searches described in section 4.1.1. The **X-Pipeline** [139] is a notable pipeline developed specifically for doing these types of directed coherent searches.

One of the difficulties of coherent algorithms is that the consistency tests are generally applicable to only a single direction at a time. In order to apply these tests to extended solid angles, minimization of the null streams over the entire area is required. Since the computational cost of a coherent analysis for a single sky location is comparable to that of an incoherent algorithms, applying the tests to large patches of the sky, or to the entire sky, can be prohibitively expensive. This weakens the power of the test considerably.

LookUp searches, on the other hand, require a reconstructed sky position with the trigger so that telescopes may be pointed at the proper location. The reconstruction algorithm must also be efficient so that it can be calculated quickly and return results in time to catch other messengers from a transient source.

In 2007, Antony Searle formulated the first fast and practical Bayesian [140, 141] interpretation of the null stream for the detection of transients in a network of detectors [142, 143]. This technique includes a solution to the inverse problem that is able to produce full probability distribution maps for source location on the sky, known as *sky maps*. It has also been shown to be the optimal solution to Markov-chain Monte Carlo (MCMC) statistics [144], and is therefore faster than analysis based on those statistics. Bayesian methods had been previously applied to gravitational wave data analysis in searches for specific signal models [145], but not for more generic transient signals, or for efficient reconstruction of sky maps. More recently they have been extended to test for the presence of detector glitches [146].

In this chapter I describe a full Bayesian algorithm that searches for transient signals in a network of detectors, produces full source probability distribution maps on the sky, and is able to reject detector glitches. The implementation of the algorithm

in a real low-latency analysis pipeline is then described in chapter 6.

5.1 Basics of network analysis

For a sky source direction (θ, ϕ) and gravitational wave polarization angle ψ , the response of an interferometric detector can be written as follows (equation (3.1) reprinted for reference):

$$F^+(\theta, \phi, \psi) = \cos 2\psi \frac{1}{2}(1 + \cos^2 \theta) \cos 2\phi - \sin 2\psi \cos \theta \sin 2\phi \quad (5.1)$$

$$F^\times(\theta, \phi, \psi) = -\sin 2\psi \frac{1}{2}(1 + \cos^2 \theta) \cos 2\phi - \cos 2\psi \cos \theta \sin 2\phi. \quad (5.2)$$

The response function and wave polarization can both be represented by vectors, $\mathbf{F} = [F^+ F^\times]$ and $\mathbf{h} = [h_+ h_\times]^T$, and the measured strain in the detector is then their dot product:

$$\begin{aligned} h_m(t, \theta, \phi, \psi) &= F^+(\theta, \phi, \psi)h_+(t) + F^\times(\theta, \phi, \psi)h_\times(t) \\ &= \mathbf{F}(\theta, \phi, \psi)\mathbf{h}(t). \end{aligned} \quad (5.3)$$

Without loss of generality we can choose an arbitrary reference polarization basis (such as $\psi = 0$) and neglect ψ in further derivations. I will also use $\hat{\Omega}$ to represent the unit vector in the direction of sky position (θ, ϕ) . The single detector response is then written

$$h_m(t, \hat{\Omega}) = \mathbf{F}(\hat{\Omega})\mathbf{h}(t). \quad (5.4)$$

Now consider a single strain measurement from a single detector, $x(t)$. Along with any gravitational wave signal, h_m , the measurement will also include any inherent detector noise, n . The measurement will be a linear combination of the response of

the detector to the gravitational wave and the inherent detector noise:

$$x(t) = \mathbf{F}(\hat{\Omega})\mathbf{h}(t) + n(t). \quad (5.5)$$

We can generalize this to D detectors spread out in space, each at position \vec{r}_i . The response of detector i at time t will be given by

$$x_i(t) = \mathbf{F}_i(\hat{\Omega})\mathbf{h}(t + \tau_i(\hat{\Omega})) + n_i(t), \quad (5.6)$$

where τ_i is the time delay of the signal in detector i relative to some origin, \vec{r}_0 ,

$$\tau_i(\hat{\Omega}) \equiv \frac{1}{c}(\vec{r}_0 - \vec{r}_i) \cdot \hat{\Omega}. \quad (5.7)$$

We can neglect this time delay factor for now by noting that it can be reincorporated by applying the appropriate time shift in each data stream during the analysis. I will therefore assume for this discussion that the detectors are all co-located (i.e. they all reside at the same location in space), but not necessarily co-aligned.

Since we wish to ultimately work in the frequency domain, I note that we can just as easily work with any linear transformation of the variables, $\tilde{\mathbf{x}}$, and drop explicit reference to time or frequency. I also drop explicit reference to $\hat{\Omega}$, except where needed for clarity or emphasis.

The generalization of (5.5) for the D -detector network is then given by

$$\begin{bmatrix} x_1 \\ x_2 \\ \vdots \\ x_D \end{bmatrix} = \begin{bmatrix} F_1^+ & F_1^\times \\ F_2^+ & F_2^\times \\ \vdots & \vdots \\ F_D^+ & F_D^\times \end{bmatrix} \begin{bmatrix} h_+ \\ h_\times \end{bmatrix} + \begin{bmatrix} n_1 \\ n_2 \\ \vdots \\ n_D \end{bmatrix}, \quad (5.8)$$

or more simply:

$$\mathbf{x} = \mathbf{F}\mathbf{h} + \mathbf{n}. \quad (5.9)$$

We have now recast the antenna response function, \mathbf{F} , as a $2 \times D$ matrix, where the two columns represent the overall network $+$ and \times polarization responses:

$$\mathbf{F} \equiv [\mathbf{F}^+ \ \mathbf{F}^\times] = \begin{bmatrix} F_1^+ & F_1^\times \\ F_2^+ & F_2^\times \\ \vdots & \vdots \\ F_D^+ & F_D^\times \end{bmatrix}. \quad (5.10)$$

This geometrical construction of the response of a network of interferometric detectors to an incoming gravitational wave is the key to any coherent analysis.

5.2 Null stream analysis

As noted originally by Gürsel and Tinto in [135], there is an interesting geometrical construction that can be applied to the network response function. The \mathbf{F}^+ and \mathbf{F}^\times polarization response vectors together form a two-dimensional subspace (i.e., plane) in the D -dimensional detector space (see figure 5-1). I will refer to this as the *signal plane*. The measured gravitational wave vector, \mathbf{h}_m , must lie within this plane since it only contributes to the measurement via its projection onto the \mathbf{F}^+ and \mathbf{F}^\times vectors. Assuming that none of the interferometers is co-aligned, this plane lies in a larger D -dimensional space. Let us now examine the remaining $D - 2$ dimensional subspace orthogonal to the signal plane, defined by a new matrix, \mathbf{A} :

$$\mathbf{A}\mathbf{F} = 0. \quad (5.11)$$

The space defined by \mathbf{A} is a space in which no signal resides and is therefore referred to as the *null space*.

What happens if we now project the data stream \mathbf{x} into this space? Since \mathbf{A} is (by construction) orthogonal to \mathbf{F} , the signal stream cancels out entirely. Using this,

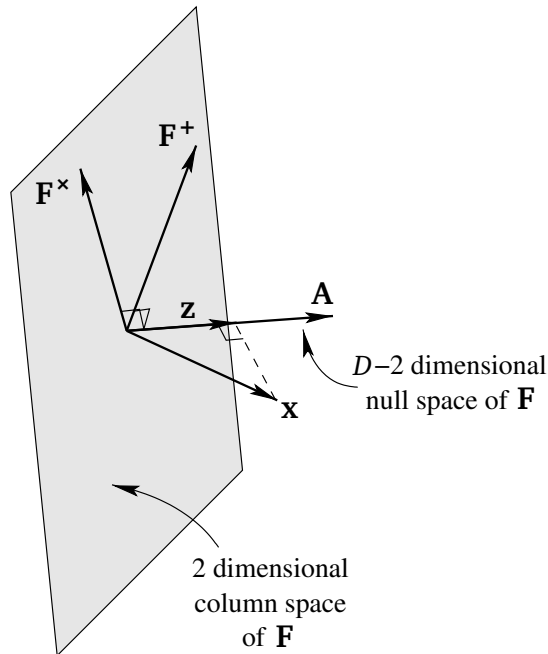


Figure 5-1: Network null stream construction. (Adopted from [138])

we can construct a new quantity from the data, \mathbf{z} :

$$\begin{aligned}
 \mathbf{z} &\equiv \mathbf{A}\mathbf{x} \\
 &= \mathbf{A}\mathbf{F}\mathbf{h} + \mathbf{A}\mathbf{n} \\
 &= \mathbf{A}\mathbf{n}
 \end{aligned} \tag{5.12}$$

The result is a set of *null streams*, z_i , which are the rows of $\mathbf{A}\mathbf{n}$. Figure 5-1 shows a schematic of the construction of the null stream.

Since \mathbf{A} is constructed from the network interferometer response function, \mathbf{F} , which is a function of source sky position, $\hat{\Omega}$, $\mathbf{A}(\hat{\Omega})$ and $\mathbf{z}(\hat{\Omega})$ are therefore also functions of sky position. The rank of \mathbf{A} , and therefore the number of independent null streams, is dependent on the relative alignments of the detectors in the network. Generally there are $D - 2$ null streams. However, if all detectors are aligned, then $\mathbf{F}^+ \propto \mathbf{F}^\times$, and there are $D - 1$ null streams. Since we are concerned here with three

nonaligned detectors, \mathbf{A} is a simple vector and there is a single null-stream vector. The construction of \mathbf{A} is not particularly complicated, but we only note here that for the three-detector case, \mathbf{A} takes on a particularly simple form [138]:

$$\mathbf{A} = \frac{\mathbf{F}^+ \times \mathbf{F}^\times}{|\mathbf{F}^+ \times \mathbf{F}^\times|}. \quad (5.13)$$

The total energy in the null stream is given by the *null energy*:

$$\begin{aligned} E_{\text{null}}(\hat{\Omega}) &= |\mathbf{z}|^2 \\ &= \mathbf{x}^\dagger \mathbf{A}^T \mathbf{A} \mathbf{x} \\ &= \mathbf{x}^\dagger \Sigma^{-1} \mathbf{x}, \end{aligned} \quad (5.14)$$

where we have defined the new quantity

$$\Sigma^{-1}(\hat{\Omega}) \equiv \mathbf{A}^T \mathbf{A}. \quad (5.15)$$

E_{null} contains contributions from the cross-correlations between detector streams ($x_i^* x_j$), as well as from the auto-correlations of each detector with itself ($x_i^* x_i$). As we shall see, it is useful to construct an energy term which represents just the contribution to the null energy from the auto-correlation terms

$$E_{\text{inc}}(\hat{\Omega}) \equiv \sum_i \Sigma_{ii}^{-1} |x_i|^2. \quad (5.16)$$

E_{inc} is a measure of the uncorrelated energy in the network and is therefore referred to as the *null incoherent energy*.

Let us now imagine that we are given a direction in the sky and a time characterized by coincident excess power in multiple detectors in our network. If the signals are just randomly coincident yet uncorrelated glitches we expect the null energy to

be dominated by the incoherent energy, i.e.,

$$E_{\text{null}} \sim E_{\text{inc}}. \quad (5.17)$$

However, if the signal is due to a true gravitational wave, then the null energy should, on average or in the large SNR limit, go to a minimum. The incoherent energy, on the other hand, should still be large, since there is actually energy in each individual detector stream. So for the case of a true gravitational wave signal we expect

$$E_{\text{null}} \ll E_{\text{inc}}. \quad (5.18)$$

5.3 Formulation of the Bayesian analysis

In a Bayesian analysis, we ask, “What is the plausibility of a hypothesis being true, given a set of initial assumptions?” Given a hypothesis, H , and set of initial assumptions, I , this is usually written $p(H|I)$ (read: “plausibility of H assuming I ”). Given that we are making physical measurements, we expand the set of initial assumptions to include the network measurement data, \mathbf{x} : $p(H|\mathbf{x}, I)$. This function is usually referred to as the *posterior* plausibility, since it is what is assigned to the hypothesis after observation.

We can’t evaluate the posterior plausibility function directly, but Bayes’s Theorem [141] tells us that we can separate the function into components that can be more easily evaluated:

$$p(H|\mathbf{x}, I) = \frac{p(H|I)p(\mathbf{x}|H, I)}{p(\mathbf{x}|I)} \quad (5.19)$$

The term $p(\mathbf{x}|H, I)$ is the *likelihood function*, since it gives the probability that a certain measurement is made given hypothesis H . The terms $p(H|I)$ and $p(\mathbf{x}|I)$ are known as the *prior* or *marginal plausibilities* of H and \mathbf{x} respectively, since they represents the plausibility of these variables before measurement. For notational

simplicity, I will from here on drop the implicit assumptions, I .

We now wish to compare two different hypotheses, H_0 and H_1 . We can compare them by looking at the ratio of their posterior plausibilities, also known as the *Bayesian odds ratio*:

$$\frac{p(H_1|\mathbf{x})}{p(H_0|\mathbf{x})} = \frac{p(H_1)p(\mathbf{x}|H_1)}{p(H_0)p(\mathbf{x}|H_0)} \quad (5.20)$$

The first factor on the right, $p(H_1)/p(H_0)$, is known as the *prior odds ratio*, and the second factor, $p(\mathbf{x}|H_1)/p(\mathbf{x}|H_0)$, is known as the *Bayes factor* or *likelihood ratio*. Note that by taking the ratio of the likelihood functions for the two hypotheses we divide out the cumbersome and difficult $p(\mathbf{x}|I)$.

The likelihood ratio is what we actually compute in the analysis from the data obtained during the observation. The prior odds ratio, on the other hand, is where we encode our prior expectation that there should be a signal versus only noise. Ultimately, the odds ratio is just a constant factor that would ideally be chosen ahead of time. In practice, though, the odds ratio becomes something more like a threshold. This threshold is determined through Monte Carlo simulations and analyses of background data known to contain no signals.

5.3.1 Marginalization

The likelihood functions in (5.20) are not trivially solvable since we typically don't know a priori all of the parameters that define the signal for which we are searching. In other words, our signal hypotheses are usually incomplete. Our ignorance in this regard is, of course, dependent on the kind of search we're doing. Generally, we perform searches over some reasonable subset of the parameter space, making explicit assumptions about the signal parameters that are well defined and then performing what is known as a *marginalization* over those that are not.

Bayesian marginalization is the process of averaging over all possible values of a parameter, weighted by the prior probability distribution we assign to the param-

eter itself given the hypothesis of interest. For example, given a hypothesis, H , parametrized with parameter, ρ , the marginalization over ρ is given by:

$$p(\mathbf{x}|H) = \int_{\rho} p(\rho|H)p(\mathbf{x}|H, \rho) d\rho. \quad (5.21)$$

By choosing priors that are both realistic and integrable we can solve these integrals analytically. Those that we can't solve are then integrated numerically, which is in effect the computational component of the analysis.

5.3.2 The gravitational wave search problem

In the case of gravitational wave observations, we are interested in comparing the hypothesis that the data contains a signal, H_s ,

$$H_s: \mathbf{x} = \mathbf{F}\mathbf{h} + \mathbf{n}, \quad (5.22)$$

versus the hypothesis that the data contains no signal and only noise, H_n ,

$$H_n: \mathbf{x} = \mathbf{n}. \quad (5.23)$$

The odds ratio for this test is then given by:

$$\frac{p(H_s|\mathbf{x})}{p(H_n|\mathbf{x})} = \frac{p(H_s)}{p(H_n)} \frac{p(\mathbf{x}|H_s)}{p(\mathbf{x}|H_n)}. \quad (5.24)$$

5.4 Noise model

Probably the most important and simultaneously most difficult part of interferometric gravitational wave antenna data analysis is understanding the detector noise. Ideally, the detector noise would be described by a simple stationary Gaussian distribution that is perfectly flat in frequency (i.e., “white”). Unfortunately, real interferometer

detector noise is quite bit more complicated than this. As we saw in figure 3-7, real detector noise distributions are certainly not ideally Gaussian. They are generally “colored” in frequency, and the measured sample amplitude distributions have long tails, particularly at low frequency, indicating the presence of low-frequency glitches.

From a Bayesian perspective, it is important to have a good model of instrument noise because we can use the prior probability distribution function of the noise to construct the signal likelihood function. Since our measurement is the linear sum of the signal response and the detector noise (5.5), and since the signal and the noise are uncorrelated, we can construct the signal likelihood function by making the substitution $\mathbf{n} \rightarrow \mathbf{x} - \mathbf{F}(\hat{\Omega})\mathbf{h}$ into the noise prior, $p(\mathbf{n}|H_n)$. In other words:

$$p(\mathbf{x}|H_s, \mathbf{h}, \hat{\Omega}) = p(\mathbf{x} - \mathbf{F}(\hat{\Omega})\mathbf{h}|H_n). \quad (5.25)$$

Probably the most important property of the noise in the network of detectors is that it is completely independent in each detector (this is in fact the main reason we have more than one detector). This independence means that the distribution in each detector is completely uncorrelated and can be separated into a product of single-detector distributions, i.e.,

$$p(\mathbf{n}|H_n) = \prod_i p(x_i|H_n). \quad (5.26)$$

From here we can describe the noise distributions in each detector individually. Since the detectors are all more or less the same, I will be using the same distributions to describe all detectors.

While acknowledging that it is imperfect, we begin by modeling the noise as a simple, normal (Gaussian) distribution with mean μ and variance σ^2 :

$$\mathcal{N}(x, \mu, \sigma^2) = \frac{1}{\sqrt{2\pi\sigma^2}} \exp\left(-\frac{1}{2} \frac{(x - \mu)^2}{\sigma^2}\right). \quad (5.27)$$

It is useful to start here since it makes the following formulations clearer. As we will see in section 5.6, we can also model deviations from this ideal as separate distributions that are added to this simple normal distribution. In the detectors the noise mean is always zero, so the distribution of the noise in detector i is then given by:

$$p(n_i|H_n) = \mathcal{N}(n_i, 0, \sigma_i^2) \quad (5.28)$$

$$= \frac{1}{\sqrt{2\pi\sigma_i^2}} \exp\left(-\frac{1}{2} \frac{n_i^2}{\sigma_i^2}\right). \quad (5.29)$$

It is convenient to describe the full network noise in matrix form as a multivariate normal distribution with mean $\boldsymbol{\mu}$ and covariance matrix $\boldsymbol{\Sigma}$:

$$\mathcal{N}(\mathbf{x}, \boldsymbol{\mu}, \boldsymbol{\Sigma}) = \frac{1}{(2\pi)^{D/2} \sqrt{|\boldsymbol{\Sigma}|}} \exp\left(-\frac{1}{2}(\mathbf{x} - \boldsymbol{\mu})^T \boldsymbol{\Sigma}^{-1}(\mathbf{x} - \boldsymbol{\mu})\right). \quad (5.30)$$

Again, since the noise mean is zero, the network noise hypothesis prior probability becomes:

$$p(\mathbf{n}|H_n) = \mathcal{N}(\mathbf{n}, \mathbf{0}, \boldsymbol{\Sigma}) \quad (5.31)$$

$$= \frac{1}{(2\pi)^{D/2} \sqrt{|\boldsymbol{\Sigma}|}} \exp\left(-\frac{1}{2} \mathbf{n}^T \boldsymbol{\Sigma}^{-1} \mathbf{n}\right). \quad (5.32)$$

5.5 Signal model

As we saw in (5.25), we can use the noise prior probability function to construct the signal likelihood function. Given (5.31) we see that

$$\begin{aligned} p(\mathbf{x}|H_s, \mathbf{h}, \hat{\Omega}) &= \mathcal{N}(\mathbf{x} - \mathbf{Fh}, \mathbf{0}, \boldsymbol{\Sigma}) \\ &= \mathcal{N}(\mathbf{x}, \mathbf{Fh}, \boldsymbol{\Sigma}) \\ &= \frac{1}{(2\pi)^{D/2} \sqrt{|\boldsymbol{\Sigma}|}} \exp\left(-\frac{1}{2}(\mathbf{x} - \mathbf{Fh})^T \boldsymbol{\Sigma}^{-1}(\mathbf{x} - \mathbf{Fh})\right). \end{aligned} \quad (5.33)$$

The parameters in this likelihood function are the gravitational waveform and amplitude, \mathbf{h} , and the sky direction, $\hat{\Omega}$ (via $\mathbf{F}(\hat{\Omega})$). However, since we don't know these parameters a priori, we can't compute the full signal likelihood directly. We must first marginalize over these unknown parameters.

We begin by marginalizing over the strain waveforms and amplitudes, \mathbf{h} :

$$p(\mathbf{x}|H_s, \hat{\Omega}) = \int_{\mathbf{h}} p(\mathbf{h}|H_s) p(\mathbf{x}|H_s, \mathbf{h}, \hat{\Omega}) d\mathbf{h}. \quad (5.34)$$

This requires that we state explicitly what our model predicts for the prior probability distribution of \mathbf{h} , i.e., $p(\mathbf{h}|H_s)$. We will use a very simple form for \mathbf{h} given by a zero-mean normal distribution with amplitudes given by the covariance matrix, \mathbf{A} :

$$p(\mathbf{h}|H_s) = \mathcal{N}(\mathbf{h}, \mathbf{0}, \mathbf{A}). \quad (5.35)$$

Combining (5.34) and (5.35), the marginalized signal likelihood then becomes

$$\begin{aligned} p(\mathbf{x}|H_s, \hat{\Omega}) &= \int p(\mathbf{h}|H_s) p(\mathbf{x}|H_s, \mathbf{h}, \hat{\Omega}) d\mathbf{h} \\ &= \int \mathcal{N}(\mathbf{h}, \mathbf{0}, \mathbf{A}) \mathcal{N}(\mathbf{x}, \mathbf{F}(\hat{\Omega})\mathbf{h}, \Sigma) d\mathbf{h} \\ &= \mathcal{N}(\mathbf{x}, \mathbf{0}, (\Sigma^{-1} - \mathbf{K})^{-1}) \\ &= \frac{1}{(2\pi)^{D/2}} \sqrt{\Sigma^{-1} - \mathbf{K}} \exp\left(-\frac{1}{2}\mathbf{x}^T (\Sigma^{-1} - \mathbf{K}) \mathbf{x}\right), \end{aligned} \quad (5.36)$$

where

$$\mathbf{K} \equiv (\Sigma^{-1} \mathbf{F})(\mathbf{F}^T \Sigma^{-1} \mathbf{F} + \mathbf{A}^{-1})^{-1} (\Sigma^{-1} \mathbf{F})^T. \quad (5.37)$$

The variable \mathbf{K} , while complicated looking, is a function of only $\hat{\Omega}$ and the prior variances assigned to the noise and signal models. We can now use equation (5.36)

to solve for the signal/noise likelihood ratio as a function of $\hat{\Omega}$:

$$\mathcal{L}_{s/n}(\hat{\Omega}) = \frac{p(\mathbf{x}|H_s, \hat{\Omega})}{p(\mathbf{x}|H_n)} \quad (5.38)$$

$$\begin{aligned} &= \frac{\mathcal{N}(\mathbf{0}, (\boldsymbol{\Sigma}^{-1} - \mathbf{K})^{-1}, \mathbf{x})}{\mathcal{N}(\mathbf{0}, \boldsymbol{\Sigma}, \mathbf{x})} \\ &= \sqrt{\mathbf{I} - \boldsymbol{\Sigma}\mathbf{K}} \exp\left(\frac{1}{2}\mathbf{x}^T \mathbf{K}\mathbf{x}\right). \end{aligned} \quad (5.39)$$

To achieve the full signal/noise likelihood ratio, we finally marginalize (5.38) over $\hat{\Omega}$:

$$\mathcal{L}_{s/n} = \frac{p(\mathbf{x}|H_s)}{p(\mathbf{x}|H_n)} \quad (5.40)$$

$$\begin{aligned} &= \int_{\hat{\Omega}} \mathcal{L}_{s/n}(\hat{\Omega}) d\hat{\Omega} \\ &= \int_{\hat{\Omega}} p(\hat{\Omega}|H_s) \sqrt{\mathbf{I} - \boldsymbol{\Sigma}\mathbf{K}} \exp\left(\frac{1}{2}\mathbf{x}^T \mathbf{K}\mathbf{x}\right) d\hat{\Omega}. \end{aligned} \quad (5.41)$$

If we are conducting an “all-sky” search, as we are for the search described in this thesis, we assume all sky locations have equal likelihood and $p(\hat{\Omega}|H_s)$ is a constant.

While equation (5.40) represents the full Bayes factor for the signal/noise hypothesis test, equation (5.38) is a very important result in its own right. Since equation (5.38) is a function of sky position, we can, by sampling over a grid on the sky, calculate equation (5.38) for each sky location. The result is then a probability distribution map over the sky.

5.6 Glitch model

As mentioned earlier, detector glitches are a significant problem for analyses [145, 146]. Glitches are loud excursions in the noise of a single detector that happen relatively infrequently. As with simple Gaussian noise, glitches happen independently in each detector. It is easiest then to think of them as a separate quantity, g , that is added to the data that we measure from an individual detector. We can then formulate a

new hypothesis, H_g , that we are measuring a detector glitch:

$$H_g: x_i = n_i + g_i. \quad (5.42)$$

A simple description of glitches is a broad normal distribution, indicating that the glitches are *energetic*, weighted by a very small factor, $\epsilon \ll 1$, meaning they are *rare*:

$$p(g_i|\sigma) = \epsilon \mathcal{N}(g_i, 0, \sigma). \quad (5.43)$$

We can improve this model by generalizing (5.43) to be scale invariant by averaging over normal distributions with a range of standard deviations and appropriate weightings:

$$p(g_i|\sigma_{max}) = \frac{1}{\sigma_{max}} \int_0^{\sigma_{max}} \frac{\mathcal{N}(g_i, 0, \sigma)}{\sigma} d\sigma, \quad (5.44)$$

or more elegantly, using the parameter $a = e^\sigma$,

$$p(g_i|\sigma_{max}) = \frac{1}{\ln \sigma_{max}} \int_0^{\ln \sigma_{max}} \mathcal{N}(g_i, 0, e^a) da. \quad (5.45)$$

The overall glitch+noise distribution is then (5.45) convolved with a unit Gaussian (the distribution for simple noise alone):

$$p(x_i|H_g, \sigma_{max}) = \frac{1}{\ln \sigma_{max}} \int_0^{\ln \sigma_{max}} \mathcal{N}(x_i, 0, \sqrt{1 + e^{2a}}) da. \quad (5.46)$$

The glitch likelihood for detector i , i.e., $p(x_i|H_g)$, is then (5.46) marginalized over the various σ_{max} .

With the glitch likelihood in hand, we can now compute a glitch/noise likelihood ratio for a single detector: (5.40):

$$\mathcal{L}_{g/n}(i) \equiv \frac{p(x_i|H_g)}{p(x_i|H_n)}. \quad (5.47)$$

As with plain noise, glitches are uncorrelated in the various detectors, so the joint

probability is just the product of the individual probabilities:

$$p(\mathbf{x}|H_g) = \prod_i p(x_i|H_g). \quad (5.48)$$

The overall network glitch/noise likelihood ratio is then

$$\mathcal{L}_{g/n} = \prod_i \mathcal{L}_{g/n}(i) = \frac{p(\mathbf{x}|H_g)}{p(\mathbf{x}|H_n)}. \quad (5.49)$$

Even more important to the analysis described in the next chapter, we can now calculate the signal/glitch likelihood ratio by taking the ratio of (5.40) and (5.49):

$$\mathcal{L}_{s/g} \equiv \frac{p(\mathbf{x}|H_s)}{p(\mathbf{x}|H_g)} = \frac{\mathcal{L}_{s/n}}{\mathcal{L}_{g/n}}. \quad (5.50)$$

Chapter 6

A Low-Latency Transient Search Pipeline for Gravitational Waves

In chapter 4, I put forth a solid scientific motivation for pursuing low-latency searches for gravitational waves. There is ample reason to push forward with this effort. If significant events can be identified quickly enough, and with precise sky origin, then there is much we may see.

The motivation is strong enough, in fact, that during the joint LIGO S6 science run, in conjunction with the Virgo observatory, a full-scale electromagnetic follow-up LookUp search was performed (described in more detail in chapter 7). In this chapter I describe one of the primary transient search pipelines that enabled the S6 low-latency search: the Ω -Pipeline Rapid Online Analysis (OROA). OROA is an “online” version of the Ω -Pipeline, an established transient search pipeline, which was adapted to run in a very low-latency mode.¹ In order to meet the needs of the EM follow-up effort, Ω -Pipeline was also extended and improved by the addition of coherent search algorithms that not only improved the sensitivity of the pipeline but also allowed for reconstruction of the most probable source location of events in the

¹In this chapter we use the term “low latency” to refer generally to latencies of minutes or less, as opposed to hours or longer. The term “online” is used to describe processes that produce results with low latency, as opposed to their “offline” counterparts that do not have the same time constraints.

sky.

Beyond searches, low-latency analyses are also very useful as tools for improving the detectors themselves. There are many metrics that can be used to measure the performance of the detectors. The most obvious and straightforward is the detector strain sensitivity (see figure 3-5). However, while this metric is useful, it does not tell the whole story. In particular, it says essentially nothing about some issues of particular importance to transient searches, such as noise non-Gaussianity, non-stationarity, and “glitchiness.” Excessive glitchiness in the detectors can reduce the significance of real events, reducing the sensitivity of the searches. In the past, the true effect of these problems did not become apparent until the data was analyzed, which was long after it was gathered, and therefore long after there was anything that instrument scientists could do about it. If the analyses are instead built to run in low-latency online modes, they can report on the quality of the data relevant to analysis when the instrument scientists are working on the detectors and can actually do something about it.

I begin this chapter by describing the underlying Ω -Pipeline transient search algorithm, which forms the basis of the Omega Rapid Online Analysis (section 6.1). I then describe how this pipeline was extended to run in a very low latency mode, able to quickly identify events, reconstruct their most likely sky location, and report them to a distribution system for follow-up observation (section 6.2). Finally, I describe the characterization of the algorithm with offline Monte Carlo simulations used to understand both the quality of event identification and the ability of the algorithm to reconstruct event source position (section 6.3).

6.1 The Omega transient search pipeline

Ω -Pipeline is a data analysis pipeline built specifically to search for short transient gravitational-wave signals in data from networks of interferometric gravitational-wave

detectors. Ω -Pipeline is a rebranding of the earlier **Q-Pipeline** [147], and extending it to include new coherent algorithms that perform multichannel coherent consistency checks and position reconstruction on significant events. **Q-Pipeline** was well tested and used in previous searches for gravitational wave bursts during LIGO science observations [148, 149]. The addition of a coherent analysis component is a significant advancement over previous incoherent analyses. The coherent algorithms added to Ω -Pipeline were discussed in detail in chapter 5, and section 6.1.4 will discuss how these algorithms were implemented.

One of the difficulties with coherent algorithms, as discussed previously, is that they tend to be much more computationally intensive than incoherent ones. Ω -Pipeline gets around this with the use of a hierarchical approach to first identify times of interest with a low-cost incoherent approach, only following up the most interesting times with coherent analyses. This greatly decreases the computational cost, freeing up time to search larger areas of the sky (or the full sky, as is the case with the “all-sky” searches described herein).

Ω -Pipeline is written primarily in the **MATLAB** programming language but includes components written in **C**, **C++**, **Python**, and **BASH**.

6.1.1 Structure of the pipeline

As described above, Ω -Pipeline uses a hierarchical approach in its analysis of the network data stream. The data from each individual detector is first analyzed independently with the **Q-Pipeline** algorithm to determine times of significant excess power (section 6.1.2). These significant times are referred to as “triggers.” These single-detector triggers include parameters such as frequency, duration, bandwidth, and normalized energy. Once all the single-detector triggers have been gathered, they are tested for time and frequency coincidence with the triggers from the other detector streams. The most significant of these multidetector coincident triggers are then passed on to a series of coherent algorithms that do fully coherent analyses around

the times of interest (section 6.1.4).

In order to facilitate the analysis, the data are broken up into smaller, more manageable segments, referred to internally as *blocks*. Figure 6-1 is a schematic overview of the structure of the full hierarchical block analysis for a three-detector H1/L1/V1 search.

6.1.2 Single detector analysis

The analysis algorithm for the individual detector data streams in Ω -Pipeline is inherited directly from Q-Pipeline, and is described in detail in [147, 150]. I will only give a brief overview here.

The Q-Pipeline algorithm is unique in that it decomposes the data into a basis of sine-Gaussians, otherwise known as a *Q transform* [150], which projects the data onto a template bank of windowed complex exponentials defined by a central time τ , a central frequency ϕ , and a quality factor Q :

$$X(\tau, \phi, Q) = \int_{-\infty}^{\infty} x(t)w(t - \tau, \phi, Q) \exp(-i2\pi\phi t) dt, \quad (6.1)$$

where w is the window function. This basis is used because it is thought to match well the expected signal morphology of gravitational wave bursts that are well localized in time.

The pipeline begins by loading in the data to be analyzed, and optionally any injection waveforms that may be added to the data for doing Monte Carlo simulations. After being loaded in, the data are “conditioned”, which refers to multiple transformations to the data that help ease further analysis. The first conditioning step is to filter down to only the frequencies of interest around the range of maximum detector sensitivity. This is done by down-sampling the data to 4096 Hz (down from the original 16,384 Hz detector sample rate), and high-pass filtering the data at 48 Hz. We then end up with data covering the frequency range of 48 - 2048 Hz.

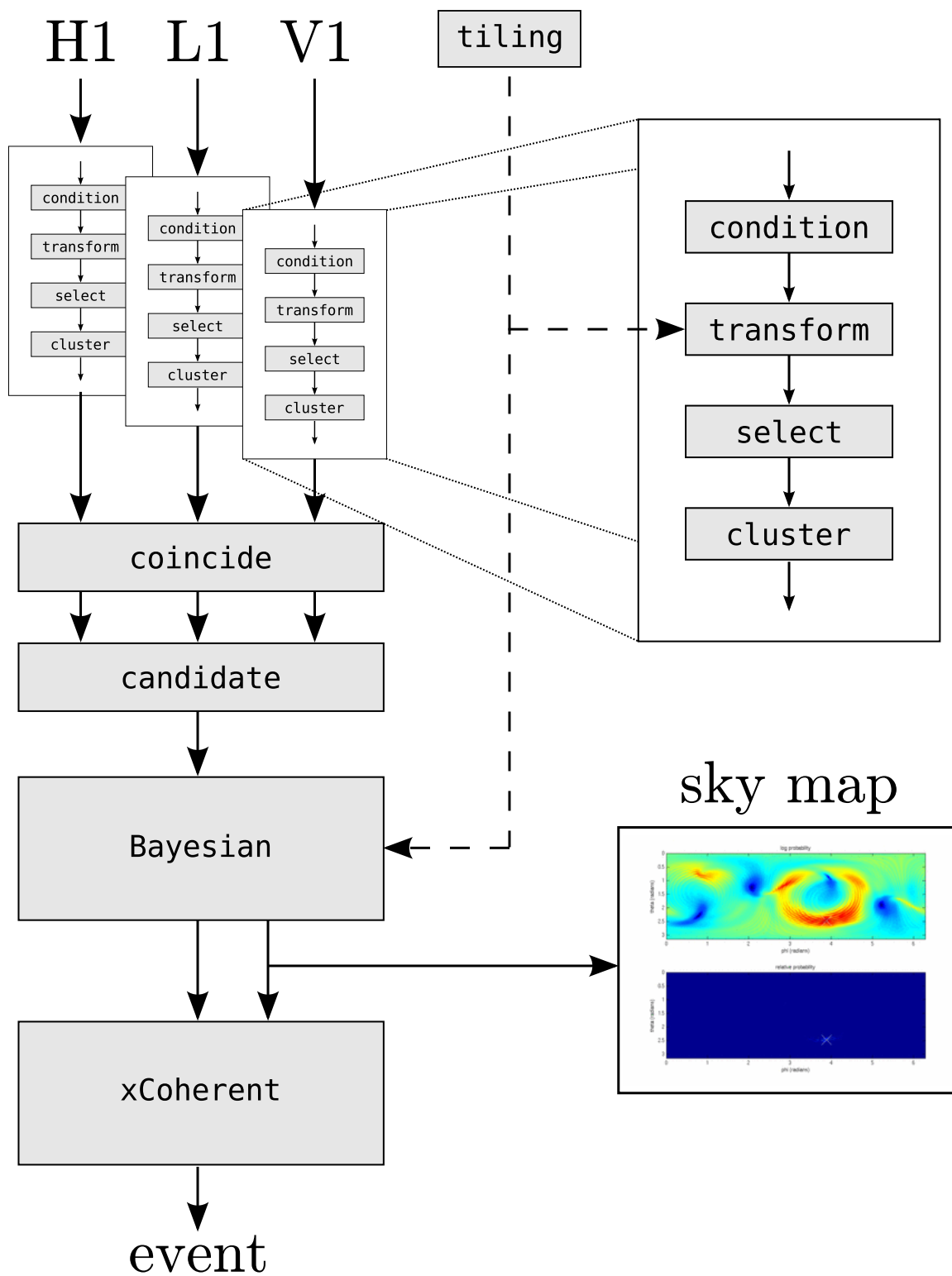


Figure 6-1: Flowchart of full Ω -Pipeline search algorithm.

One of the more important conditioning steps is to *whiten* the data. Whitening is done by filtering the data by the inverse of the data power spectral estimate. This puts roughly equal power into each frequency bin and reduces auto-correlation in the data as much as possible. The whitening algorithm used in Ω -Pipeline is known as the *median-mean-average* approach, first outlined in the FINDCHIRP algorithm [151]. This is a change over the linear predictive whitening algorithm used by Q-Pipeline.

Once the data has been conditioned, it is decomposed into the Q basis, producing a set of *Q planes*, which are time-frequency maps of constant Q. Each tile in each Q plane has a *normalized energy*, which is a measure of the energy (squared amplitude) in the tile, normalized by the mean energy in the other tiles in the same Q plane and frequency row (after rejecting outliers). Figure 6-2 shows time-frequency spectrogram plots of these various constant Q planes for a sine-Gaussian hardware injection.

After decomposition, statistically significant tiles in the various Q planes are picked out from the background. This is done by thresholding on the normalized energy in the tile at a specified white noise false alarm rate. The tiles are then sorted in order of decreasing significance and selected for non-overlap. Figure 6-3 shows plots of just the significant tiles from the various Q planes in figure 6-2.

The final step of the single detector analysis is to *cluster* the significant tiles in time and frequency [152]. This clustering is demonstrated in figure 6-4. Clustering generates a new set of interesting trigger properties. Not only do we have the Q-tile information from each of the individual triggers, but we also have the information from the clusters, including the cluster central time, frequency, bandwidth, duration, and normalized energy (the latter being the sum of the normalized energy of the individual cluster triggers). The cluster parameters are important since they give a better overall sense of the true nature of the underlying signal.

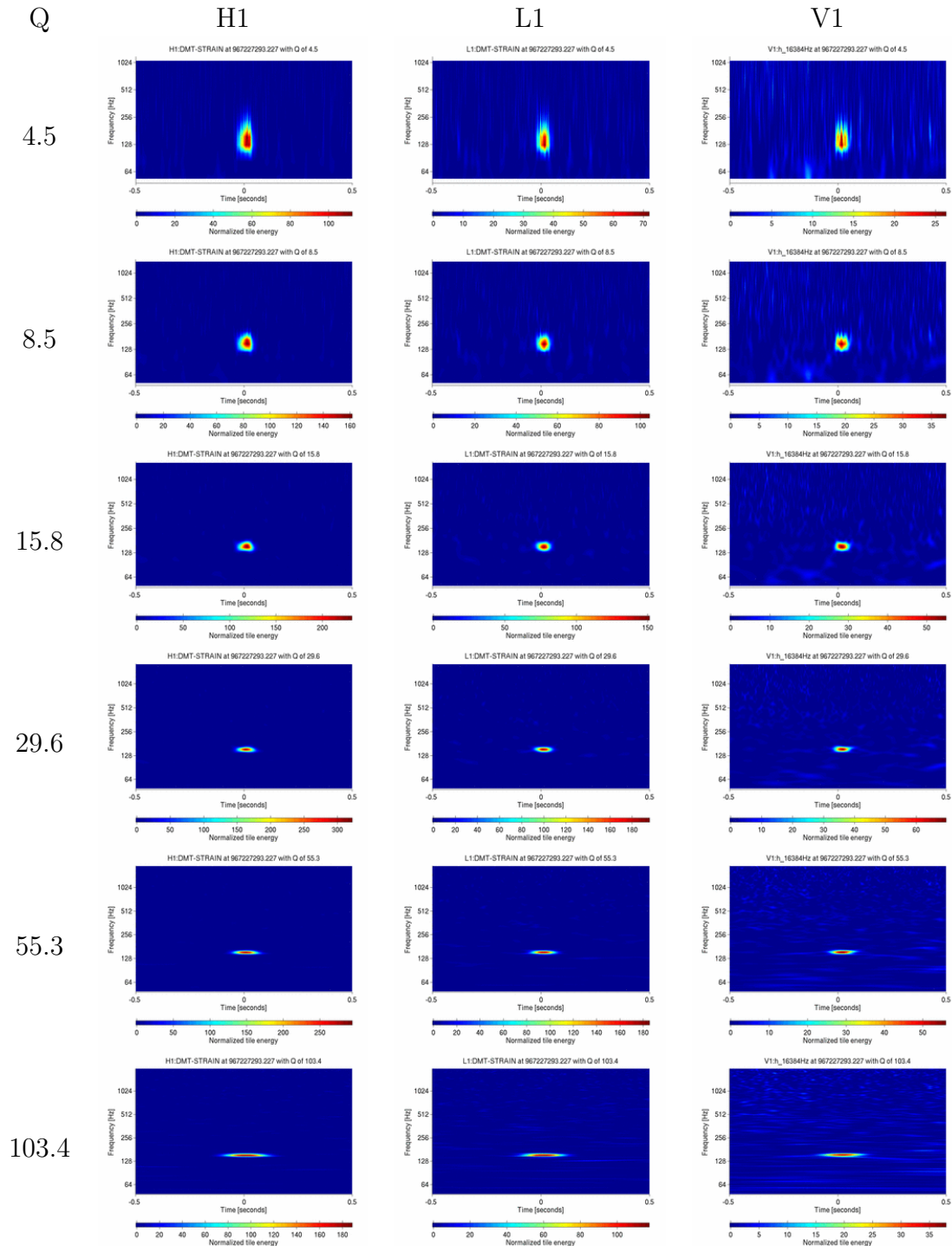


Figure 6-2: Omega single detector constant-Q spectrograms at the time of a 153.0 Hz, Q 25 sine-Gaussian hardware injection with H1, L1, V1 SNR of 18.629, 17.891, 11.067 respectively. The three columns are the spectrograms for the three detectors H1, L1, and V1, and the Q of the row is specified in the left-most column. The color map indicates the normalized energy, with red being highest and blue being lowest energy (see the color bars underneath the individual plots).

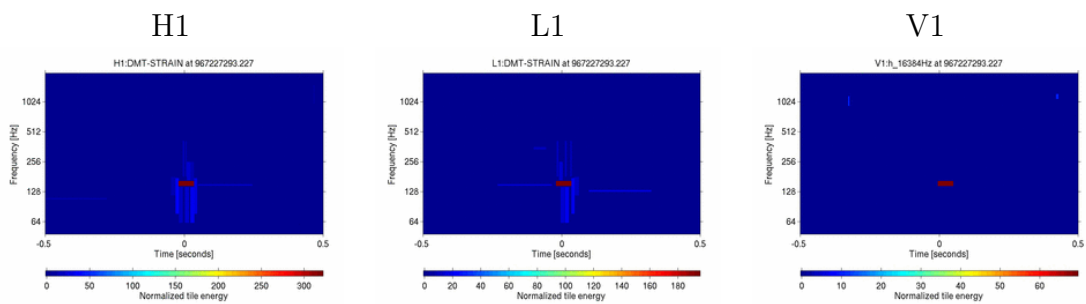


Figure 6-3: Selected significant tiles from all Q planes for the same event in figure 6-2.

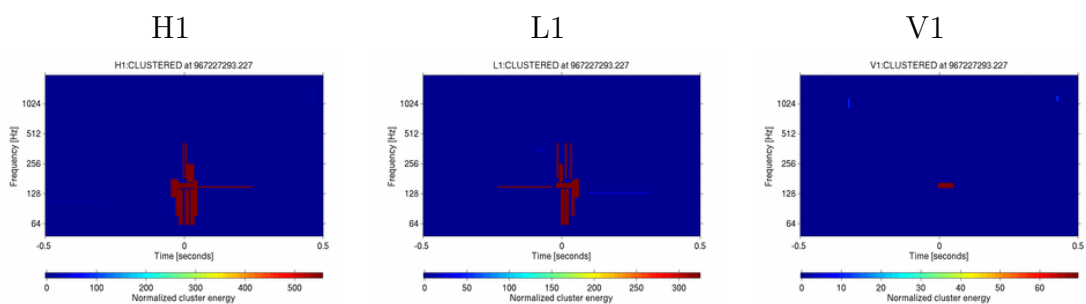


Figure 6-4: Clustered tiles from all selected tiles from figure 6-3.

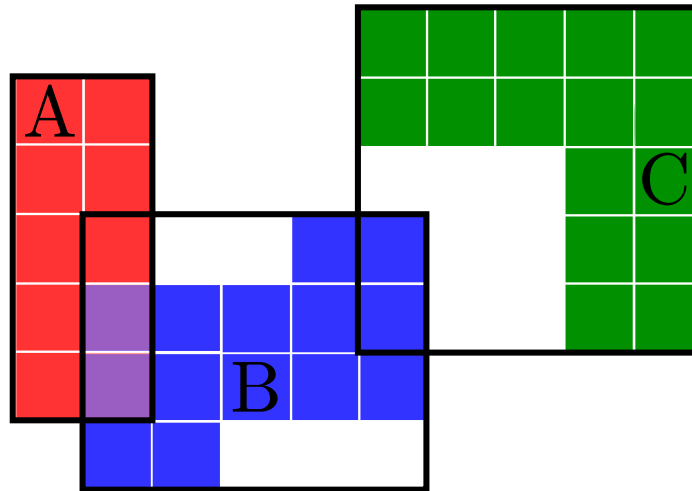


Figure 6-5: Determination of cluster coincidence. A (red), B (blue), and C (green) represent trigger clusters in different detectors. Cluster A and B have two overlapping triggers (purple), which qualifies them for coincidence. Even though clusters B and C have overlapping bounding boxes, they do not qualify for coincidence since they have no overlapping triggers.

6.1.3 Coincidence and candidate selection

Once the final set of significant triggers from each individual data stream are in hand, the pipeline searches for triggers from different detectors that are coincident in time and frequency. Instead of looking for overlap in the cluster bounding boxes in the time-frequency plane, we actually look for time-frequency coincidence between the individual triggers that comprise the clusters. This is illustrated in figure 6-5.

6.1.4 Coherent follow-ups

At the end of the independent analysis part of the pipeline we are left with a candidate event, which includes the coincident clusters from the various detectors and their constituent triggers. This candidate event is then passed to the coherent search algorithms. Ω -Pipeline employs two separate coherent statistics. The first is a Bayesian analysis based on the coherent Bayesian algorithm described in chapter 5. This analysis produces a Bayesian event statistic, as well as a source sky map. The second

coherent analysis uses the most likely position from the Bayesian sky map to produce an event statistic based on the standard null stream analysis described in 5.2. Finally, these two statistics are combined to form a single event statistic that is used to rank events.

The new Bayesian algorithm

Ω -Pipeline’s new Bayesian coherent search algorithm is a direct implementation of the algorithm described in detail in chapter 5. Since the Bayesian analysis stage is given a time already characterized as significant by the incoherent part of the pipeline, we are interested in comparing the hypothesis that the event is a signal, H_s , against the hypothesis that the event is a glitch, H_g . The Bayesian analysis therefore calculates the signal/glitch likelihood ratio of equation (5.50):

$$\mathcal{L}_{s/g} \equiv \frac{p(\mathbf{x}|H_s)}{p(\mathbf{x}|H_g)}. \quad (6.2)$$

The analysis begins by calculating the glitch hypothesis for each detector, i . We work in log space because of the enormous range of values that we’re working with. The calculated statistic is then known as `logGlitch`:

$$\text{logGlitch}(i) = \log(\mathcal{L}_{g/n}(i)). \quad (6.3)$$

The overall glitch hypothesis likelihood for the network is then the sum of the values of (6.3) for each detector:

$$\text{logGlitch} = \sum_i \text{logGlitch}(i). \quad (6.4)$$

To calculate the signal hypothesis likelihood, we first calculate the sky map, which

is the signal likelihood unmarginalized over the sky,

$$\mathbf{logSkymap}(\theta, \phi) = \log(\mathcal{L}_{s/n}(\theta, \phi)). \quad (6.5)$$

The sky map is a measure of probability as a function of θ and ϕ on the sky. It is calculated with an adaptive integrator that is able to concentrate more time on areas with higher probability.

The sky map is one of the most important outputs of Ω -Pipeline. It is what gives us the position reconstruction that is so important for LookUp searches. The electromagnetic follow-up pipelines use the sky map to determine where to point telescopes. Figure 6-6 is an example of a sky map produced by the pipeline for a sine-Gaussian injection. It includes a zoom in on the region with maximal probability indicating how close to the true injected location this area is.

The overall signal likelihood is calculated directly from the sky map. This is done by taking the sum of the probabilities in each sky pixel, weighted by the area of each pixel, $\mathbf{area}(\theta, \phi)$, and normalizing by the full 4π radians² of the sky. Again working in log space, this is explicitly given as:

$$\begin{aligned} \mathbf{logSignal} = \log & \left(\sum_{\theta, \phi} [\exp(\mathbf{logSkymap}(\theta, \phi) - \max(\mathbf{logSkymap})) \right. \\ & \left. \times \mathbf{area}(\theta, \phi) \times \sin \theta] \right) \\ & + \max(\mathbf{logSkymap}) \\ & - \log(4\pi). \end{aligned} \quad (6.6)$$

The use of $\max(\mathbf{logSkymap})$ is a technique to prevent overflow when taking the exponential of the sky map probabilities.

The final Bayesian event statistic is the likelihood ratio or, equivalently, the odds ratio, given that we consider the prior odds ratio as a kind of threshold on the

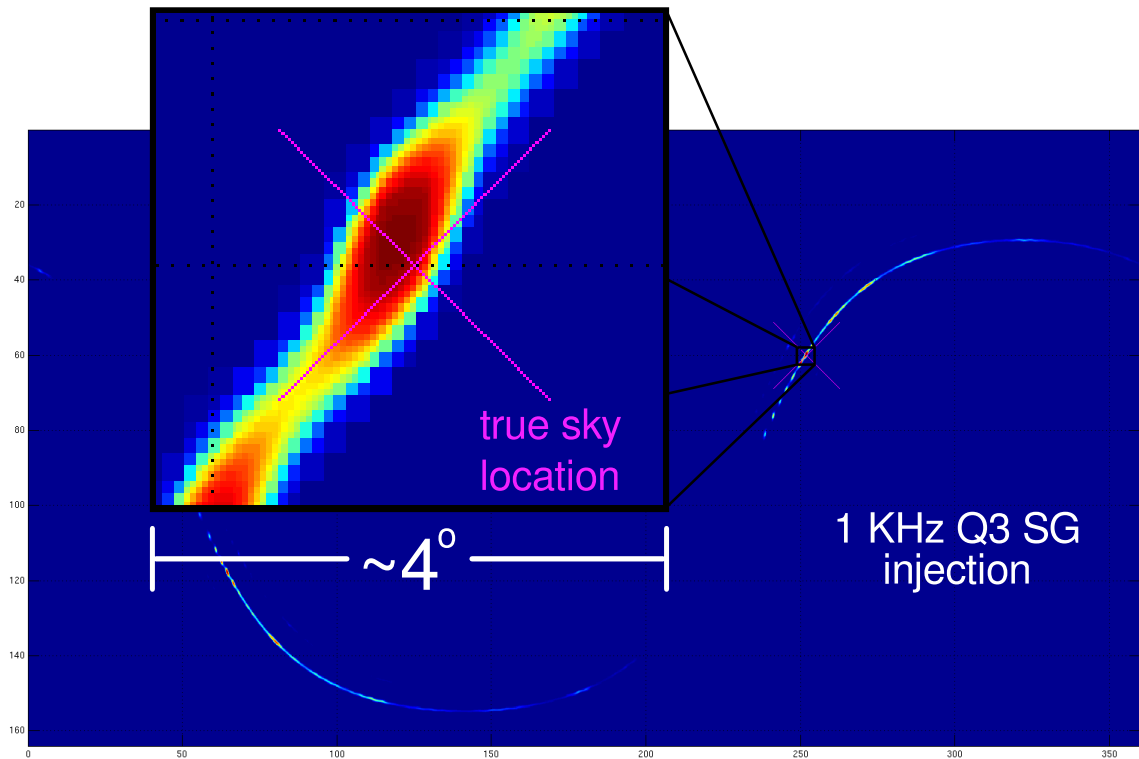


Figure 6-6: Example of the Omega Bayesian reconstructed probability distribution skymap of a 1 KHz, Q 3 sine-Gaussian waveform injection “at threshold”, i.e. with a SNR of roughly 10. The scale goes from zero probability (blue) to unity probability (red), with an integrated probability over the whole map of unity. The true location of the injection is indicated by the magenta cross. The 4° field of view of the zoomed region is roughly equivalent to the field of view of the QUEST telescope. The work of the adaptive integrator can be seen in the variation of pixel sizes in the zoomed area.

likelihood ratio. In log space, this is just the difference between the log of the signal and glitch hypothesis likelihoods:

$$\text{logOdds} = \text{logSignal} - \text{logGlitch}. \quad (6.7)$$

The null-stream statistic

Once the Bayesian analysis has completed and returned its best estimate of the sky position of the signal, Ω -Pipeline performs a more standard coherent null-stream analysis on the event as described section 5.2.

As mentioned above, this statistic requires a sky position so as not to have to maximize across the entire sky. Conveniently, the Bayesian analysis has produced such a sky position in the form of the most probable position in the Bayesian sky map. The null stream analysis is then done for this position.

$$\text{nullEnergy}(\theta, \phi) \equiv E_{\text{null}}(\theta, \phi) \quad (6.8)$$

$$\text{nullIncoherentEnergy}(\theta, \phi) \equiv E_{\text{inc}}(\theta, \phi) \quad (6.9)$$

$$\begin{aligned} \text{nullCoherentEnergy}(\theta, \phi) \equiv & \text{nullIncoherentEnergy}(\theta, \phi) \\ & - \alpha \times \text{nullEnergy}(\theta, \phi). \end{aligned} \quad (6.10)$$

The factor α is a tuning factor used to put an upper bound at zero on events from the background. It is tuned with the results of background time-slide analyses (see section 6.3.2) and typically is set to a value of around 1.1.

The combined event statistic

The final step of the pipeline is to combine the Bayesian and nullstream event statistics into a single overall detection statistic that can be used to rank events. The final

`omega` statistic is determined as follows:

$$\text{logOddsMod} = \text{arcsinh}(\text{logOdds}) \quad (6.11)$$

$$\text{xStatMod} = \text{arcsinh}(\beta \times \text{xStat}) \quad (6.12)$$

$$\text{omega} = \max(\text{logOddsMod}, \text{xStatMod}). \quad (6.13)$$

As with α , the factor β is another tuning factor used to “normalize” the two statistics and is determined via background analysis over some relevant data set. It is set such that the maximum of `logOddsMod` and `xStatMod` in the background have the same value. The statistic `omega` is used as the ranking statistic for events from coherent Ω -Pipeline.

6.2 The Omega-Pipeline Rapid Online Analysis

The Ω -Pipeline described above was originally designed to analyze large amounts of data in offline end-to-end analyses on large Beowulf² computer clusters. While Beowulf clusters provide high throughput and performance for large computing tasks, they have latencies that are unacceptable for online analyses.

In this section I describe how the Ω -Pipeline was modified to run in a low-latency mode. This new pipeline is known as the Omega Rapid Online Analysis (OROA). With the modifications described below, the OROA was able to achieve latencies of mere minutes between the time of identifying a candidate event, with full parameter estimation and position reconstruction, and the actual event time in the data. This enabled for the first time successful electromagnetic follow-up observations of gravitational wave event candidates.

²“Beowulf cluster” refers to a large number of computers configured to operate in parallel for high-performance applications. See the following Wikipedia entry for more information: [http://en.wikipedia.org/wiki/Beowulf_\(computing\)](http://en.wikipedia.org/wiki/Beowulf_(computing)).

6.2.1 Structure of the online pipeline

In offline analyses, all needed data have already been gathered in the experiment and been made available ahead of time. However, an online analysis needs to read in and analyze data as soon as it becomes available, with the goal of identifying event candidates as quickly as possible. Achieving this required many structural changes. The biggest challenges for achieving robust, low-latency results were what I will refer to as *data inflow management* and *process management*.

Data inflow management has to do with control of the analysis in the face of data not being available in a timely or deterministic manor. For instance, the sites of three interferometers used in the S6 analysis are widely dispersed across the globe. The computer network connecting them together (the “Internet”) is a notoriously spotty and unpredictable beast. The latencies involved in transferring the data from the remote sites to the central location where the online analysis is run can vary over a fairly wide range of times. The online analysis needs to be able to wait for all needed data from all interferometers and must incorporate graceful timeouts and be able to proceed in case some blocks of data do not show up.

Process management involves making sure that the analysis continues to run as smoothly and quickly as possible even if part of the analysis chokes or encounters problems. If a stretch of data is corrupt and causes the analysis to crash, or is extremely noisy and causes the analysis to take an inordinately long time to run, we do not want this to affect the analysis of subsequent stretches of data.

In order to handle both of these issues, the OROA implements an independent block analysis structure. In this process the data to be analyzed is broken into small chunks in time, similar to what is done with the offline analyses described in section 6.1.1. However, in this independent block analysis each block of data is analyzed by a completely separate and independent analysis process, each of which can be executed in parallel. Independent block processes allow the pipeline to gracefully and robustly handle data inflow by allowing each block analysis to wait for the data it

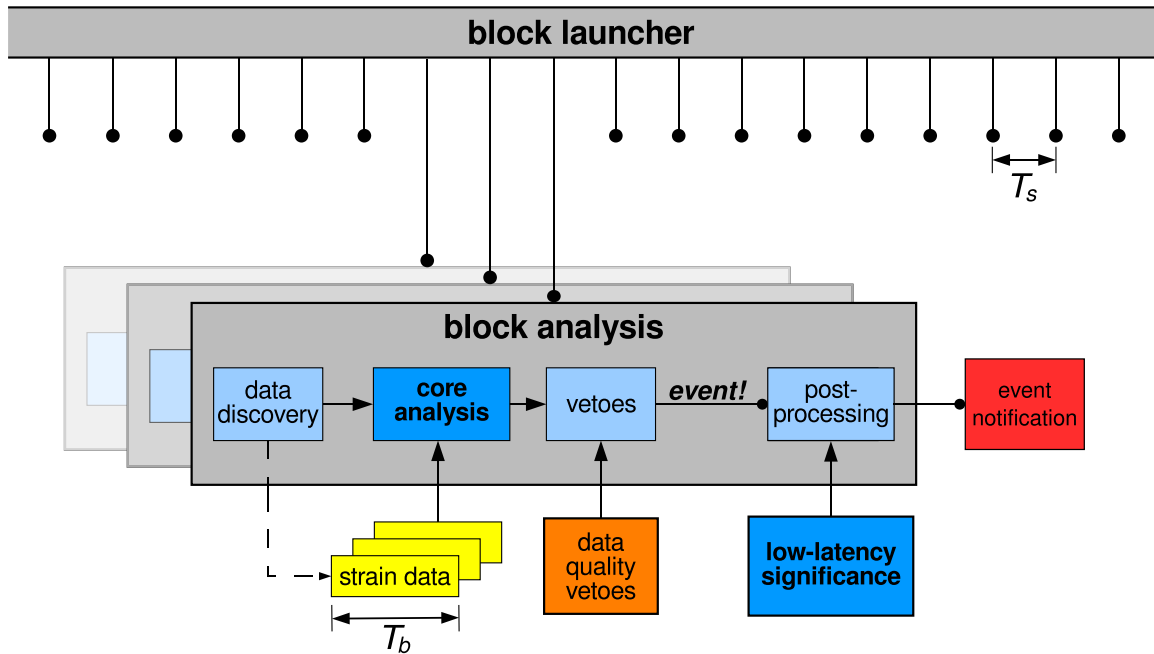


Figure 6-7: Block diagram of the Omega Rapid Online Analysis pipeline. T_b is the time length of data analyzed as a single block, and T_s is the stride time.

needs for as long as necessary, while simultaneously keeping the analysis of any given block from impeding the analysis of subsequent blocks.

Figure 6-7 is a schematic diagram of how this independent block analysis was implemented. The pipeline consists two main components: the *block launcher* and the *block processor*. The block launcher manages the launching of block analysis jobs, and each block processor job actually handles the analysis of a given block of data. Each is described in more detail in the following sections.

The block launcher

The block launcher (also known as the *supervisor*) is the program that launches all of the individual block analysis processes. The block launcher is little more than a single continuously running loop. At each iteration of the loop it checks the current GPS time. If the current GPS time is later than the start time of the next block, the block is launched in the background. Finally, the start time of the next block is

calculated, and the loop continues.

The GPS start time of block N is just N times the stride time, T_s . The stride time is the length of each block, T_b , minus the overlap time of each block, T_o :

$$T_s = T_b - T_o. \quad (6.14)$$

It is worth noting that while the block processor can just be run on its own, managing long-running processes like the OROA brings its own set of challenges, such as gracefully handling starting, stopping, restarting, logging, etc. The OROA was designed to use the `runit` UNIX service supervision scheme³ which handles all of these various issues with aplomb.

The block analysis

The block analysis is what actually prepares the analysis environment and launches the core Ω -Pipeline analysis code on the given block of data. It then reads in the results of the core analysis and applies post-processing to the results to determine if anything interesting was seen in that block of data and if any further action should be taken.

The block analysis handles the following tasks:

- Data discovery
- Core analysis (including process monitoring)
- Post-processing and vetos
- Event notification and follow-up scripts

The various tasks are described below.

³<http://smarden.org/runit/>

6.2.2 Data discovery

The first task of the block processor is to determine if the needed data is available (*data discovery*). This process is not necessarily as straightforward as it may sound. The data to be analyzed must be transferred from the three remote detector locations, which are spread across the globe. The transfer latencies are varying and nondeterministic.

The way that data discovery is done in the block processor is based on how data are made available by the data-transfer mechanisms that distribute data to the analysis sites. The basic idea is to determine which data are needed for the given block and to continue to poll for the presence of the data until it appears or until a timeout is reached. If the timeout is reached and the data from all detectors did not become available, the analysis continues with the available data in reduced-network mode.

6.2.3 Core analysis

Once all needed data are in hand, the block processor launches the actual core Ω -Pipeline analysis engine on the block of data in question. The core analysis engine is a byte-compiled version of the core `MATLAB` code. It reads in the data for the block and performs the full analysis. The compiled binary is executed in the background, as opposed to the block processor waiting on its completion. This allows the block processor to monitor the progress of the analysis process and kill the process if something goes wrong or it is taking too long to complete the analysis. In practice this has not been needed, and the analysis processes complete in a timely manor. Upon completion of the analysis of the block of data in question, the block processor reads in the results from the analysis output files. In particular, the processor reads in the time and event statistics of the event.

6.2.4 Rapid significance estimation

Determination of event significance is a bit trickier for low-latency analyses than for offline analyses. For offline analyses time is much less of an issue. More time can be taken to perform more time slide analyses to produce better estimates of the background as needed. Low-latency analyses, on the other hand, need to determine the significance of events quickly.

The OROA handles this by running many parallel “time-slide” analyses on a large computer cluster in the background while the main “zero-lag” analysis⁴ runs in the foreground. In particular, every 30 minutes we run 100 time-slide analyses on the last 30 minutes of data (i.e., one *set*). Each set of 100 time-slide analyses over 30 minutes of data represents a potential livetime of $100 \times 30 = 3000$ minutes, or roughly two days of analyzed livetime. However, livetime is also affected by the duty cycle of the detectors. The various detectors can never, in practice, be operational in a scientific mode 100% of the time, so livetime is usually reduced significantly from this level.

These time-slide analyses allow us to provide various different useful significance estimations for a given event:

- Last set (maximum ~ 2 days livetime)
- Last 48 sets (last day’s sets, maximum ~ 96 days livetime)
- All sets since beginning of run (maximum $\sim 96 \times N$ days in the run)

The comparison of an event against these various sets can tell us the relative significance against both global and local backgrounds.

6.2.5 Vetos, thresholds, post-processing, and notification

Once the data block has been analyzed, the block processor looks to see if a suitable event candidate was found. Determining if an event candidates is suitable to pass on

⁴The term “zero-lag” refers to the analysis that looks for actual gravitational wave events in the data. This is in contrast to “time-slide” background analyses which analyze the network with shifts in the relative times of the detector data streams (described further in section 6.3.2).

depends on a number of different criteria:

- Network analyzed: data from all three detectors (H1, L1, V1) must have been analyzed in the block
- Data quality vetos: event time must pass all data quality checks
- Event strength: event statistic must pass a minimal fixed threshold

Once all of these test have been passed, a series of post-processing scripts are run

- Generate spectrogram, triggergrams, and sky map plots of the event time
- Scan auxilliary environmental channels for notable activity
- Note data-quality vetos that were undefined at event time
- Determine if event was coincident with a *hardware injection*
- Send event announcement to notification system.

6.3 Characterizing the search algorithm

In order to prepare for the online search, the full Omega algorithm had to be characterized to understand its behavior. The general method for characterizing gravitational wave search algorithms is to run the algorithms through rigorous sets of Monte Carlo simulations, in which simulated gravitational waveforms are injected into the data at random times and the analysis algorithm is then tested to see how well it finds them. The results from these searches are then compared to the results from the analysis of background data known to not contain any true signals. The better the algorithm, the more distinct the injection results will look from the background results, thereby providing a means to determine the probability that a certain signal returned from the analysis looks like a true signal.

The two important aspects of the new Omega algorithm that required careful consideration were the behavior of the overall detection statistic and the Bayesian position-reconstruction capabilities. For the online search, both the detection statistic

and the position-reconstruction capabilities are important. The online analysis needs to be able to distinguish real events from background with reasonable confidence. But since one of the primary goals of the search is to provide pointing information for follow-up electromagnetic observations, the position reconstruction must be both accurate and precise to within the requirements of the follow-up observatories.

In this section, I describe the new Bayesian statistic and its detection and position-reconstruction capabilities, followed in sections 6.3.2 and 6.3.3, by a description of the characterization of the background and the results from various simulation searches.

6.3.1 Preparing the data

The characterization study described in this section used data from a stretch of the S6/VSR2 science run known as “S6b”, lasting from September 26, 2009 to January 08, 2010. Before the data were analyzed, periods of unacceptable data or poor data quality had to be removed. Only data in which all three interferometers (H1, L1, and V1) were in “science mode” were analyzed.

6.3.2 Understanding the background

The first step to characterizing a search pipeline is understanding the background of signal-like triggers. It is impossible to gauge how significant a trigger produced by the algorithm is without first understanding how frequently the data stream randomly produces signals that just *look* like gravitational waves. However, determining this background for gravitational wave detectors is a nontrivial task. Gravitational wave detectors can not be shielded from gravitational waves, so the true noise distribution can never be measured with 100% certainty. Furthermore, the detector noise distribution is neither Gaussian nor stationary, so the rate and distribution of random signal-like events occurring in the background cannot be calculated a priori.

The way we get around these issues is by performing what are known as *time-shift* or *time-slide* analyses. In a time slide the data streams from the various detectors

are shifted in time relative to one another by more than the light travel time between the detectors. For instance, the light travel time between the Hanford and Livingston detectors is roughly 30 milliseconds. As long as the relative time shift between the Hanford and Livingston data streams is much greater than this light travel time of 30 milliseconds, we can be sure that no signals in this new shifted interferometer network could have come from the same gravitational wave signal.⁵ However, assuming that there are no non-gravitational wave correlations between the data in the various detectors,⁶ this new stream should retain all of the same statistical properties as the unshifted stream.

This last point is the key to why we believe time-slide analyses provide an effective means of measuring the background. It is the statistical properties of the data in the absence of gravitational waves that we wish to measure.

A full background analysis consists of many different time-slide analyses over a distribution of relative time slides. This helps make sure that any systematic correlations between the detectors on various time scales get washed out. The ten time slides used in the background analysis for the current search are listed in table 6.1.

Figure 6-8 shows cumulative histograms of the various detection statistics in the full background analysis for all time slides listed in table 6.1. They are measured as a *false alarm rate* for the statistic. The false alarm rate is the number of times the algorithm produces a trigger of that value per unit data time analyzed. For this background analysis the total livetime is 12389521.5 seconds, or 143.4 days.

As more background is analyzed, the more the tail of this distribution is probed, and it is the behavior of the tail of the distribution that it is most important to understand. A good analysis should assign statistics to true signals that fall high in

⁵This assertion assumes, of course, that all gravitational waves travel *subluminally*. Since gravitational waves have still not been directly observed (thus this experiment), we don't know this for certain. All reasonable theories assume this to be true, though. The interaction of a *superluminal* gravitational wave with an interferometric detector would be speculative at best.

⁶With the exception of a few easily veto-able cases (such as electrical storms), no such correlations have been found.

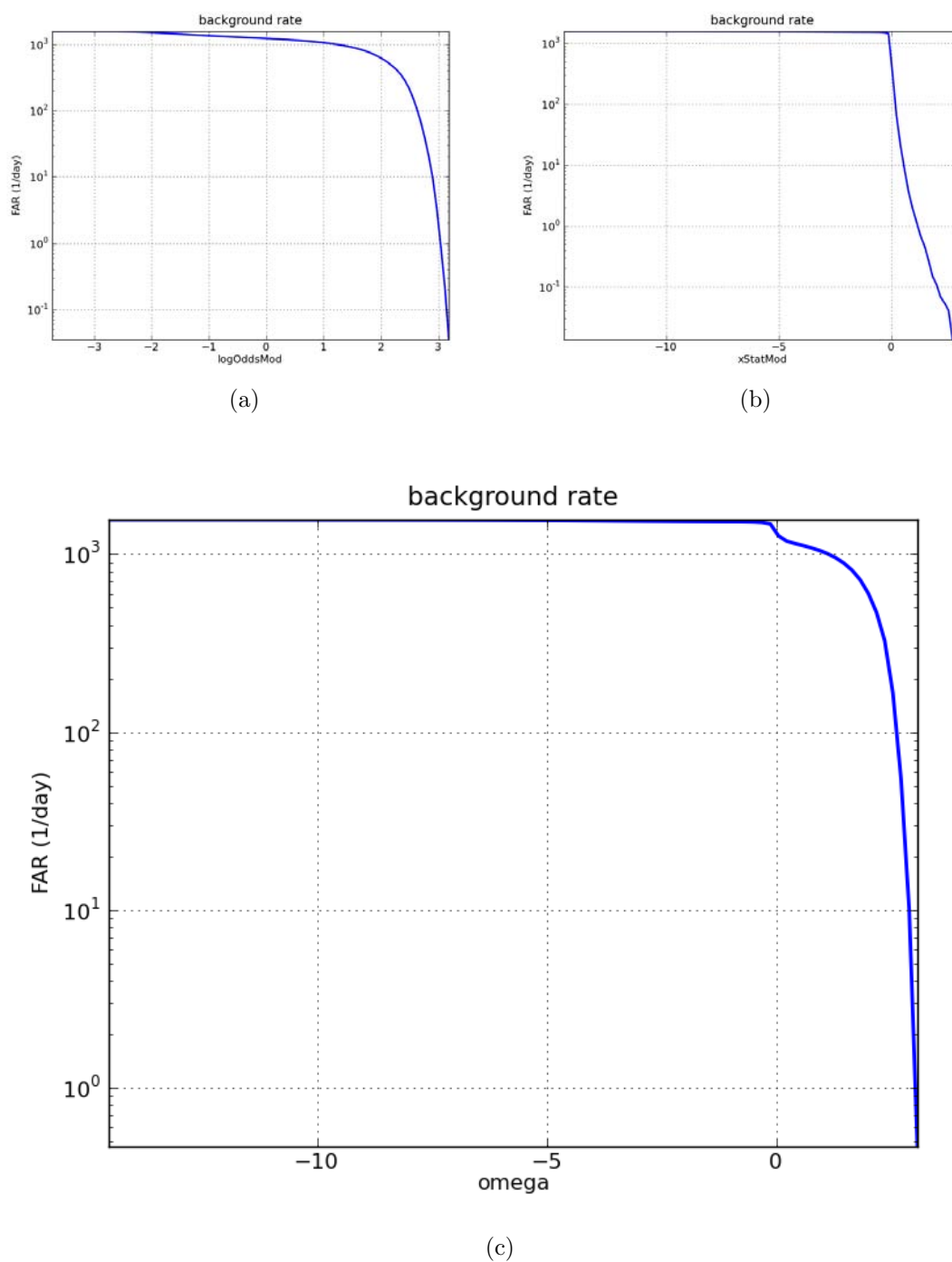


Figure 6-8: Cumulative histograms of the Omega events from 100 time-slide background analyses of the S6b analysis run. The distributions for the “logOddsMod” and “xStatMod” statistics are shown in plots 6-8a and 6-8b, and for the combined “omega” statistic in 6-8c.

H1	L1	V1
+0	-25	-167
+0	-256	-78
-19	-176	+0
-91	+0	-39
+0	-98	-23
-55	-299	+0
-129	-257	+0
-115	-266	+0
+0	-112	-279
-230	+0	-275

Table 6.1: Time slides used in the background analysis.

the upper (right most) tail of the background distribution. The more background that is analyzed, the higher the confidence of assignment of significance for a given value of the detection statistic. Given that the analyzed background livetime is roughly 143 days, the minimum false alarm rate in the background that can be assigned to any event is one over 143 days, or 6.974×10^{-3} events per day.

6.3.3 Monte Carlo simulations

One of the big challenges in gravitational wave data analysis is that we do not have a clear idea of what we are looking for. General relativity does provide some constraints by restricting the forms that a signal could possibly take, and astronomy provides further constraints through the known distribution of observed physical phenomena. The search for gravitational waves is a test of both the nature of general relativity and the limits of our astronomical knowledge.

The goal of simulations, then, is to test as much of the potential signal parameter space as we can, or at least some relevant subset. For burst analyses, we generally restrict ourselves to three generic waveform types: sine-Gaussians (SG), Gaussians (GA), and white noise bursts (WNB). The full set of simulation injections is listed in table 6.2.

name	duration (ms)	name	frequency (Hz)	Q
GA0d1	0.1	SG70Q3	70	3
GA1d0	1.0	SG235Q3	235	3
GA2d5	2.5	SG849Q3	849	3
GA4d0	4.0	SG1615Q3	1615	3

(a) GA

(b) SGQ3

name	frequency (Hz)	Q
SG70Q8d9	70	8.9
SG100Q8d9	100	8.9
SG153Q8d9	153	8.9
SG235Q8d9	235	8.9
SG361Q8d9	361	8.9
SG554Q8d9	554	8.9
SG849Q8d9	849	8.9
SG1053Q9	1053	9
SG1304Q9	1304	9
SG1615Q9	1615	9
SG2000Q9	2000	9

(c) SGQ9

name	frequency (Hz)	Q
SG70Q100	70	100
SG235Q100	235	100
SG849Q100	849	100
SG1615Q100	1615	100

(d) SGQ100

name	center frequency (Hz)	bandwidth (Hz)	duration (ms)
WNB_100_100_0d1	100	100	100
WNB_250_100_0d1	250	100	100
WNB_1000_10_0d1	1000	10	100
WNB_1000_1000_0d01	1000	1000	10
WNB_1000_1000_0d1	1000	1000	100

(e) WNB

Table 6.2: Parameters of simulated waveforms used in S6b Monte Carlo run.

Within the LIGO project, a particular procedure has been developed for analyzing these simulations that facilitates the comparing of results between different analysis pipelines. This is known as the *mock data challenge* (MDC). A set of noiseless data is generated with the full set of various waveforms inserted with constant amplitude at various random time, covering the full span of data to be analyzed. At analysis time, these frames are loaded by the analysis pipelines, multiplied by various scaling factors, and then summed onto the actual data. This procedure assures that all analysis pipelines are analyzing the exact same set of simulations, thereby eliminating any possible selection effects.

Figure 6-9 is an example of the results of an analysis run for one of the injection waveform types. It shows a scatter plot of the `logOddsMod` and `xStatMod` event statistics for all “SGQ3” Q 3 sine-Guassians injections, over all injections scales. The background distribution of events is also plotted in black. Figure 6-10 shows histograms of the projections of these events onto the two axis (6-10a and 6-10b), as well as for the combined `omega` statistic in figure 6-10c. The black dashed lines in these figures indicate the values of maximum statistic in the background distribution, which in this case is 3.25 for all statistics. The colored injection events that fall above or to the right of these dashed lines are clearly separated from the background distribution.

These plots have been very useful in seeing the behavior of the various event statistics. For instance, figure 6-9 illustrates that various portions of the injection space are better covered by the different statistics. The numbers on the plot indicate that 8% of the injections are “seen” (i.e., separated from background) by the `xStatMod` statistic and not by the `logOddsMod` statistic (upper left quadrant), while 17% are seen by `logOddsMod` and not by `xStatMod` (lower right quadrant). This was motivation to develop the combined statistic, `omega`, that sees all the injection events that fall in the upper-most and right-most quadrants.

Another useful measure of the performance of an algorithm is *efficiency curves*.

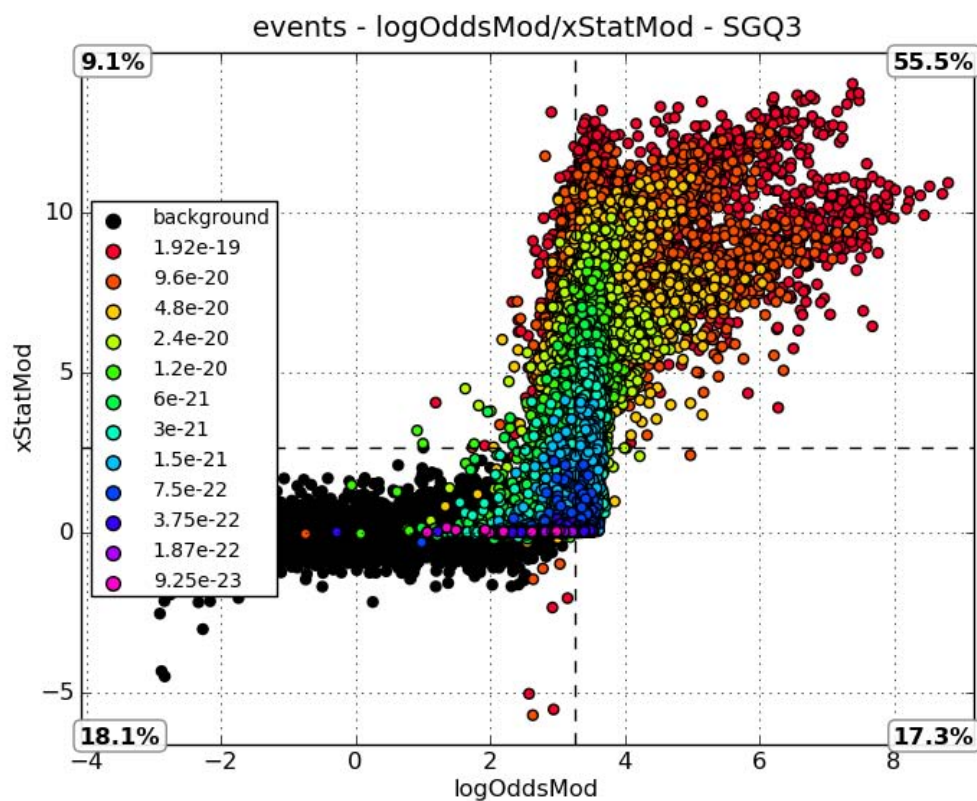
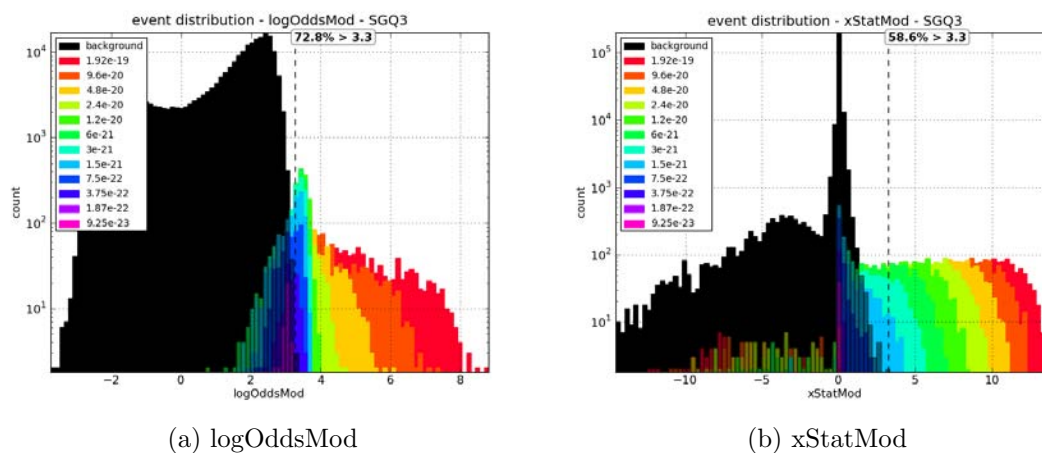
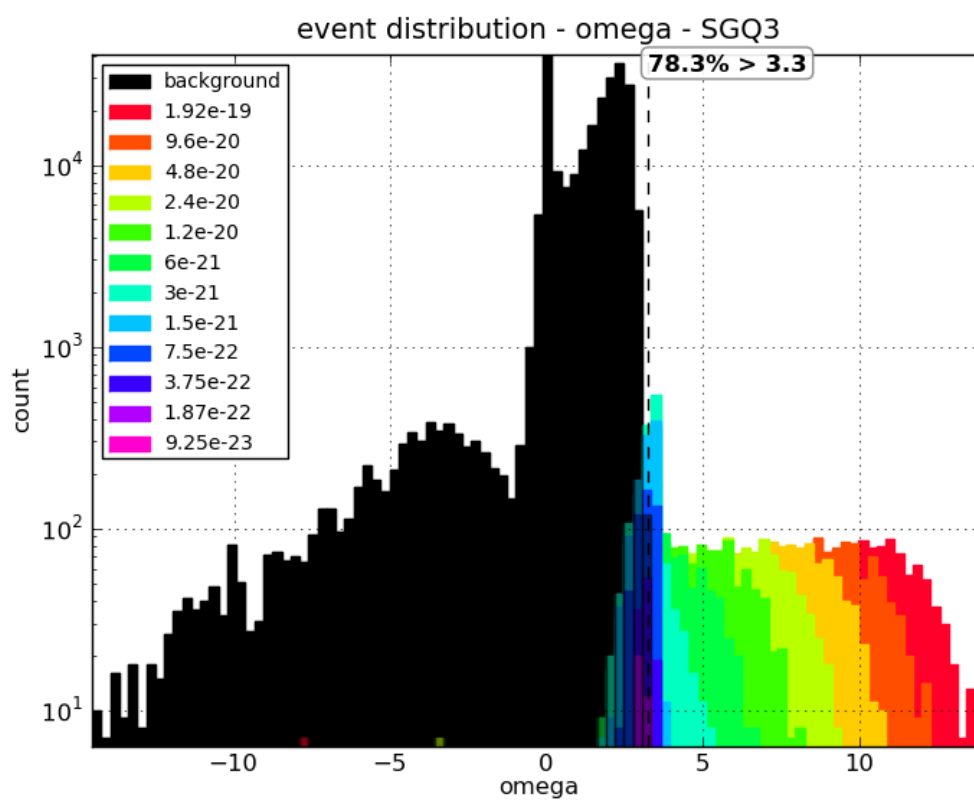


Figure 6-9: Scatter plots of events for all Q 3 sine-Gaussian injections in the S6b Monte Carlo study. All injection scales (colored dots) are plotted over the background distribution (black). The black dashed lines indicate the values of maximum statistic in the background distribution. Colored injection events that fall above or to the right of these dashed lines are well distinguished from the background distribution.



(a) logOddsMod

(b) xStatMod



(c) omega

Figure 6-10: Histograms of detection statistics for the Q 3 sine-Gaussian injections in the S6b Monte Carlo study. All injection scales (colored bars) are plotted over the background distribution (black).

Efficiency curves show the fraction of injections that are detected as a function of injection signal amplitude. A detection in this case is a value of the event statistic that falls above the maximum measured in the background. This detection threshold also corresponds to the minimum measured background FAR.

Figure 6-11 shows efficiency curves for the same SGQ3 injections. These efficiency curves provide a reasonable estimate of the sensitivity of the algorithm. The usual quoted value is the strain for the 50% and 90% detection efficiency levels. For instance, in figure 6-11c the cyan curve shows the detection efficiency for the SG235Q3 waveform over various injection amplitudes. The 50% detection efficiency level corresponds to a strain of slightly greater than 1×10^{-21} . Another way to say this is that the algorithm will detect 50% of all 235 Hz, Q 3 sine-Gaussian signals with a strain amplitude of 1×10^{-21} , while producing a false detection no more frequently than once every 143 days.

The receiver operating characteristic, or ROC curves, are also useful for understanding the sensitivity trade-offs of a detection algorithm. An ROC curve typically plots the true positive rate (i.e., detections of injected signals) versus the false alarm rate in the background. The curves start in the lower left corner (zero detections, zero false positives) and move to the upper right, increasing in detection efficiency as the threshold on the detection statistic is lowered, thereby increasing the false alarm rate. The better the detection algorithm the faster it climbs, reaching to higher detection efficiencies without sacrificing with a higher false alarm rate. An ideal algorithm would produce a single point in the upper-left corner of the plot: perfect detection efficiency with no false alarms. In general, the more area under the ROC curve, the better.

Figures 6-12 and 6-13 show example ROC curves for the Omega detection statistics in the S6b characterization run. Figure 6-12 shows the ROC for the various Q 3 sine-Gaussian injections, while figure 6-13 shows the ROC for just the SG235Q3 injections, but over all injection amplitude scales. The latter shows that performance improves

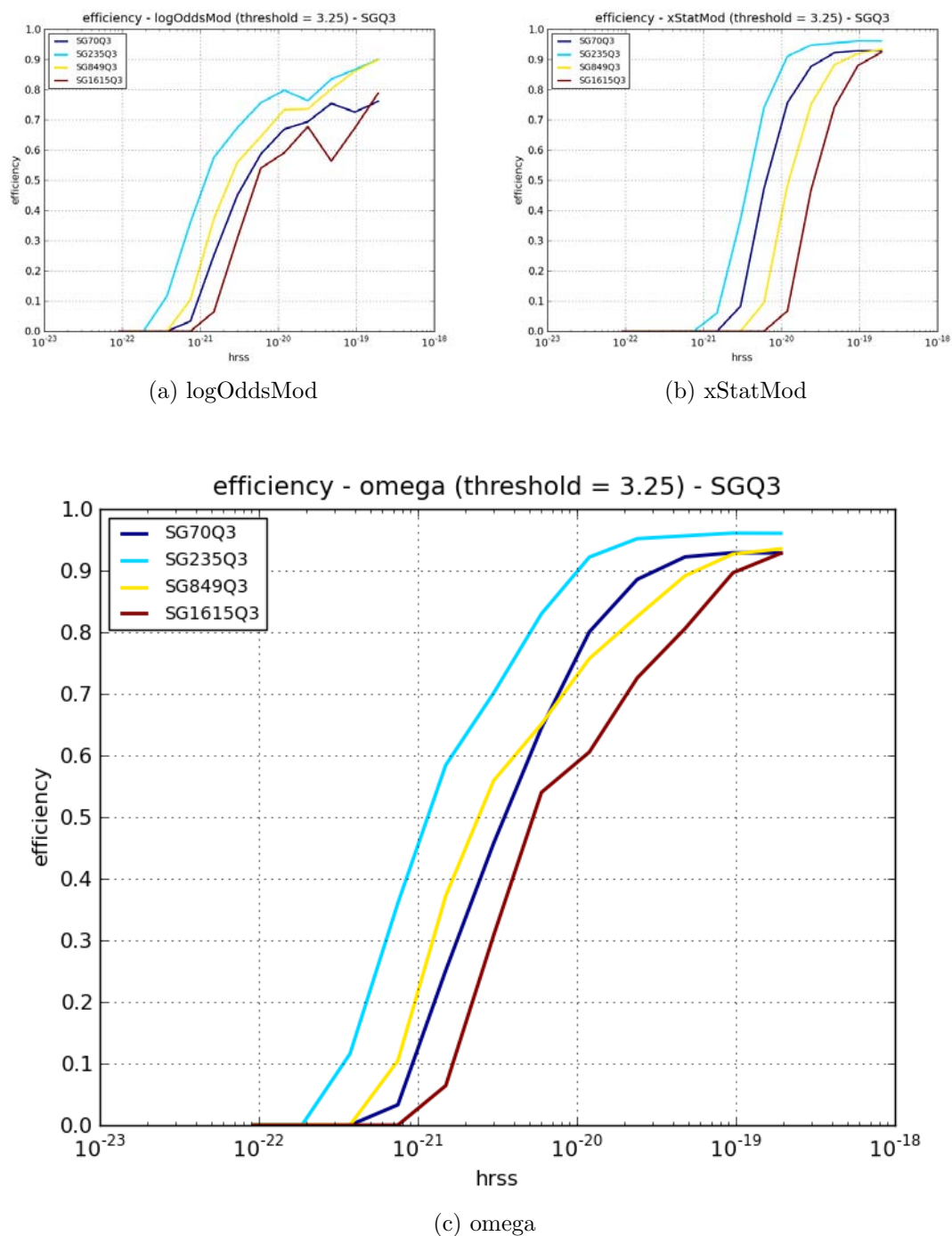


Figure 6-11: Detection efficiency for Q 3 sine-Gaussian injections in the S6b Monte Carlo study. The detection threshold on the event statistics is 3.25, which is the maximum of the statistic measured in the background.

for louder injections, which is to be expected.

The fact that even at the most energetic injection scales (red curves) the ROC do not reach a detection efficiency of unity indicates that some signals are misclassified as glitches, even if they are very loud. This can also be seen in the scatter plot in figure 6-9, where some of the loud injections fall within the center of the black background region.

6.3.4 Characterizing position reconstruction

The other important aspect of the analysis that required extensive testing was the position-reconstruction capability. As described in section 6.1.4, the Bayesian analysis algorithm completely handles the position reconstruction in Omega. The output of the Bayesian analysis is a two-dimensional probability distribution map over directions in the sky (figure 6-6). As with the detection statistic, the best way to measure the performance of the position reconstruction is to run the analysis on data with simulated coherent injections.

Since the Bayesian sky maps are probability distribution functions, we can measure not only how far off in degrees the most likely reconstructed position is from the true position but also where in the probability distribution the true location lies.

Figure 6-14 shows the angle between the most probable reconstructed location and the true injection location for Q 9 sine-Gaussian injections over a variety of injection scales. This plot is meant to exhibit similar behavior to an ROC plot, whereby an ideal algorithm would produce a single point in the upper left corner indicating that all events were perfectly reconstructed. The increased reconstruction accuracy at higher injection amplitudes is indicated by the increased area under the curves.

Figure 6-15 shows a measure of the confidence of the reconstruction for the events in figure 6-14. The curves indicate what fraction of events fall within a given confidence region. We expect that ideally these curves would be diagonal lines from lower left to upper right. This would indicate that the sky maps were well calibrated and

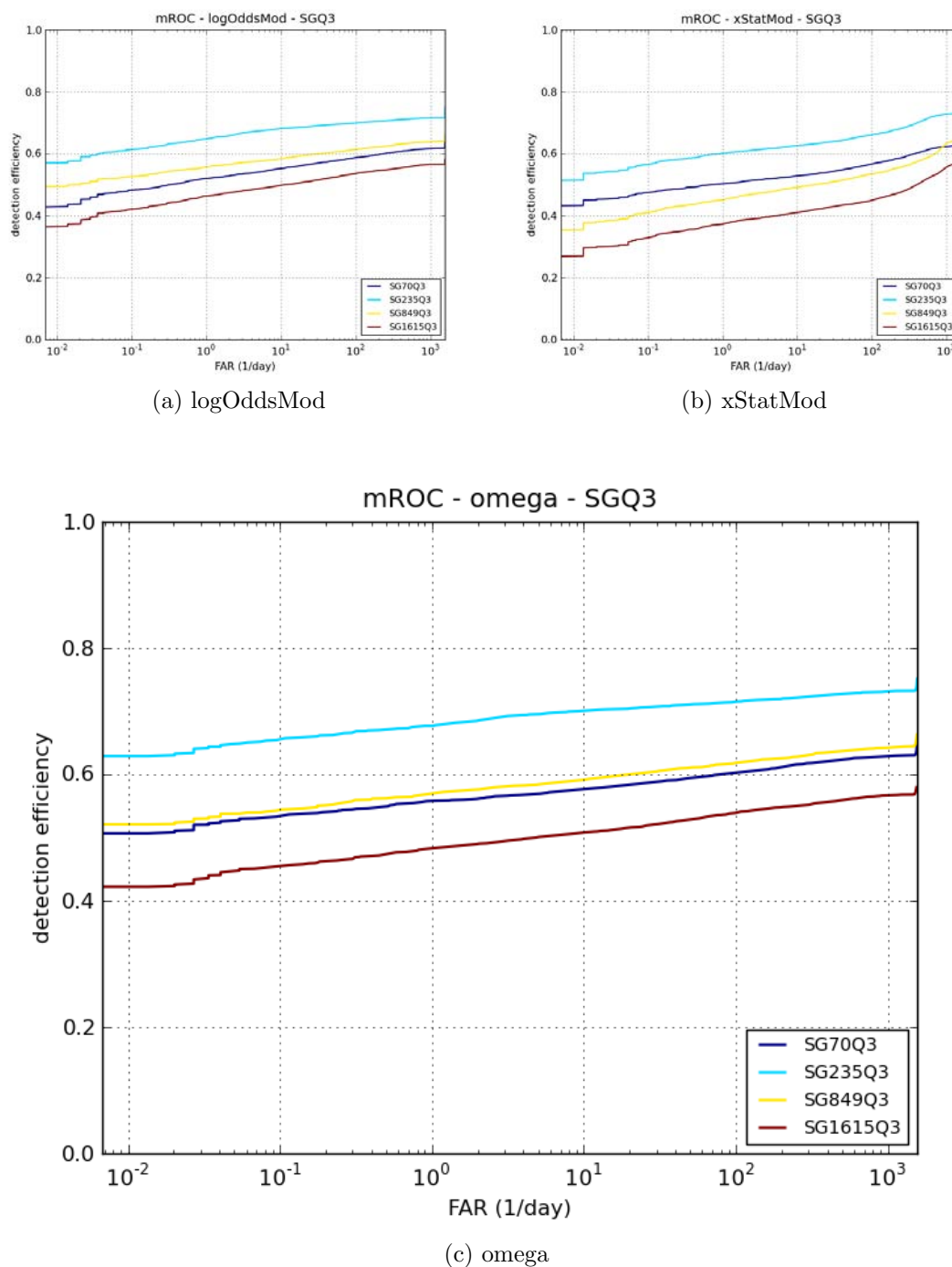


Figure 6-12: Receiver operating characteristic plots for Q 3 sine-Gaussian injections in the S6b Monte Carlo study. The detection threshold is set to an event statistic of 3.25, which is the maximum measured in the background.

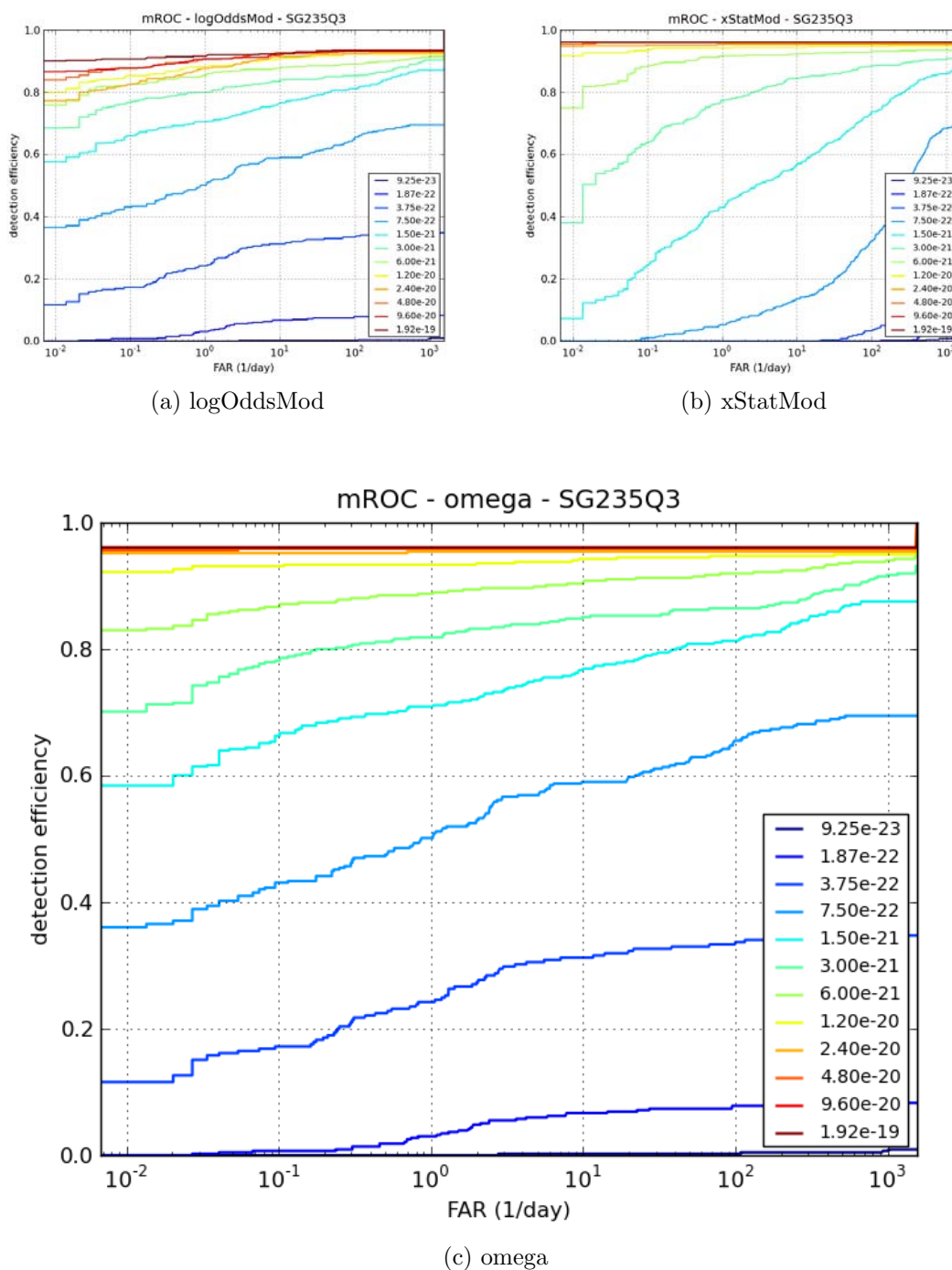


Figure 6-13: Receiver operating characteristic plots for 235 Hz, Q 3 sine-Gaussian injections in the S6b Monte Carlo study, as a function of injection amplitude. The detection threshold is set to an event statistic of 3.25, which is the maximum measured in the background.

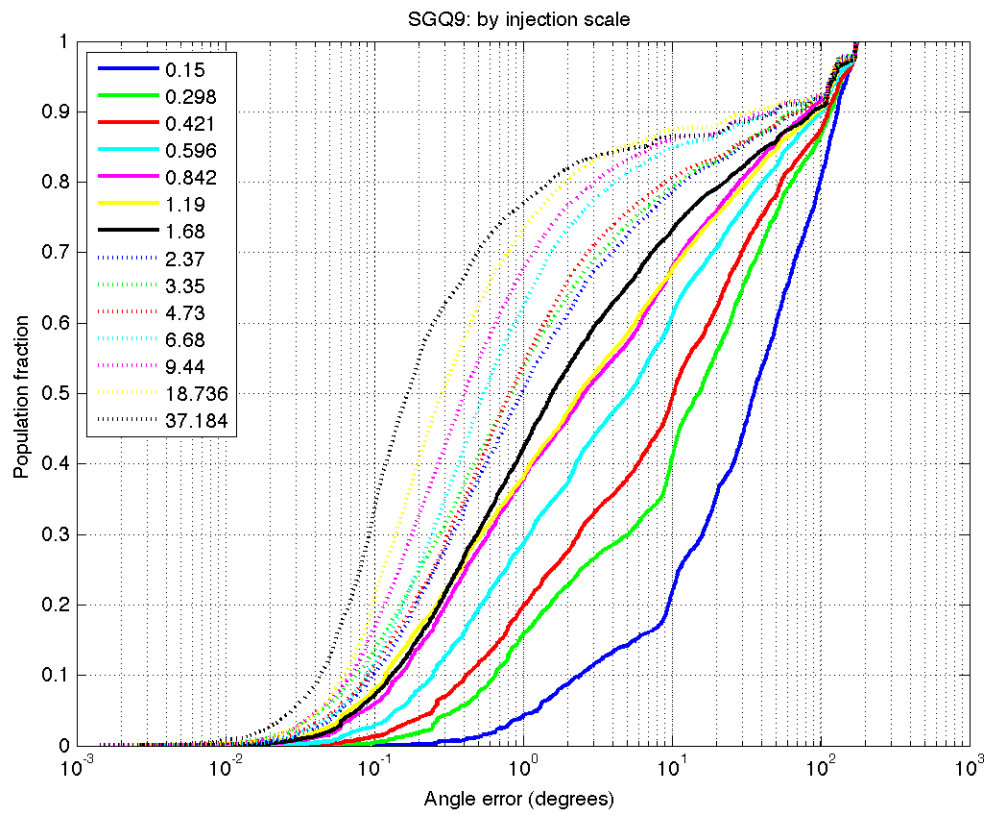


Figure 6-14: Angle between true injection location and reconstructed most probable location, for Q 9 sine-Gaussian injection waveforms over a variety of injections scales.

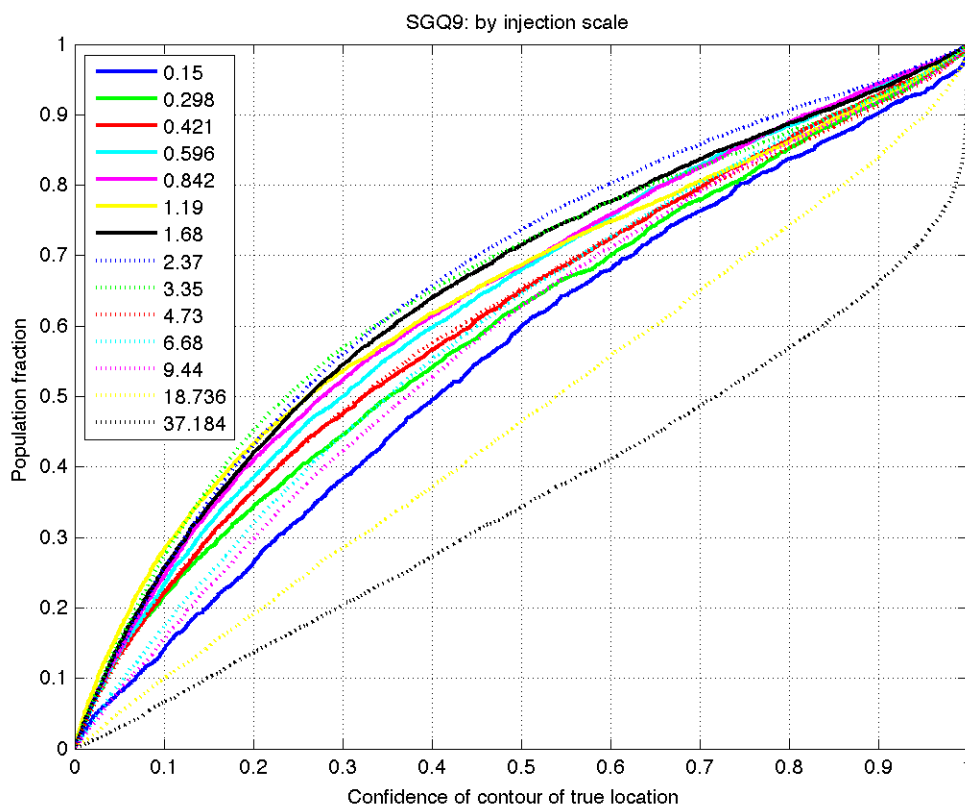


Figure 6-15: Confidence contours for Q 9 sine-Gaussian injection waveforms over a variety of injection scales.

that the confidence the true location lies in a given region corresponds well to the frequency of it actually lying in that region; in other words, that $X\%$ of injections fall within the $X\%$ confidence region. The “bowing up” of the curves is reflective of a built-in compensation for the uncertainty of the absolute strain calibration of the data, both in phase and amplitude. These simulated software injections do not include calibration uncertainty, therefore the confidence contours appear to overcompensate.

Chapter 7

Results from the S6 Search

In this chapter I present preliminary results from the S6 online EM follow-up search for gravitational waves. I also present results from an offline search of a subset of the S6 data set with an improved version of the Ω -Pipeline algorithm.

DISCLAIMER: The results presented in this chapter are preliminary, were not reviewed by the LIGO/Virgo Scientific Collaboration, and therefore cannot be endorsed in any way by the LIGO/Virgo Scientific Collaboration.

7.1 The S6 low-latency/EM follow-up search

In Chapter 6 I described the Ω -Pipeline and how it had been adapted to run in a “on-line” mode to analyze data from the LIGO/Virgo detector network with low latency. The motivation for this development was a full-scale LookUp search for electromagnetic transients associated with gravitational wave triggers that was executed during the S6 science run.

The triggers were the product of two analysis pipelines: The Ω -Pipeline Rapid Online Analysis (OROA), and a low-latency version of the Coherent WaveBurst pipeline (cWBOnline). A third low-latency matched filter inspiral analysis, MBTAOnline, came online later in the run. These pipelines (known as “event trigger generators”

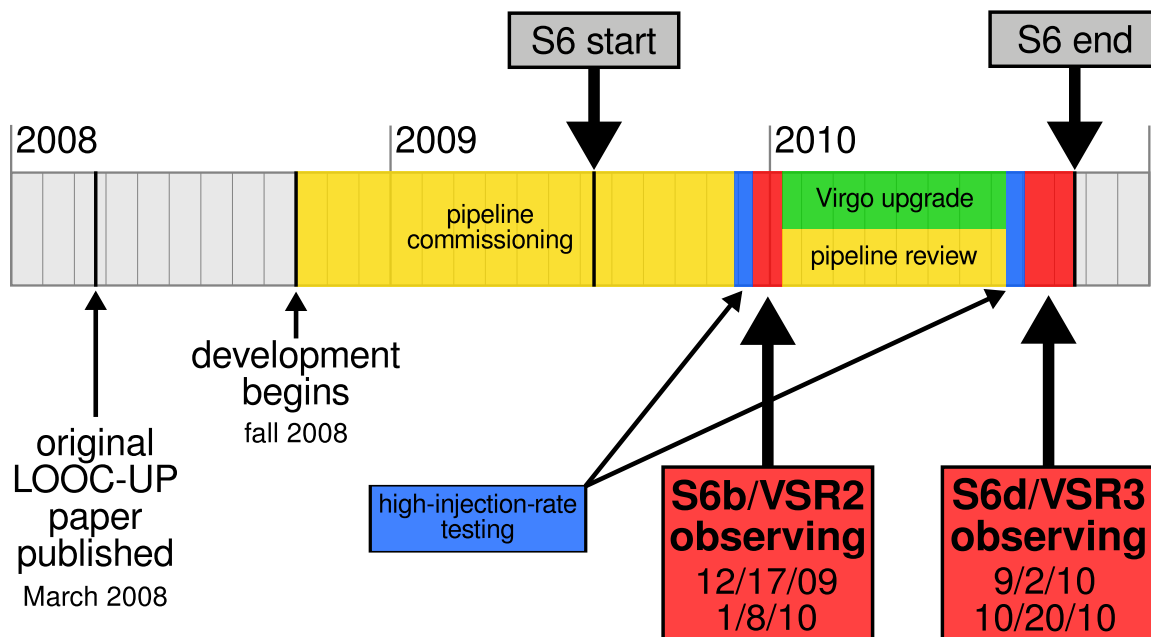


Figure 7-1: Timeline of S6 online analysis runs.

or ETGs) produced triggers, including trigger significance and reconstructed source position, as quickly as possible. Once the triggers were identified, the trigger information was passed to multiple follow-up analysis processors that convolved the reconstructed sky maps with local galaxy maps to opportunistically point available electromagnetic observatories (referred to simply as “EM follow-ups”).

After intensive development, commissioning, testing and review, comprising more than a years worth of work from dozens of researchers, the search went live for the first time on December 17, 2009. The first trigger was passed to the EM follow-ups three days later. Over the course of S6, the search operated for over two months and sent over 20 triggers, prompting dozens of images. The timeline of this search is shown in figure 7-1

The collaboration is currently analyzing the results from the online analyses and the images from the follow-up observations. After internal review, the published results are expected in about two years from now.

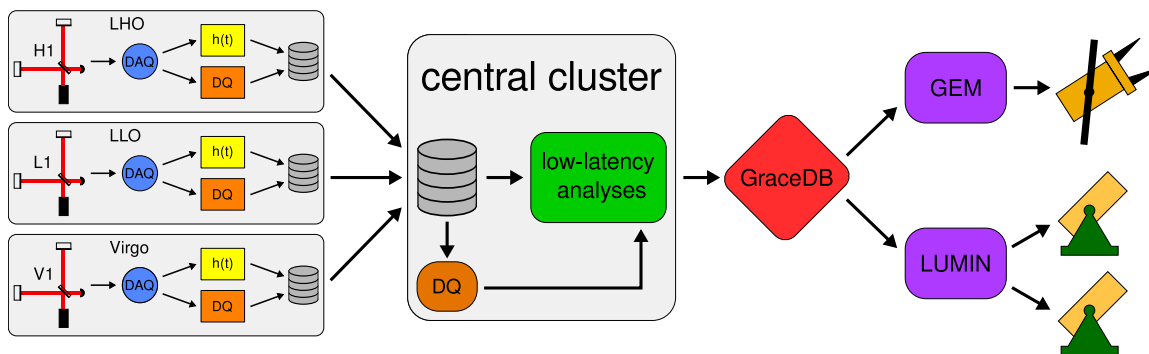


Figure 7-2: The full S6 low-latency analysis and EM follow-up pipeline. On the left are the two LIGO and on Virgo observatories and the detectors they house. The data is calibrated in real-time, written to disk, and then transferred to the central processing facility at Caltech, where the low-latency analyses were run. Trigger information from analyses was passed to the GraceDB notification system, that then forwarded it on to the LUMIN and GEM EM follow-up processors. The EM follow-ups finally directed EM telescopes at the reconstructed sky location for the event.

7.1.1 The full pipeline

Figure 7-2 is a diagrammatic overview of the full low-latency analysis and EM follow-up pipeline that operated during the S6 run. On the left are the three observatories (LIGO Hanford (LHO), LIGO Livingston (LLO), and Virgo) and the three detectors that they house (H1, L1, and V1 respectively) that were involved in S6 search. The data from the detectors was calibrated in real time as it was taken. The data and corresponding data quality (DQ) products were written to local disks at the observatories.

Data from Virgo V1 detector was transferred to the LIGO Hanford observatory, where it was re-written into a similar format as the H1 and L1 data. As soon as it was available at each observatory, the calibrated data and DQ information was transferred to the central processing facility at the California Institute of Technology (Caltech). Caltech administers a large computing facility for the LIGO/Virgo collaboration where the full analyses could be run. The low-latency analysis pipelines would await the arrival of the data and begin processing as soon as the needed data

arrived. The green box in figure 7-2 represents the multiple ETGs that were running at Caltech, of which the OROA described in chapter 6 was one.

Dedicated computers were made available for the online trigger generation. The background time-slides analyses were performed on the local computer cluster with increased priority.

Upon identification of a gravitational-wave event candidate the ETGs reported their findings to a notification distribution system developed specifically for this LookUp search, known as the *Gravitational-wave Candidate Event Database* or GraceDB. GraceDB accepts triggers and trigger information, archives them in a database, and then sends out immediate notification of the event to subscribers of notifications from particular ETGs.

Figure 7-3 is a histogram of the overall latencies for all events from the OROA during S6. Latency time is measured from the reconstructed time of the event to when the event was sent to GraceDB.

7.1.2 The EM follow-up processors

Subscribed to the gravitational wave triggers were the EM follow-up processors. These EM follow-ups received notification of the triggers from GraceDB. The primary function of the EM follow-up processors was to determine the most effective pointings for the EM telescopes that would be taking pictures of the events. This was done by convolving the ETG sky maps with catalogs of all known local galaxies, taking into account the sky visible to the telescope at the time, in order to maximize the number of galaxies in the field of view of the telescope. Obviously, since each telescope has a different location and field of view this had to be done independently for each telescope.

The primary EM follow-up processor is known as LUMIN. Its primary function was to read in the reconstructed source probability sky maps and calculate the optimal pointings for each of the various telescopes. A separate nearly identical pipeline known

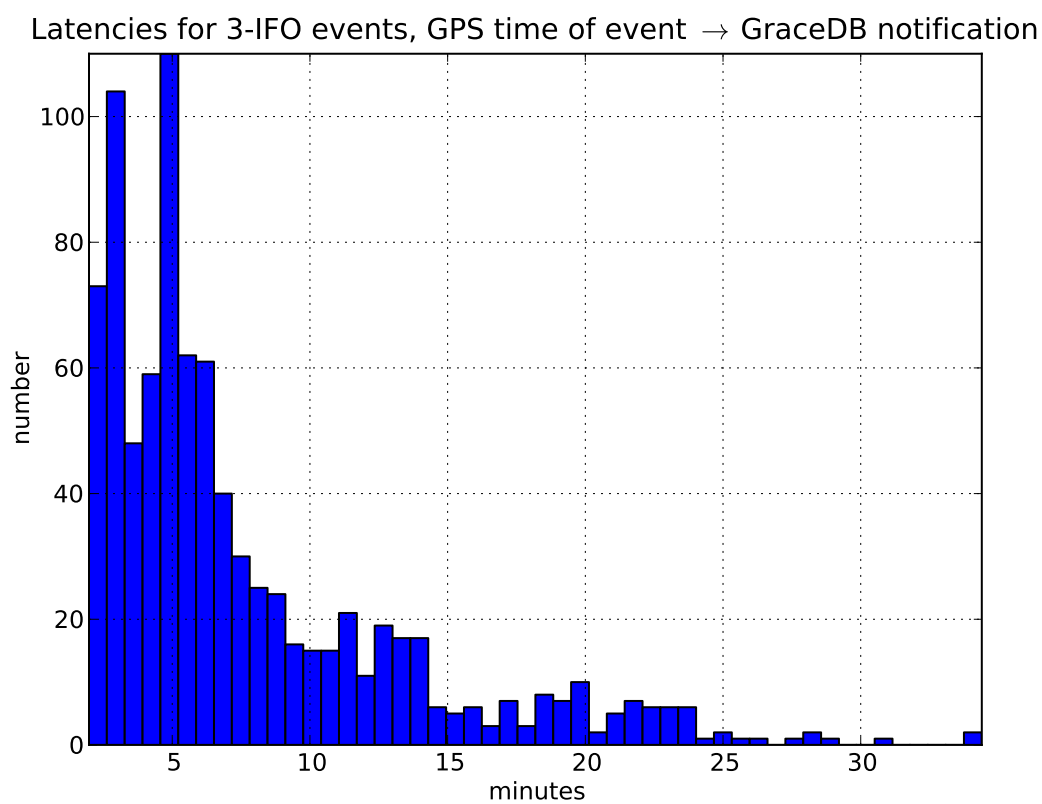


Figure 7-3: Latency of event notification relative to GPS time of event.

as GEM calculated pointing specifically for the Swift satellite.

The sending of alerts to the telescopes was almost entirely automated. However, a human was required to do a final validation and approve all events and pointings before passing them to the EM telescopes. The human intervention actually accounted for the largest single delay in the pipeline, typically taking anywhere from 15 minutes to an hour.

7.1.3 The EM observatories

By the end of the S6 run, the pipeline was sending triggers to more than a dozen different telescopes. Table 7.1 lists all telescopes that participate, as well as some relevant information about each of the telescopes.

7.2 Preliminary results from the S6 online search

There were two periods of observation during S6:

	start (UTC)	finish (UTC)
S6b/VSR2	2009 December 17 00:00	2010 January 8 22:00
S6d/VSR3	2010 September 2 00:00	2010 October 20 22:00

During S6b/VSR2, eight events were reported as significant by the ETGs. During S6d/VSR3, 14 events were reported as significant by the ETGs. Table 7.2 is a summary of the events from the S6d/VSR3 run. Of the reported events, six were approved by the human monitors and forwarded to the EM telescopes for follow-up observation, three from the cWB pipeline, two from MBTAOnline, and one from OROA. Below, we report preliminary results from the OROAevent at GPS time 970159718.9375.

7.2.1 Event 970159718

On Sunday, October 3, 2010, at 16:48:24 UTC, the Ω -Pipeline Rapid Online Analysis recorded an event that exceeded the pre-defined fixed threshold. The event was

telescope	location	wavelength	size	field of view	notes
Liverpool Telescope [153]	Canary Islands	visible	2 m	20° / 1°	robotic
LOFAR [154]	Northern Europe	radio (10-250 MHz)			
Palomar Transient Factory [155]	Palomar Observatory, USA	visible	1.2 m	3.4° / 2.3°	
Pi of the Sky [156]	San Pedro de Atacama Observatory, Chile	visible			prototype
QUEST [157]	La Silla Observatory, Chile	visible	1 m	4.6° × 3.6°	
ROTSE-IIIa [158]	Coonabarabran, Australia				
ROTSE-IIIb [158]	McDonald observatory, USA				
ROTSE-IIIc [158]	Mt. Gamsberg, Namibia	visible	45 cm	1.85° × 1.85°	robotic
ROTSE-IIId [158]	Bakiritepe, Turkey				
SkyMapper [159]	Coonabarabran, Australia	visible	1.35 m	2.4° × 2.4°	
Swift [41]	Space	gamma, X, UV, optical			
TAROT-N [160]	Calern, France				
TAROT-S [160]	La Silla Observatory, Chile	visible	25 cm	1.85° × 1.85°	
Zadko [161]	Perth, Australia	visible	1 m	23' × 23'	robotic

Table 7.1: Telescopes used in the S6 EM follow-up search

Event	ETG	FAR	result	observations/notes
967930683.685	cWB	0.13	GO	R(30)
968654557.950	cWB	0.00	GO	R(75), T(20), Z(129)
968932960.381	MBTA	0.16	GO	Q(12), R(30), S(9), T(3), Z(159)
968933008.009	MBTA	0.07	rejected	V1 detector fluctuations
969567886.927	cWB	0.00	GO	P(10)
970159718.938	Ω	0.21	GO	L(22), Q(36), R(30), S(5)
970399241.001	MBTA	0.18	GO	source in direction of sun
970920228.555	cWB	0.00	rejected	high V1 glitch rate

Table 7.2: All events reported by online ETGs during the S6d/VSR3 run. The green events were passed on to telescopes for observation and the yellow events were rejected by the human monitors for the reasons noted. The dark green event is the one from OROA. Definitions: L: Liverpool Telescope; P: Palomar Transient Factory; Q: QUEST; R: ROTSE; S: SkyMapper; T: TAROT; Z: Zadko.

reported to GraceDB and was received by the LUMIN EM follow-up processor. The event had an inverse false alarm rate of roughly one event every five days, which was deemed sufficient for consideration for passing on to telescopes. After review by the human monitors, it was deemed acceptable and was passed on to EM follow-up observatories for observation. The following telescopes took images as a result of event:

- Liverpool
- QUEST
- ROTSE
- SkyMapper

Table 7.3 lists the reconstructed parameter from Ω -Pipeline for the event, and table 7.4 describes the significance of the event relative to the low-latency background. Figure 7-4 shows the reconstructed Bayesian sky map for this event.

Figure 7-5 shows the LUMIN tiling for the Pi of the Sky telescope for event 970159718. In this figure, only the top 1000 most probably locations from the Bayesian sky map are shown. The red crosses indicate the locations of local galaxies

time	GPS 970159718.9375
2010 October 3 16:48:24 UTC	
discovery	GPS 970160293
latency	574 s
network	H1/L1/V1
frequency	935.516 Hz
duration	8.928 ms
bandwidth	112.004 Hz
modeTheta	1.394839 radians
modePhi	2.734910 radians
logOdds	10.683
nullEnergy	0.673
nullIncoherentEnergy	2.824
xStat	2.084
logOddsMod	3.064
xStatMod	0.025
omega	3.064

Table 7.3: Omega reconstructed event parameters for the 970159718 event.

background	# events in background	livetime (days)	rank	FAR (events/day)
entire run to date	1944456	1259.433	322	0.3
previous day of clock time	29134	18.870	4	0.2
last background run	2555	1.655	0	0.0

Table 7.4: Omega significance of the 970159718 event.

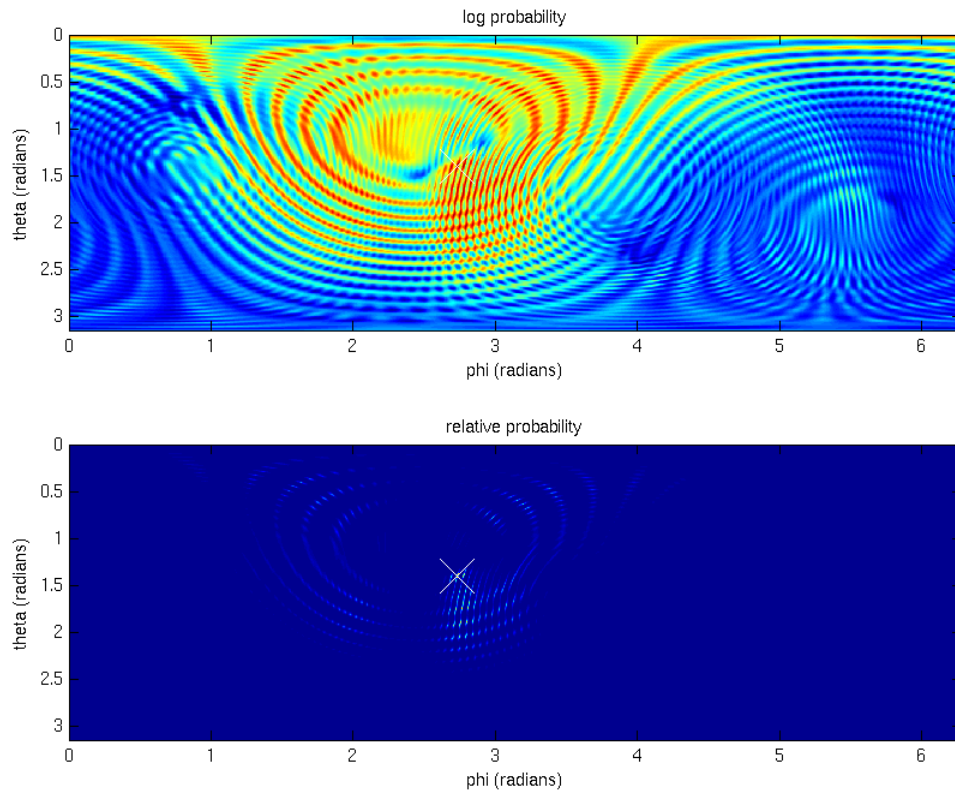


Figure 7-4: Ω -Pipeline sky map for event 970159718. The bottom plot shows the absolute probability for each sky pixel, while the top plot shows the log of the probability. The most probable location is marked in both plots with a cross ($\theta \approx 1.4$ radians, $\phi \approx 2.7$ radians).

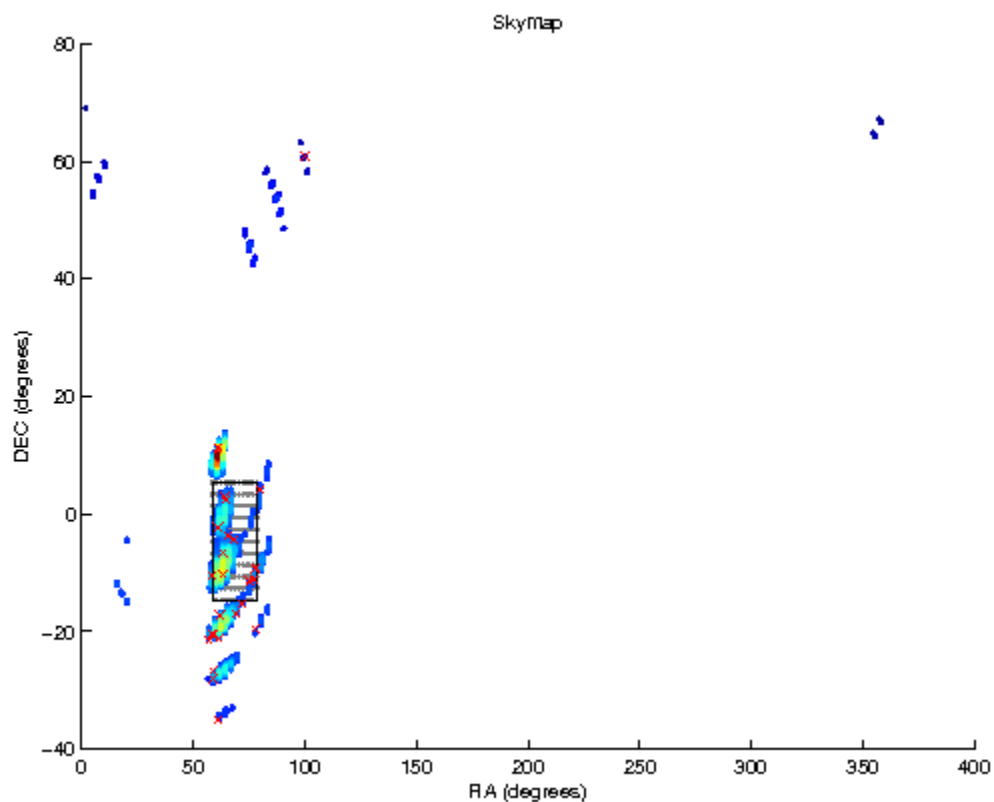


Figure 7-5: LUMIN tiling for the Pi of the Sky telescope for the 970159718 event. Only the top 1000 most probably locations from the Bayesian sky map are shown. The red crosses indicate the location of local galaxies that overlap with the top 1000 locations. The box indicates the field of view of the telescope, centered on the location LUMIN determined to be most optimal.

that overlap with these most probably locations. The box in the figure indicates the field of view of the Pi of the Sky telescope, centered on the location LUMIN determined to be most optimal. There are approximately 10 galaxies in the field of view.

Figures 7-6, 7-8, and 7-7 show images taken of the 970159718 event by the Liverpool, QUEST and SkyMapper telescopes respectively.

As noted previously, all results presented in this chapter are preliminary and have not been reviewed or endorsed by the LIGO/Virgo Scientific Collaboration.

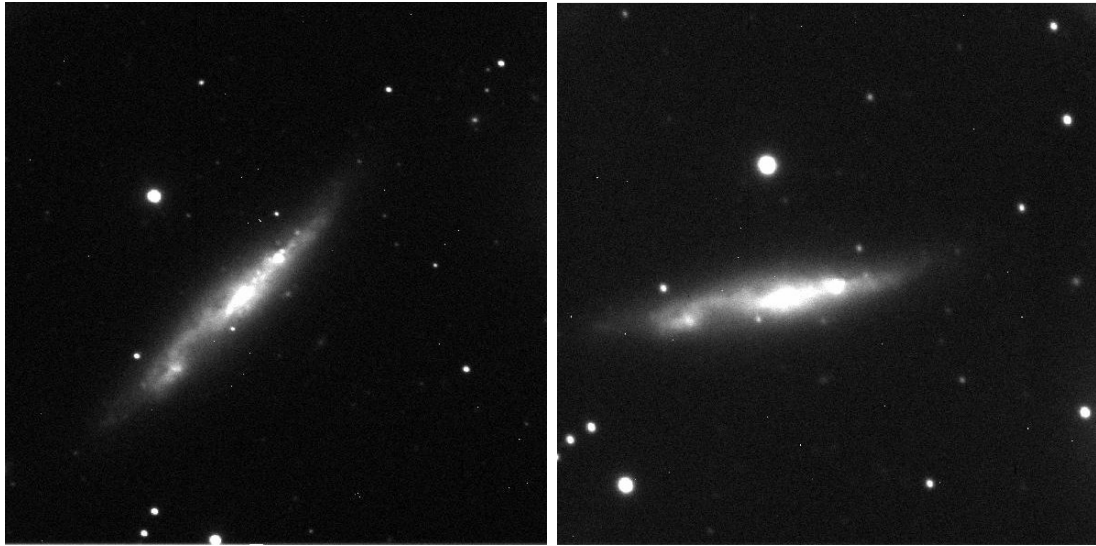


Figure 7-6: Liverpool Telescope image of NGC1507, one of 11 taken around 1am GMT on the October 4, 2010. SDSS r' band filter. Another 11 images were taken on the 3rd of November.

7.3 Recent improvements to Ω -Pipeline candidate selection

Two improvements to the selection of the most significant coincident clusters have been made since the version of the algorithm used in the S6/VSR2 online search. Both improvements attempt to eliminate the selection of clusters associated with glitches, and therefore dig deeper into the noise.

Glitches are problematic because they tend to be very loud. While the coherent algorithms are designed to be good at rejecting glitches, Ω -Pipeline sends only one coincident event to the coherent follow-up analyses per block. If the algorithm selects only the loudest coincident cluster in the block, glitches will be preferentially selected, only to be rejected by the coherent algorithms in the next stage. This leaves other quieter but more interesting candidates in the same block uninvestigated. If the glitches can be rejected during the selection process, more interesting events will be followed up, digging deeper into the noise.

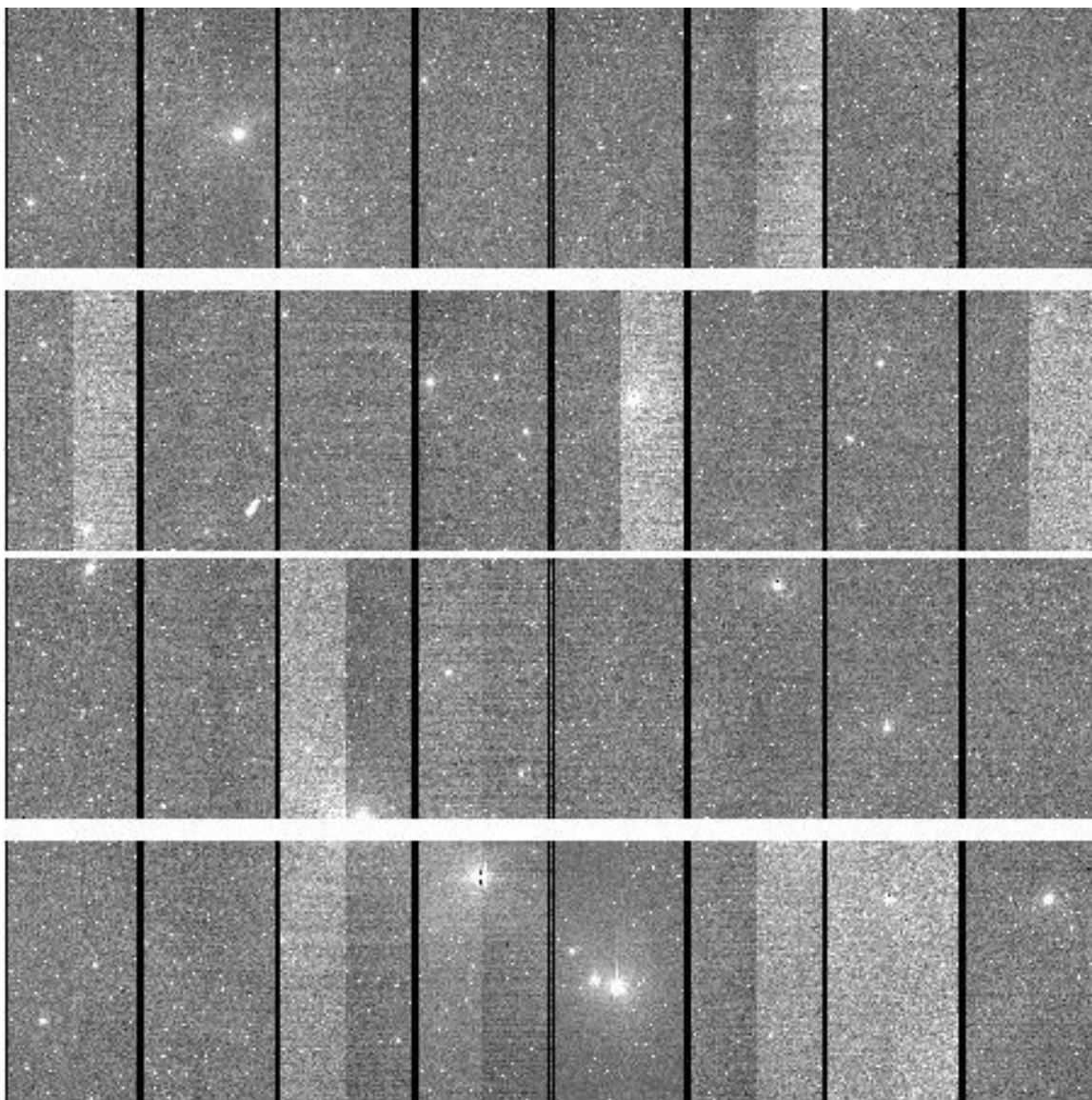


Figure 7-7: SkyMapper images taken on October 4, 2010.

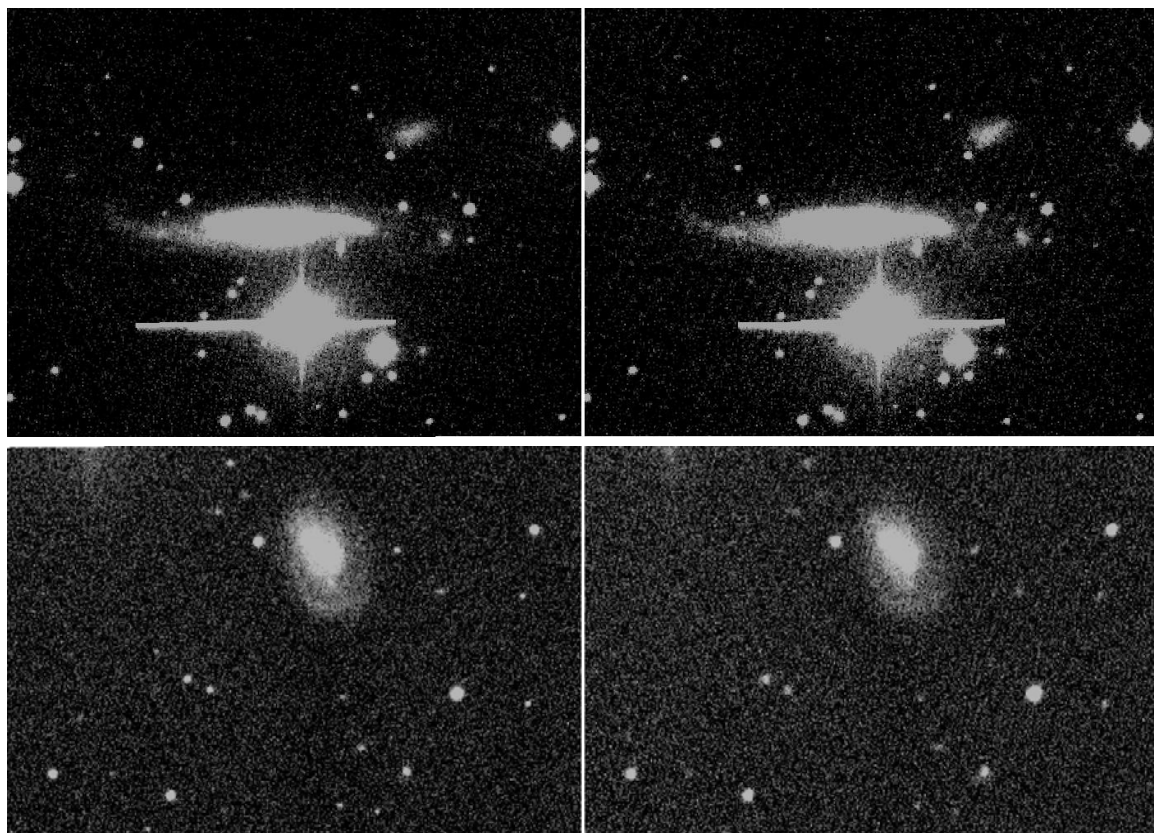


Figure 7-8: QUEST images of two galaxies targeted from on October 4, 2010.

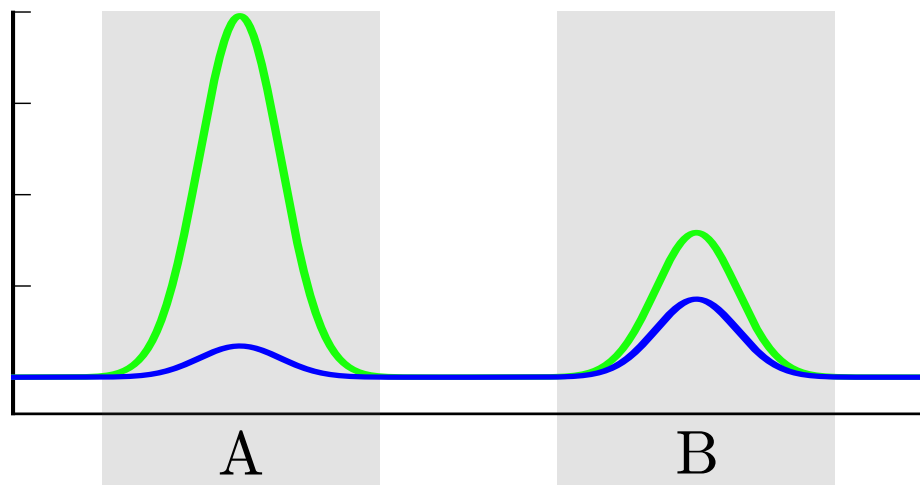


Figure 7-9: Example of selection of coincident triggers. Two data streams are represented by the green and blue curves. The previous selection algorithm would have chosen the event represented by A, since the energy in one of the detectors (green curve) is larger than all others. The new selection algorithm would choose B, since the energy in the second-most energetic trigger in B (blue curve) is bigger than the second-most energetic trigger in A (also blue curve). Event B is more representative of a signal, whereas event A is more representative of a “glitch.”

The high SNRs of single-detector glitches can be used to help identify them. The first improvement to the coincidence selection therefore involves identifying extremely loud glitches by looking at the relative SNR of the signals in the loudest and second-loudest detectors. If this ratio is too large, then the event is likely a glitch and can be excluded. Since very loud glitches tend to pollute the area around them, the time around the glitch is also blocked out, and any other triggers that fall within those times are also excluded.

Once the loudest glitch times have been excluded, the algorithm attempts to identify the most significant of the remaining coincident clusters. Again, the loudest cluster is not necessarily the best choice. Since real signals will likely deposit similar amounts of energy in at least two of the three detectors, the next improvement is to select the coincident trigger that has the most energy in the *second*-loudest detector. Figure 7-9 illustrates how this selection is done.

7.4 Results from an offline search of S6b

At the conclusion of the S6 low-latency search, and after the above improvements were made, the S6b foreground data were analyzed by the version of the pipeline used in the S6 online analysis, which we will refer to as “vO”, and the improved version of the pipeline, referred to as “vSCGR”.

The overall event distributions for the background and foreground events for S6b from the two versions of the pipeline are shown in figure 7-10. Both analyses indicate no significant events in the foreground data larger than the largest event in the background. The livetimes and maximums in the background and foreground are given in table 7.5 below.

version	livetime (days)		max background	max foreground
	background	foreground		
vO	147.6	16.5	3.254	3.136
vSCGR	149.4	16.8	3.254	3.217

Table 7.5: S6b offline foreground and background events

The loudest event in the vO foreground was rejected by the coherent Bayesian analysis because of excessive SNR ratio between the L1 and V1 detectors of 34, and therefore has no corresponding sky map. The largest event in the vSCGR foreground was analyzed by the Bayesian follow-up, and its sky map is shown in figure 7-11.

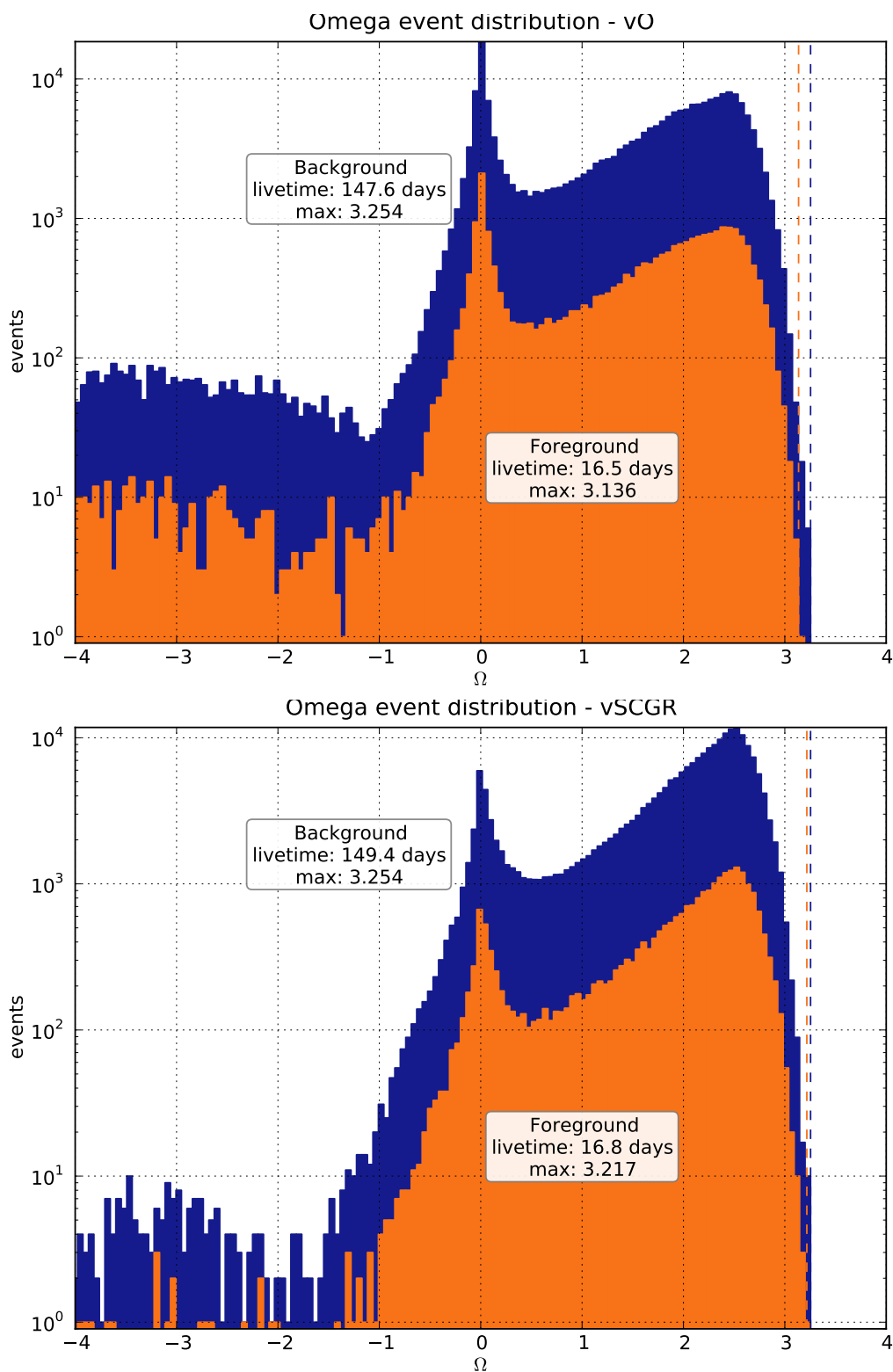


Figure 7-10: Final event distribution with Ω -Pipeline; vO top, vSCGR bottom. Events $\Omega < -4$ not shown. See ?? for disclaimer.

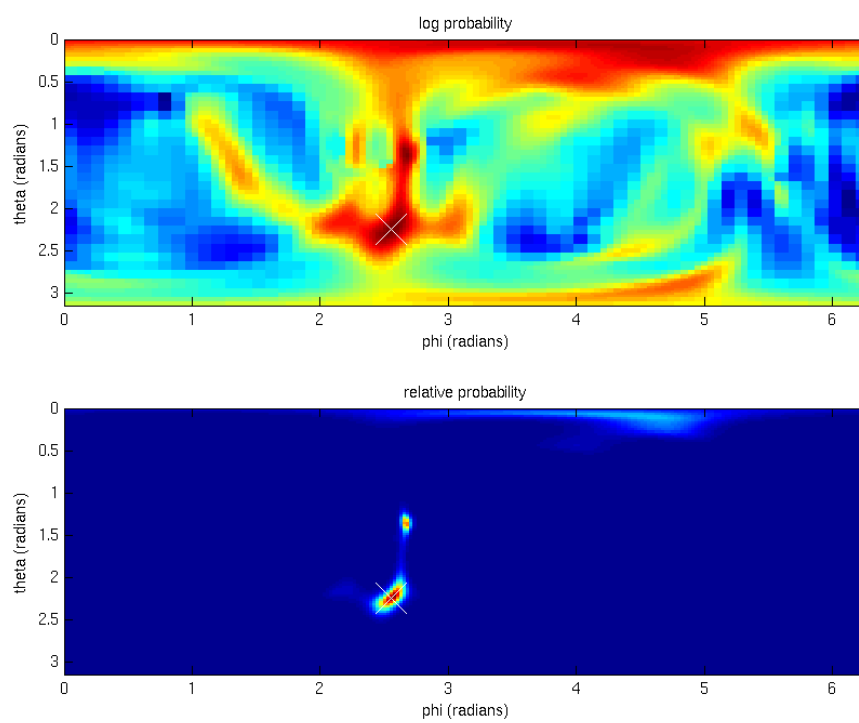


Figure 7-11: Sky map from the largest event in the vSCGR foreground.

Chapter 8

Conclusion

8.1 Success of the S6 low-latency search

While the analysis of the LIGO/Virgo S6 LookUp search is not yet complete, the search has already proven itself to be a success. Even before any data was taken, the search prompted new levels of coordination and collaboration both within the LIGO/Virgo project, and between gravitational-wave astronomers and astronomers in other fields. Infrastructural improvements within the WGDN enabled the low-latency analyses and the expedient communication of their results. New close collaboration with many different astronomy projects is leading to new fruitful scientific advancements. The project has helped bring the field of gravitational-wave physics into the fold of collaborative astronomy.

A momentous effort within the LIGO/Virgo collaboration led to notable infrastructure improvements in the network that enabled the S6 EM follow-up search to happen:

- Data from the LIGO interferometers needed to be calibrated in real time to produce calibrated strain data (“real-time calibrated data” [RCD]) necessary for correct and accurate analysis results. This was done with latencies of less than a minute.

- Data sharing between observatories was significantly improved. In particular, data transfer latencies between the observatories and the central Caltech computing center was dramatically decreased. Previous to S6, data transfer between the observatories and the computing centers was done as needed for offline analyses, with latencies usually on the order of days to weeks after collection. The online analyses required the RCD at the processing center with latencies on the order of minutes in order to be able to produce triggers suitable for EM follow-up. This was achieved, typically with latencies of around a couple of minutes.
- Beyond just the RCD, the online analyses required low-latency access to data quality information. This too required new infrastructural improvements to both produce the data quality information quickly, and to transfer it to the central analysis location.
- A new intra-collaboration real-time message passing system, known as *GraceDB*, was built to enable passing of information between analysis pipelines. This was developed specifically to facilitate the notification by the ETGs of gravitational-wave event candidates to the EM follow-up pipelines.

This thesis also describes many significant improvements to the Ω -Pipeline data analysis platform that enabled the full EM follow-up search to be successful:

- The algorithm used to whiten the data was replaced with a new more-well-established algorithm that is more robust against loud transient glitches in the data.
- The code to transform the data into the Q basis and then select significant tiles was combined in order to make it much more memory efficient.
- A new efficient Bayesian coherent algorithm was integrated to follow-up significant multi-detector coincident events. Most notably, this new coherent al-

gorithm can quickly produce source probability distribution maps on the sky that are required to localize EM follow-up observations. This algorithm also produced coherent event statistic that was used in characterizing the significance of event candidates. This algorithm is also notable in its inclusion of a model for non-gravitational-wave glitches that is effective at rejecting spurious detector glitches. This was the first to include a significant glitch model prior to the analysis proper.

- Also implemented was a coherent null-stream analysis that used the most likely sky position returned by the Bayesian coherent algorithm to produce coherent null-stream event statistic. This algorithm also further reduced the sensitivity of the analysis to detector glitches.
- The Ω -Pipeline Rapid Online Analysis (OROA) was developed for low-latency analysis using the improved Ω -Pipeline. The new infrastructure was capable of robust, continual analysis of the RCD from the full LIGO/Virgo network.
- In conjunction with the OROA, infrastructure was developed for continuous time-slide analysis of RCD for characterization of local background for use as a low-latency measure of significance estimation of OROA event candidates.
- The OROA was also used as low-latency single-detector characterization tool that greatly aided detector commissioning.

As important as all of these infrastructure and analysis improvements was the new collaborations that were forged with many new astronomy projects.

8.2 Low-latency searches in the advanced detector era

Low-latency analysis will be a crucial for realizing the scientific reach of advanced detectors.

Electromagnetic follow-ups

In the advanced detector era of frequent detection, LookUp searches such as those described in this thesis will only become more important and relevant. Some have even speculated that observation of an electromagnetic or neutrino counterpart to a gravitational-wave event might even be *necessary* to claim first detection. But even far beyond first detection, the importance of joint observation of EM and gravitational-wave signals can not be understated.

As previously mentioned, searches for EM counterparts allow for the detection of gravitational-wave events that would otherwise not be detectable. By requiring spatially and temporally coincident EM observation, the GW searches can accept much higher false alarm rates than would otherwise be required to claim detection. This means the searches can be sensitive to signals with lower signal-to-noise ratio, digging deeper into the noise and further into space.

Advanced detectors will be more sensitive to signals from the inspiral and merger of binary black holes (BBH). BBHs have the unique property that their distance can be inferred directly from their gravitational waveforms [162]. This means that localization of the host galaxy of such sources by electromagnetic follow-up observations could provide a powerful independent probe of the Hubble law.

The increased number of sources detectable with advanced detectors (expected to be up to 40 or more a year) means that there will be many more opportunities to observe EM counterparts. Collaboration with more astronomical observatories will further increase the reach of these searches. Optical telescopes such as the Large Syn-

optic Survey Telescope (LSST) [163], and radio telescopes such as the Low Frequency Array (LOFAR) [154], the Green Bank Telescope (GBT) [164], and Arecibo [165] are just some of the many that are expected to become involved. Integration with the Supernova Early Warning System (SNEWS) [166] and GRB Coordinates Network (GCN) [167] systems will allow us to disseminate triggers more efficiently to the community.

Detector characterization

During the analysis of previous science runs it was discovered that the transient searches were primarily limited by the presence of frequent glitches in the individual detectors. These glitches were frequent enough to produce spurious coincidences in the detectors that significantly decreased the significance of event candidates. What was particularly unfortunate was that this issue was not identified until the analyses were executed, which was long after the data had been collected and there was anything that could have been done to reduce the frequency of glitches.

Low-latency analysis are therefore critical for identifying issues in the detectors that adversely affect the analyses but would maybe otherwise not be seen. If low-latency analyses can be run during the commissioning of the detectors they can be a powerful tool to help identify these problematic issues at the time when they are most likely able to be fixed.

8.2.1 Challenges

The development of the S6 low-latency analyses laid the groundwork for future low-latency analyses. It also helped identify many of the challenges that will lie ahead. In this section I outline some of the challenges that were identified, and where improvements can be made and efforts should be focused. Some of these involve improvements to the analyses themselves, while others involve larger changes to the low-latency infrastructure or to the detectors.

Improving event statistics

A number of important improvements can be made to the Bayesian coherent analysis to improve both the quality of the event statistic and the reconstruction of the source location.

- The analysis currently uses the overcomplete Q basis. This makes it difficult for the Bayesian analysis to use multiple Q tiles in its follow-up analysis since the tiles will interfere. It may be preferable to instead use an orthogonal basis.
- Precise modeling of detector noise is very important for the Bayesian analyses, as discussed in chapter 5. However, the noise from interferometric detectors is notoriously difficult to model. Empirical measurements of the noise distributions could help. It's possible that this could even be done efficiently online with measurements of the cumulative distribution functions (CDF) of past noise.

Improving accuracy and precision of source localization

Precise and accurate source position reconstruction of event candidates is crucial for gravitational-wave astrophysics. Follow-up observations are only effective if the analyses are able to properly identify the source location of the event.

Other than the improvements to the Bayesian analysis mentioned above which will also improve the quality of the sky map, two of the most important improvements for source localization come from the nature of the network itself and how the data is calibrated.

- Generally speaking, the angular resolution of a network of detectors is a matter of comparing the phase of the signal in the different detectors. This means that the more widely spaced detectors there are in the network, the better the source localization. This provides a very strong argument in favor of proposed detector Australia (AIGO) and the LCGT detector already under construction in Japan.

Their inclusion in the WGDN would greatly increase the phase sensitivity and therefore angular resolution of the network [20].

- The importance of phase discrimination to position reconstruction further means that calibration of the strain data, both in phase and amplitude, is critical. Calibration is notoriously difficult, with errors typically limited to about 10% in magnitude and several degrees in phase [168]. If calibration errors can be reduced in advanced detectors, the quality of position reconstruction can be improved.

Decreasing latency

It goes without saying that the more we decrease latencies to identify event candidates the easier we make it for EM observatories to image the events.

- During S6 there was a latency of ~ 1 minute for online strain calibration. It is likely that this can be significantly decreased for Advanced LIGO.
- Transfer latencies from the observatories to the central computing facility account for another minute or so of latency. Streaming data from the observatories, as opposed to transferring individual blocks of data covering many seconds, may help decrease latencies further.
- It should be possible to increase the efficiency of the coherent algorithms themselves. The largest latency within the OROA was the coherent Bayesian reconstruction of the sky map. This could take tens of minutes for low SNR events. Using a streaming algorithm to process streaming data may help reduce latencies. It may also be possible to parallelize aspects of the algorithm to speed up computation.
- The largest fraction of the latencies seen by the follow-up observatories in S6 came from the need for human intervention to validate and approve individual

events. If the pipelines can be well tested and approved before the science searches it may be possible to move to full automation of event notification. This alone could reduce latencies from by a factor of 10 or more, from $\mathcal{O}(\text{hours})$ to $\mathcal{O}(\text{minutes})$.

One of the more intriguing possibilities for LookUp-type searches would be identifying potential events *before* they happen. This might be possible with low-latency matched filter searches for CBC inspirals. Most of the EM and neutrino emissions from CBCs, as discussed in chapter 4, occur during the merger and coalescence of the binary stars. If binary inspirals can be identified during the earlier inspiral phase it may be possible to trigger EM follow-up observations early enough to observe the first EM emissions from the source.

Low-latency significance estimation

By far the most computationally intensive part of the low-latency analysis was the generation of the low-latency significance estimation. Current methods rely on time-slide analyses which are identical analyses performed on shifted data. This means that N processor-days are then required to measure false alarm rates of 1 in N days of livetime. Increasing computational efficiency of the algorithms would help, but it may be that time-slide analyses are generally too computationally expensive, and that cumulative measurements of separable noise distributions may be used to gauge event significance.

Other infrastructure issues

Other general infrastructural improvements may benefit the low-latency and EM follow-up efforts. Redundancy of the analyses at multiple processing locations can help mitigate inevitably outages. Proper monitoring of all processes involved will also be necessary for reliable operation.

A new era begins

The current focus of gravitational-wave search efforts is primarily on first detection. This is quite understandable, given that direct detection has remained elusive. With the next generation of detectors scheduled to come on-line in just a couple of years though, we are on the verge of an enormous breakthrough in physics. The age of gravitational wave astronomy is here.

Appendix A

S6b/VSR2 Monte Carlo

Characterization Plots

This appendix includes all plots from the Ω -Pipeline MDC analysis over the S6b/VSR2 data set. See section 6.3 for a description of the analysis and the plots, and table 6.2 for the parameters of the injected waveform.

A.1 Gaussian injections

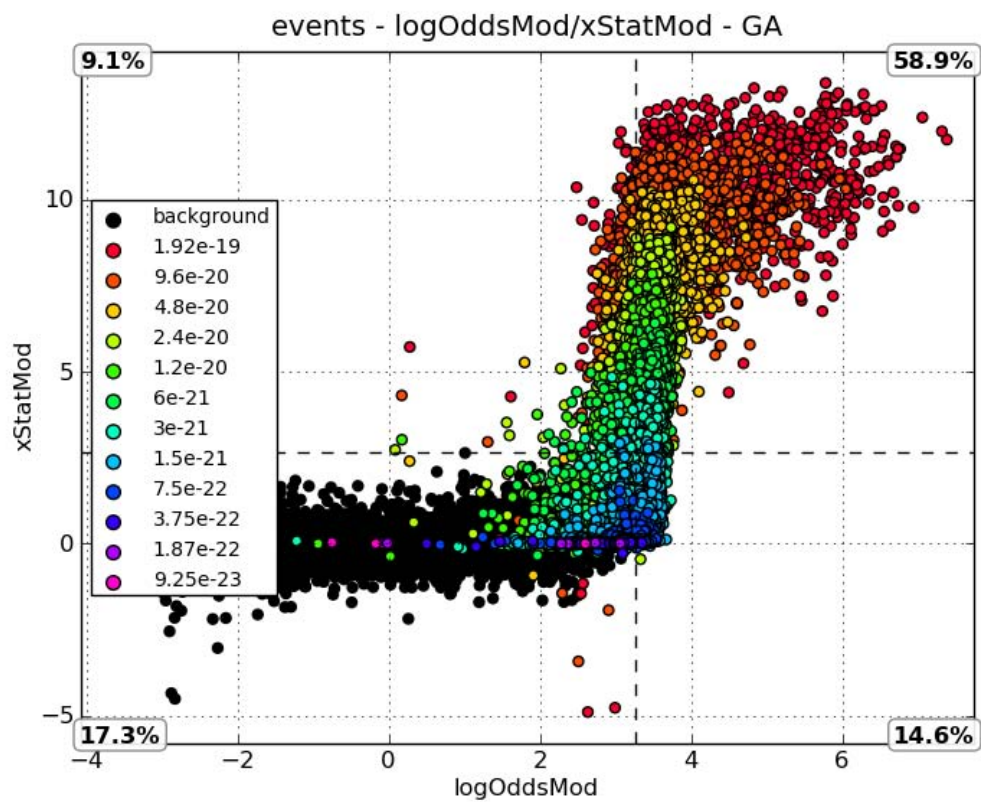


Figure A-1: GA injections scatter plot. Colors represent injection strain amplitude.

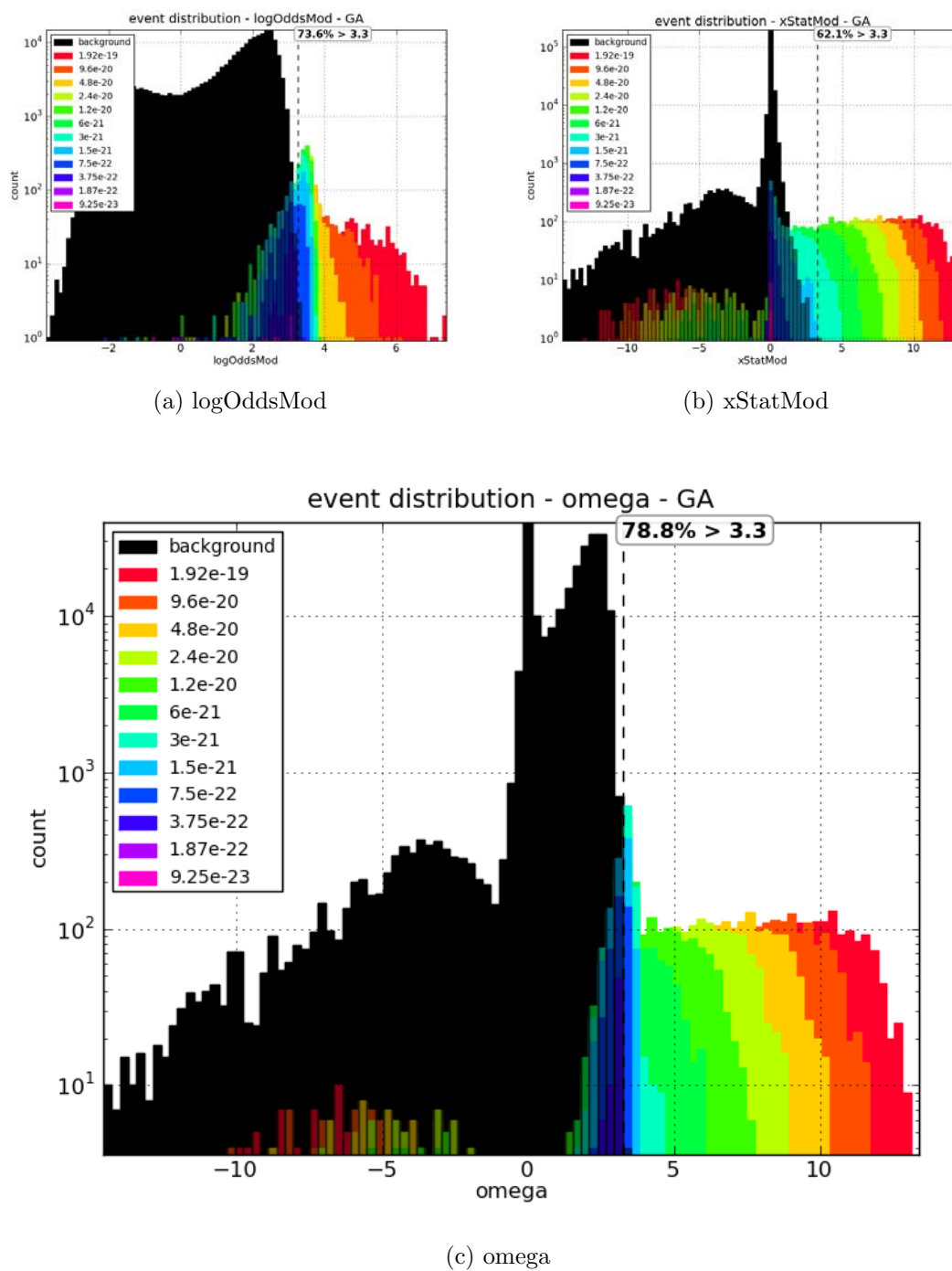
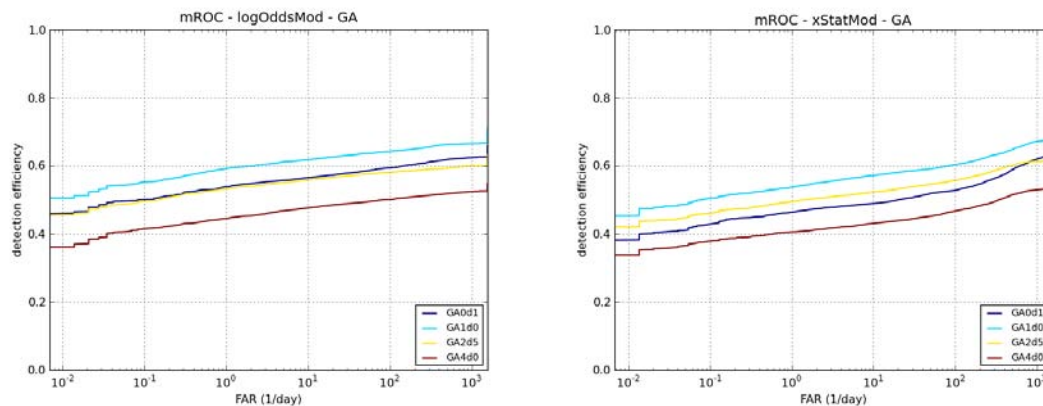
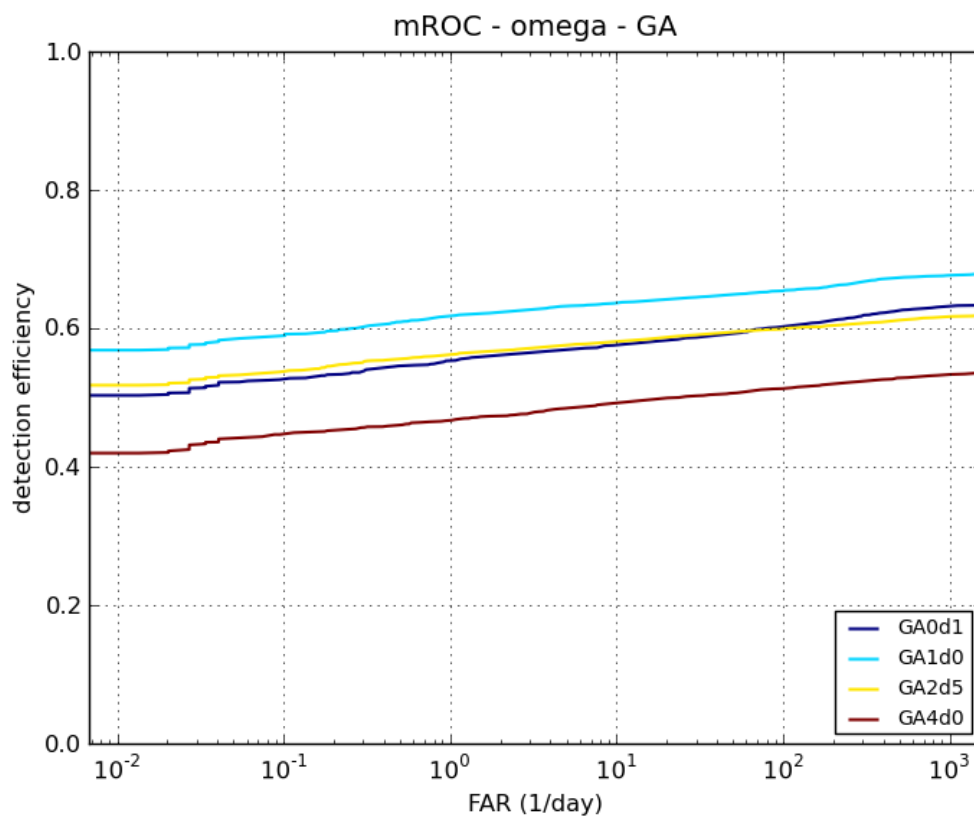


Figure A-2: GA injections histograms. Colors represent injection strain amplitude.



(a) logOddsMod

(b) xStatMod



(c) omega

Figure A-3: GA ROC plots

A.1.1 GA0d1 injections

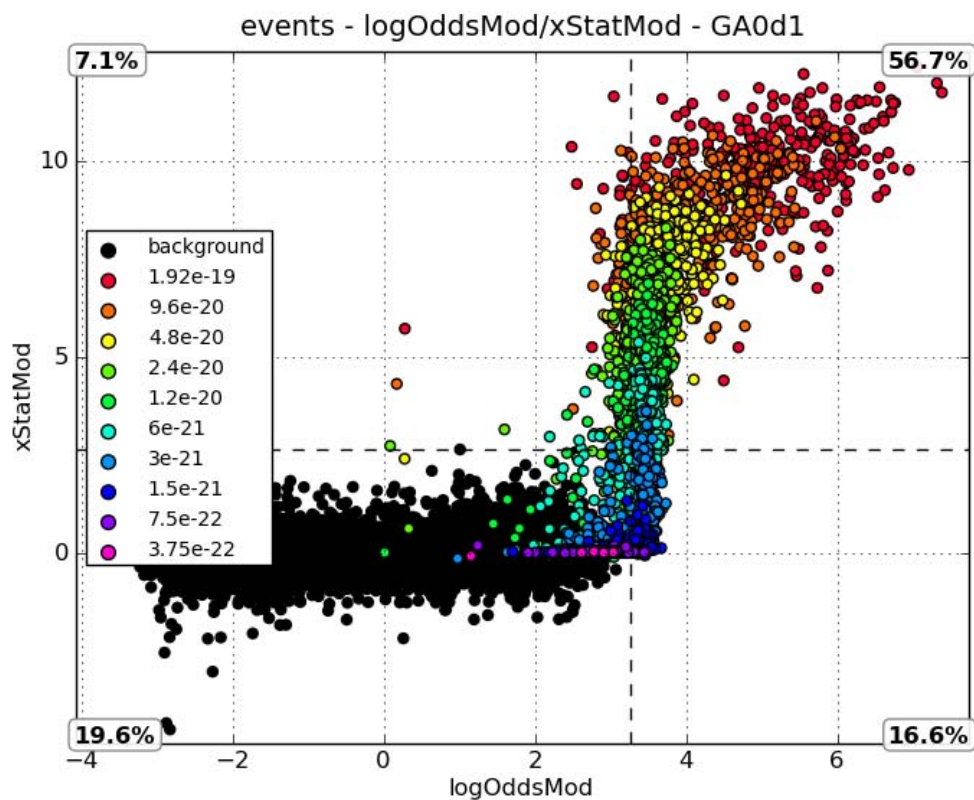


Figure A-4: GA0d1 injections scatter plot. Colors represent injection strain amplitude.

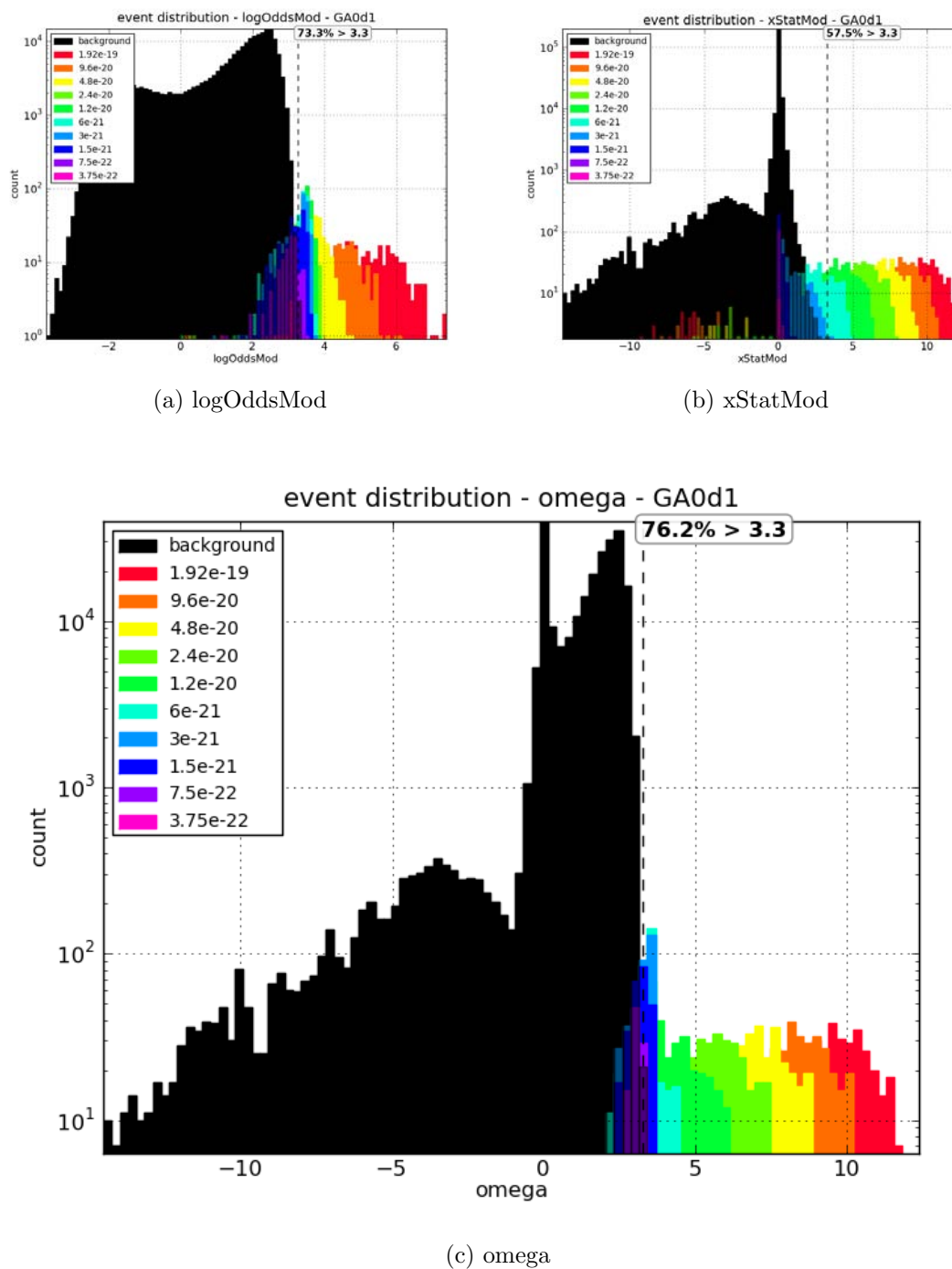
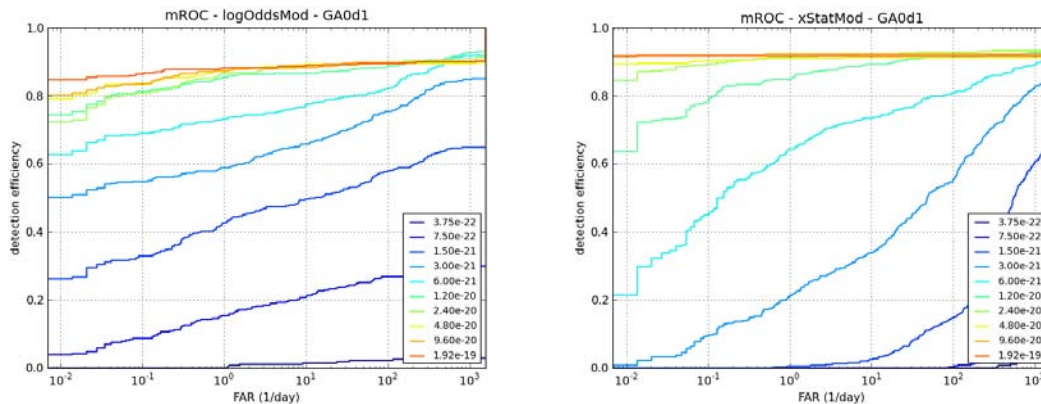
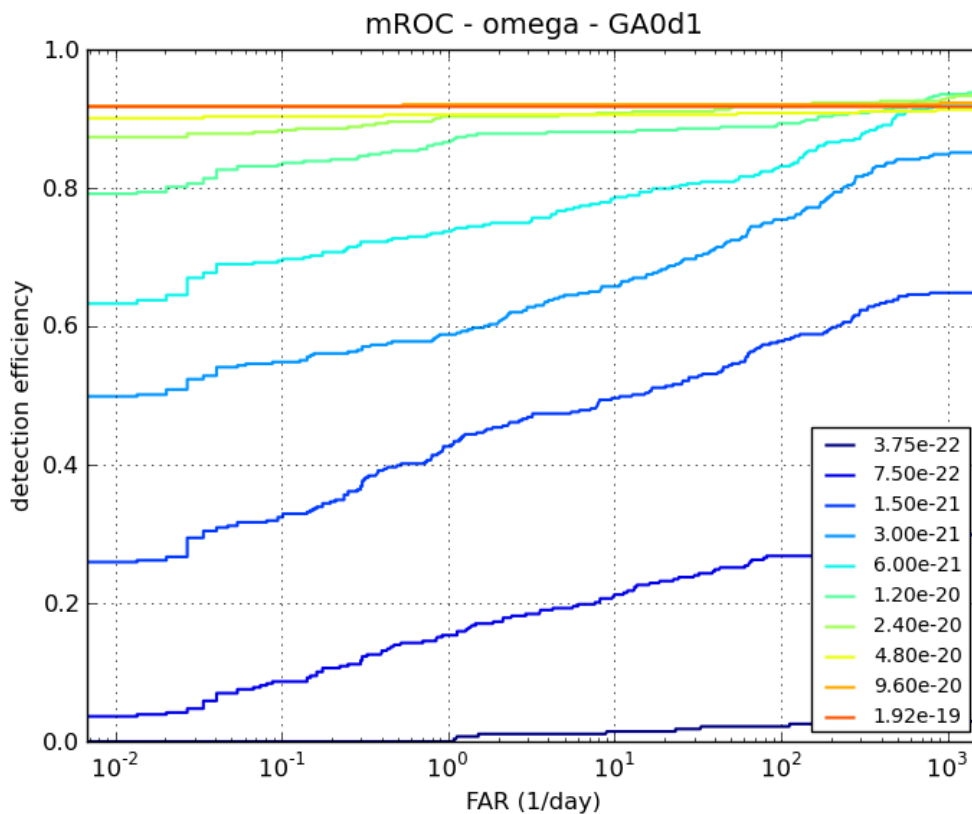


Figure A-5: GA0d1 injections histograms. Colors represent injection strain amplitude.



(a) logOddsMod

(b) xStatMod



(c) omega

Figure A-6: GA0d1 ROC plots

A.1.2 GA1d0 injections

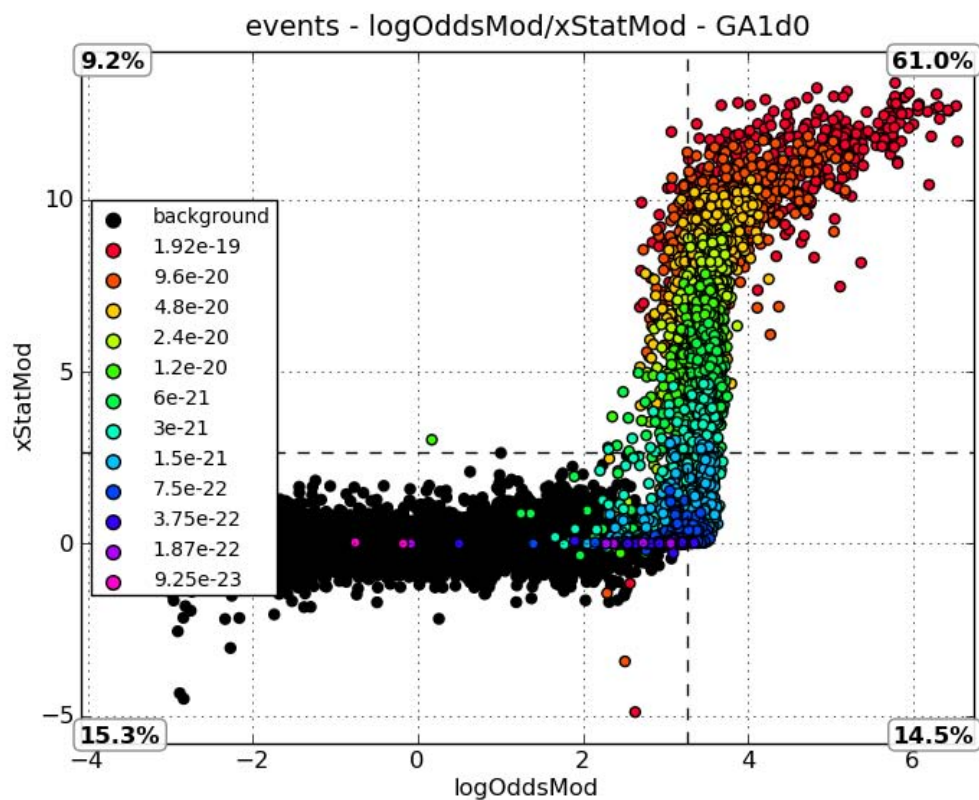
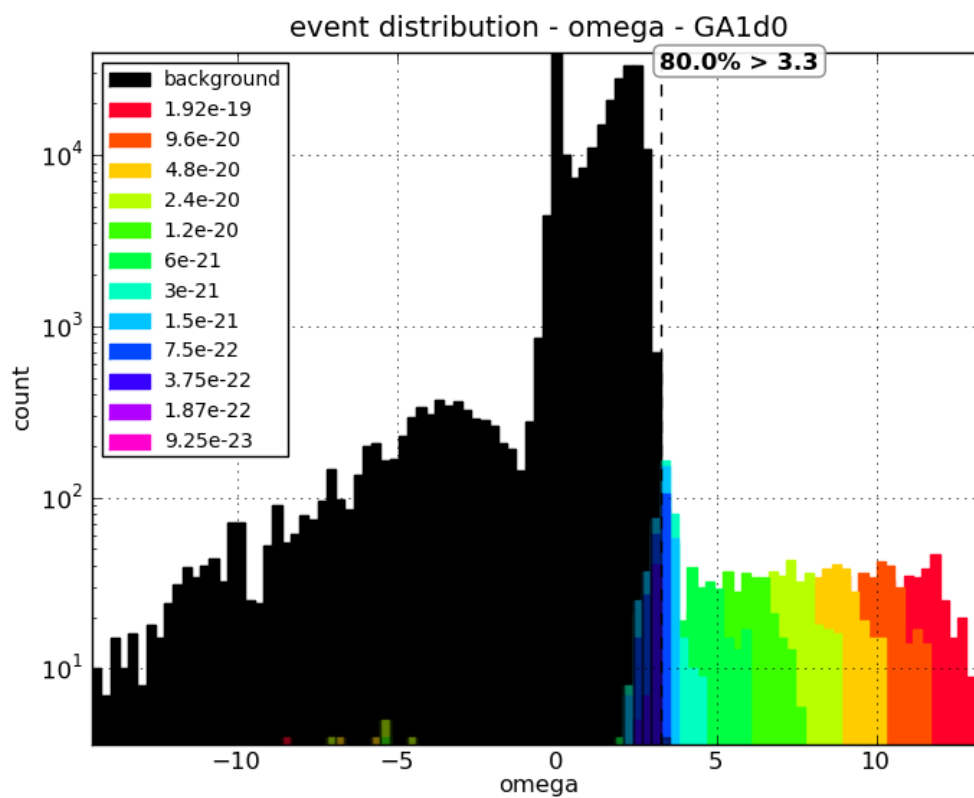
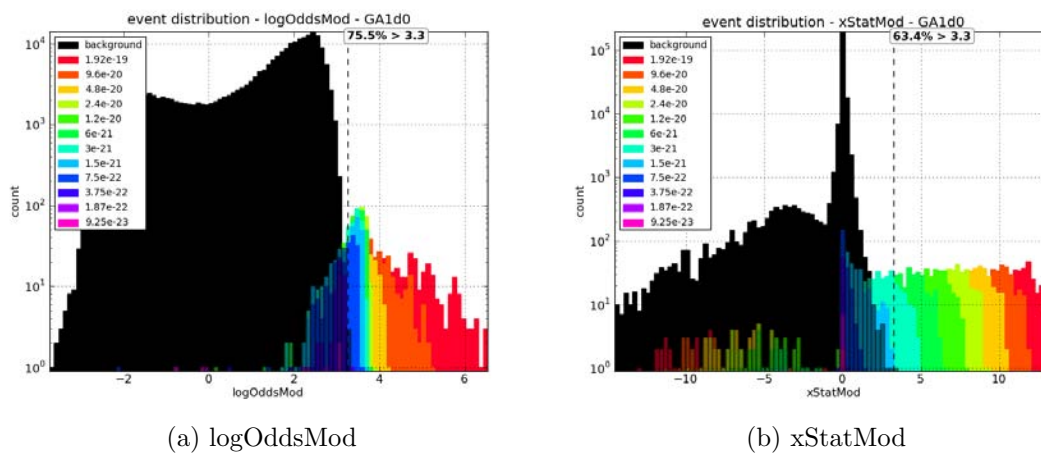
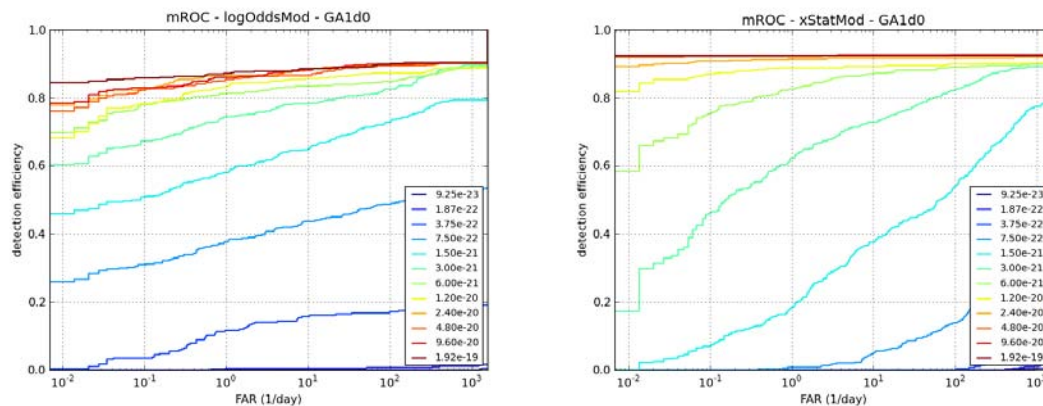


Figure A-7: GA1d0 injections scatter plot. Colors represent injection strain amplitude.



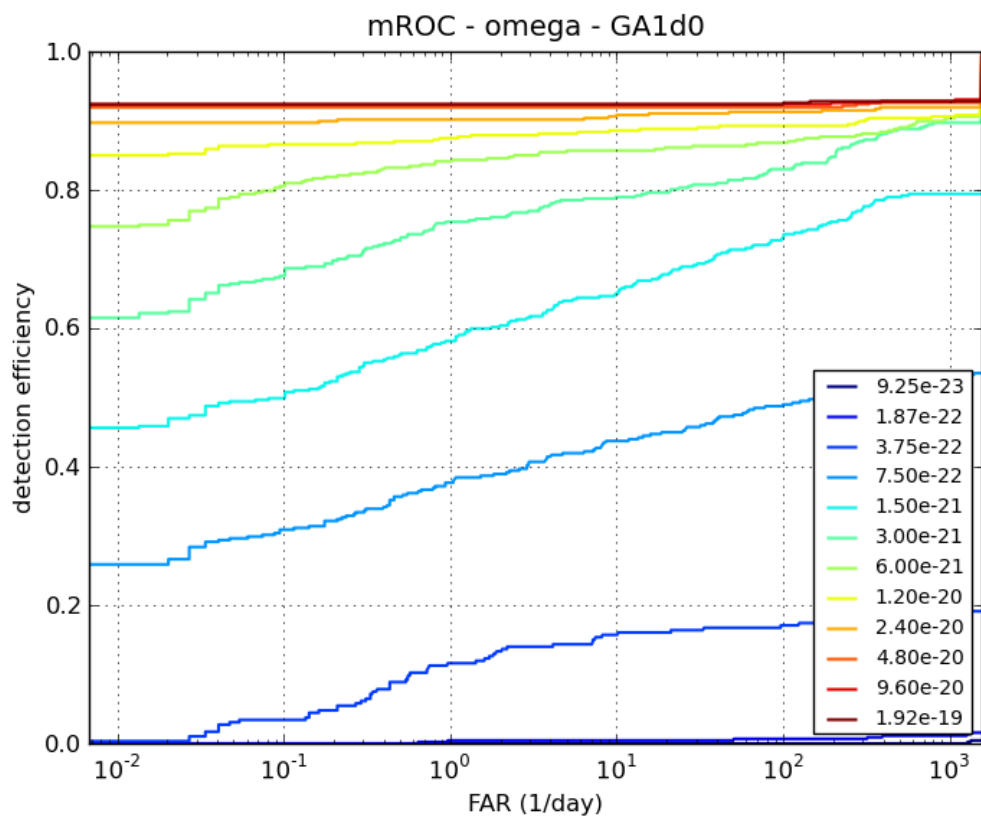
(c) omega

Figure A-8: GA1d0 injections histograms. Colors represent injection strain amplitude.



(a) logOddsMod

(b) xStatMod



(c) omega

Figure A-9: GA1d0 ROC plots

A.1.3 GA2d5 injections

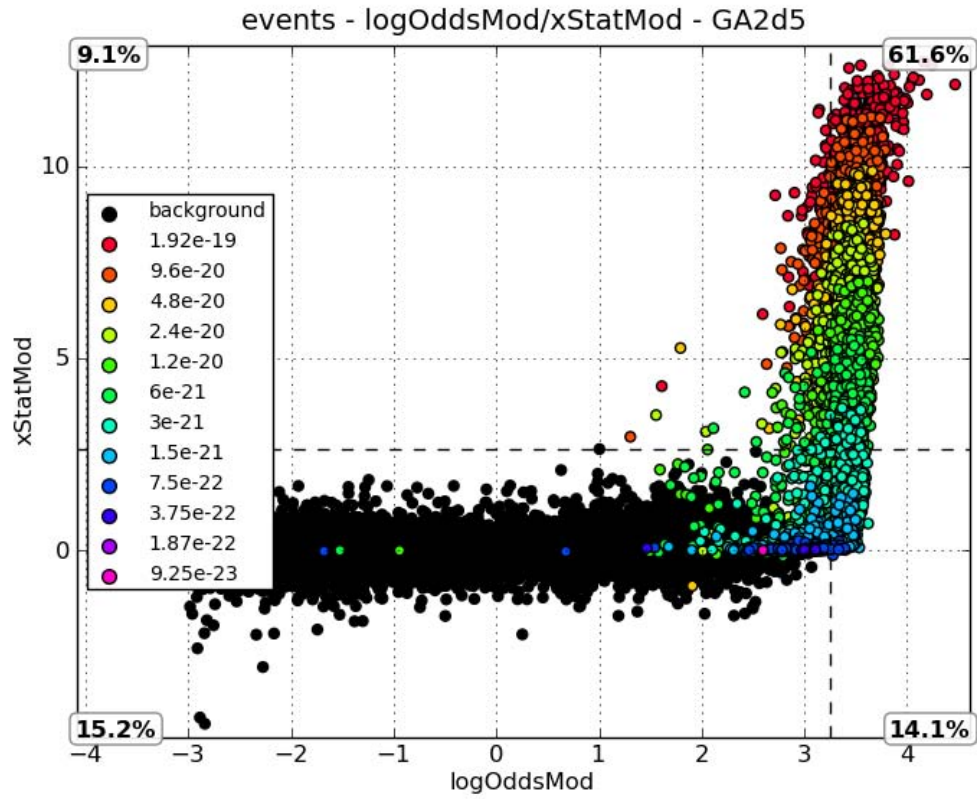


Figure A-10: GA2d5 injections scatter plot. Colors represent injection strain amplitude.

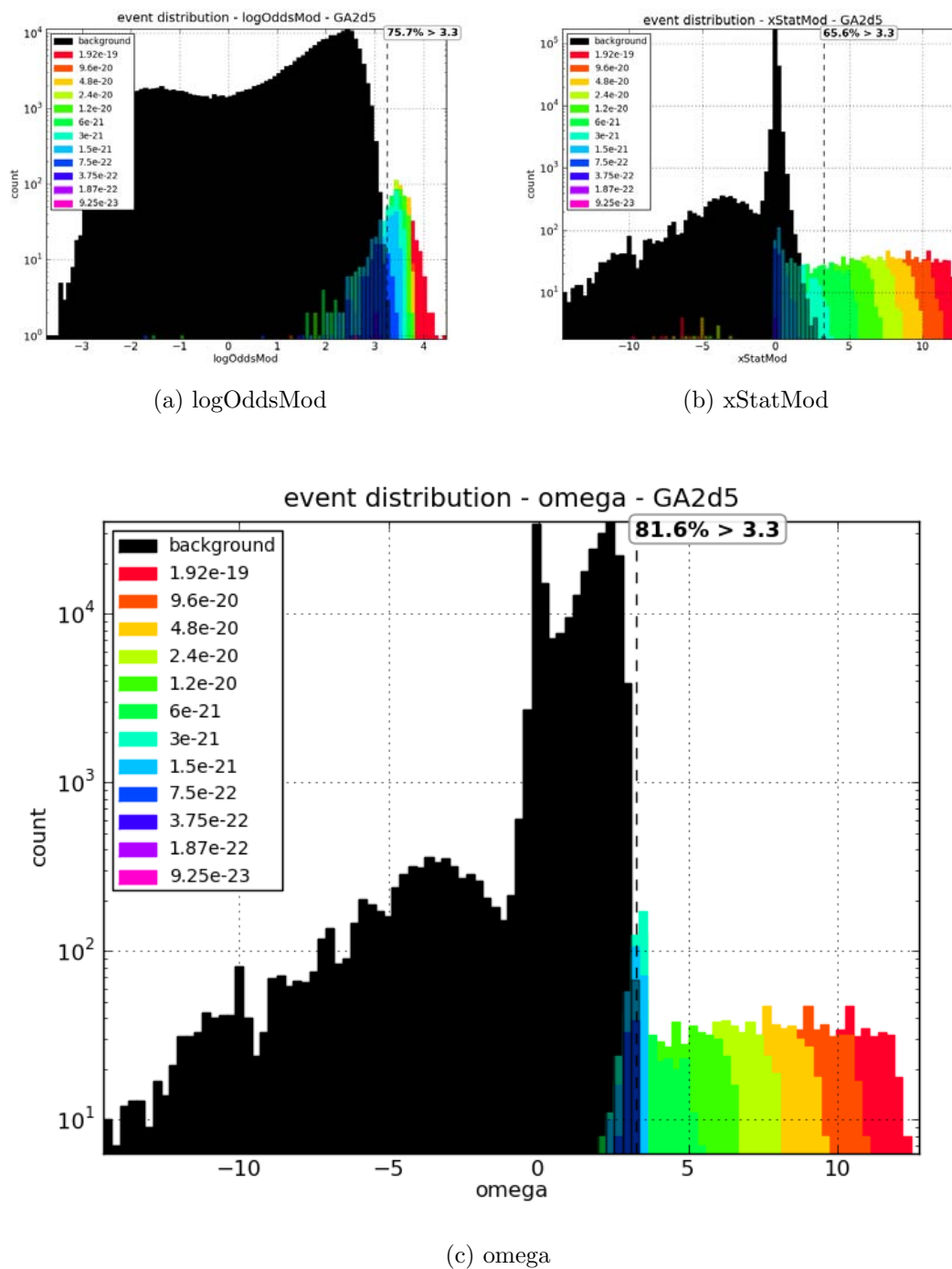
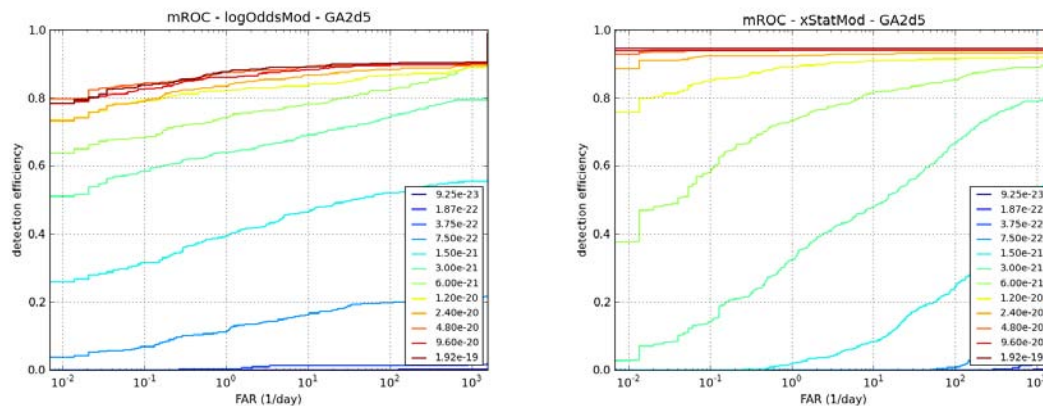
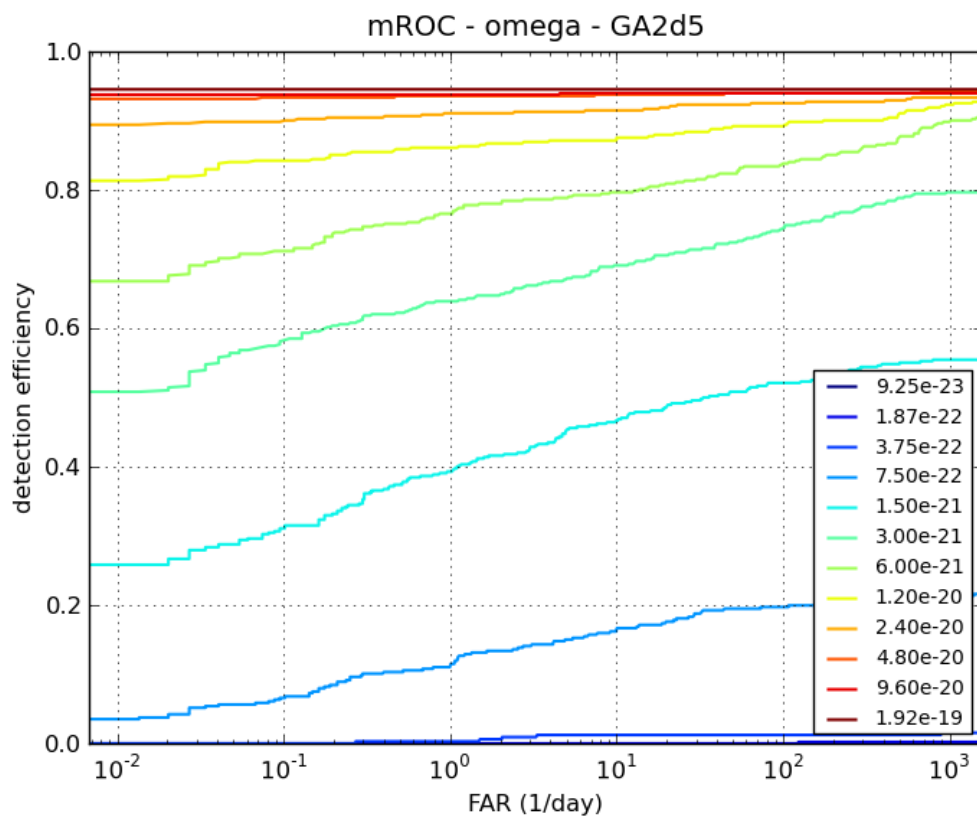


Figure A-11: GA2d5 injections histograms. Colors represent injection strain amplitude.



(a) logOddsMod

(b) xStatMod



(c) omega

Figure A-12: GA2d5 ROC plots

A.1.4 GA4d0 injections

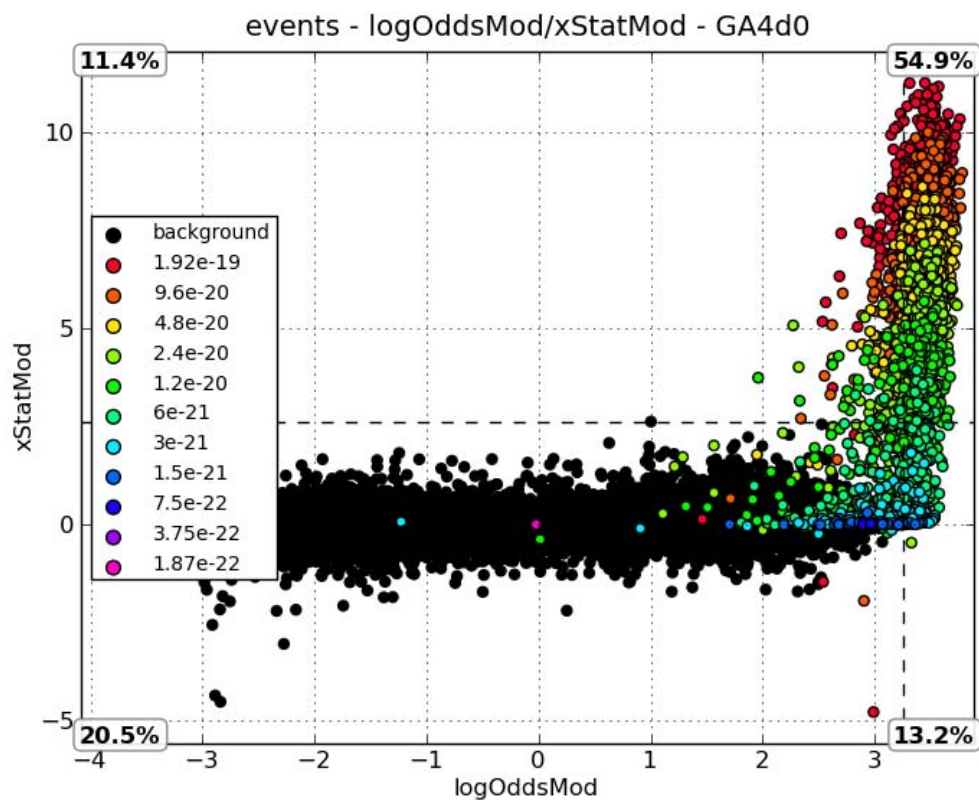
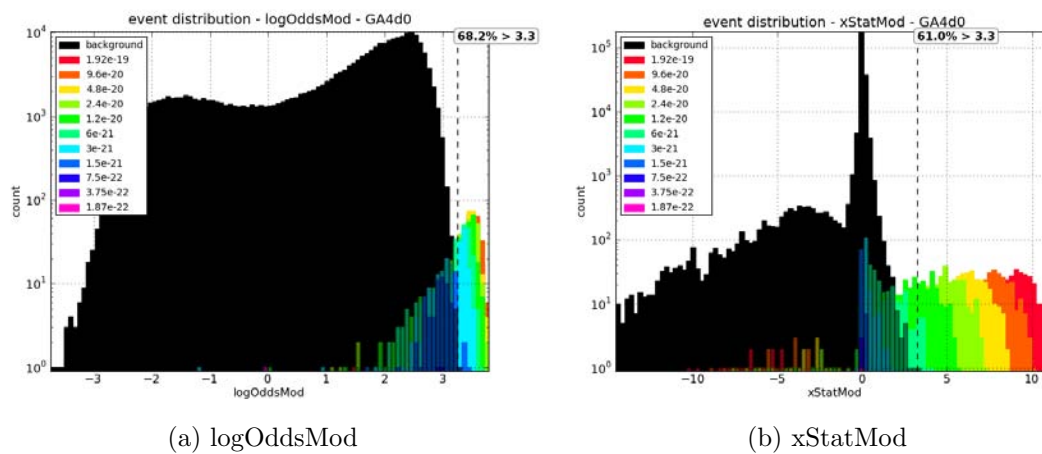
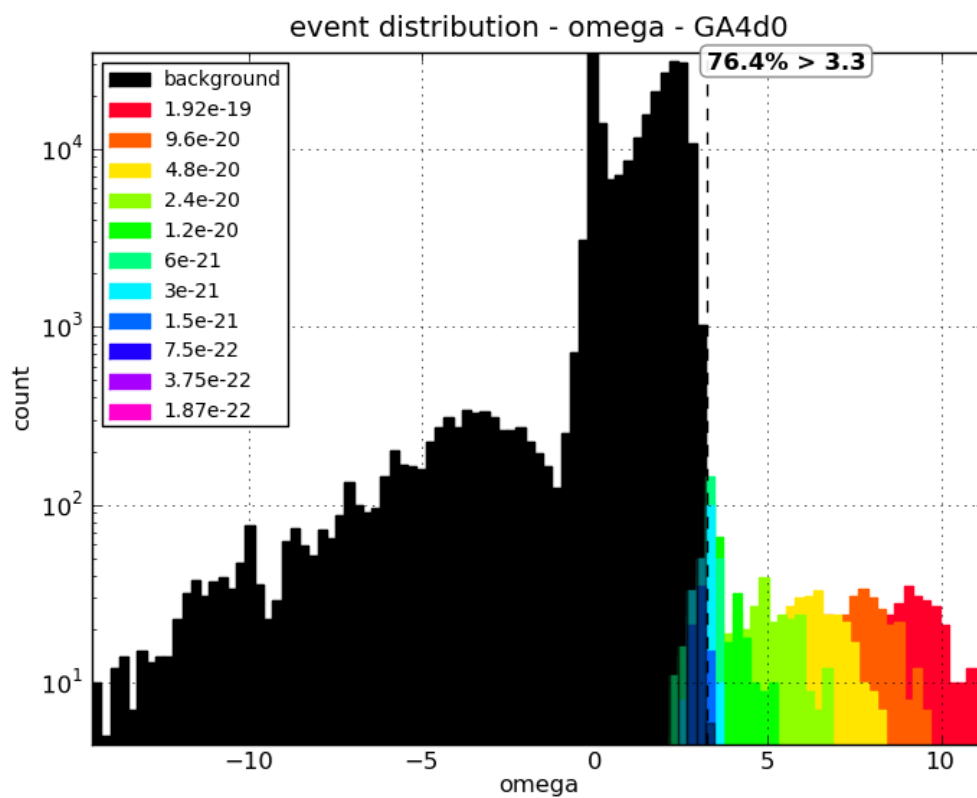


Figure A-13: GA4d0 injections scatter plot. Colors represent injection strain amplitude.



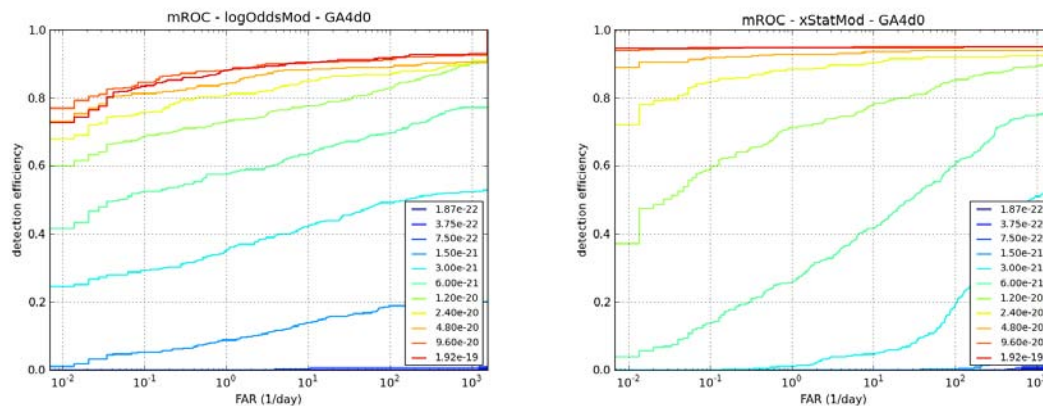
(a) logOddsMod

(b) xStatMod



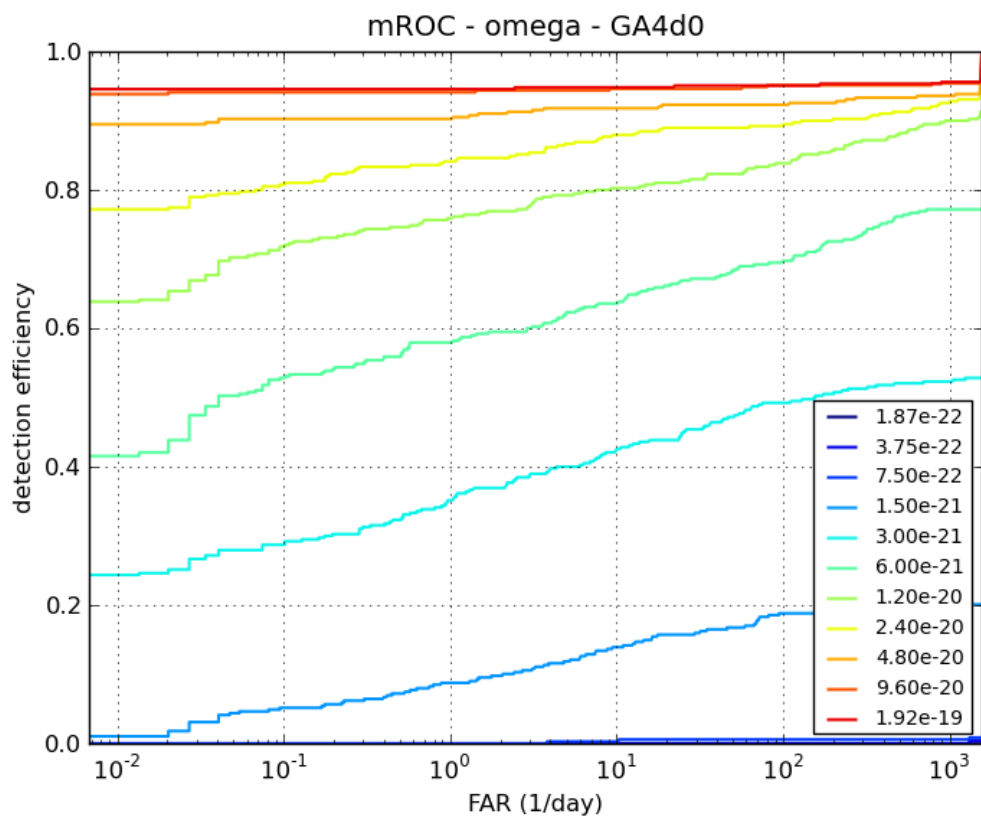
(c) omega

Figure A-14: GA4d0 injections histograms. Colors represent injection strain amplitude.



(a) logOddsMod

(b) xStatMod



(c) omega

Figure A-15: GA4d0 ROC plots

A.2 Sine-Gaussian, Q 3 injections

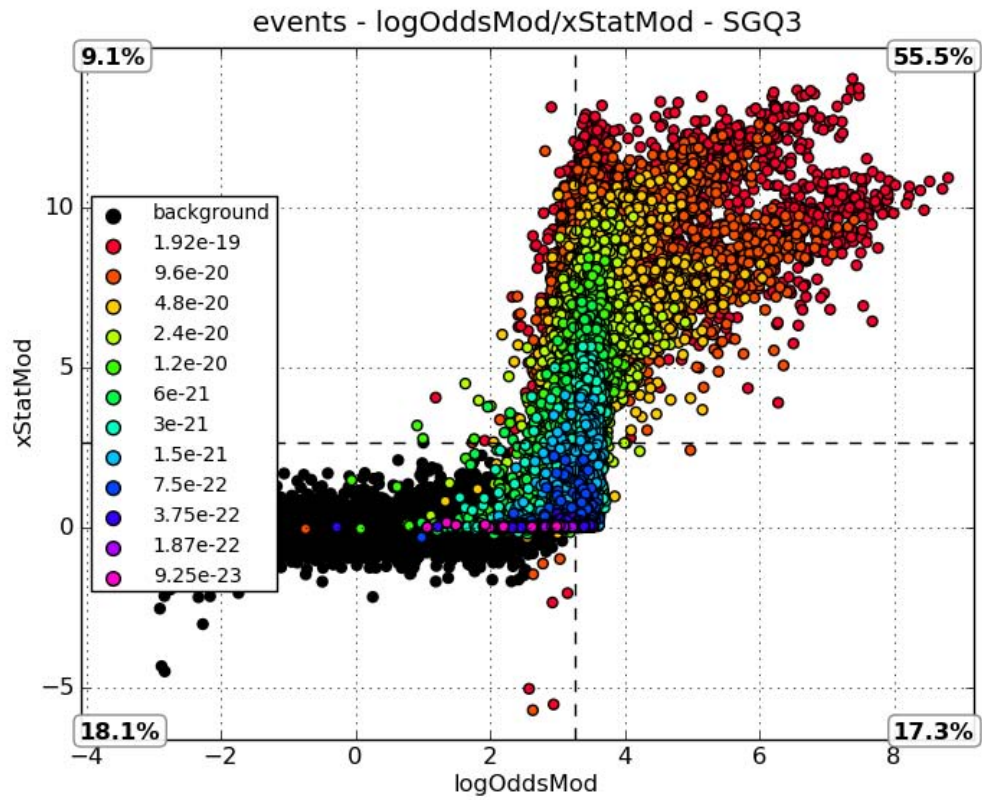


Figure A-16: SGQ3 injections scatter plot. Colors represent injection strain amplitude.

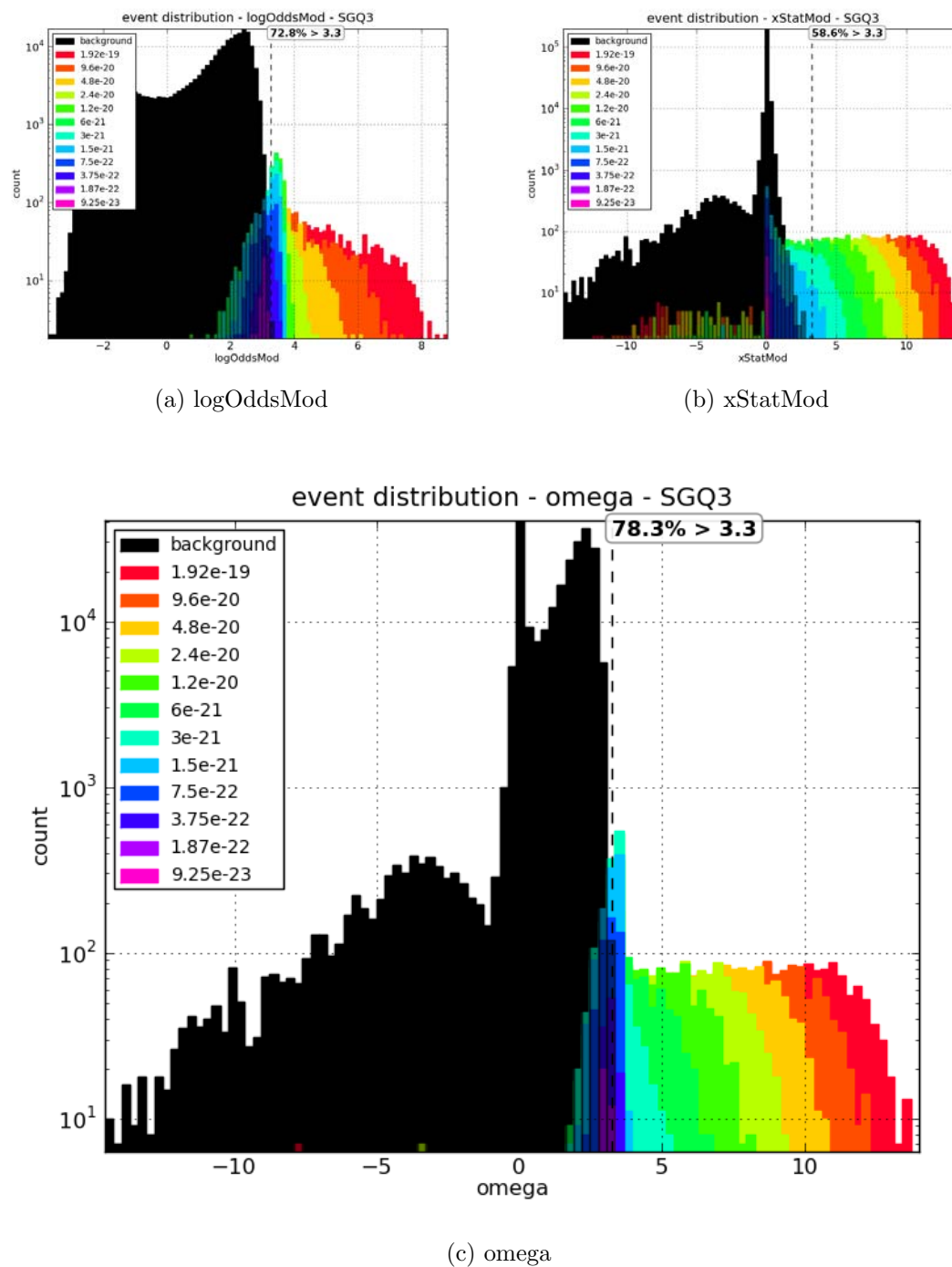
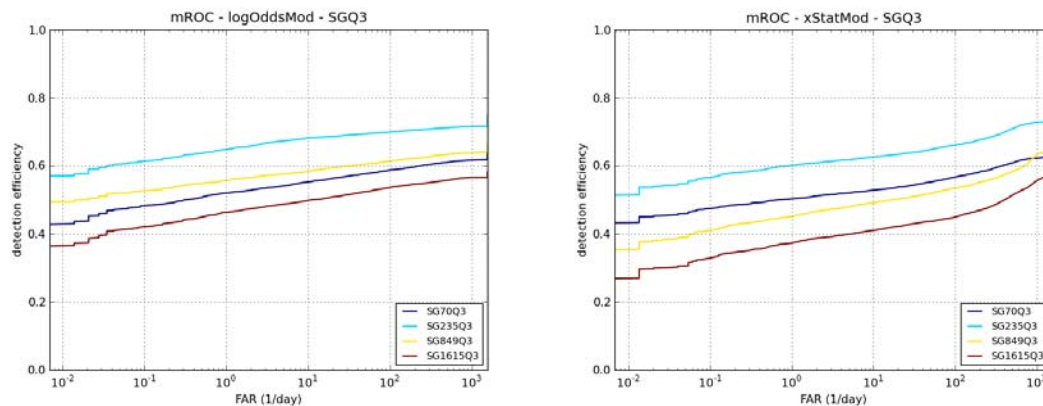
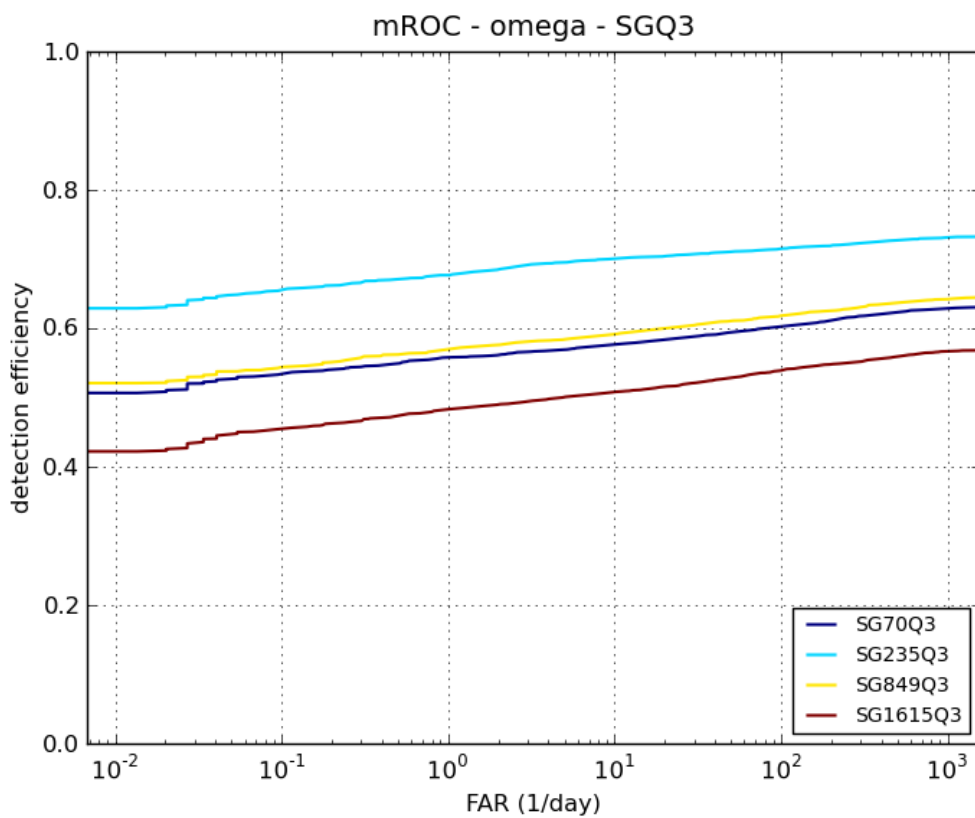


Figure A-17: SGQ3 injections histograms. Colors represent injection strain amplitude.



(a) logOddsMod

(b) xStatMod



(c) omega

Figure A-18: SGQ3 ROC plots

A.2.1 SG70Q3 injections

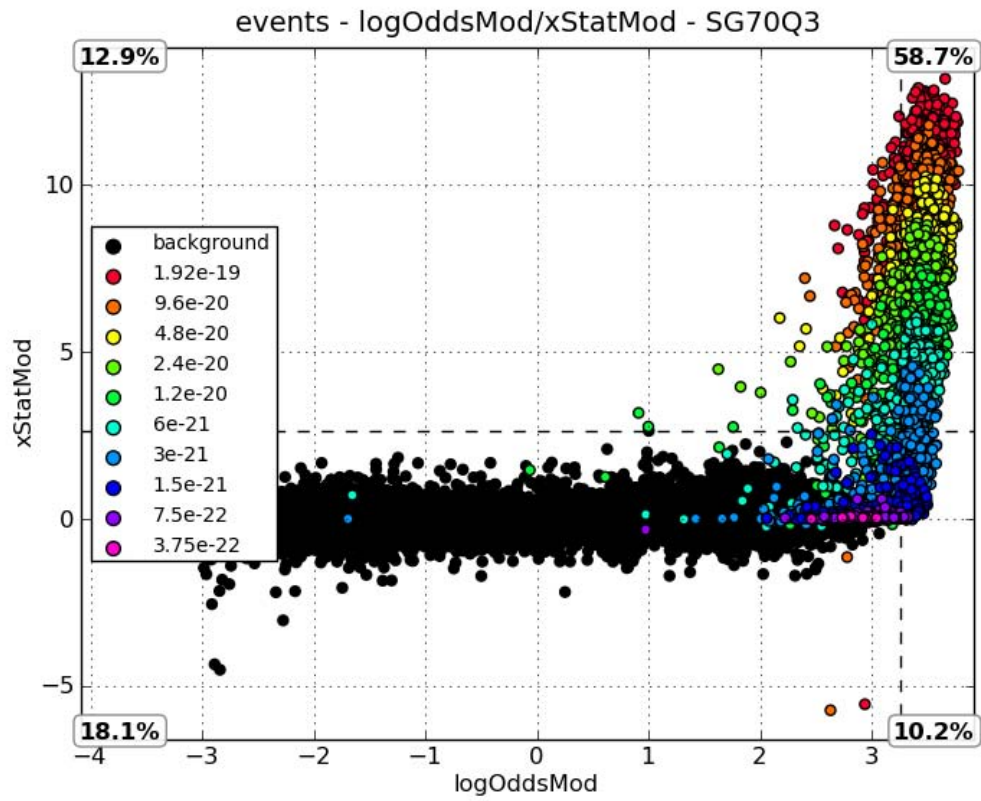
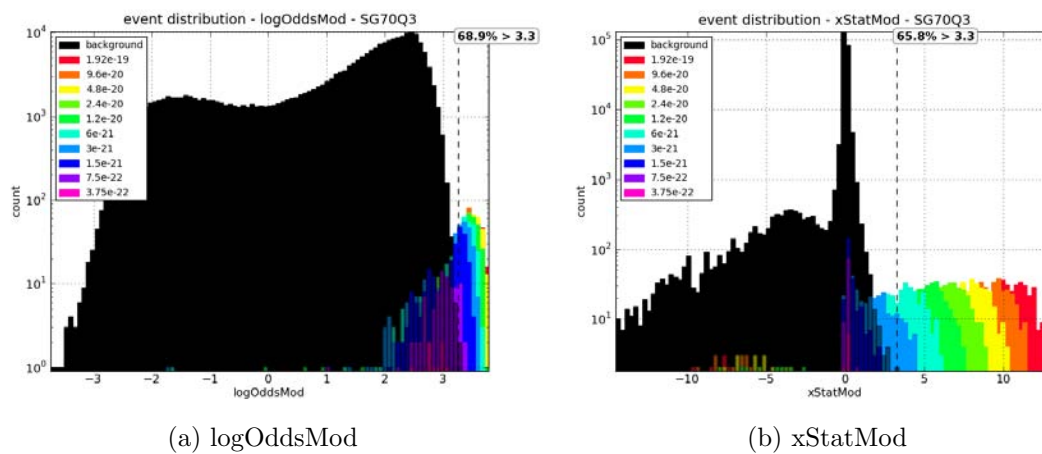
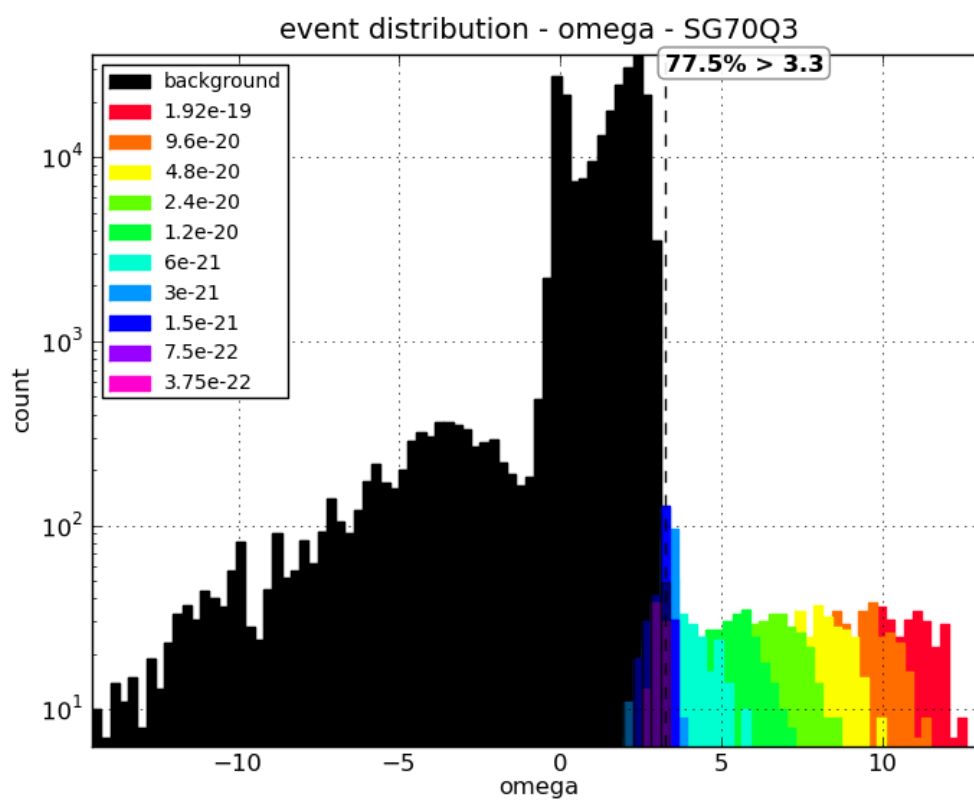


Figure A-19: SG70Q3 injections scatter plot. Colors represent injection strain amplitude.



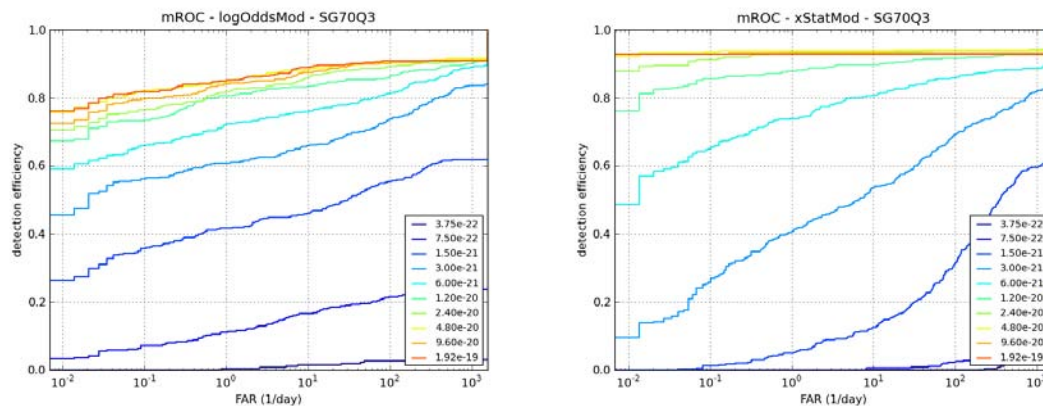
(a) logOddsMod

(b) xStatMod



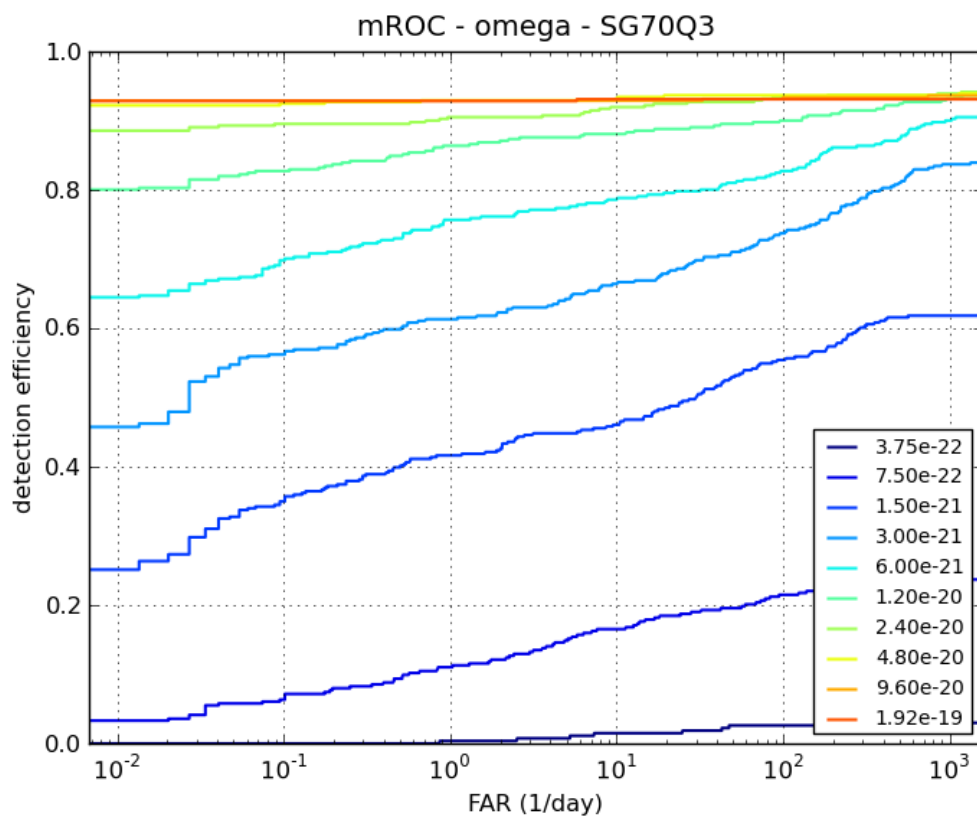
(c) omega

Figure A-20: SG70Q3 injections histograms. Colors represent injection strain amplitude.



(a) logOddsMod

(b) xStatMod



(c) omega

Figure A-21: SG70Q3 ROC plots

A.2.2 SG235Q3 injections

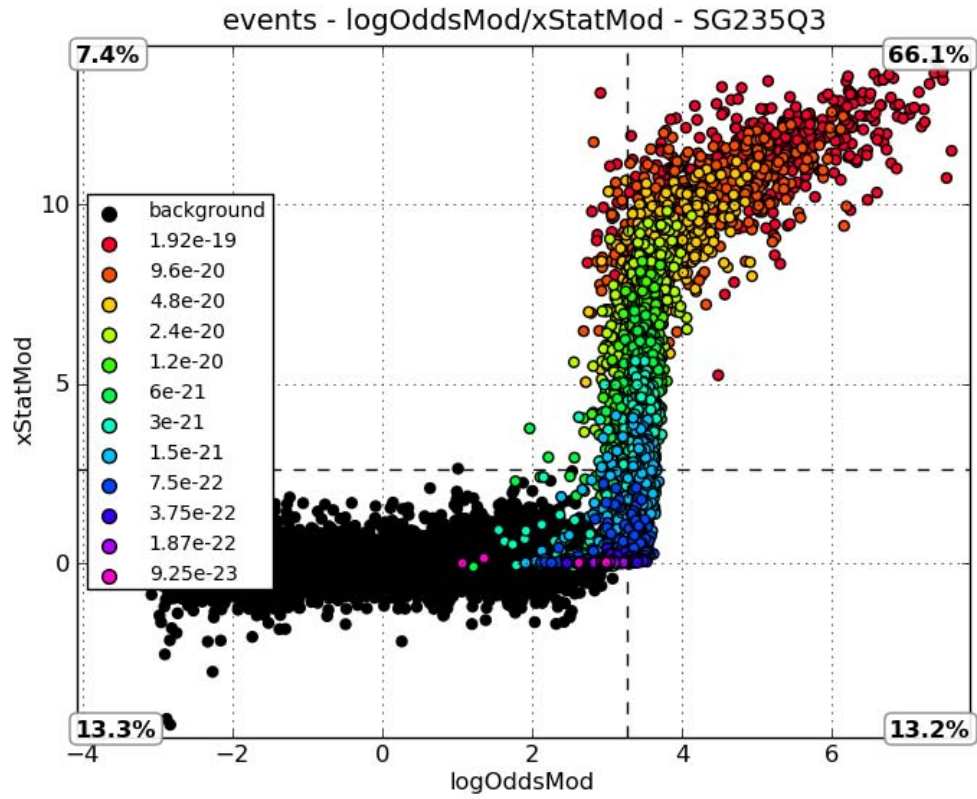


Figure A-22: SG235Q3 injections scatter plot. Colors represent injection strain amplitude.

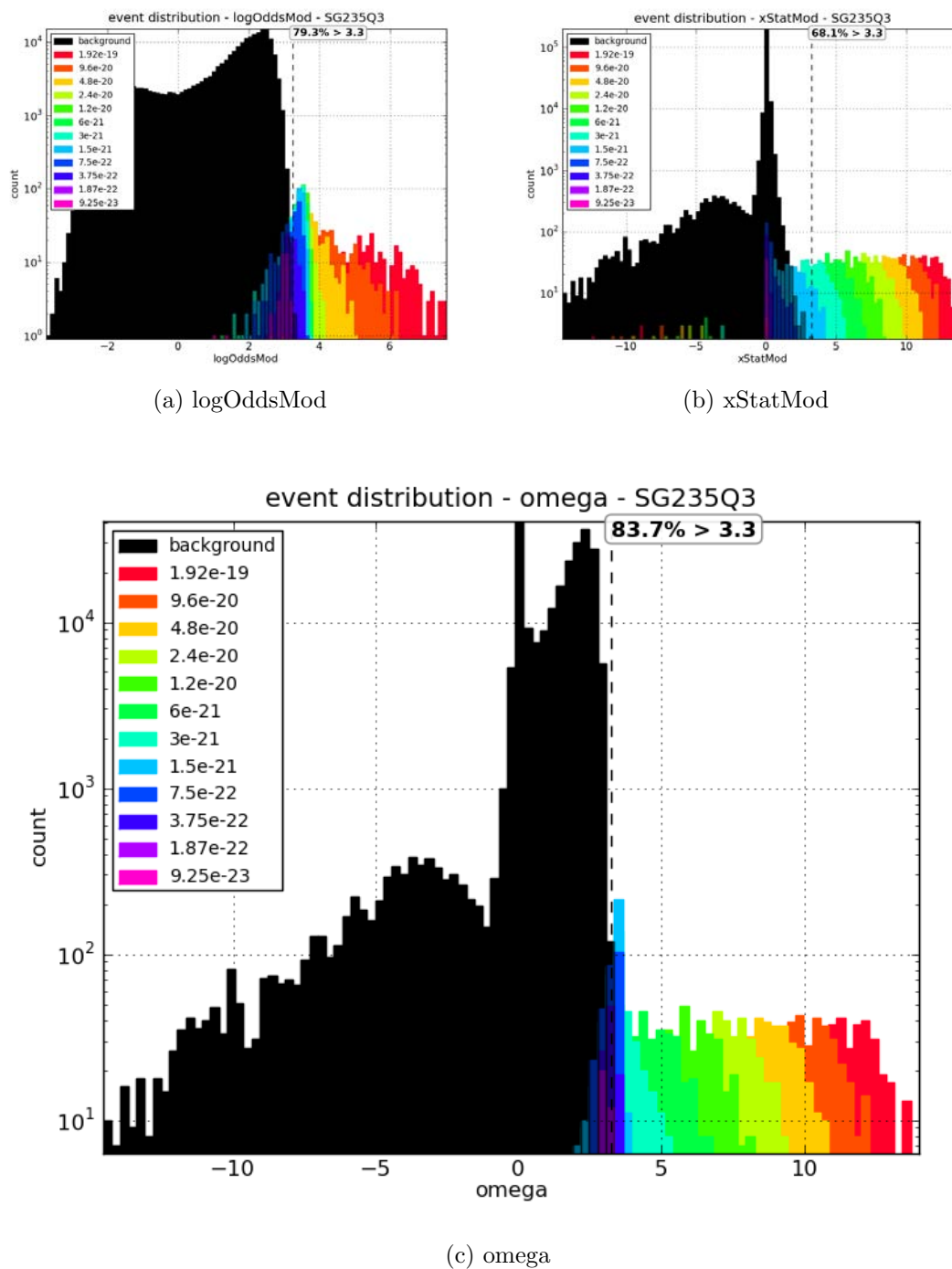
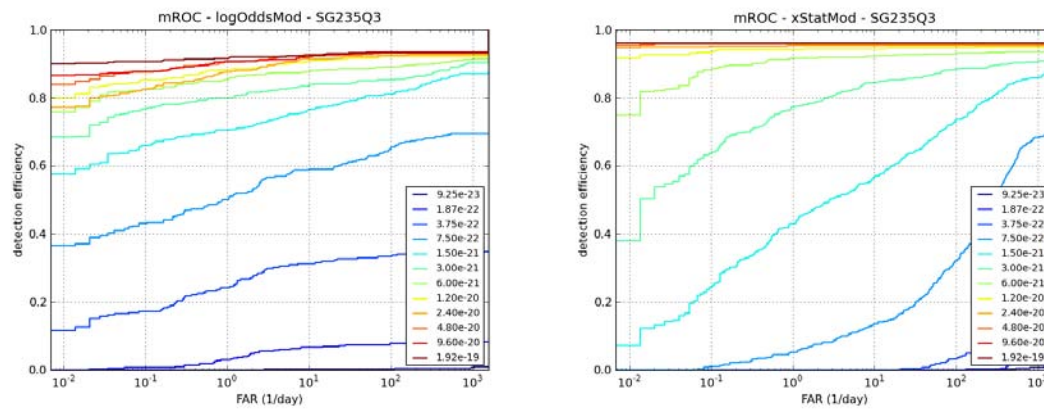
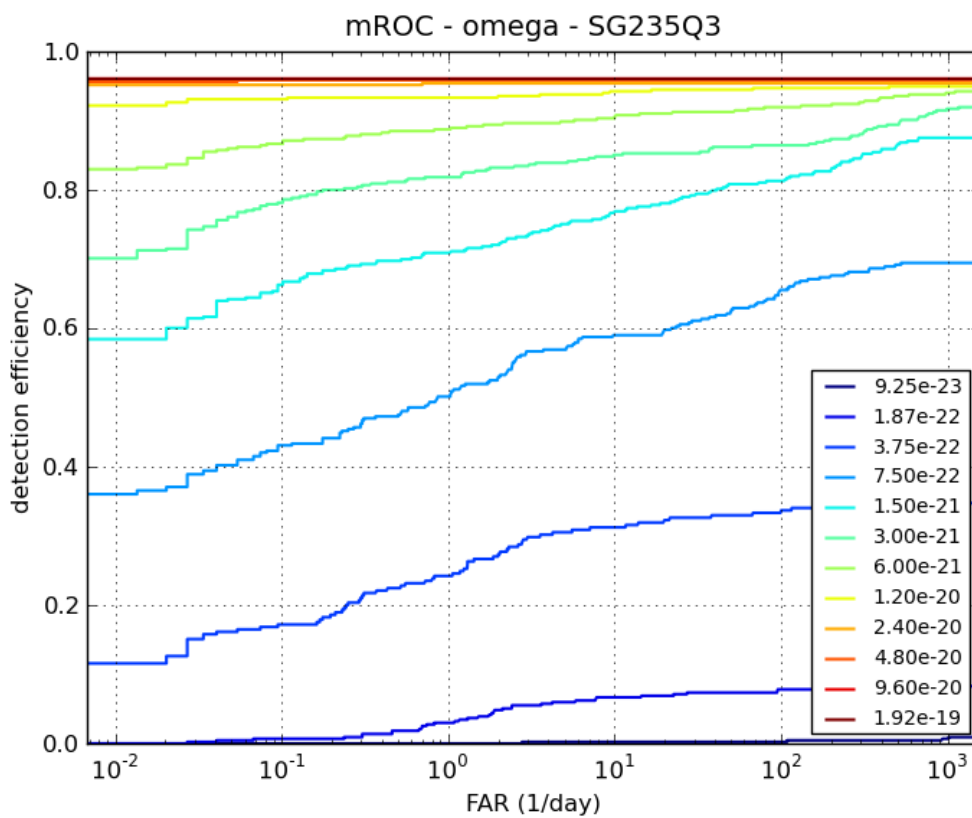


Figure A-23: SG235Q3 injections histograms. Colors represent injection strain amplitude.



(a) logOddsMod

(b) xStatMod



(c) omega

Figure A-24: SG235Q3 ROC plots

A.2.3 SG849Q3 injections

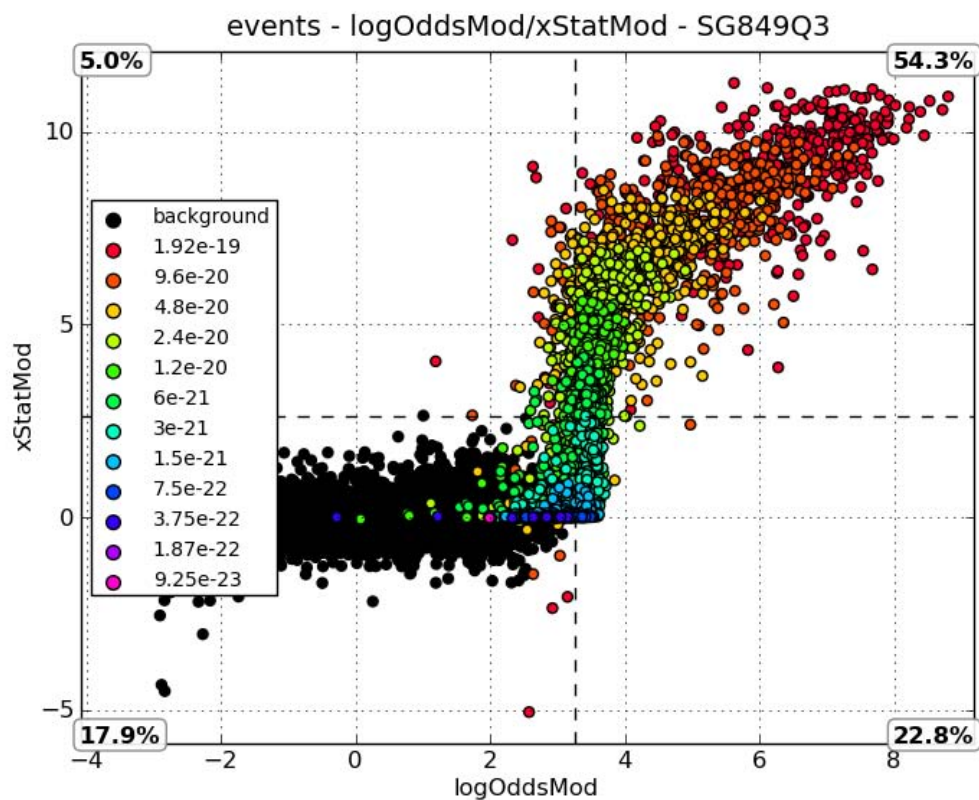


Figure A-25: SG849Q3 injections scatter plot. Colors represent injection strain amplitude.

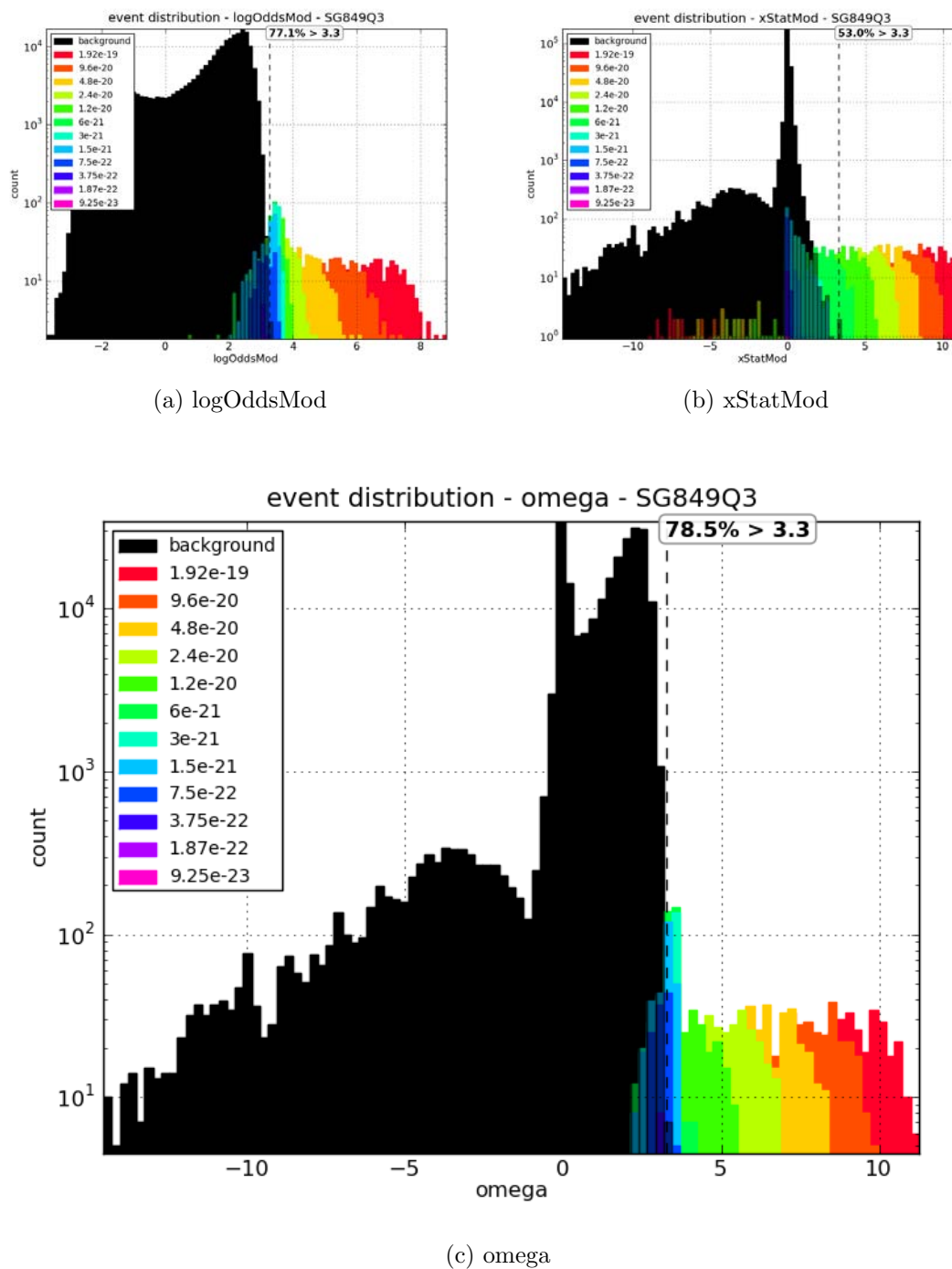
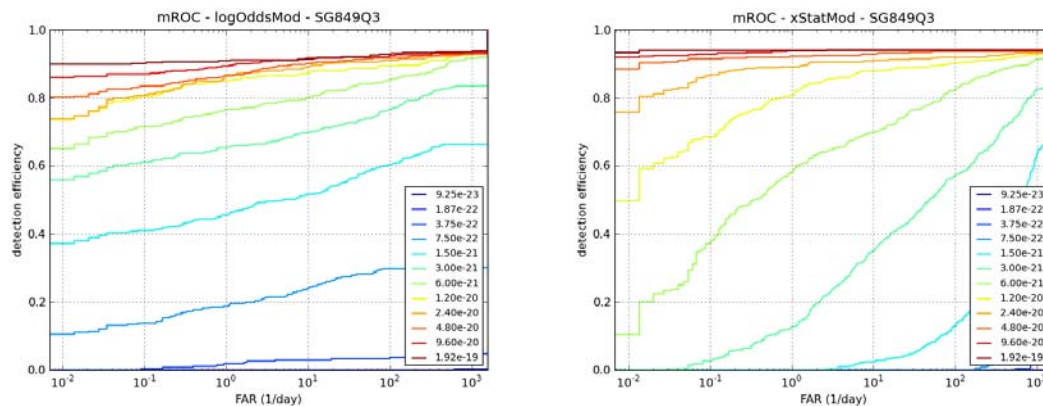
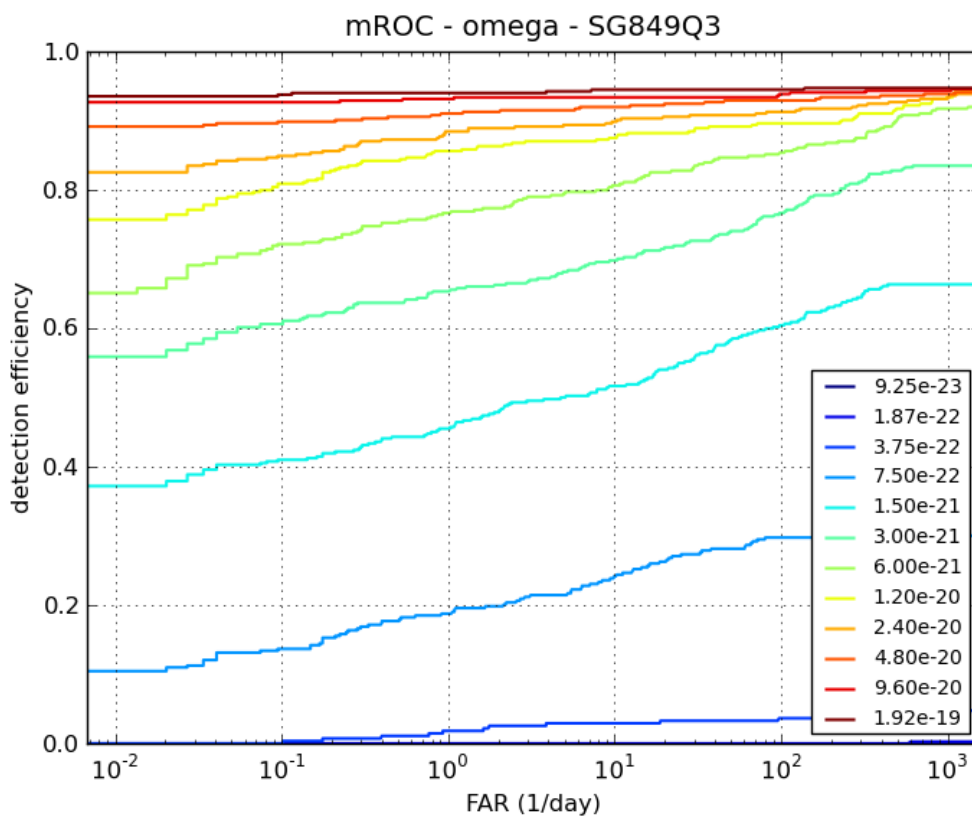


Figure A-26: SG849Q3 injections histograms. Colors represent injection strain amplitude.



(a) logOddsMod

(b) xStatMod



(c) omega

Figure A-27: SG849Q3 ROC plots

A.2.4 SG1615Q3 injections

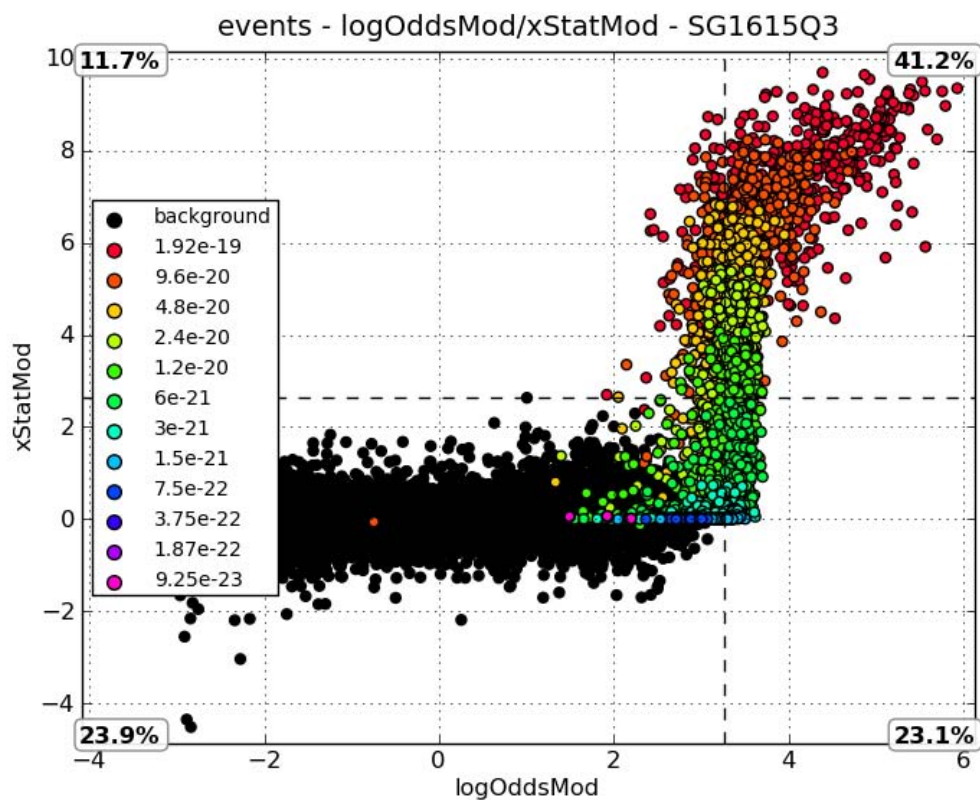


Figure A-28: SG1615Q3 injections scatter plot. Colors represent injection strain amplitude.

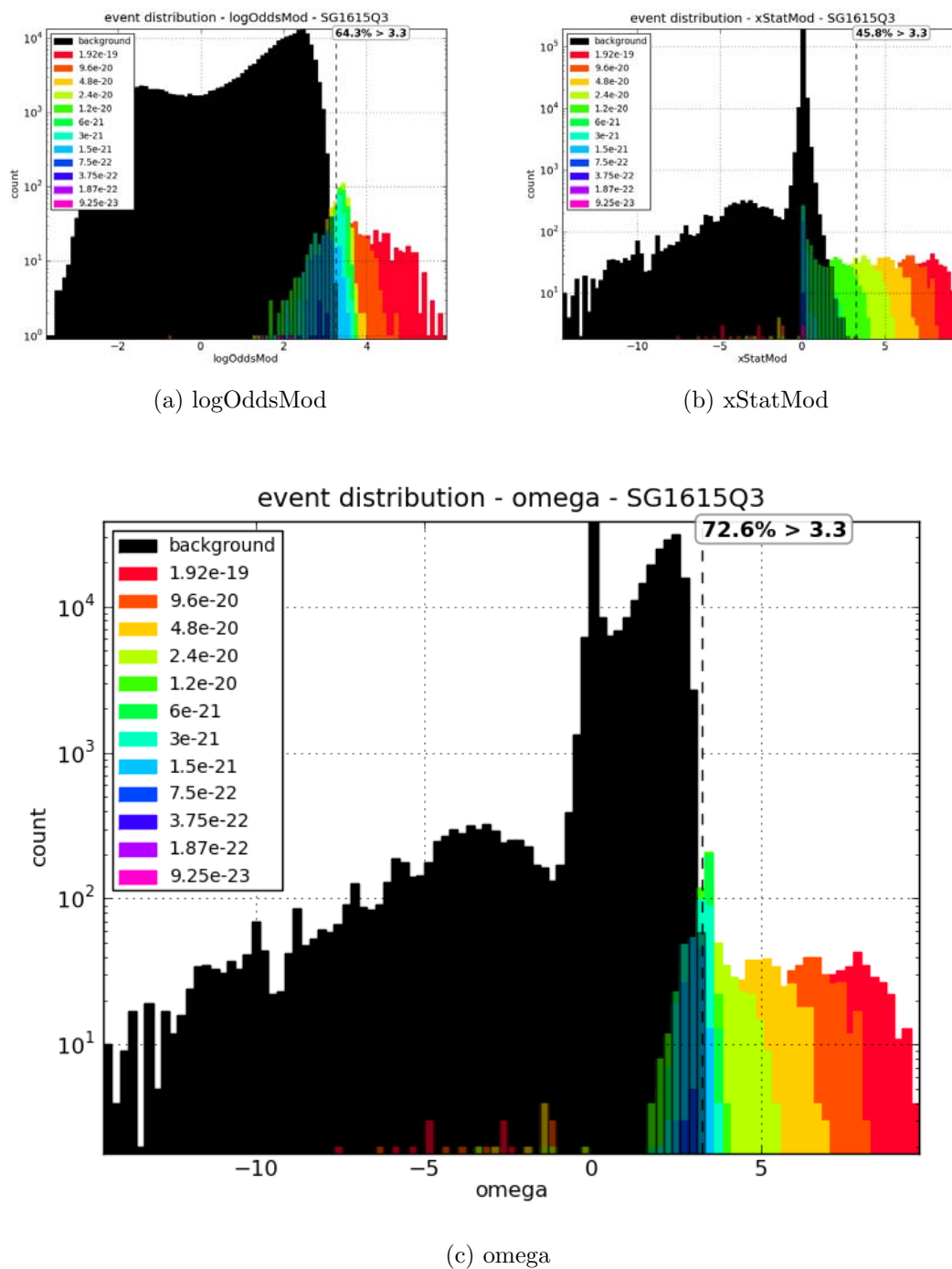


Figure A-29: SG1615Q3 injections histograms. Colors represent injection strain amplitude.

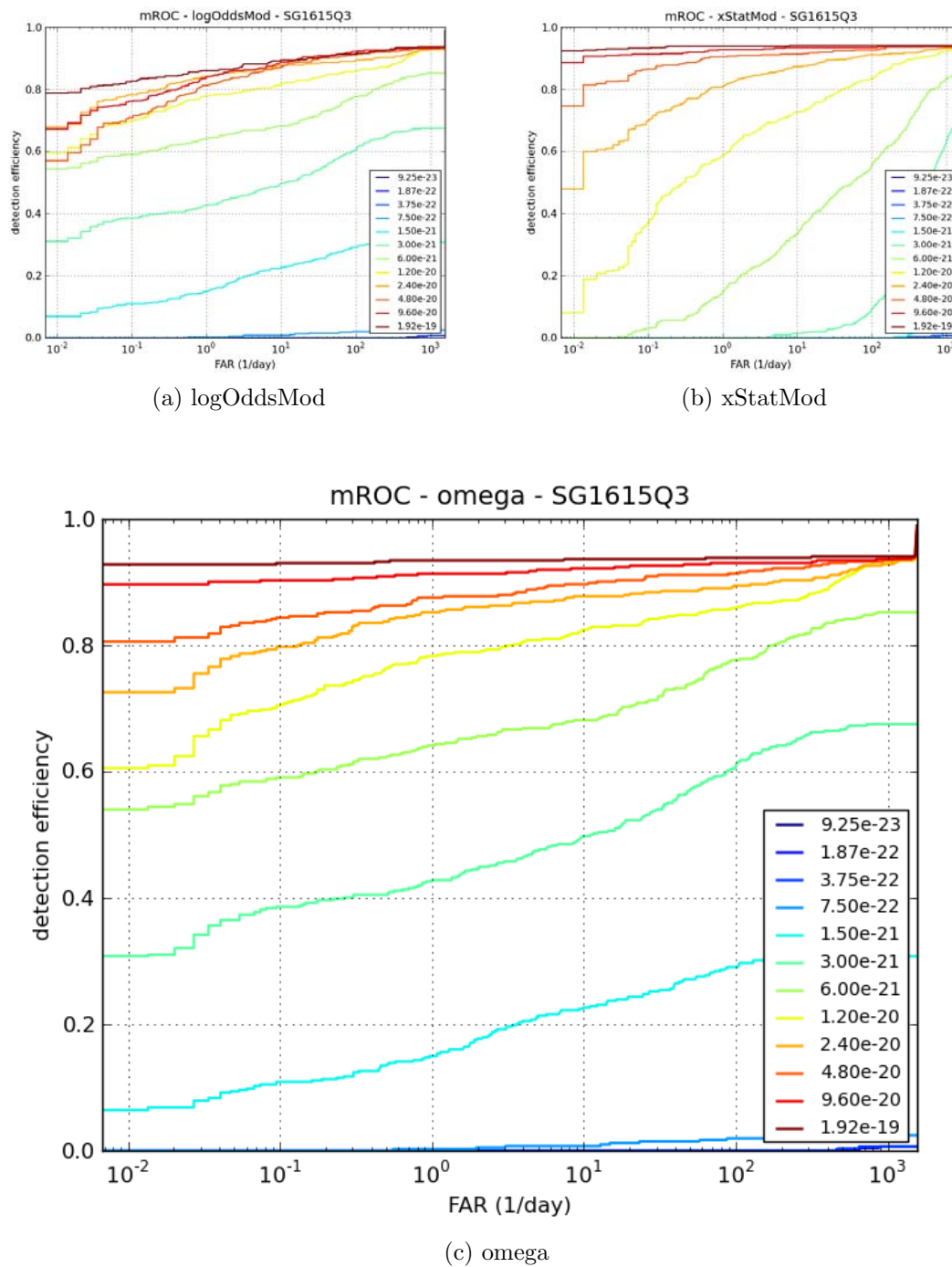


Figure A-30: SG1615Q3 ROC plots

A.3 Sine-Gaussian, Q 9 injections

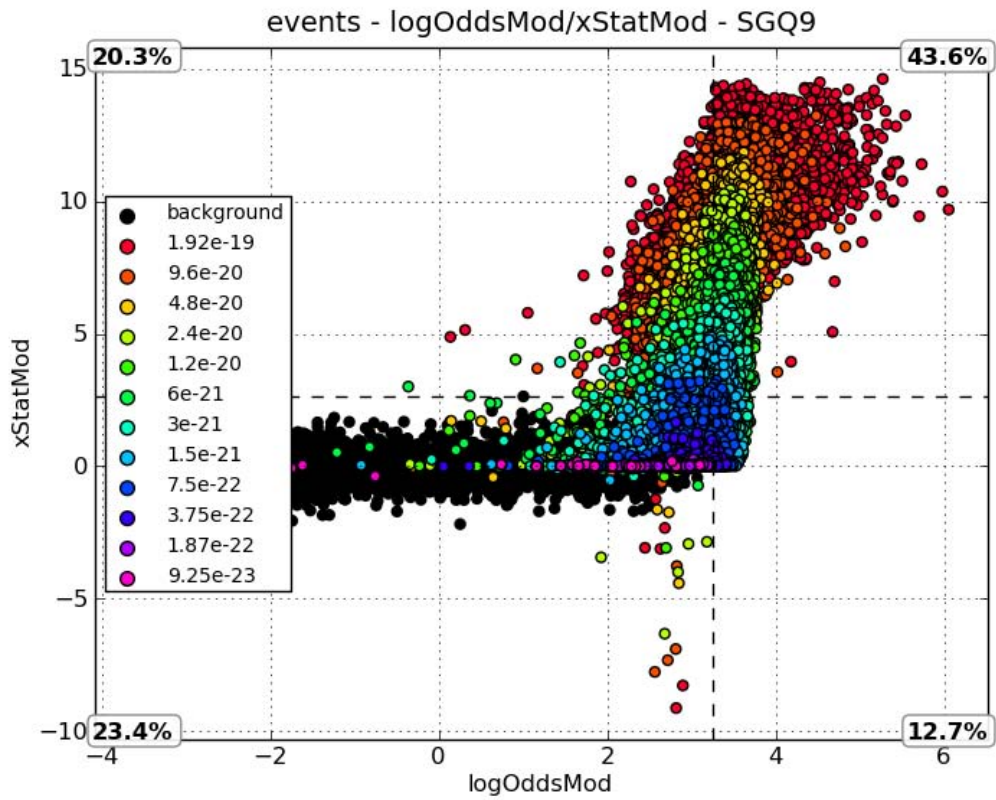


Figure A-31: SGQ9 injections scatter plot. Colors represent injection strain amplitude.

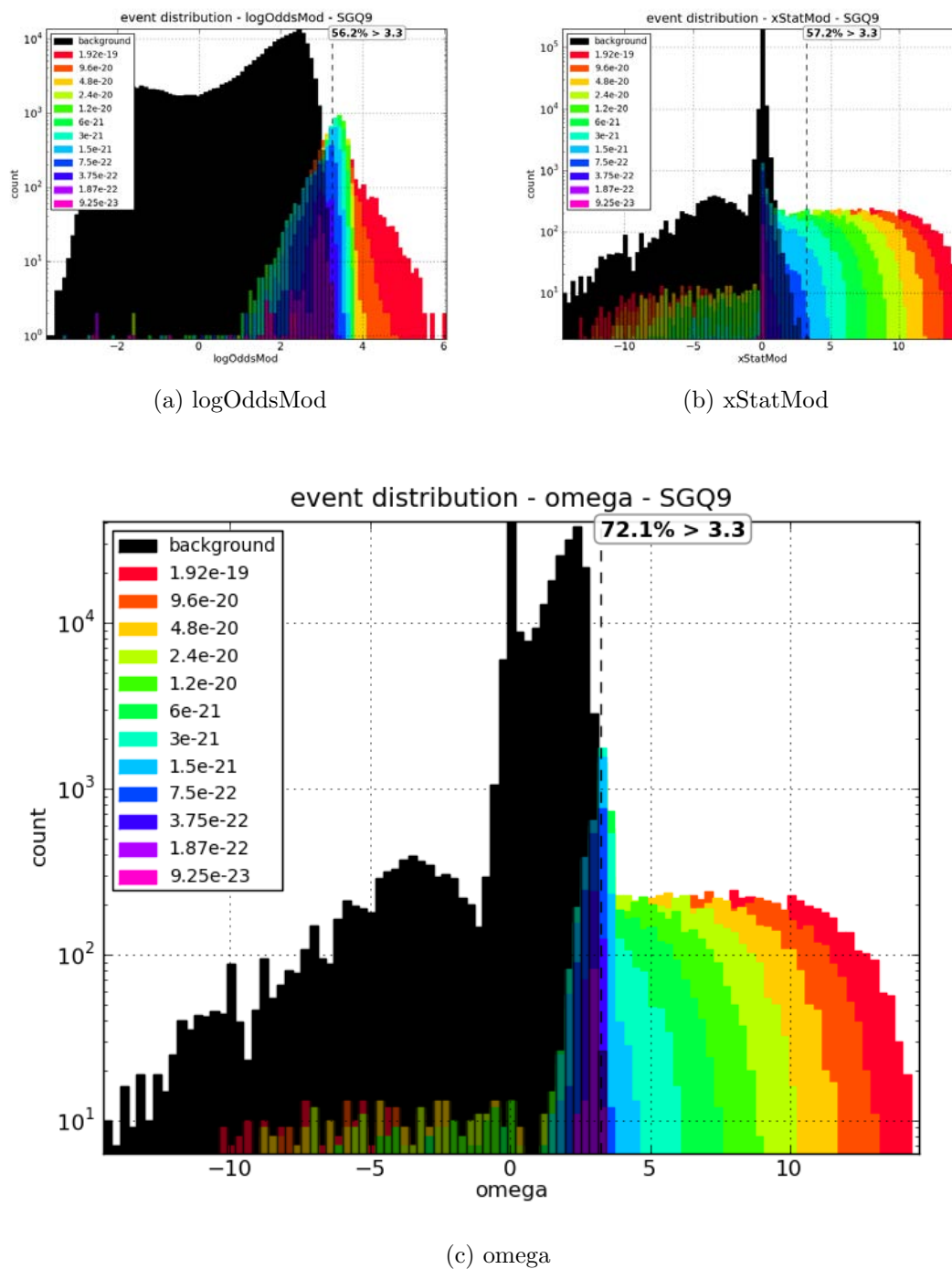
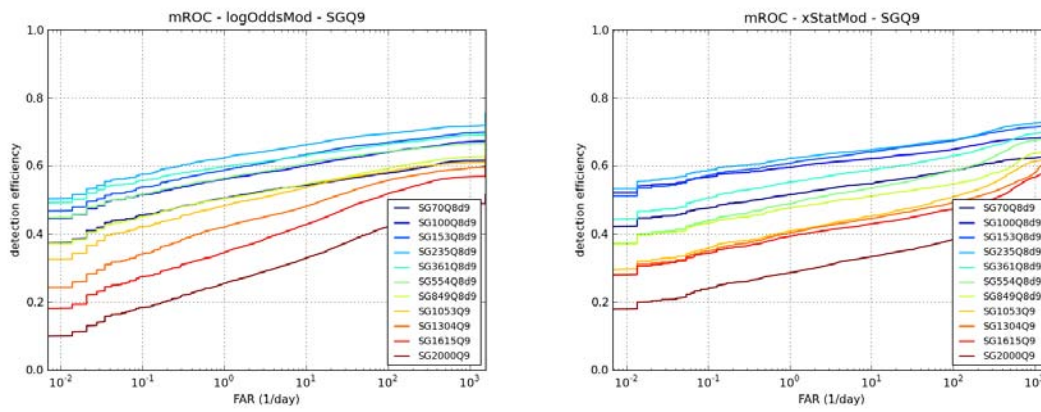
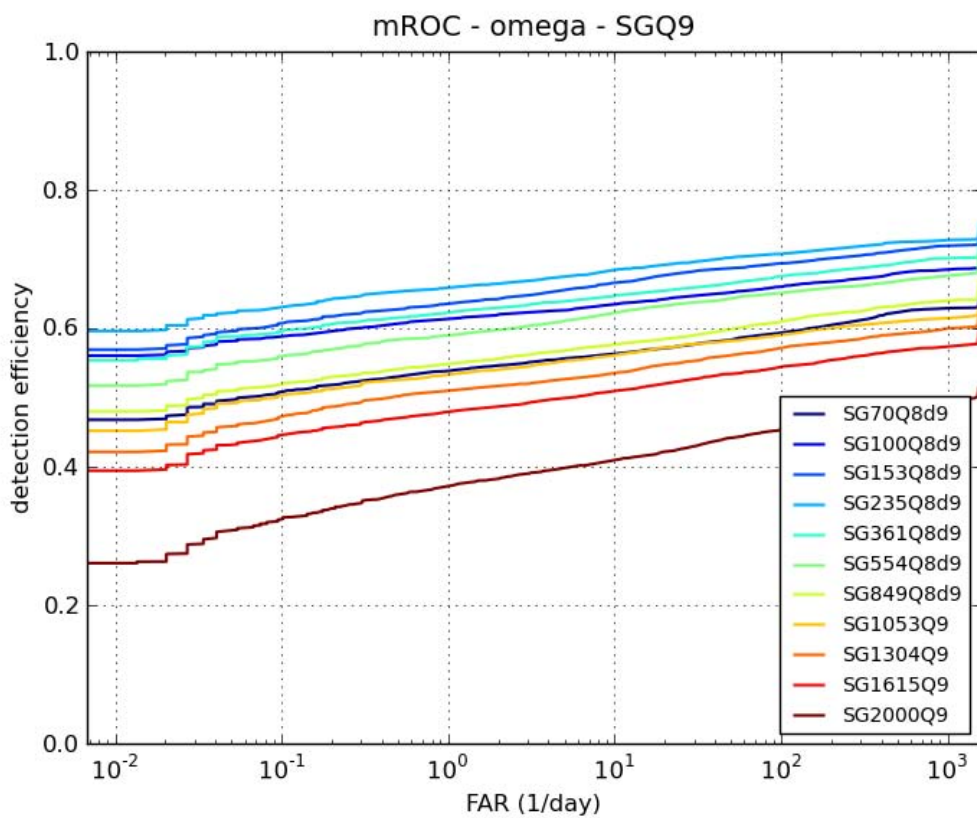


Figure A-32: SGQ9 injections histograms. Colors represent injection strain amplitude.



(a) logOddsMod

(b) xStatMod



(c) omega

Figure A-33: SGQ9 ROC plots

A.3.1 SG70Q8d9 injections

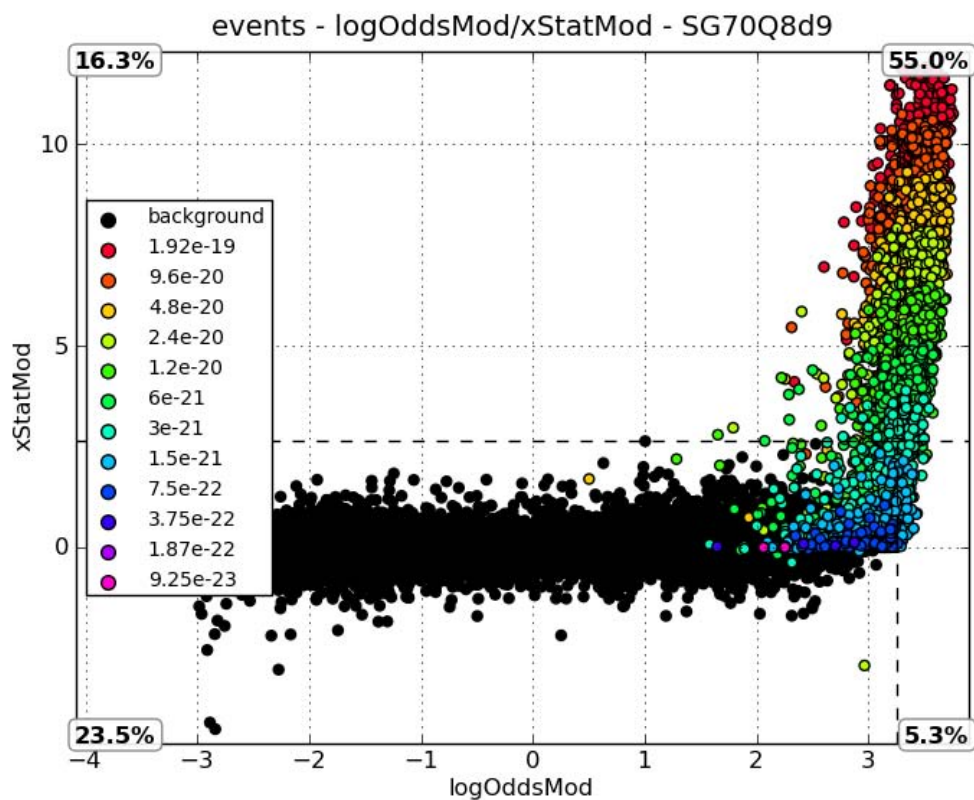


Figure A-34: SG70Q8d9 injections scatter plot. Colors represent injection strain amplitude.

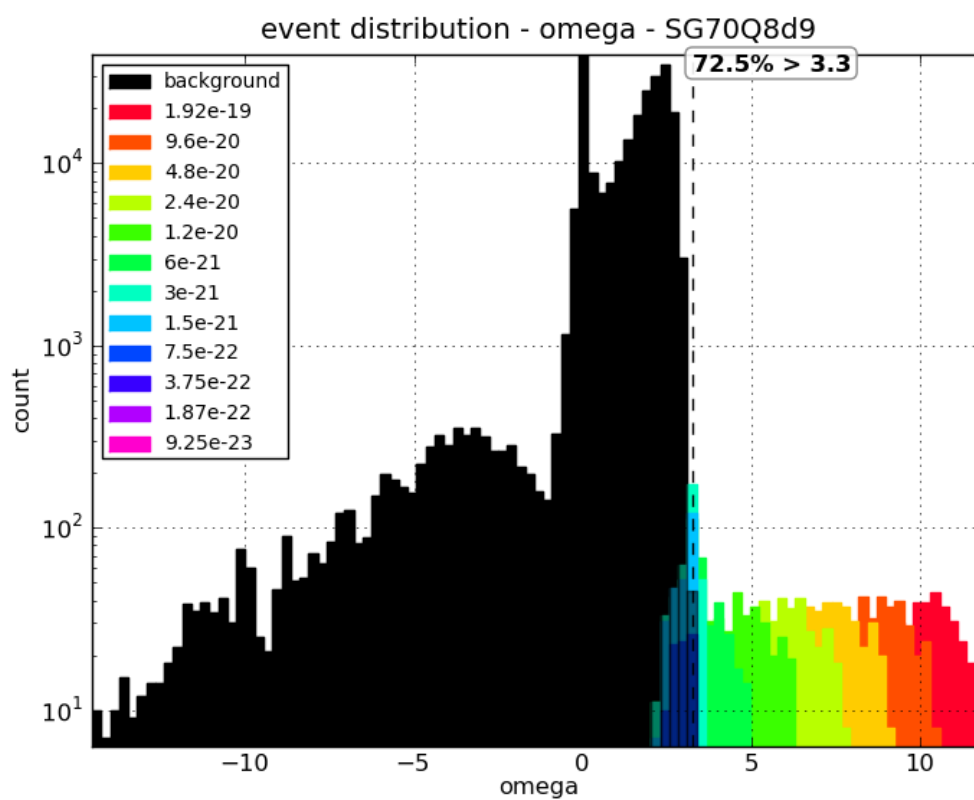
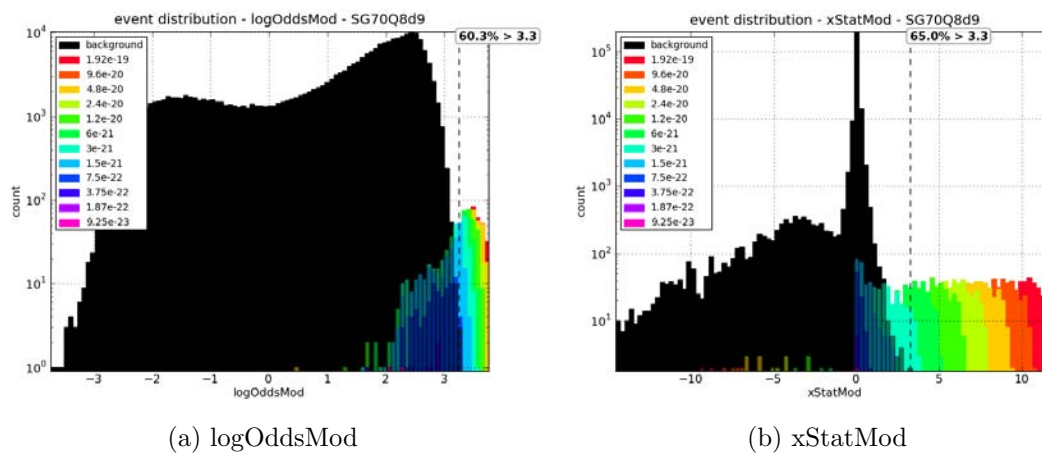


Figure A-35: SG70Q8d9 injections histograms. Colors represent injection strain amplitude.

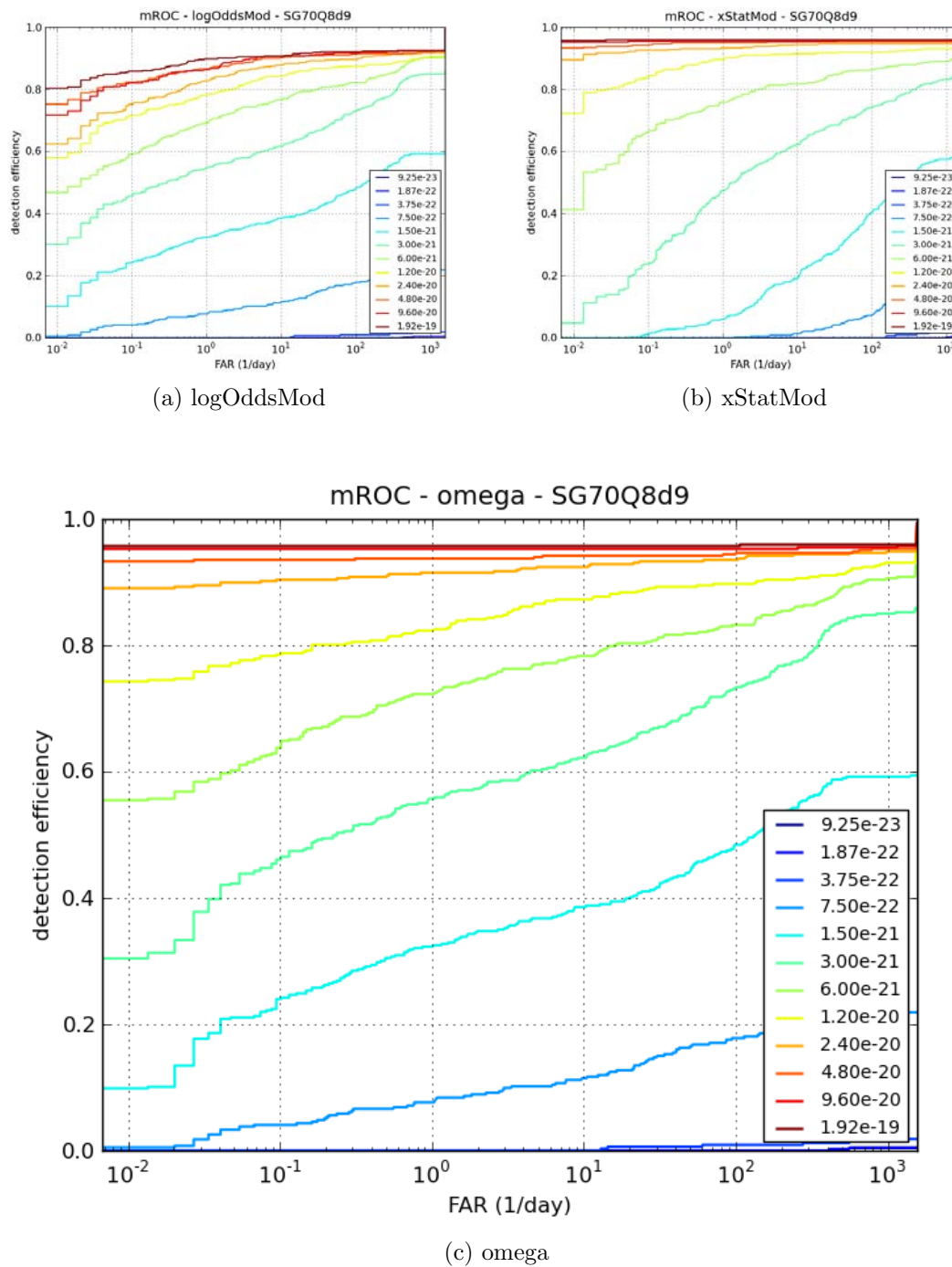


Figure A-36: SG70Q8d9 ROC plots

A.3.2 SG100Q8d9 injections

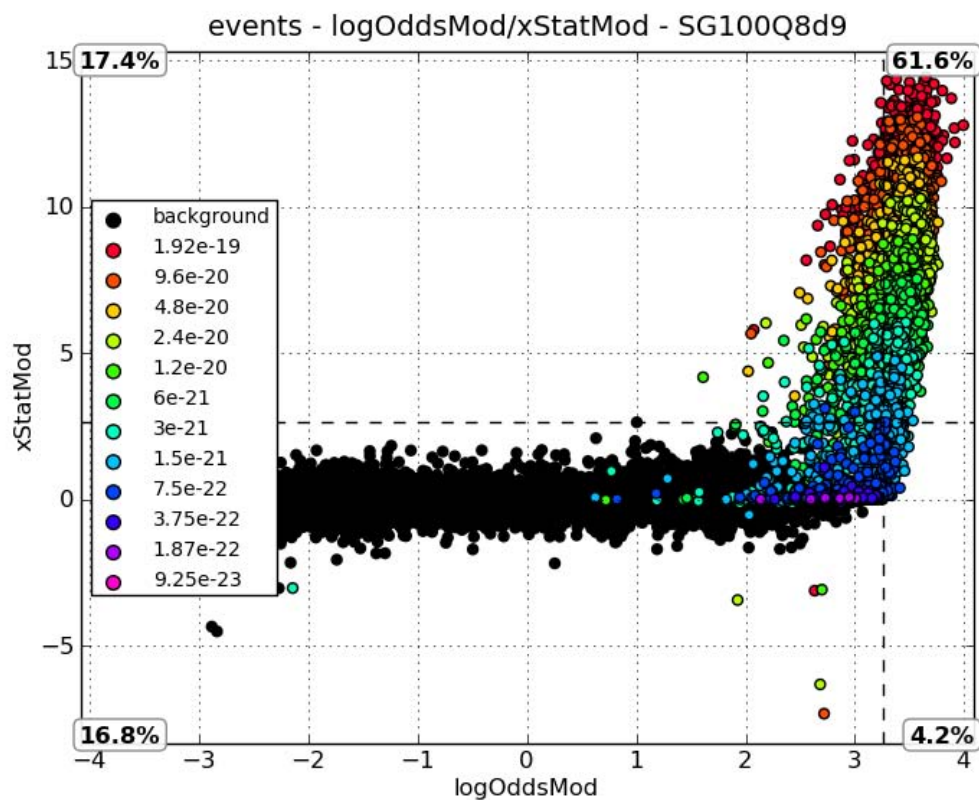


Figure A-37: SG100Q8d9 injections scatter plot. Colors represent injection strain amplitude.

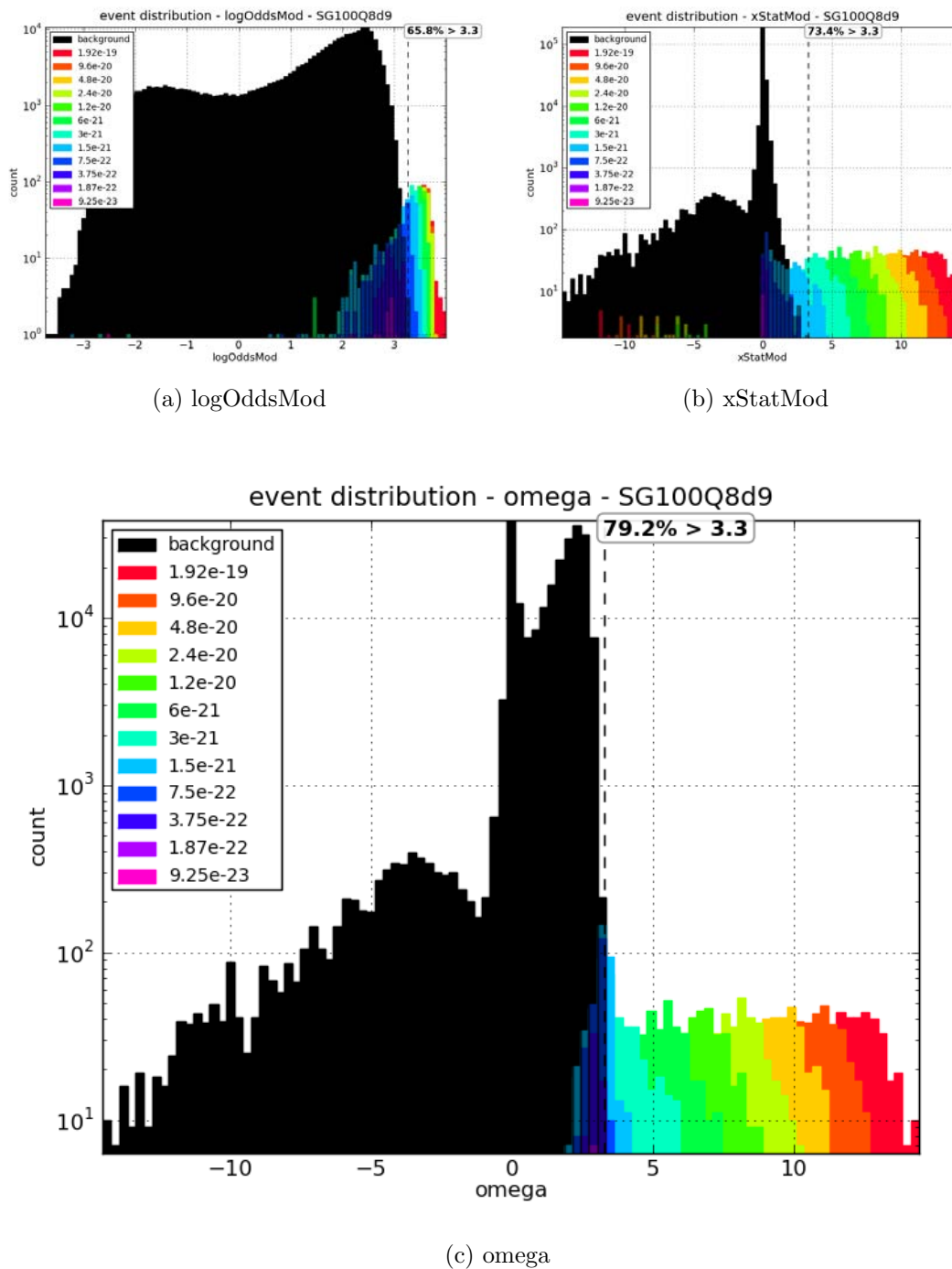
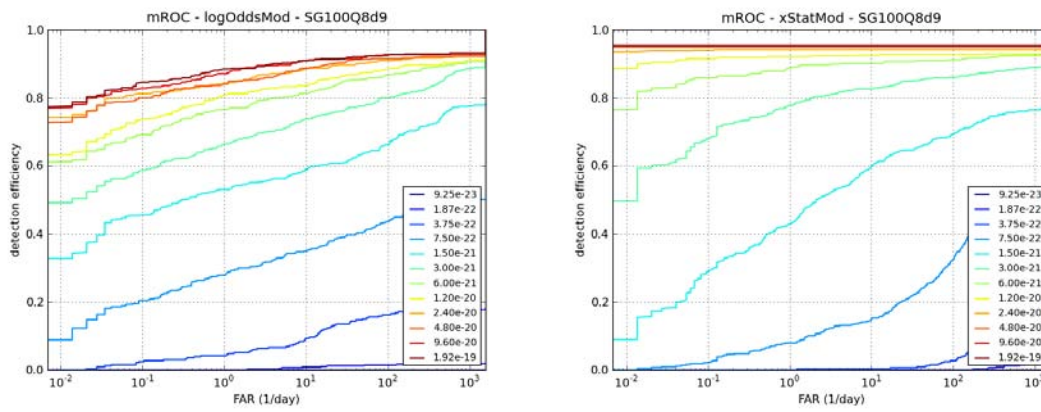
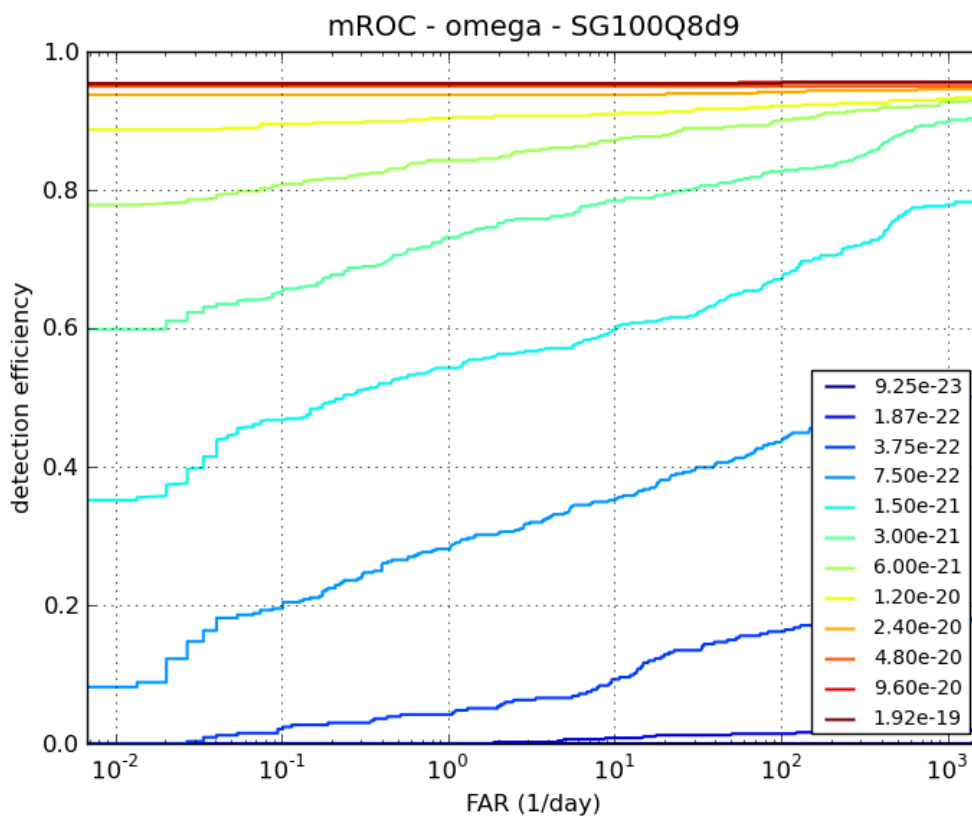


Figure A-38: SG100Q8d9 injections histograms. Colors represent injection strain amplitude.



(a) logOddsMod

(b) xStatMod



(c) omega

Figure A-39: SG100Q8d9 ROC plots

A.3.3 SG153Q8d9 injections

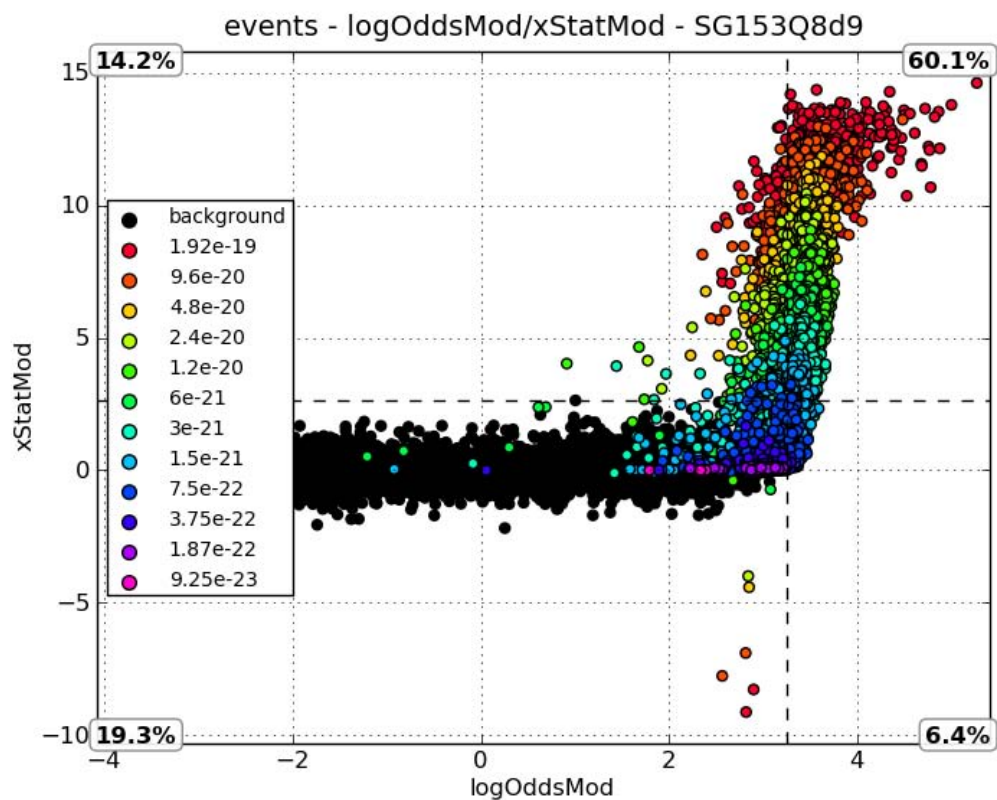


Figure A-40: SG153Q8d9 injections scatter plot. Colors represent injection strain amplitude.

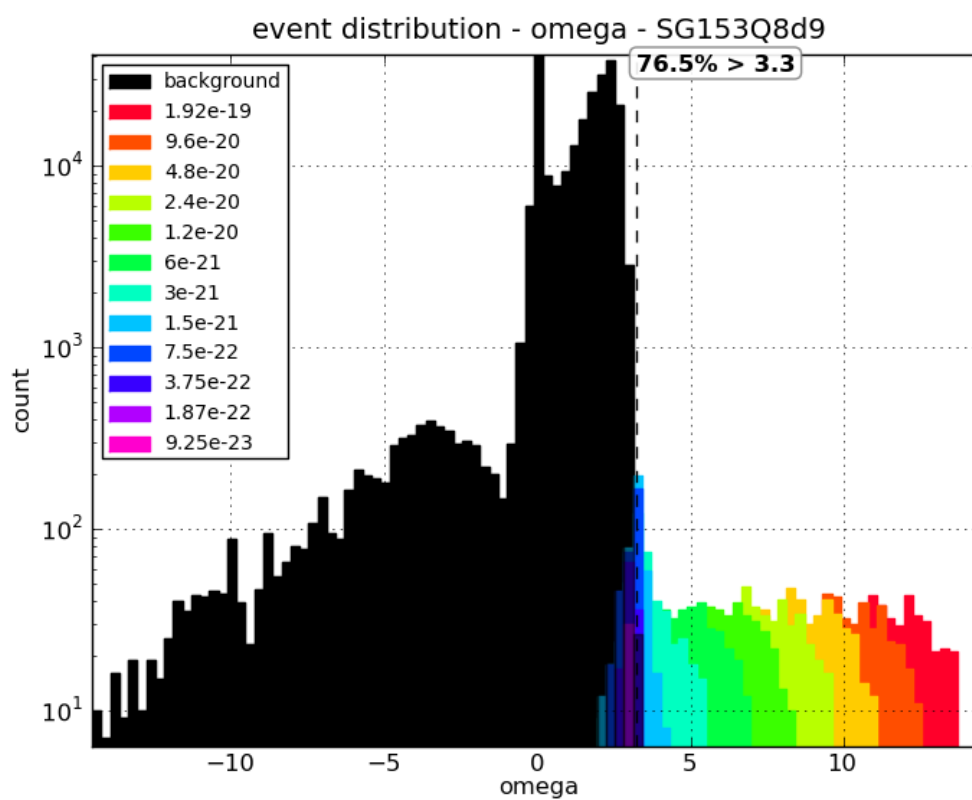
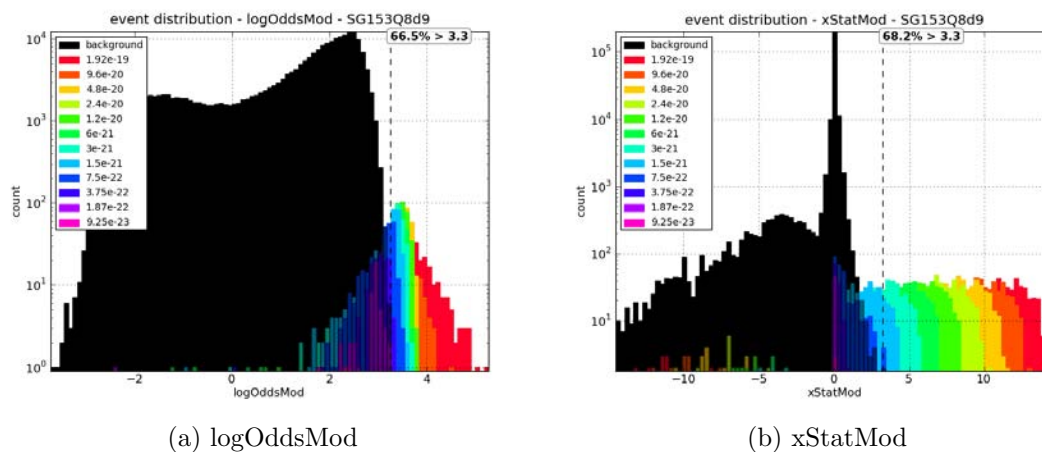
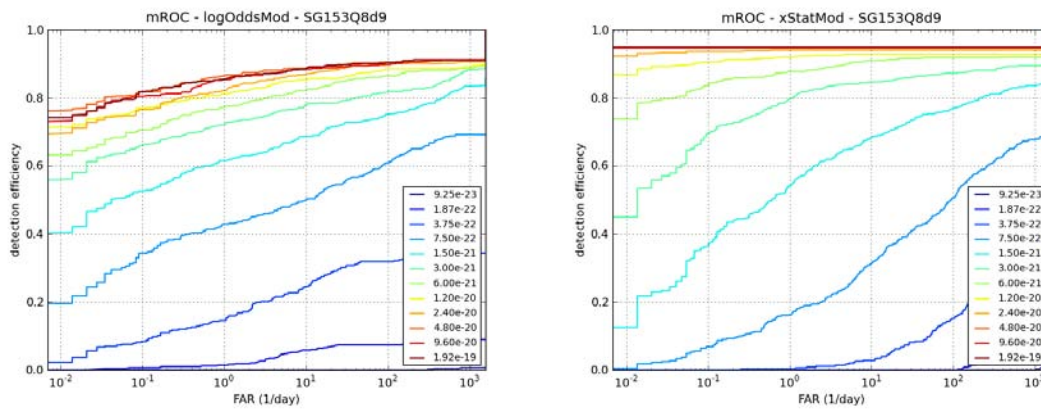
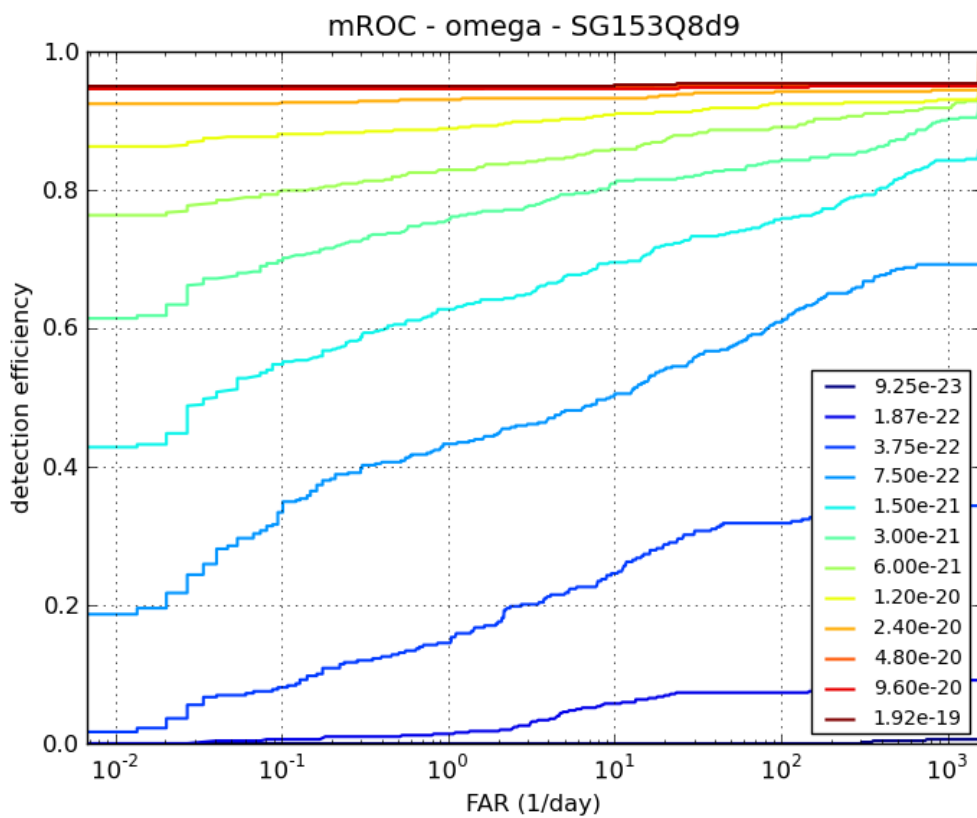


Figure A-41: SG153Q8d9 injections histograms. Colors represent injection strain amplitude.



(a) logOddsMod

(b) xStatMod



(c) omega

Figure A-42: SG153Q8d9 ROC plots

A.3.4 SG235Q8d9 injections

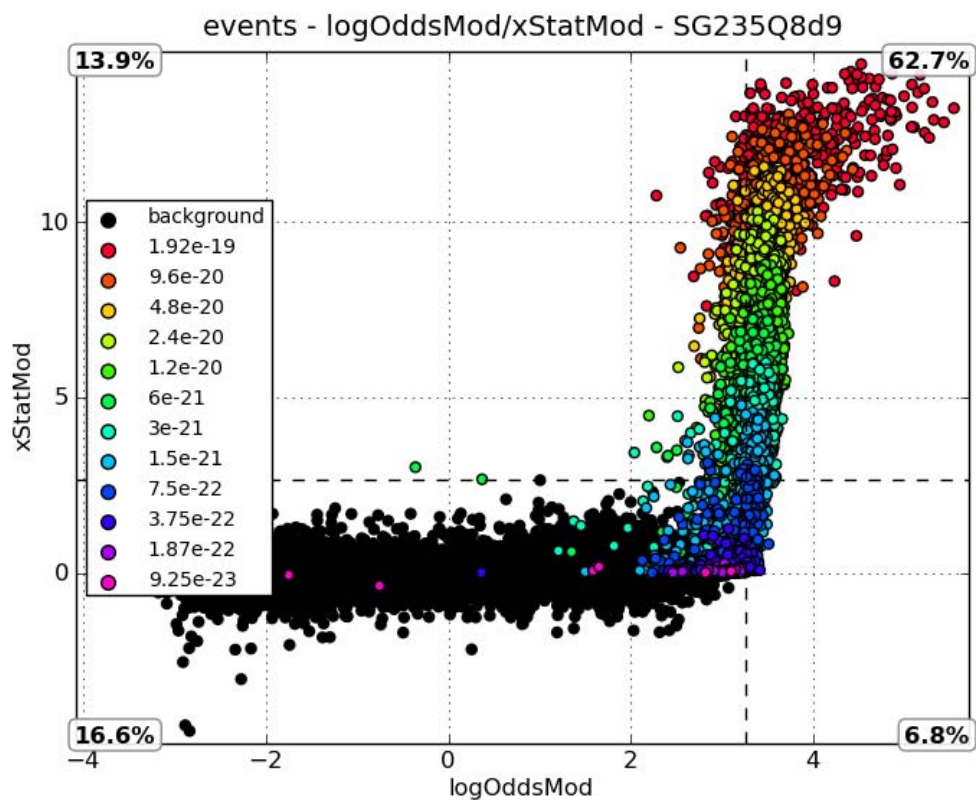


Figure A-43: SG235Q8d9 injections scatter plot. Colors represent injection strain amplitude.

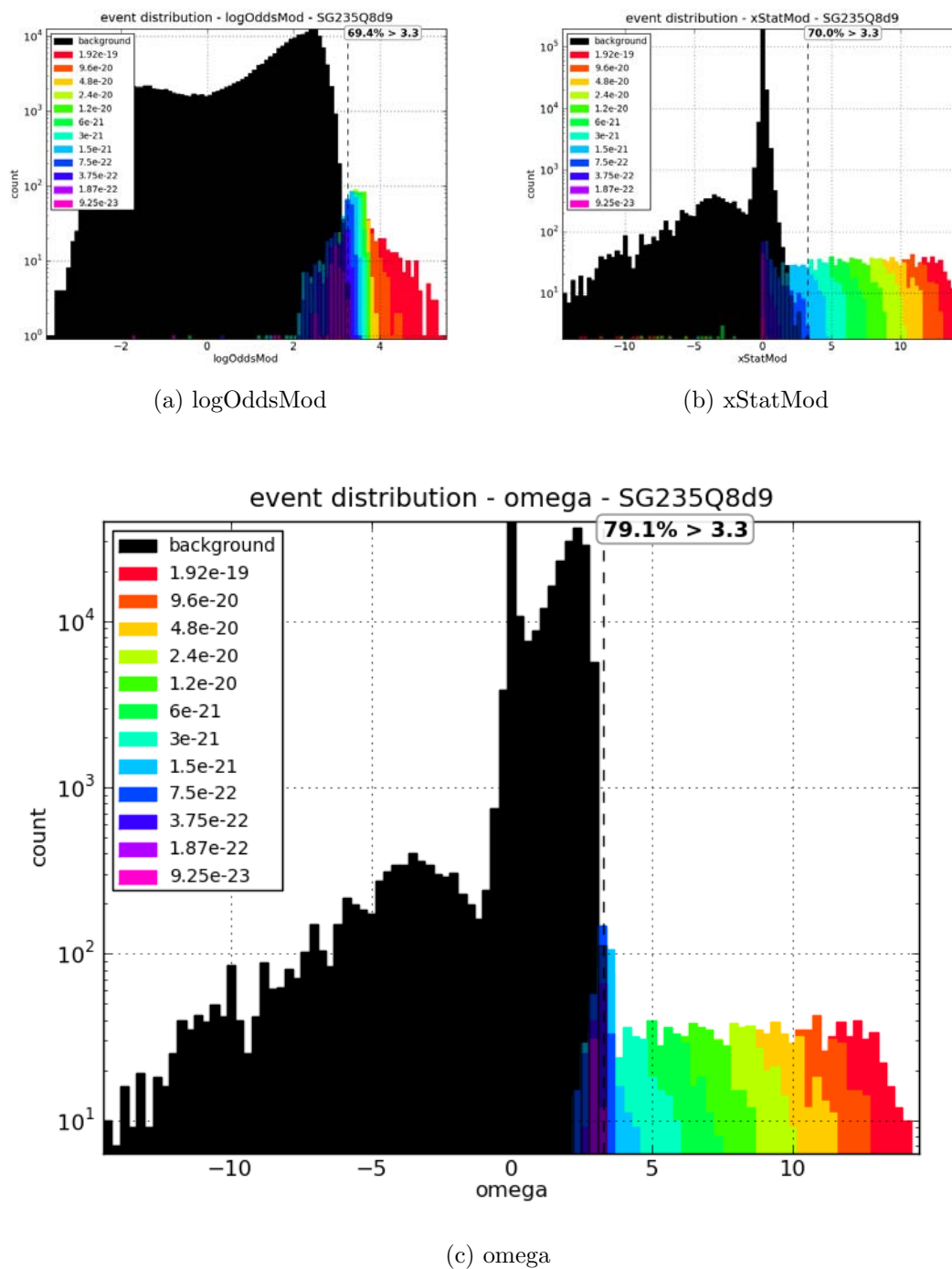


Figure A-44: SG235Q8d9 injections histograms. Colors represent injection strain amplitude.

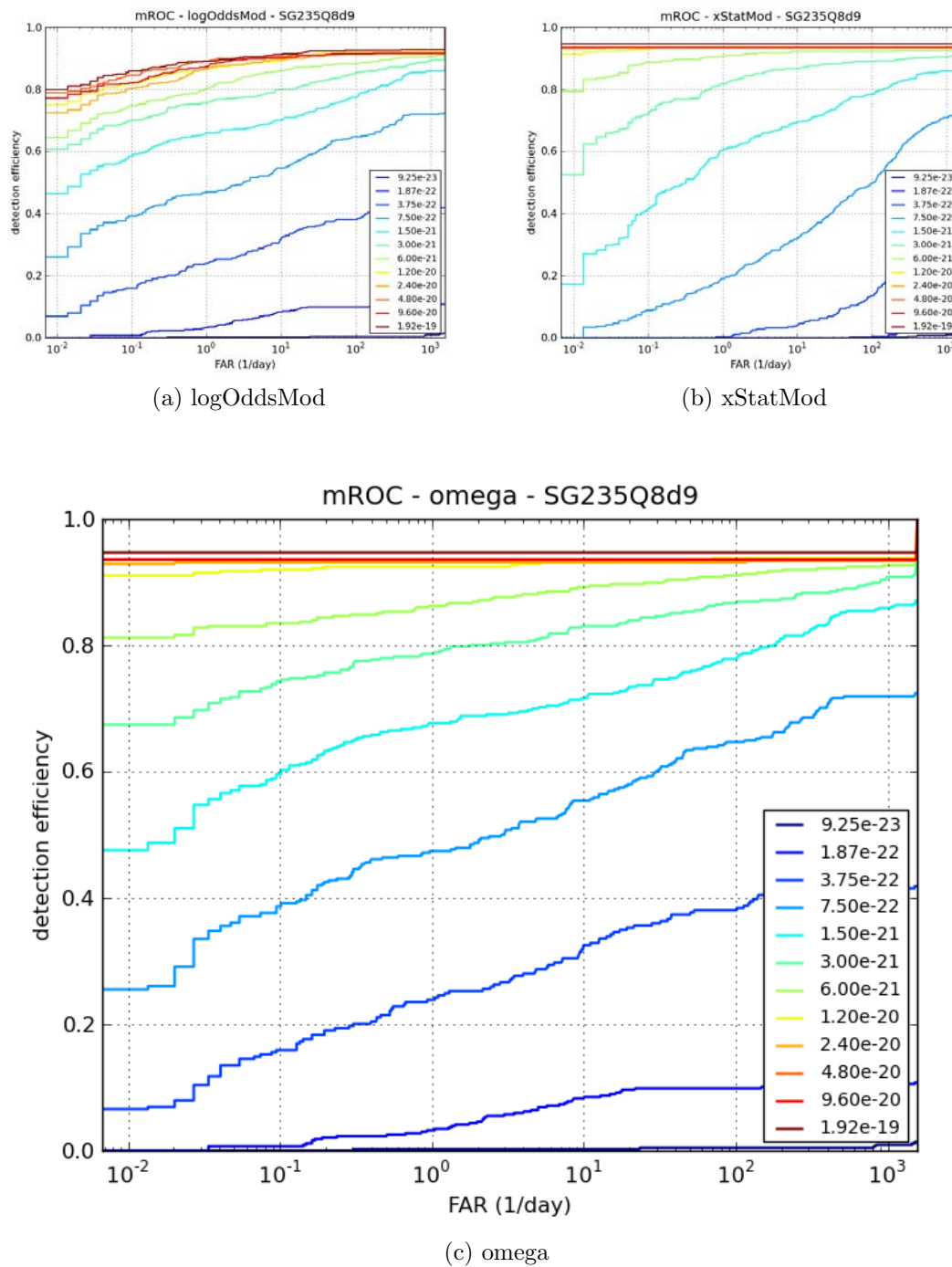


Figure A-45: SG235Q8d9 ROC plots

A.3.5 SG361Q8d9 injections

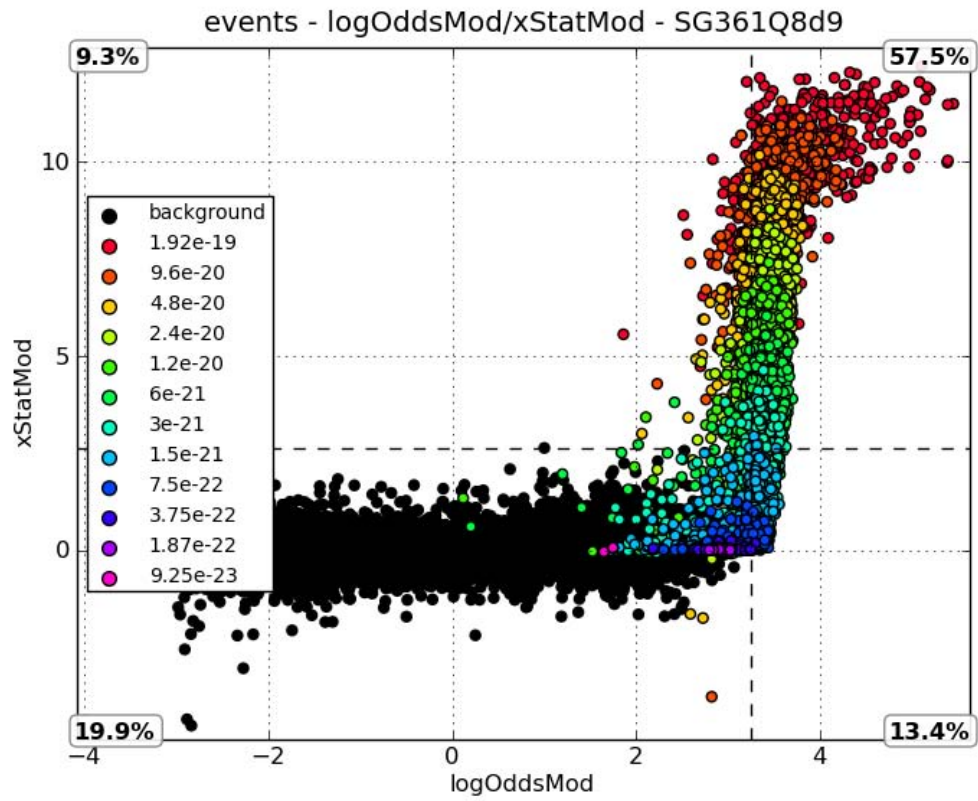


Figure A-46: SG361Q8d9 injections scatter plot. Colors represent injection strain amplitude.

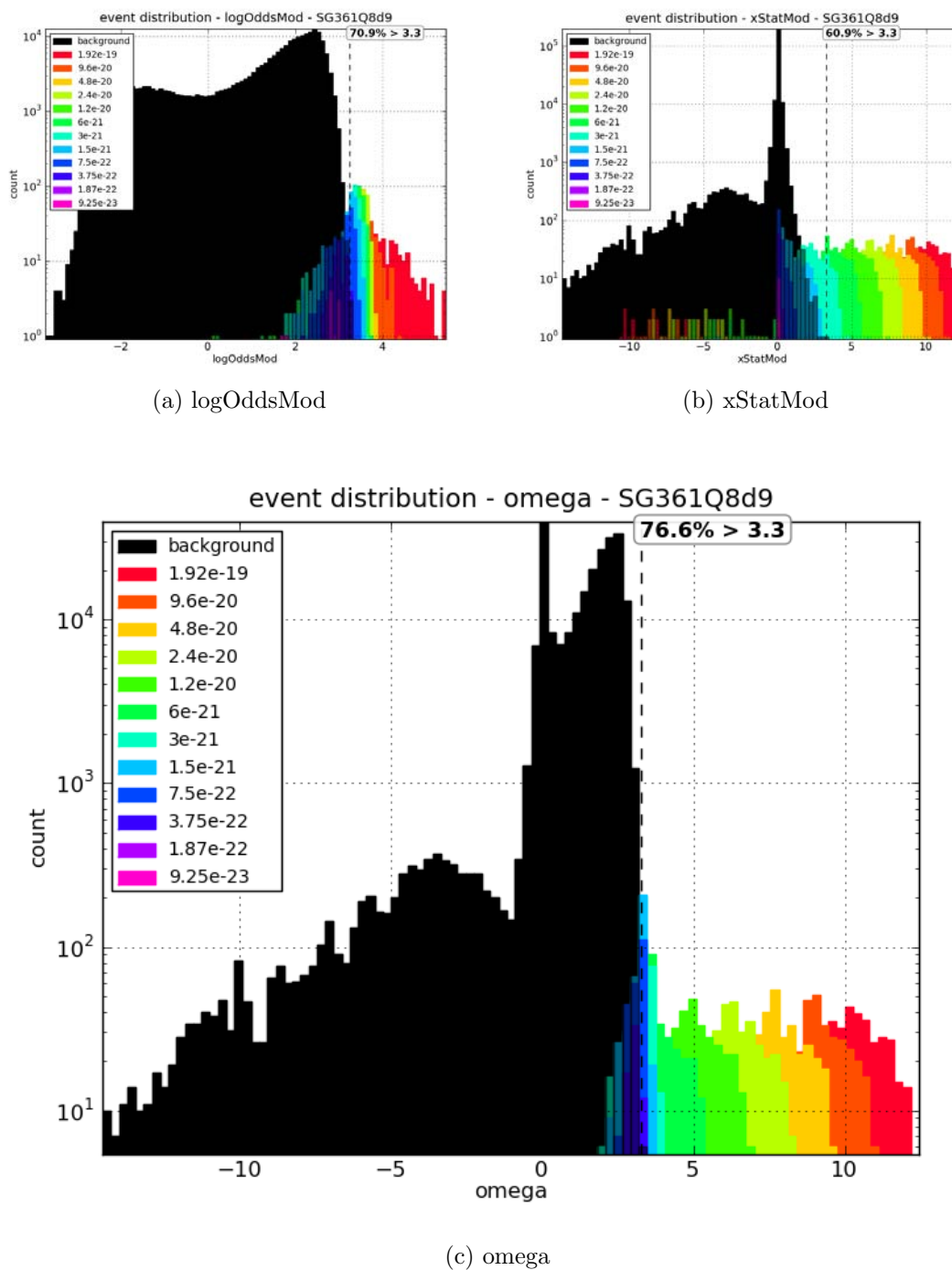
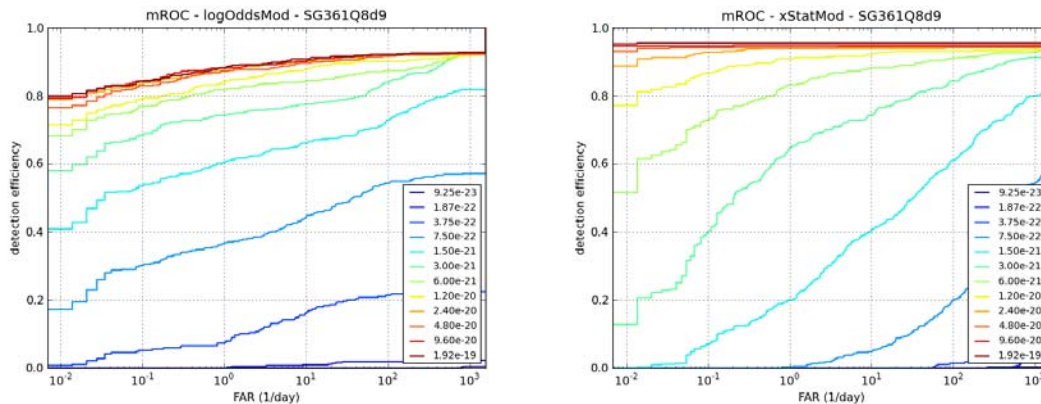
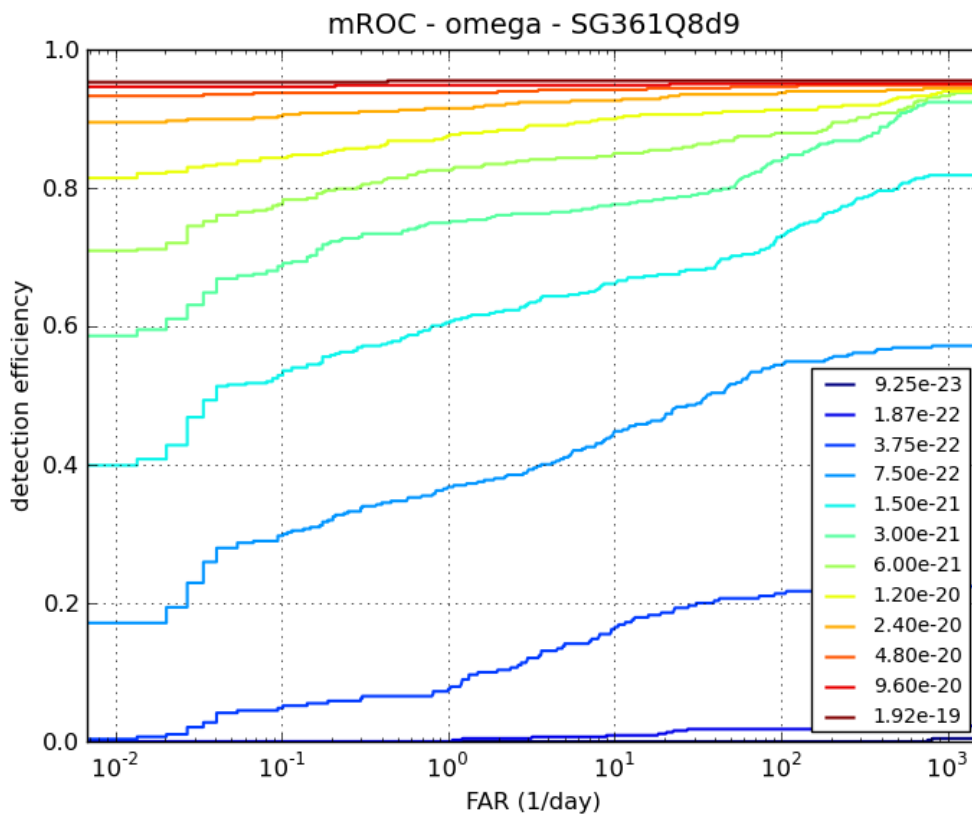


Figure A-47: SG361Q8d9 injections histograms. Colors represent injection strain amplitude.



(a) logOddsMod

(b) xStatMod



(c) omega

Figure A-48: SG361Q8d9 ROC plots

A.3.6 SG554Q8d9 injections

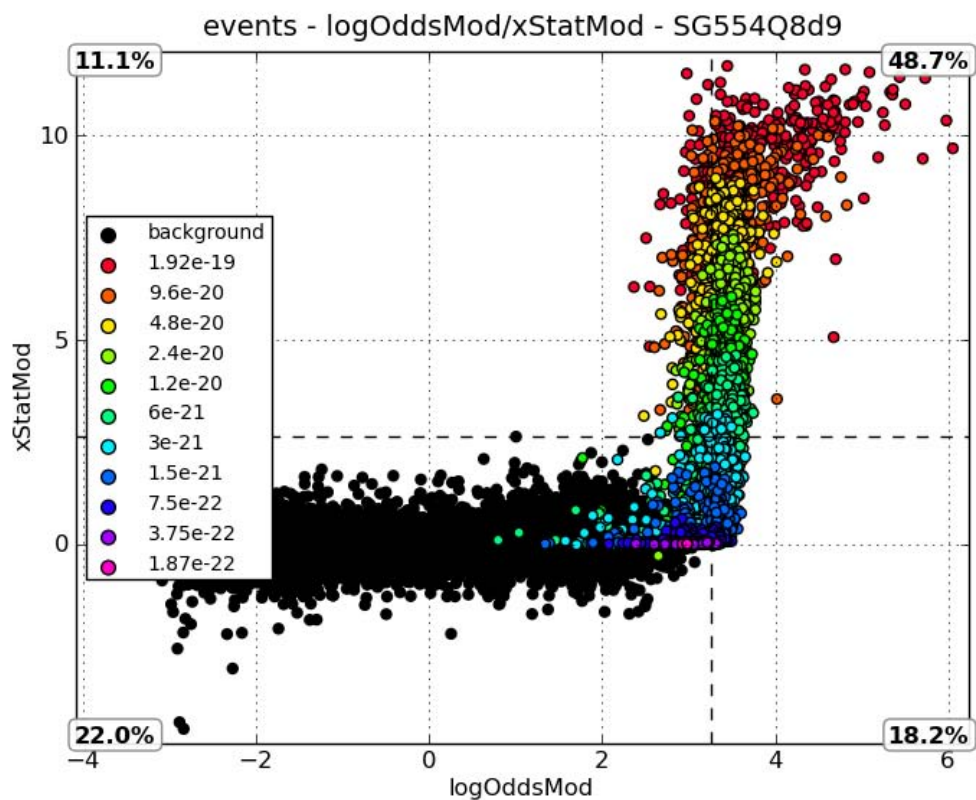
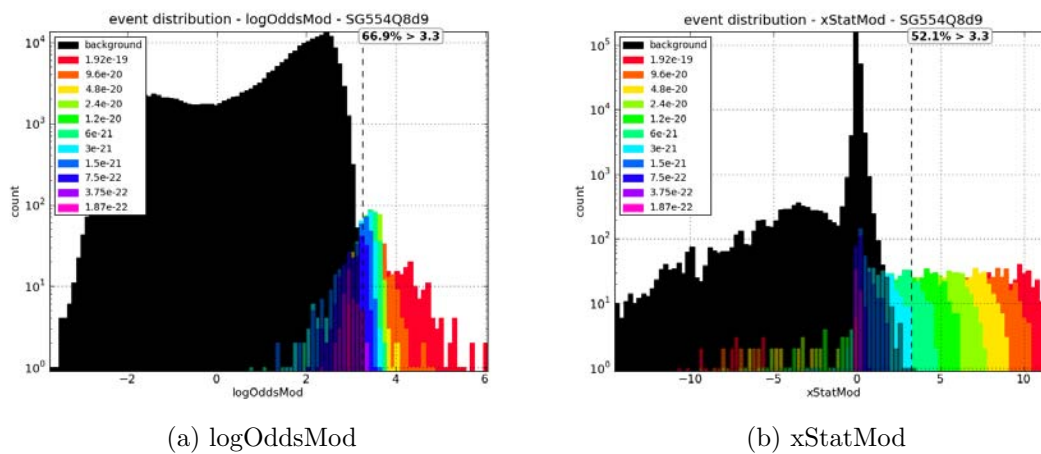
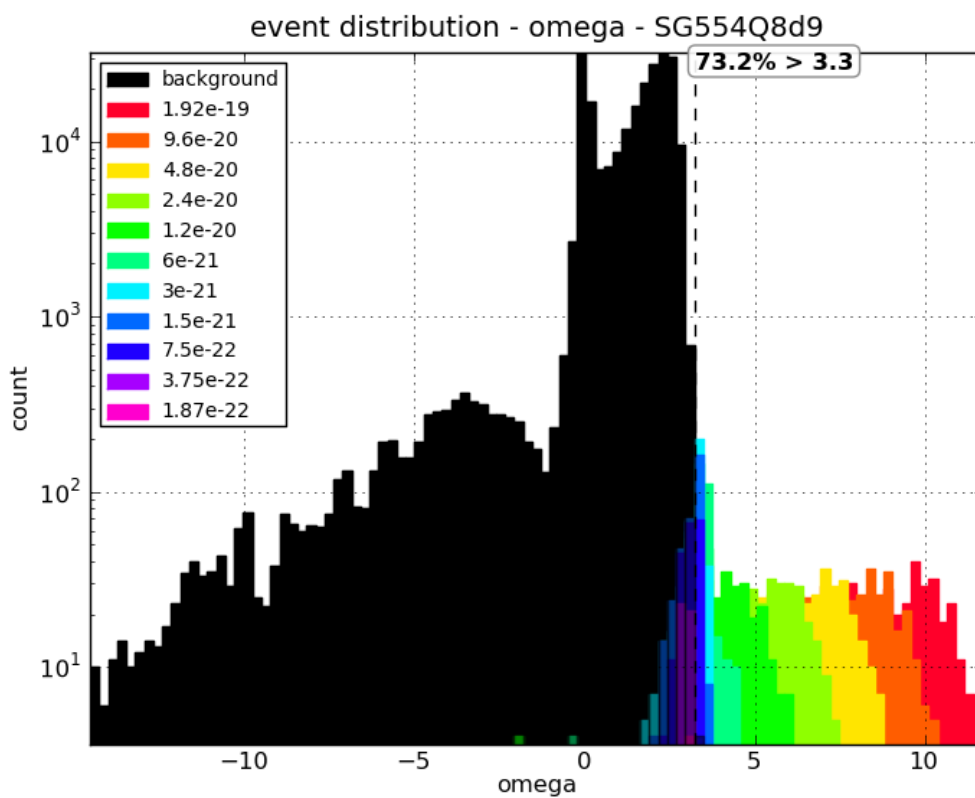


Figure A-49: SG554Q8d9 injections scatter plot. Colors represent injection strain amplitude.



(a) logOddsMod

(b) xStatMod



(c) omega

Figure A-50: SG554Q8d9 injections histograms. Colors represent injection strain amplitude.

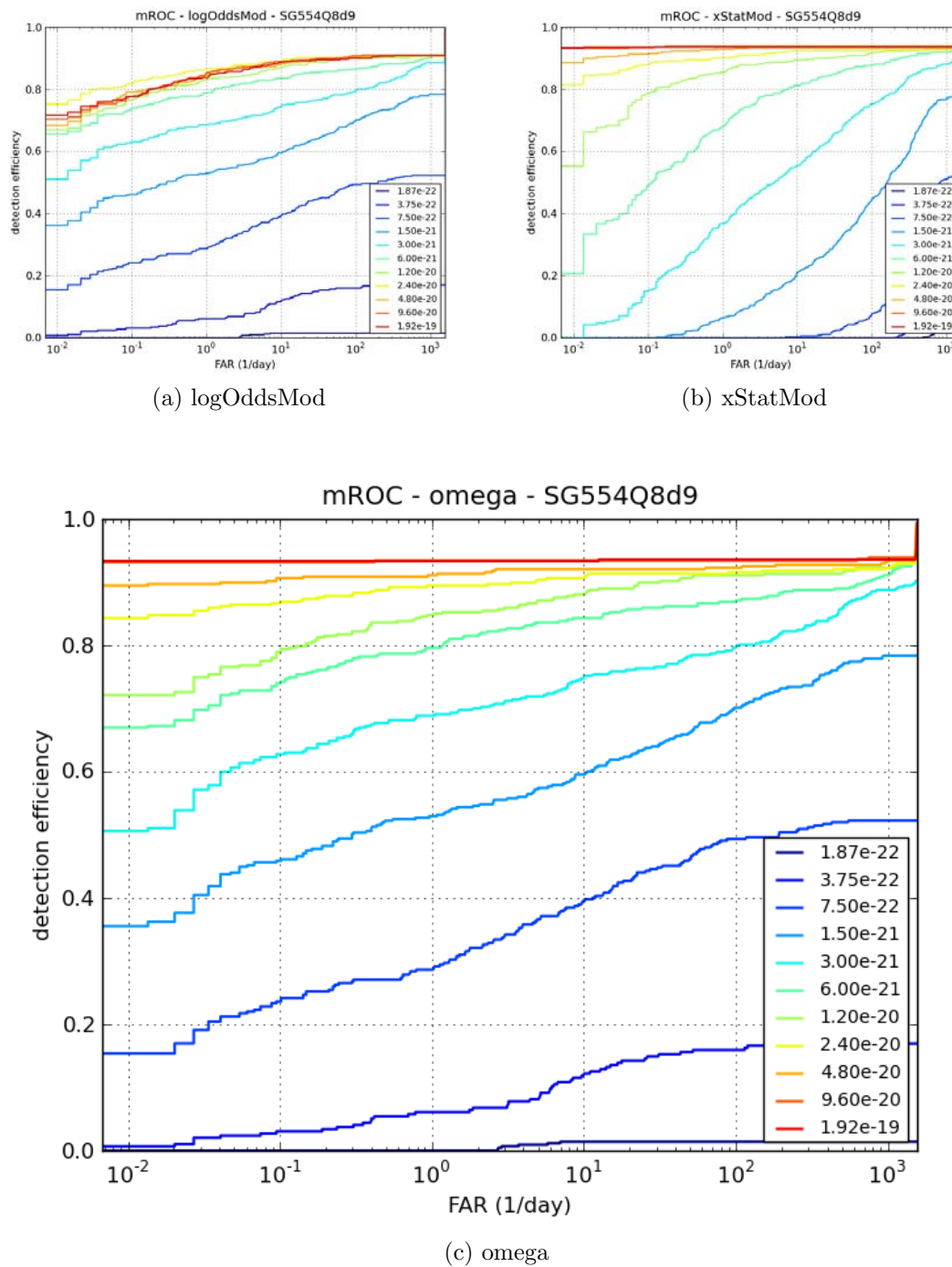


Figure A-51: SG554Q8d9 ROC plots

A.3.7 SG849Q8d9 injections

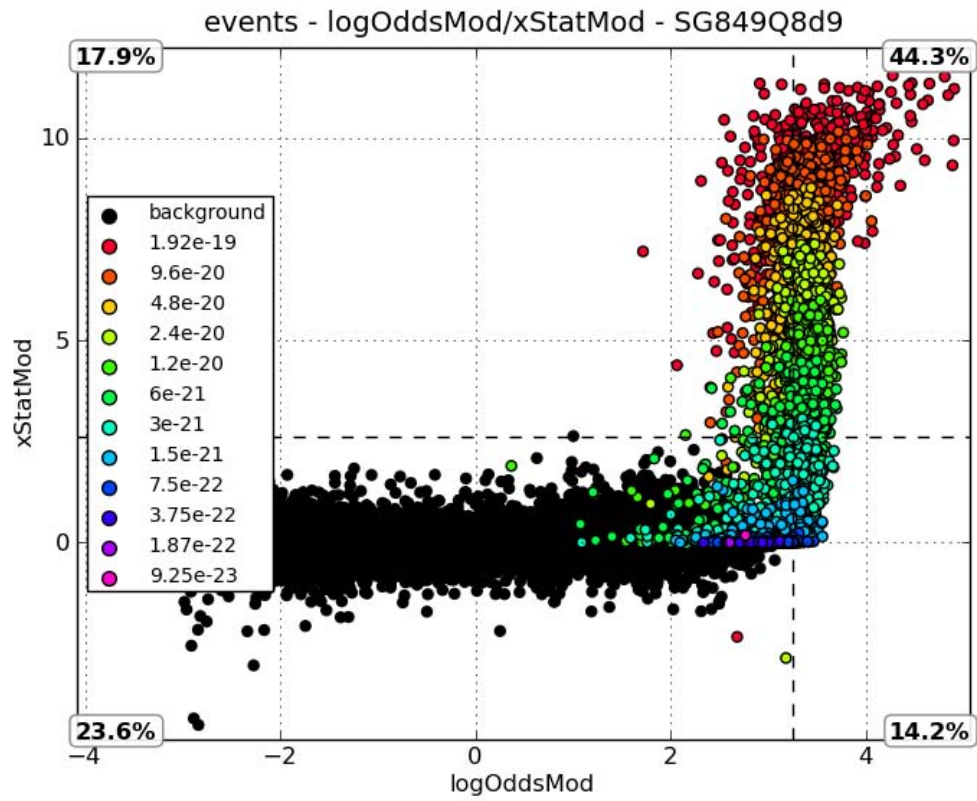
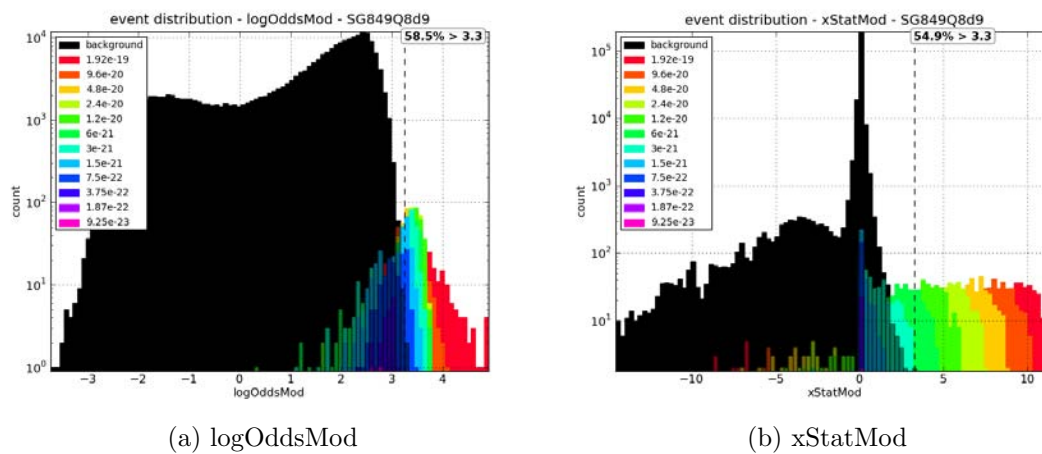
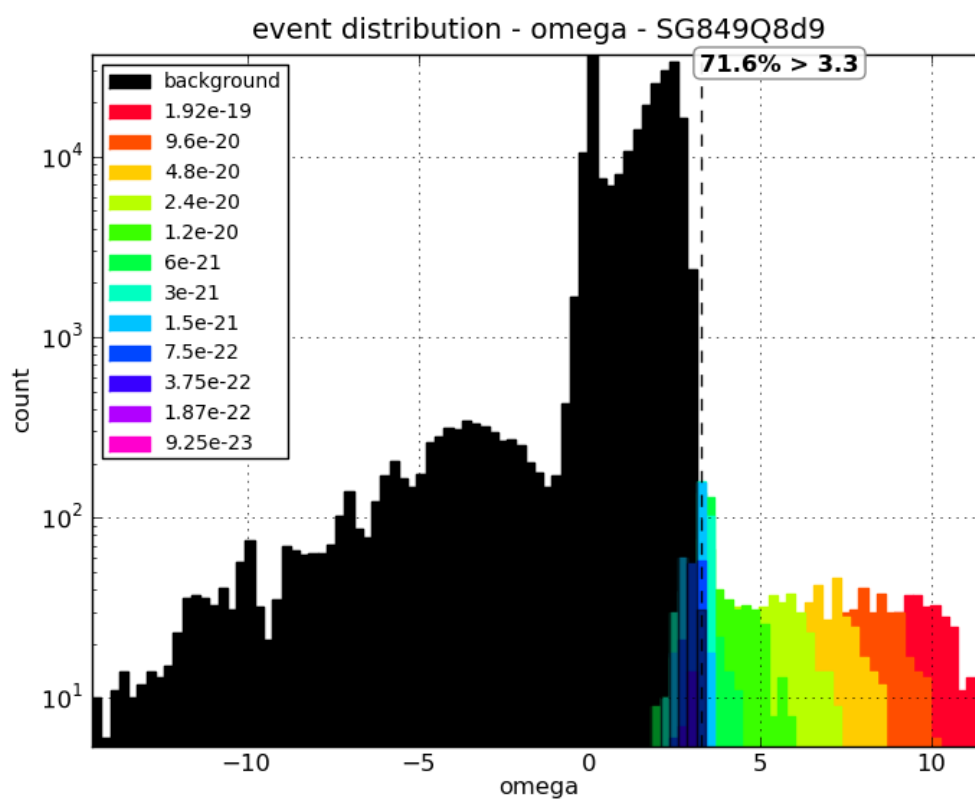


Figure A-52: SG849Q8d9 injections scatter plot. Colors represent injection strain amplitude.



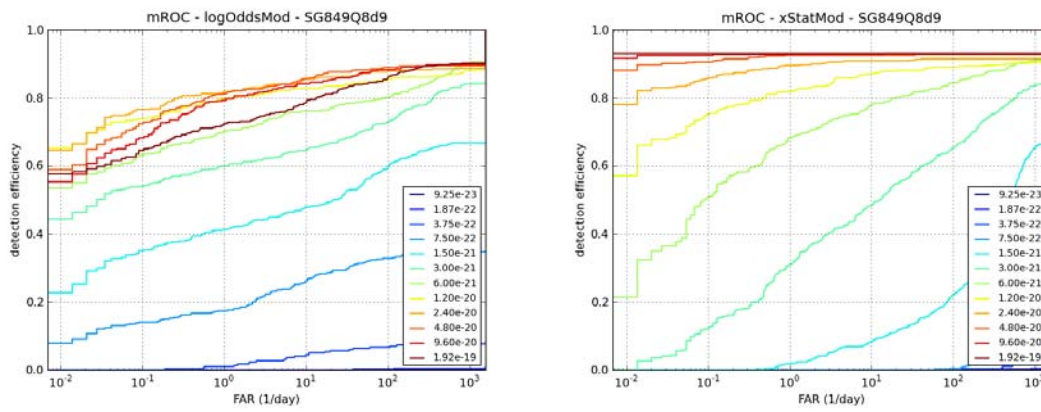
(a) logOddsMod

(b) xStatMod



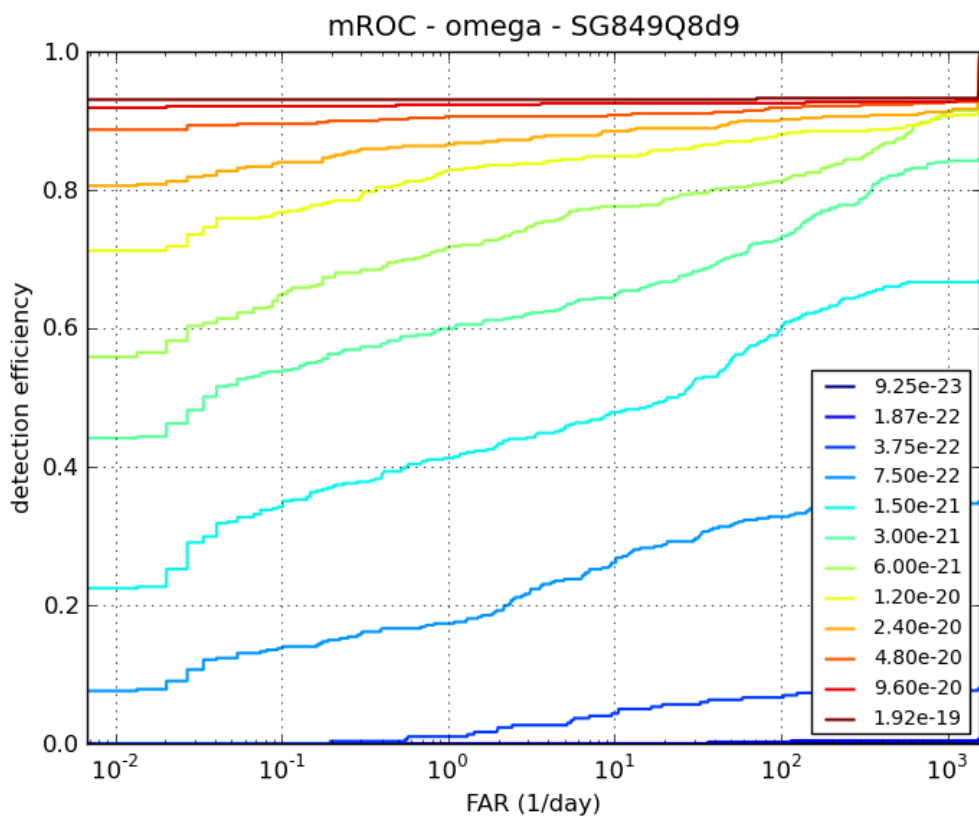
(c) omega

Figure A-53: SG849Q8d9 injections histograms. Colors represent injection strain amplitude.



(a) logOddsMod

(b) xStatMod



(c) omega

Figure A-54: SG849Q8d9 ROC plots

A.3.8 SG1053Q9 injections

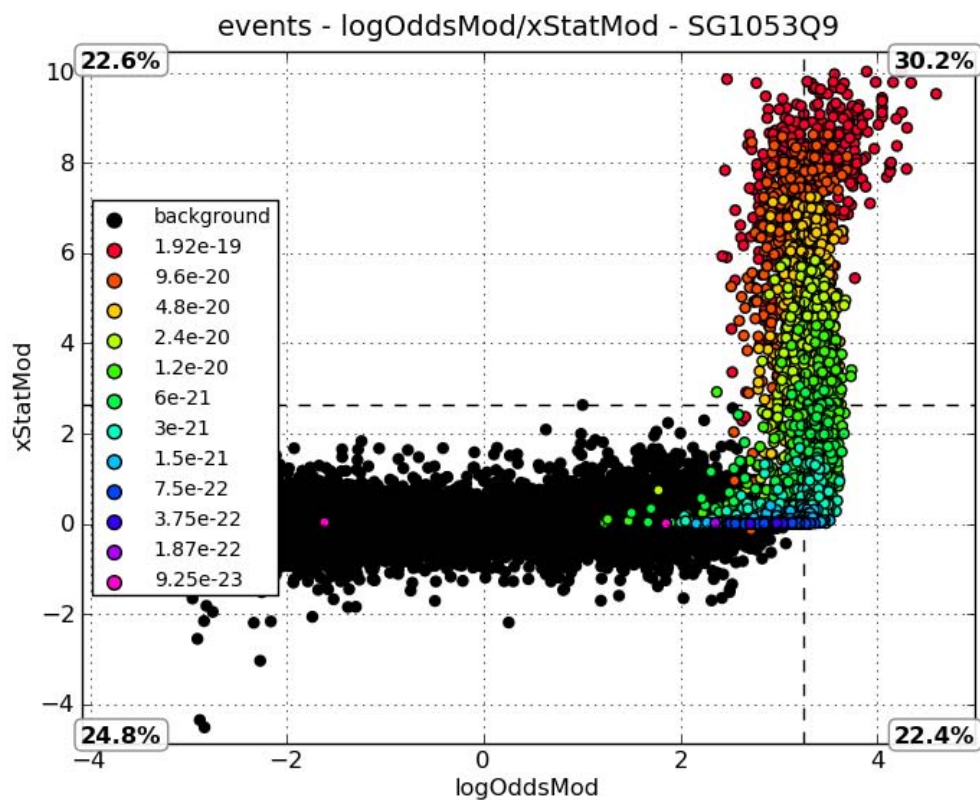


Figure A-55: SG1053Q9 injections scatter plot. Colors represent injection strain amplitude.

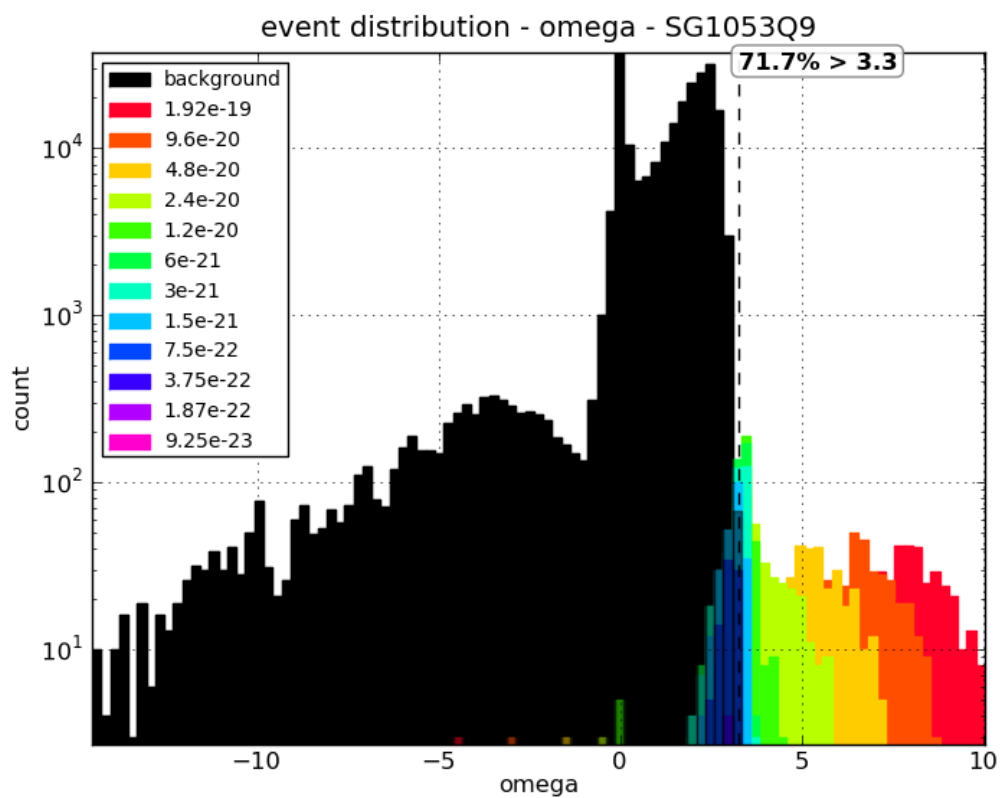
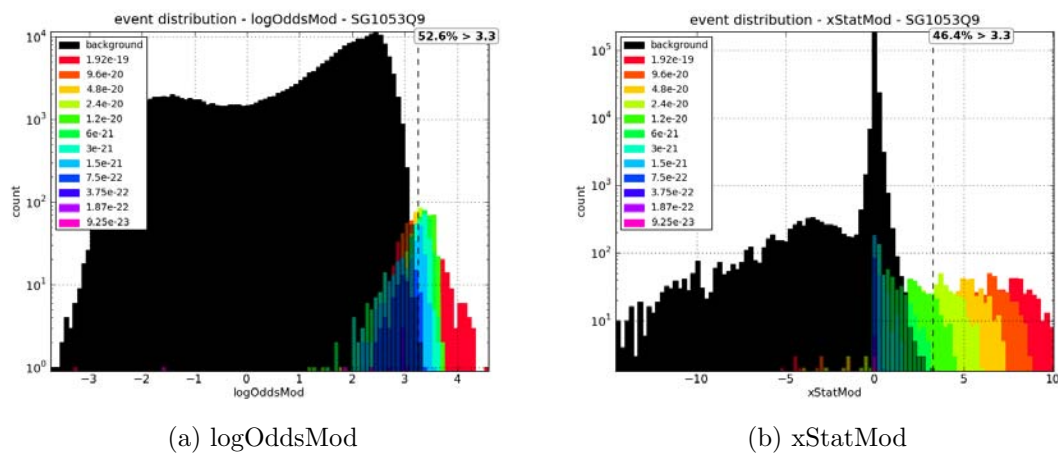


Figure A-56: SG1053Q9 injections histograms. Colors represent injection strain amplitude.

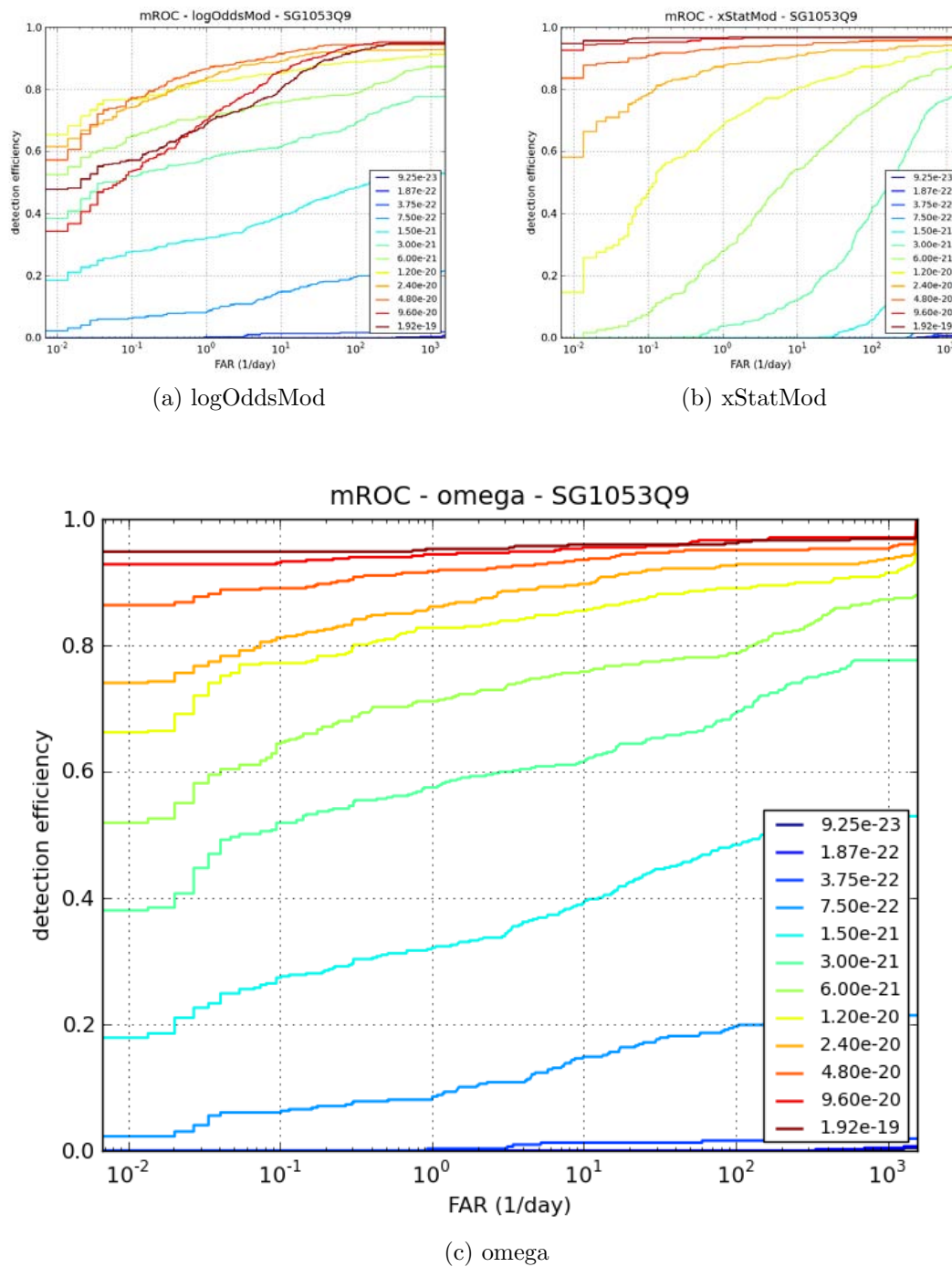


Figure A-57: SG1053Q9 ROC plots

A.3.9 SG1304Q9 injections

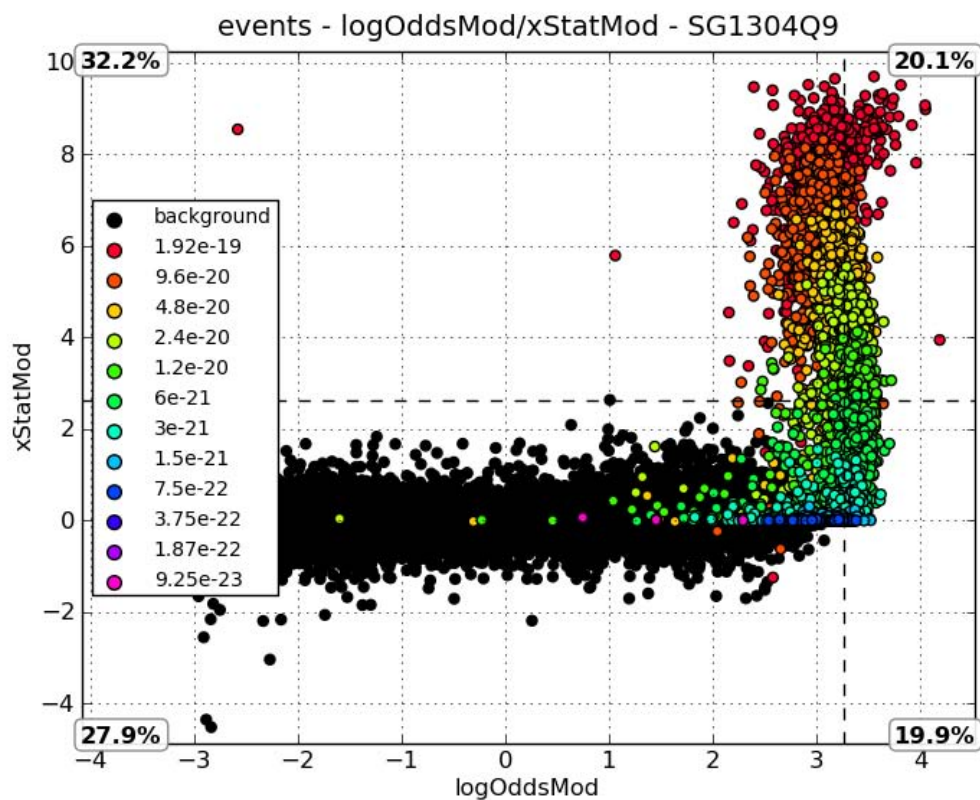
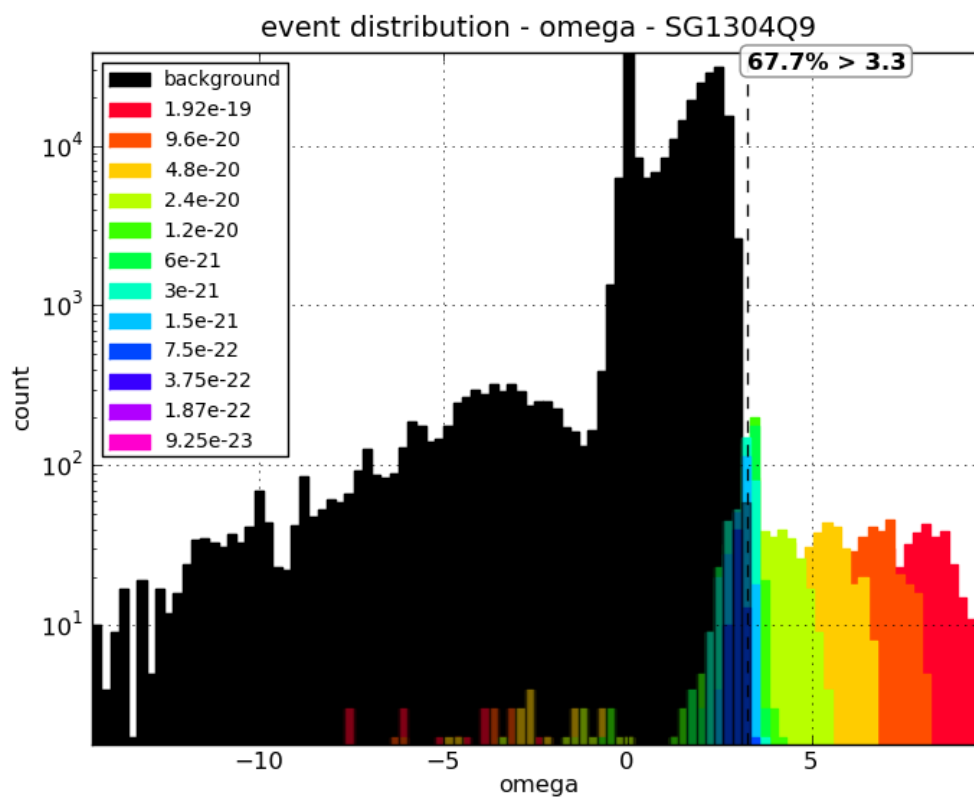
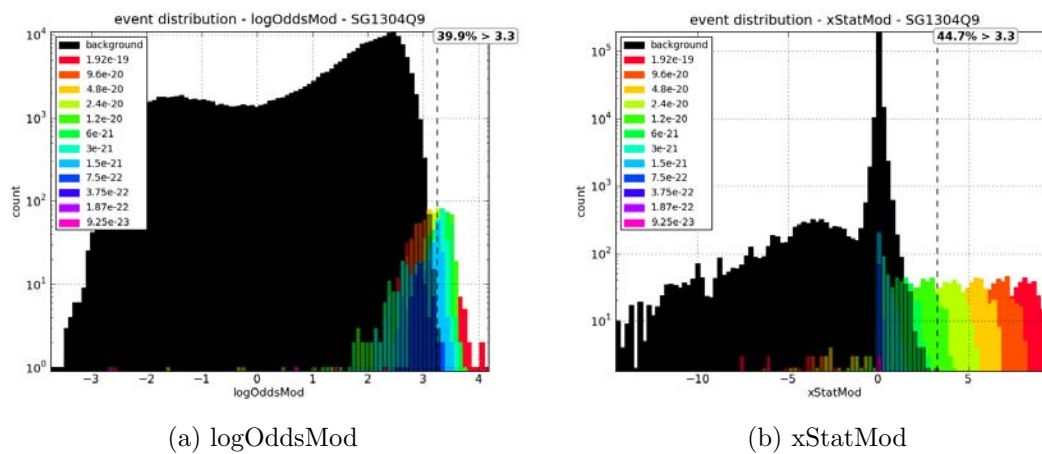


Figure A-58: SG1304Q9 injections scatter plot. Colors represent injection strain amplitude.



(c) omega

Figure A-59: SG1304Q9 injections histograms. Colors represent injection strain amplitude.

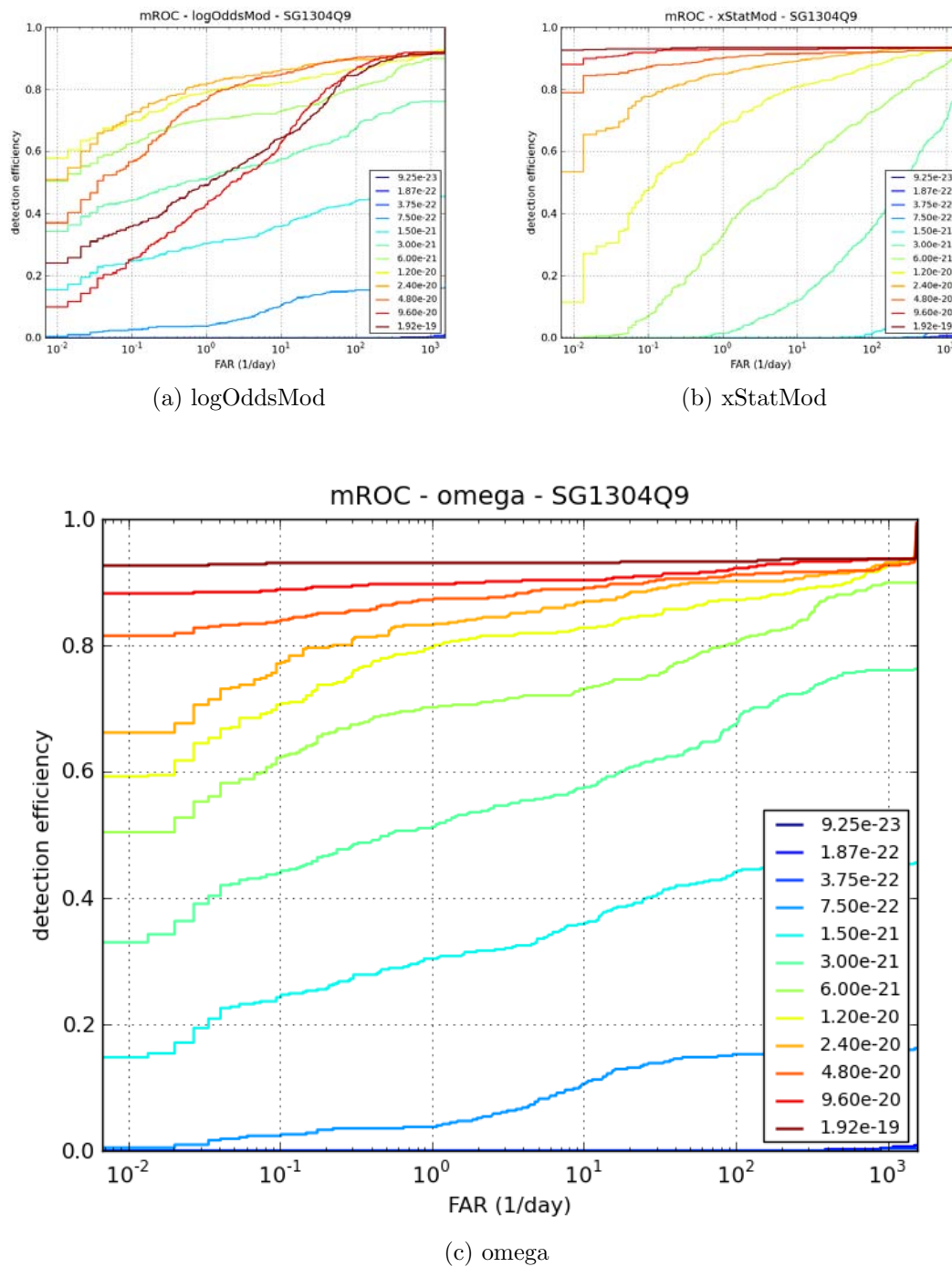


Figure A-60: SG1304Q9 ROC plots

A.3.10 SG1615Q9 injections

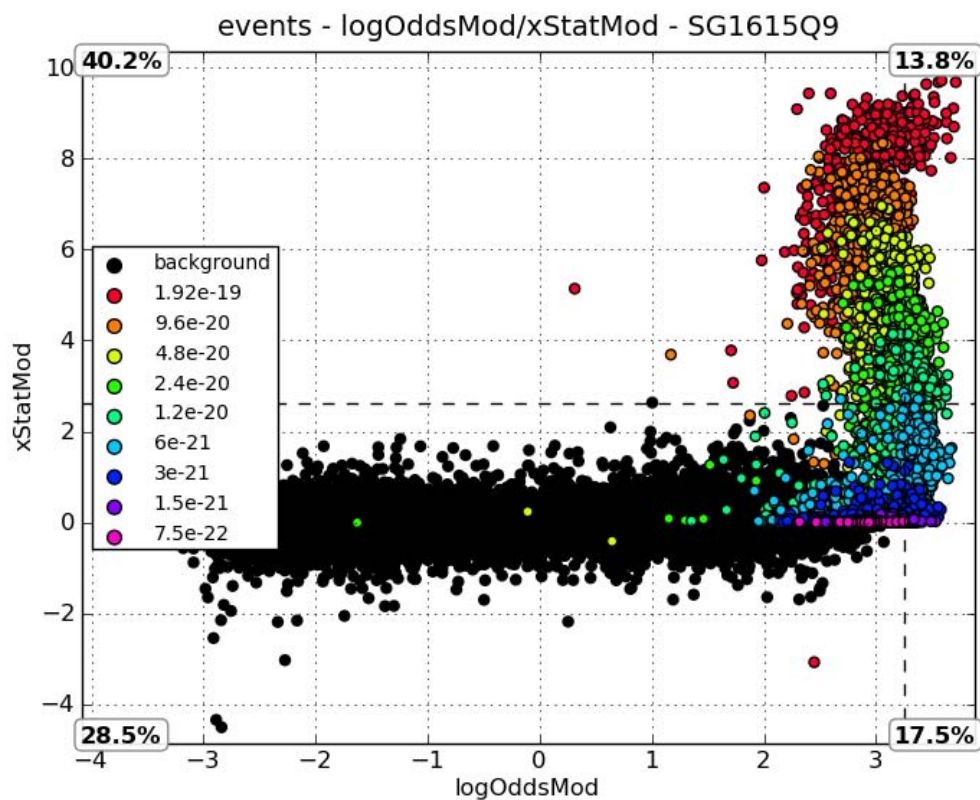


Figure A-61: SG1615Q9 injections scatter plot. Colors represent injection strain amplitude.

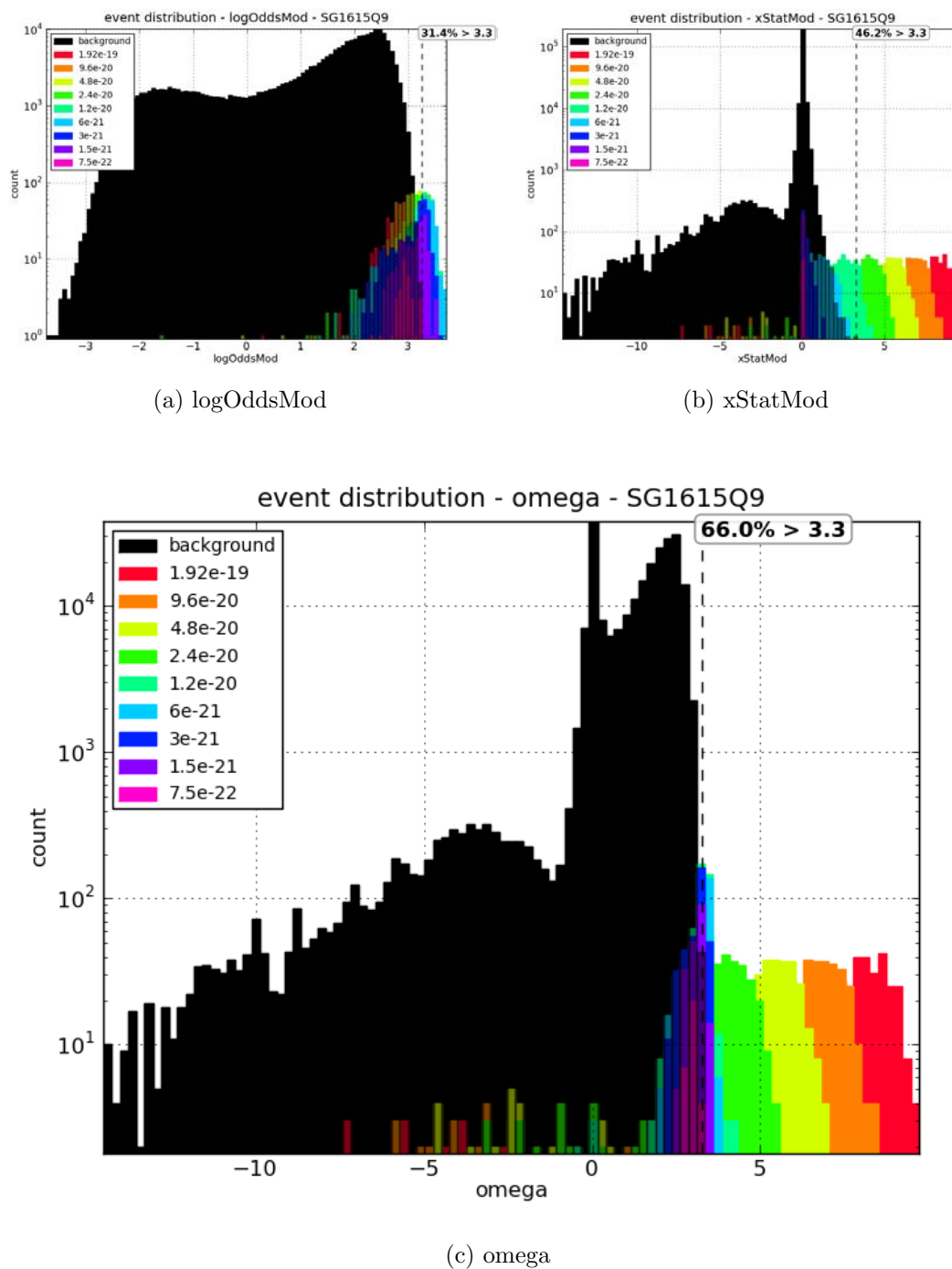
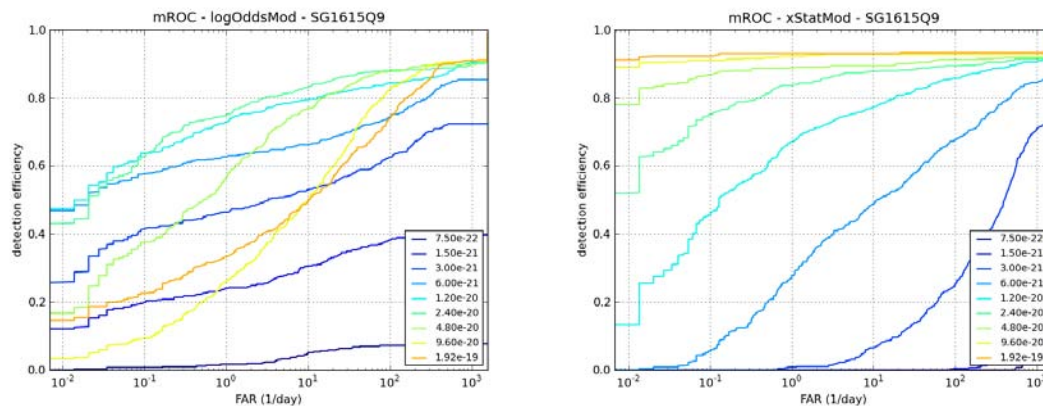
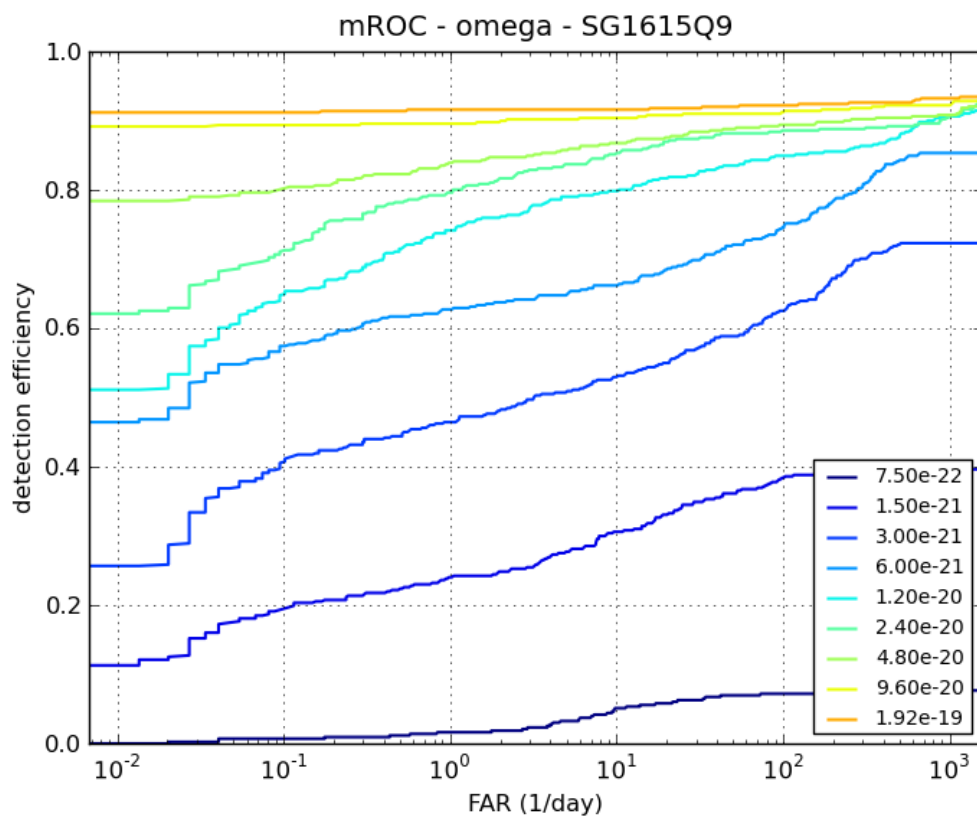


Figure A-62: SG1615Q9 injections histograms. Colors represent injection strain amplitude.



(a) logOddsMod

(b) xStatMod



(c) omega

Figure A-63: SG1615Q9 ROC plots

A.3.11 SG2000Q9 injections

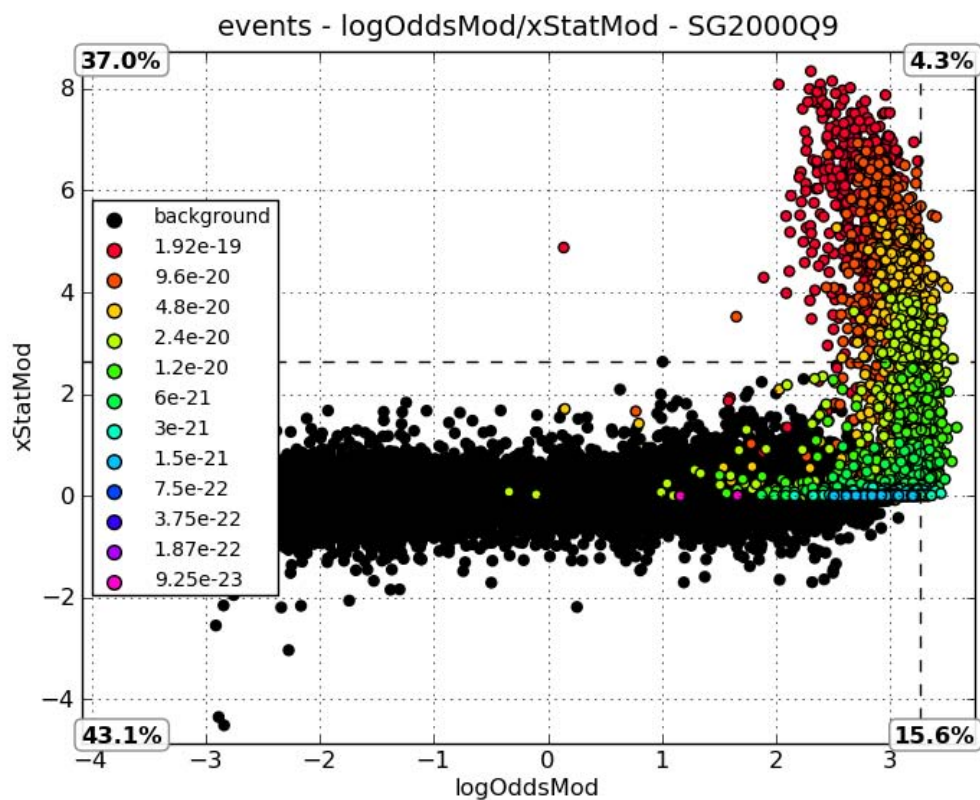


Figure A-64: SG2000Q9 injections scatter plot. Colors represent injection strain amplitude.

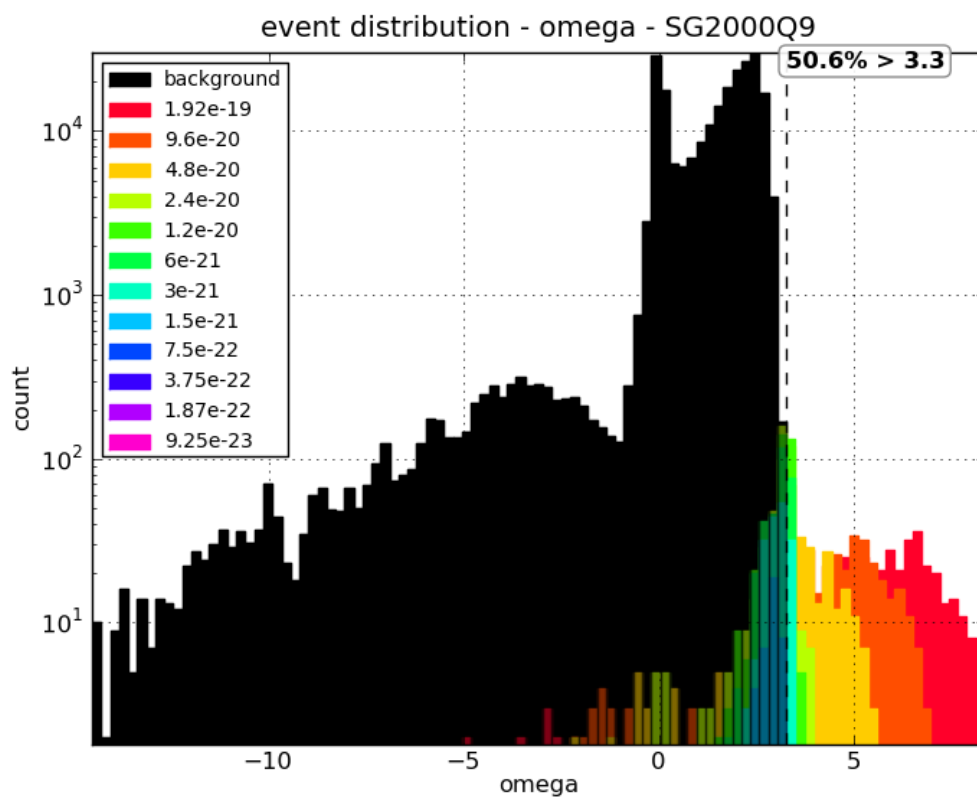
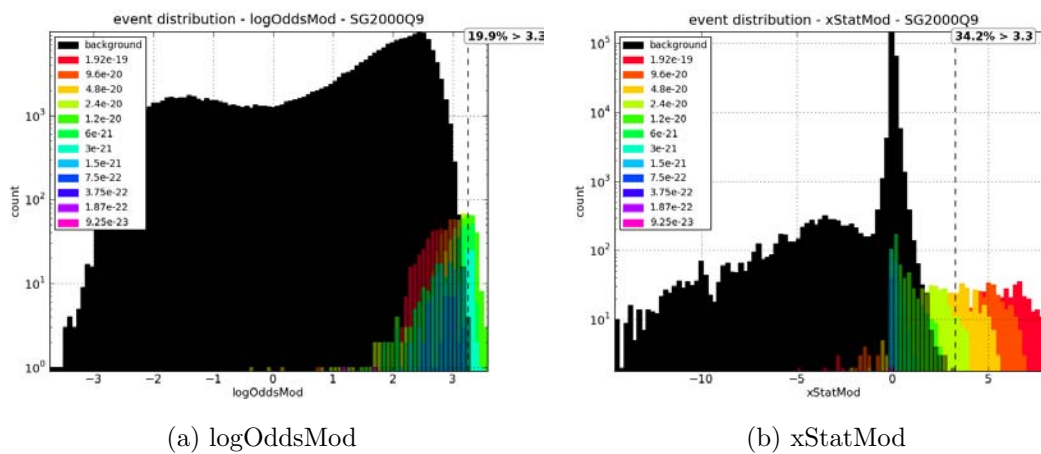
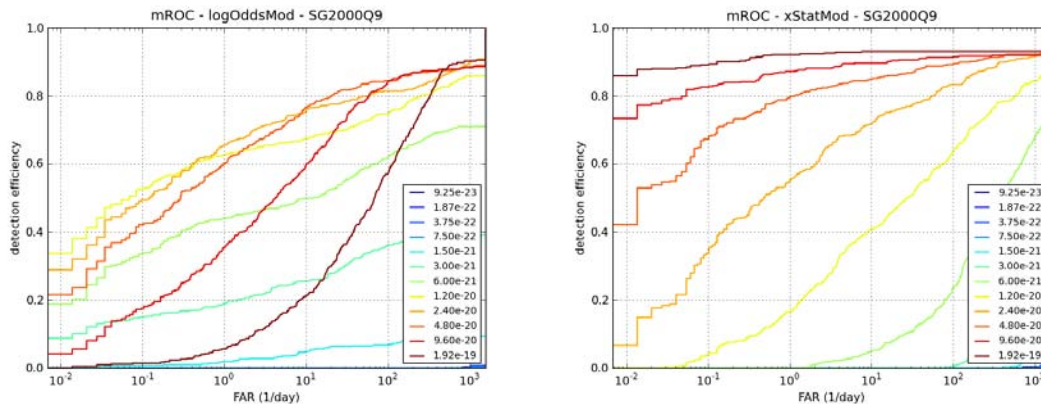
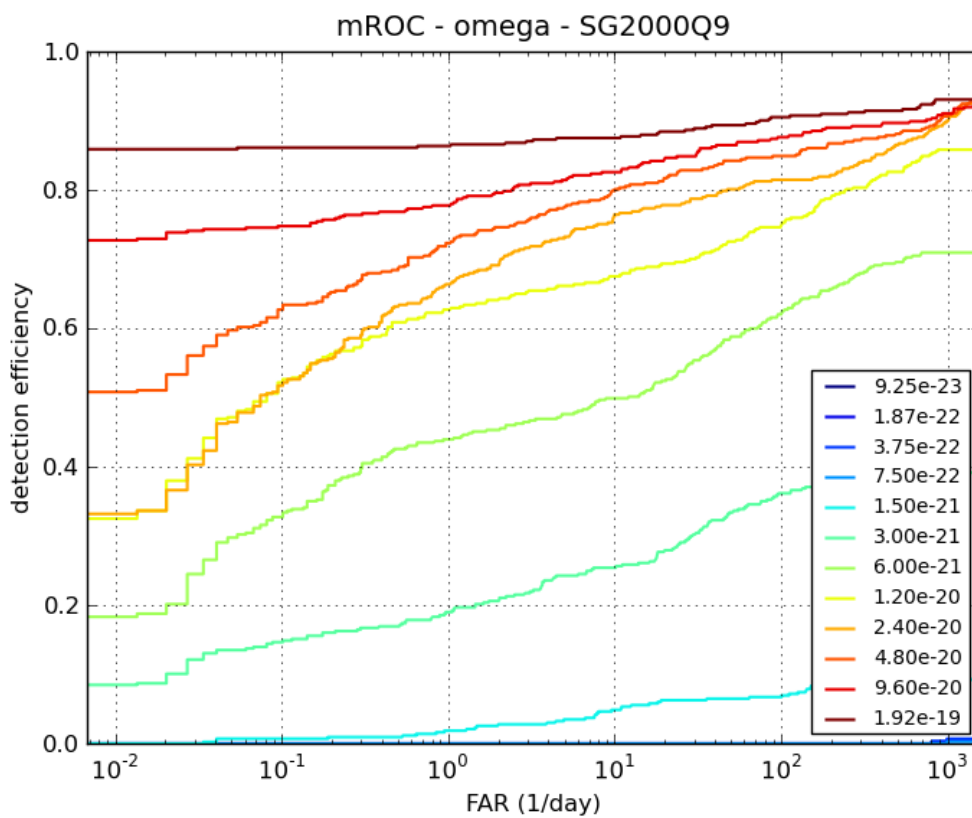


Figure A-65: SG2000Q9 injections histograms. Colors represent injection strain amplitude.



(a) logOddsMod

(b) xStatMod



(c) omega

Figure A-66: SG2000Q9 ROC plots

A.4 Sine-Gaussian, Q 100 injections

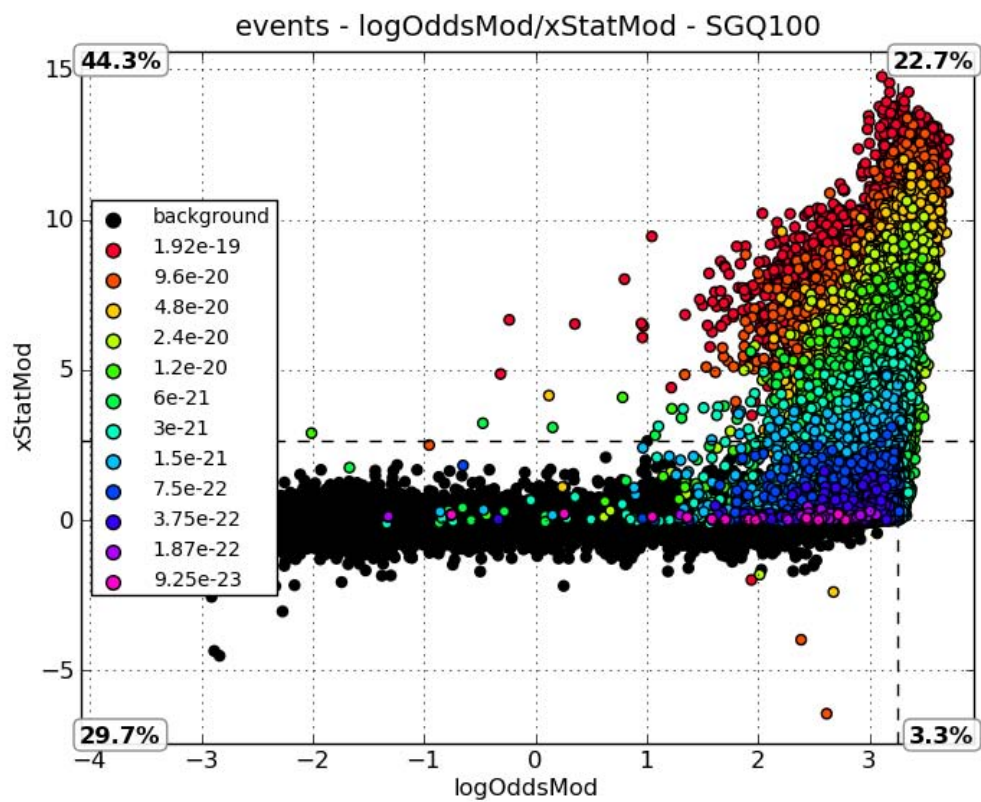


Figure A-67: SGQ100 injections scatter plot. Colors represent injection strain amplitude.

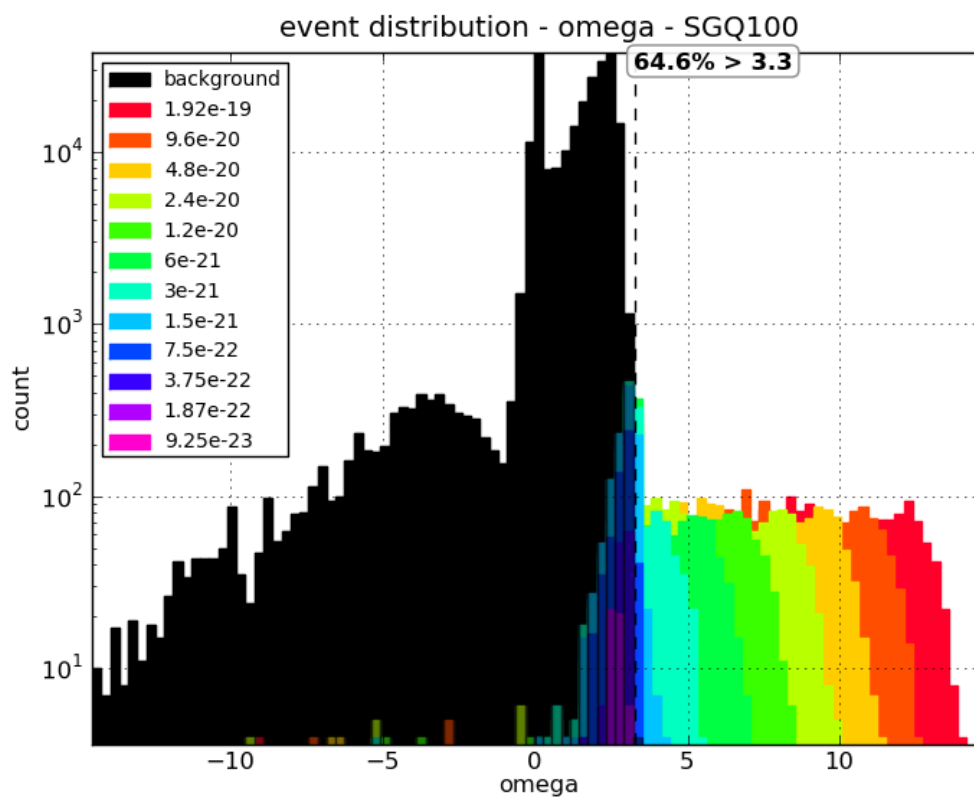
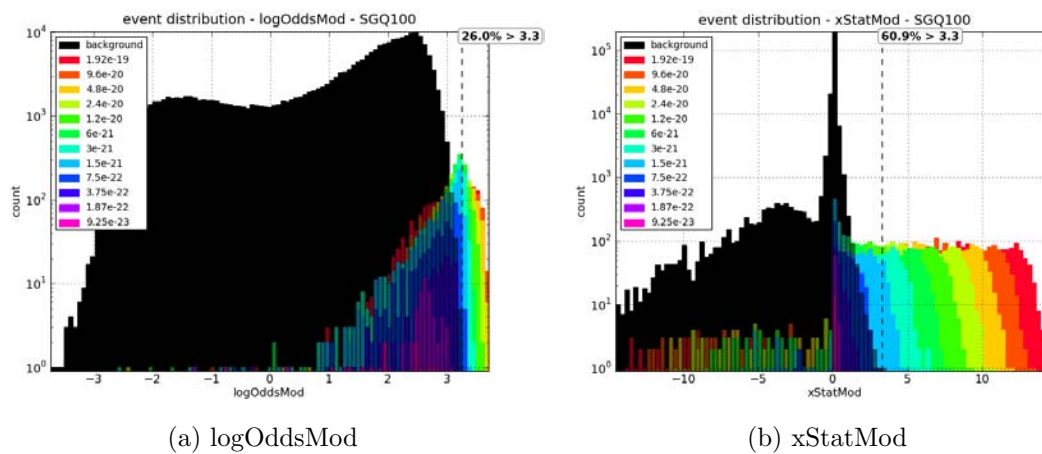
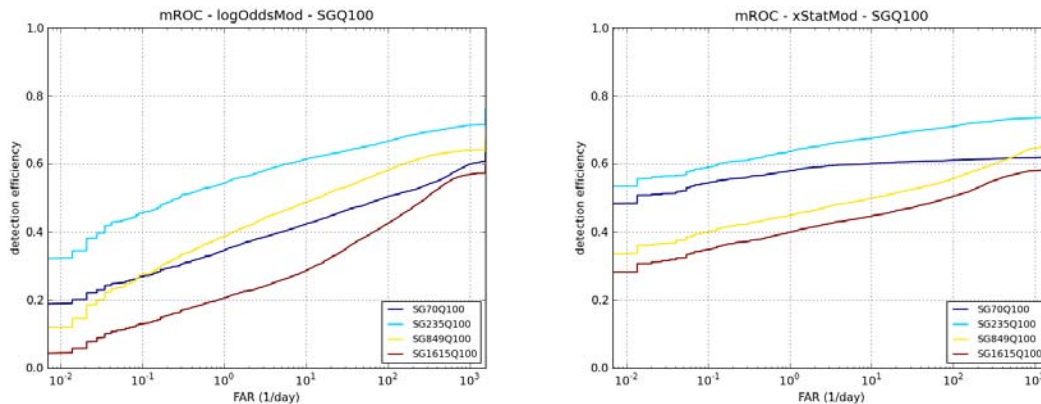
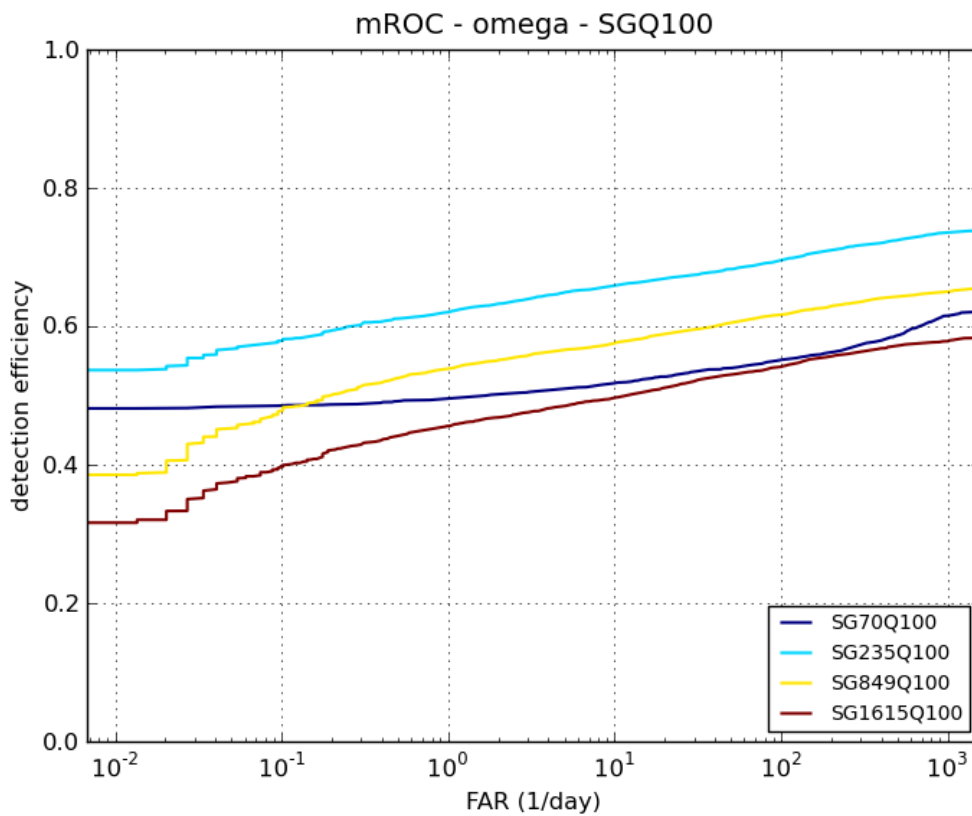


Figure A-68: SGQ100 injections histograms. Colors represent injection strain amplitude.



(a) logOddsMod

(b) xStatMod



(c) omega

Figure A-69: SGQ100 ROC plots

A.4.1 SG70Q100 injections

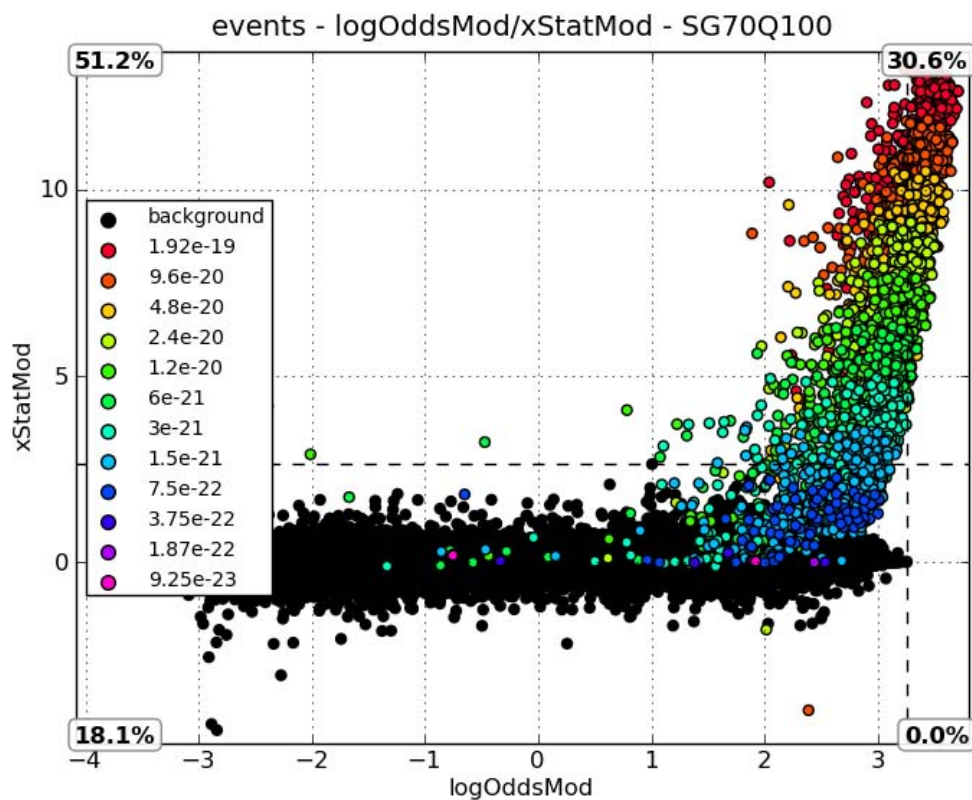


Figure A-70: SG70Q100 injections scatter plot. Colors represent injection strain amplitude.

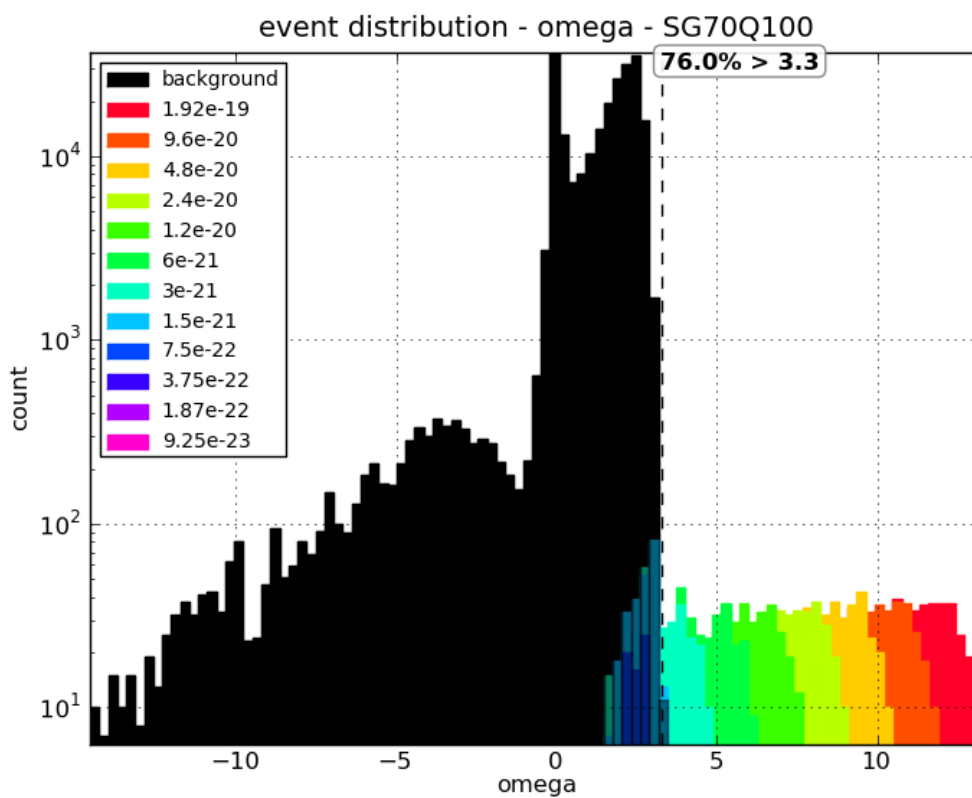
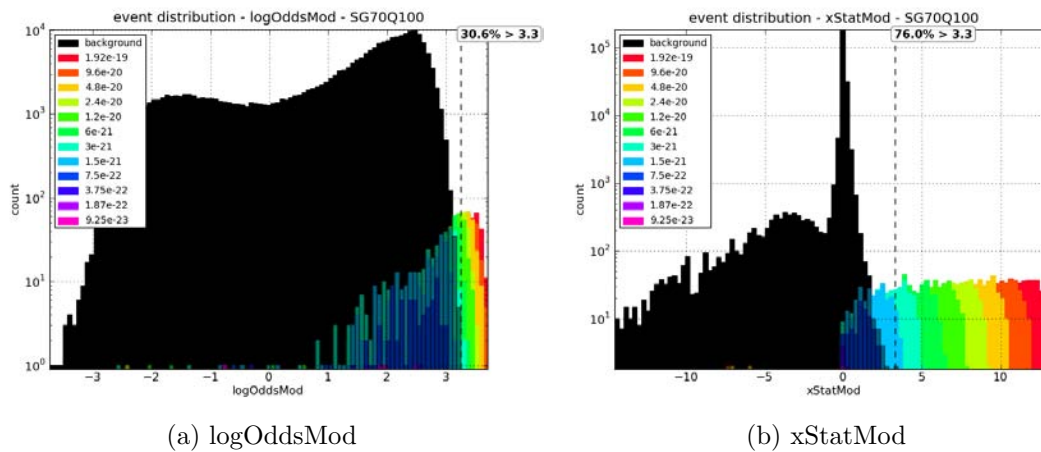


Figure A-71: SG70Q100 injections histograms. Colors represent injection strain amplitude.

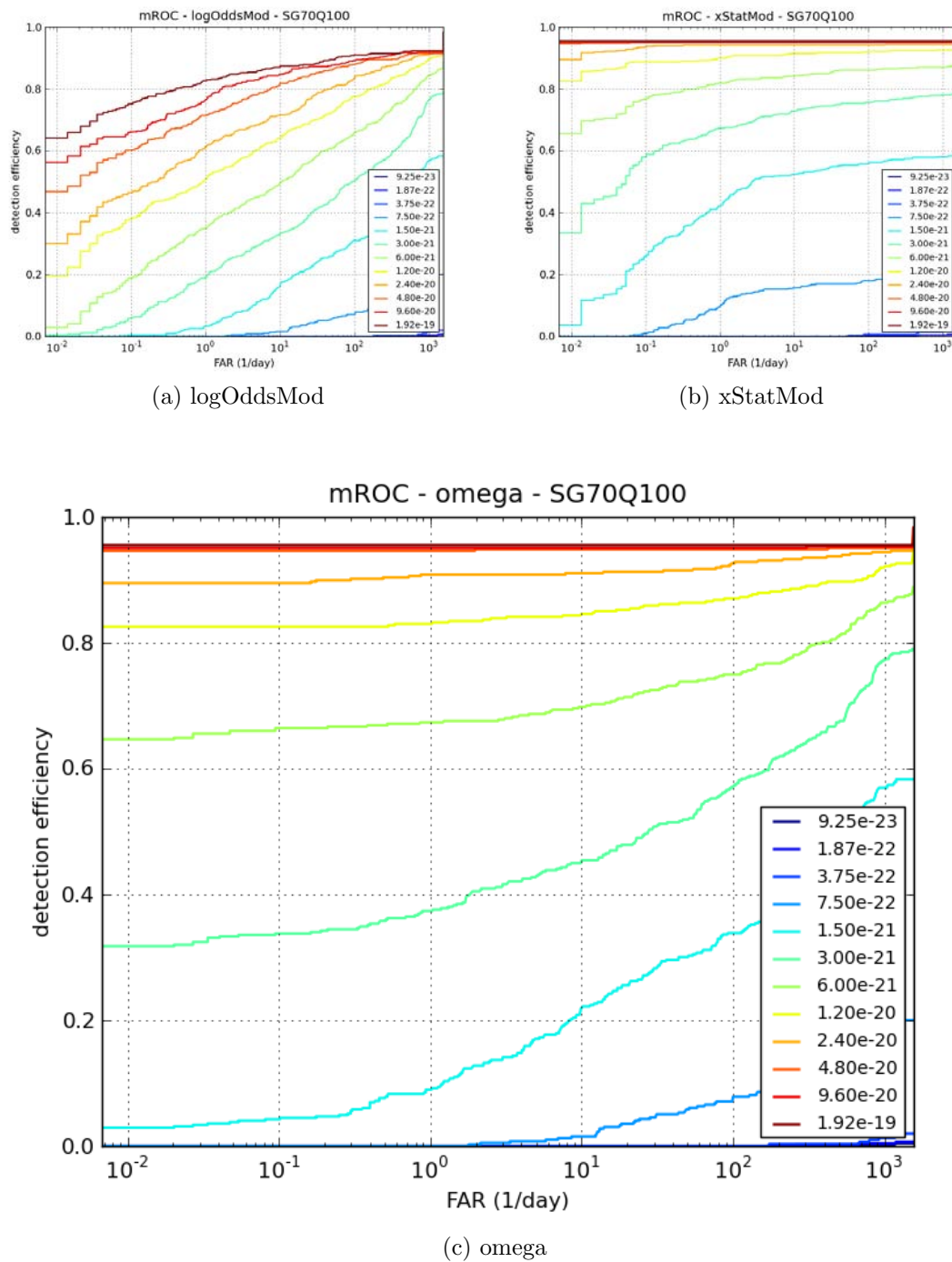


Figure A-72: SG70Q100 ROC plots

A.4.2 SG235Q100 injections

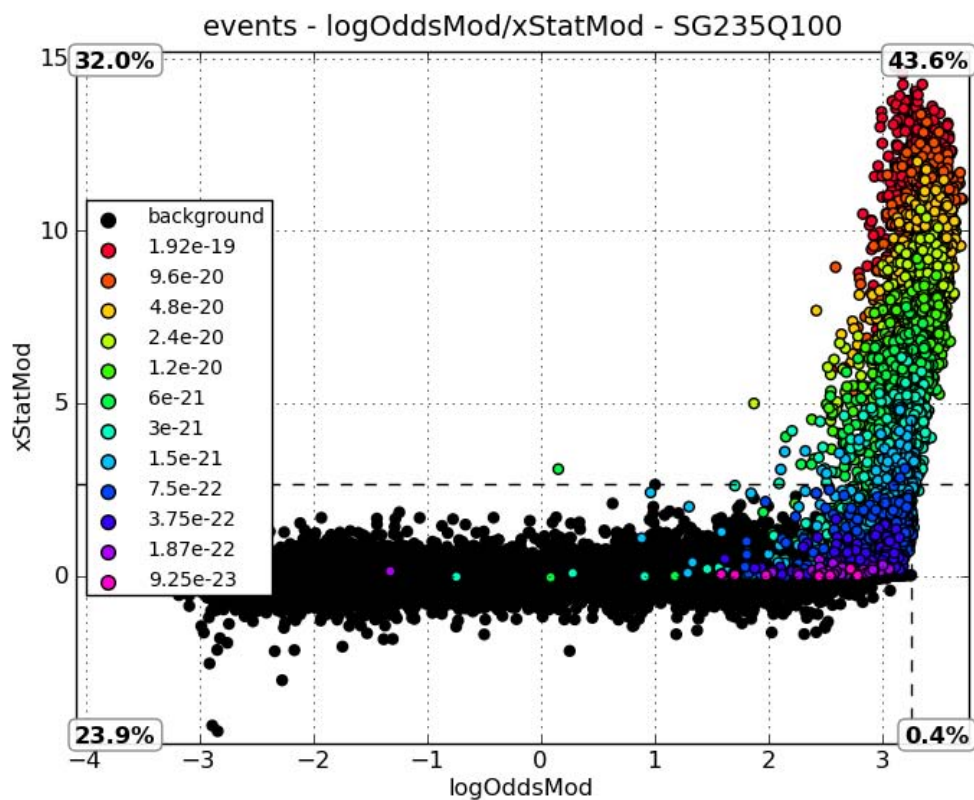
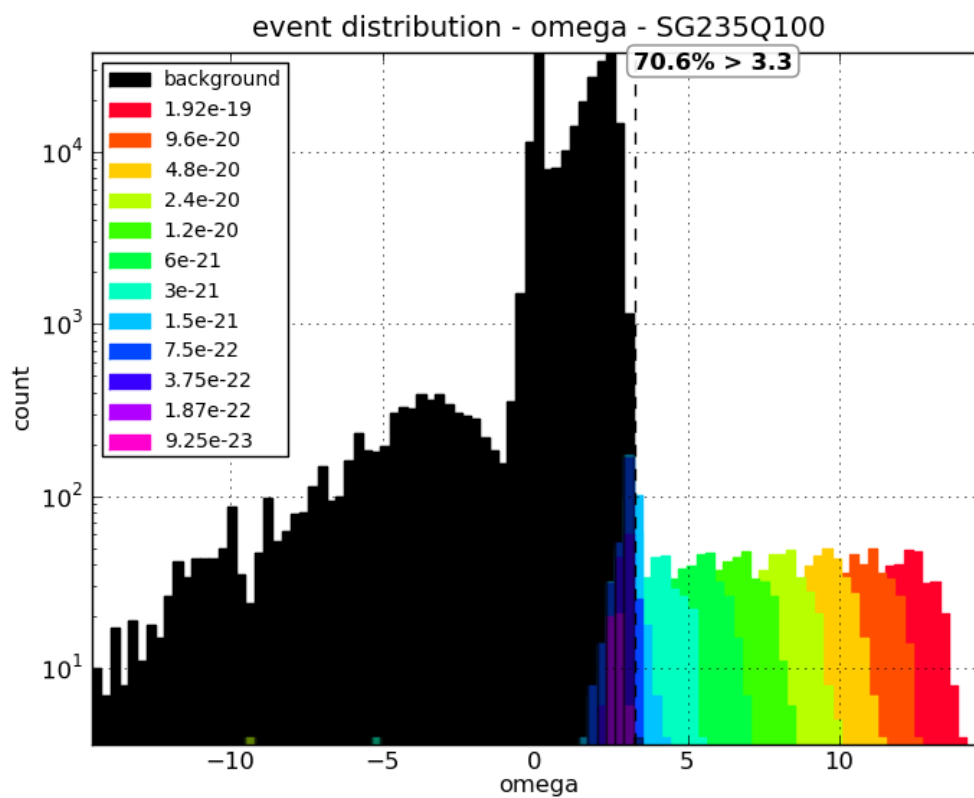
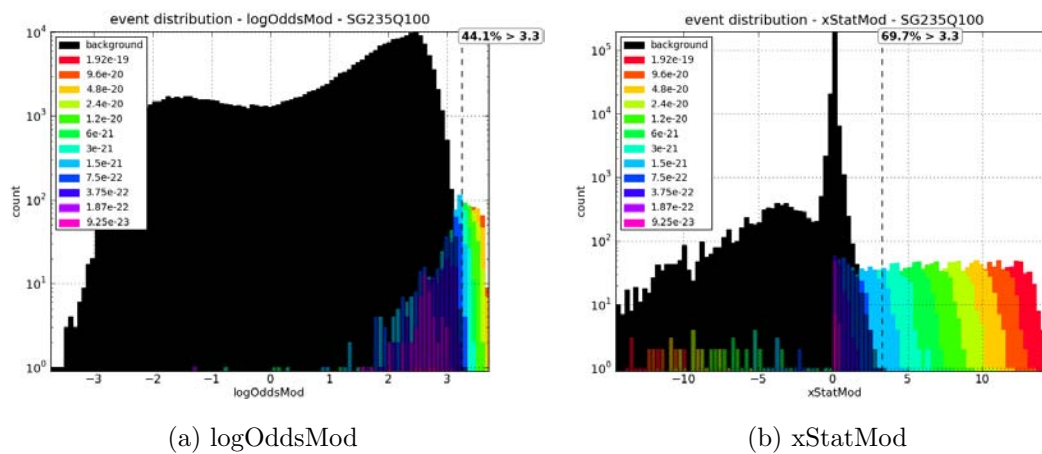


Figure A-73: SG235Q100 injections scatter plot. Colors represent injection strain amplitude.



(c) omega

Figure A-74: SG235Q100 injections histograms. Colors represent injection strain amplitude.

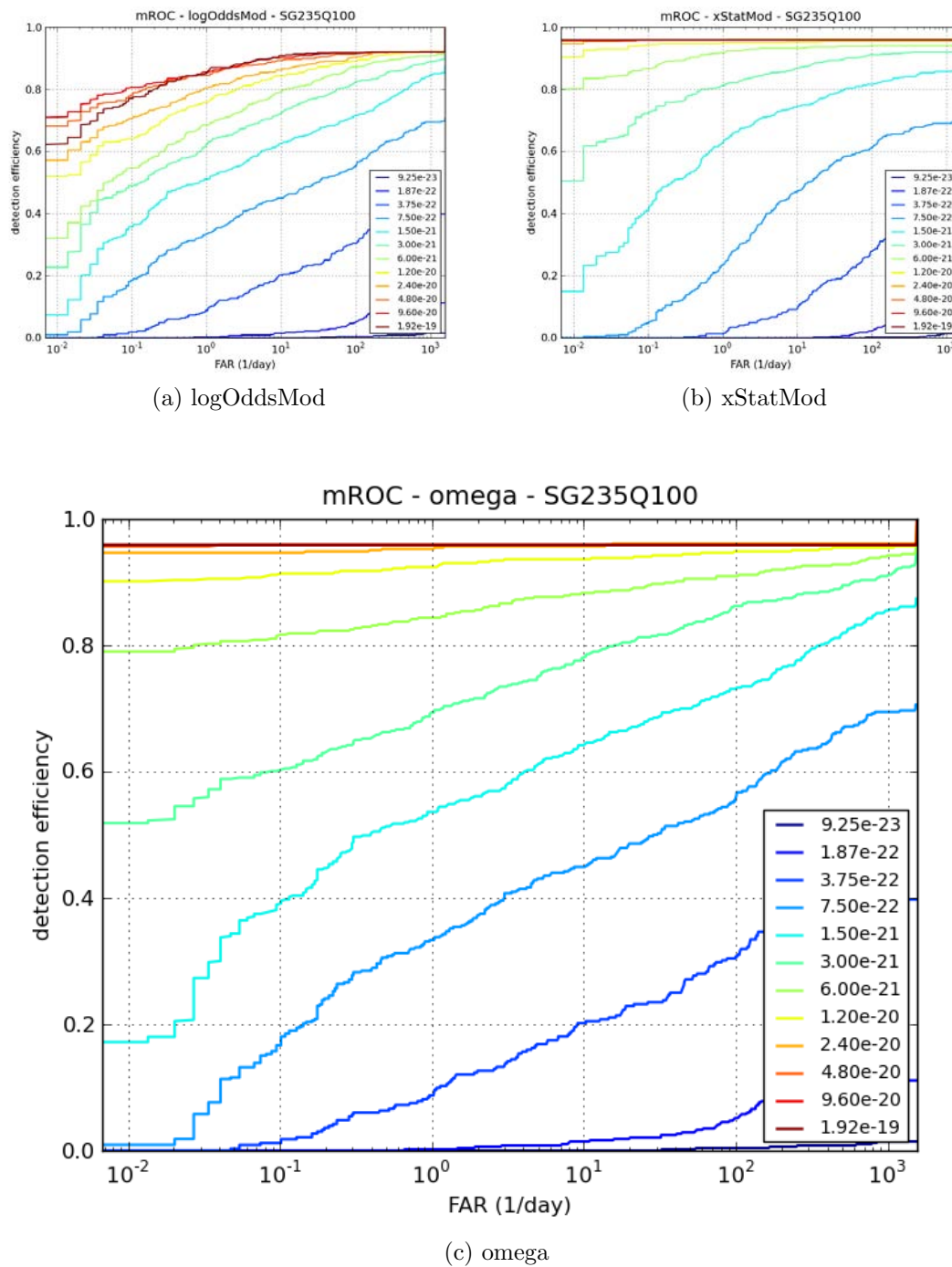


Figure A-75: SG235Q100 ROC plots

A.4.3 SG849Q100 injections

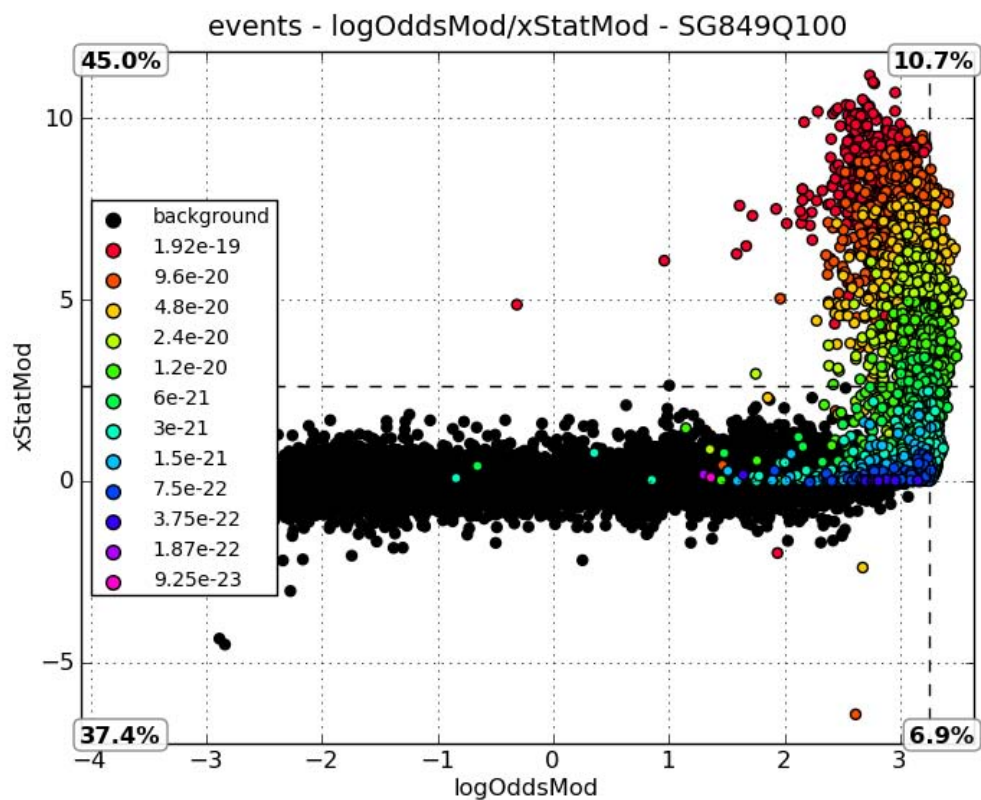


Figure A-76: SG849Q100 injections scatter plot. Colors represent injection strain amplitude.

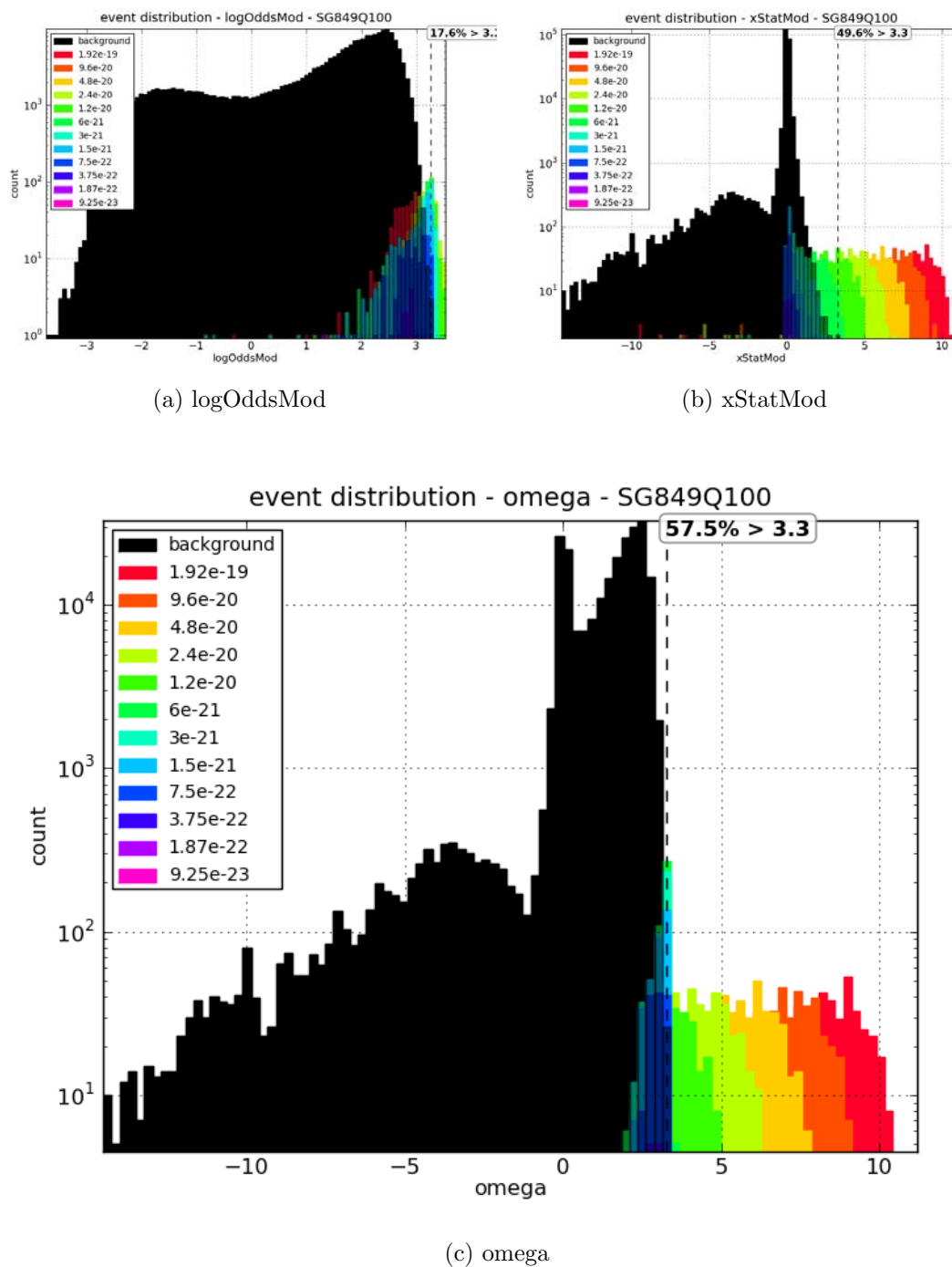


Figure A-77: SG849Q100 injections histograms. Colors represent injection strain amplitude.

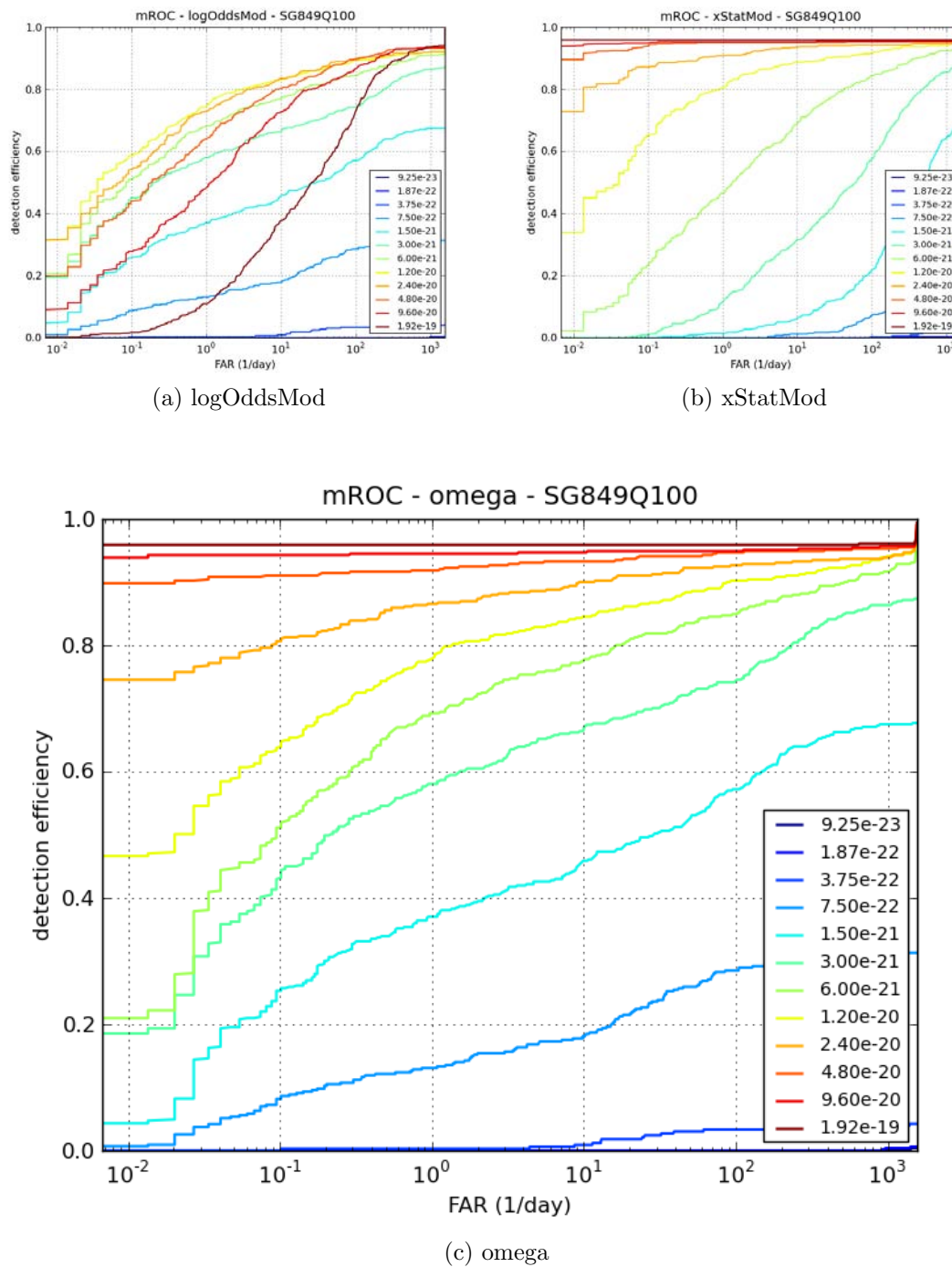


Figure A-78: SG849Q100 ROC plots

A.4.4 SG1615Q100 injections

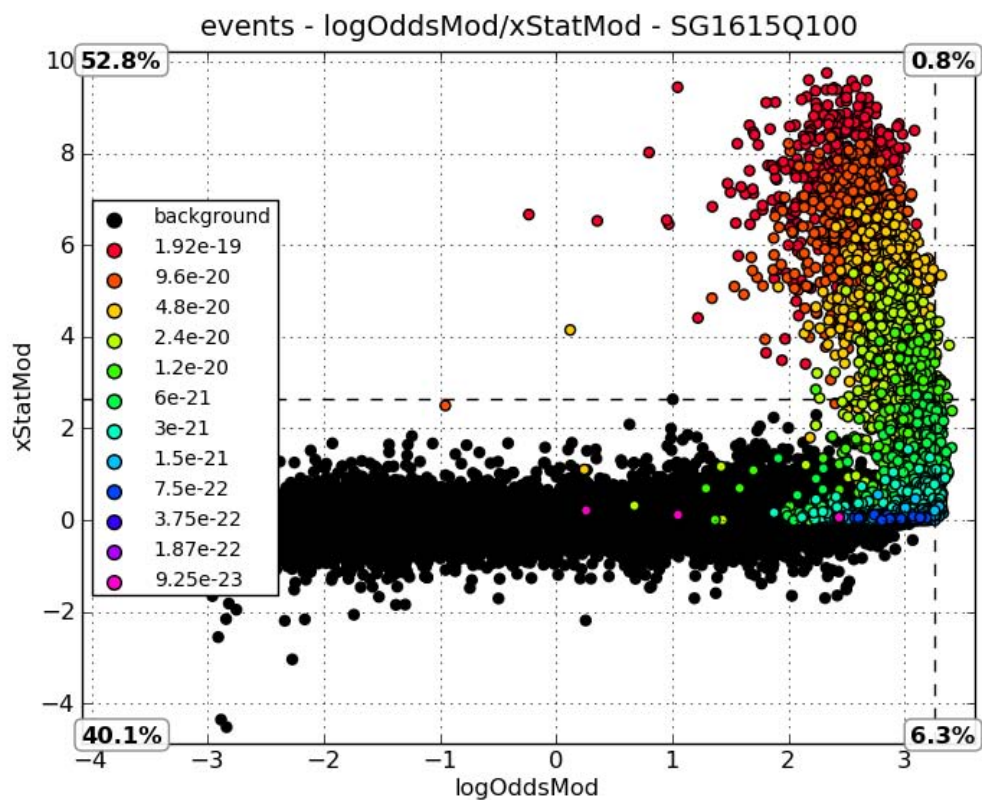


Figure A-79: SG1615Q100 injections scatter plot. Colors represent injection strain amplitude.

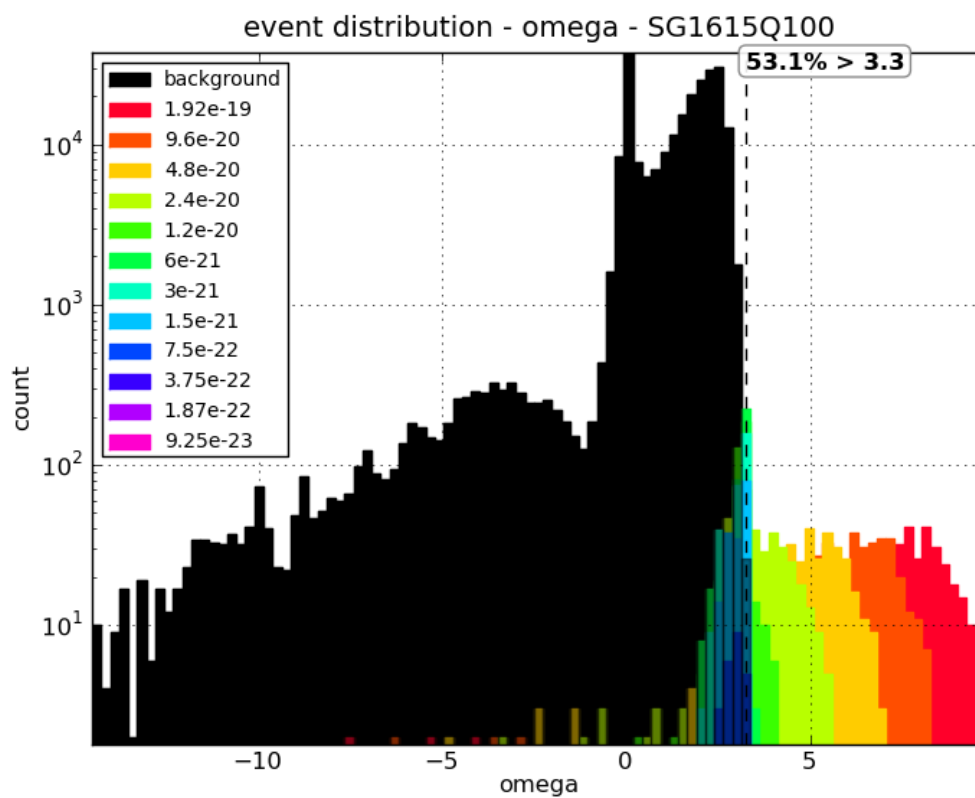
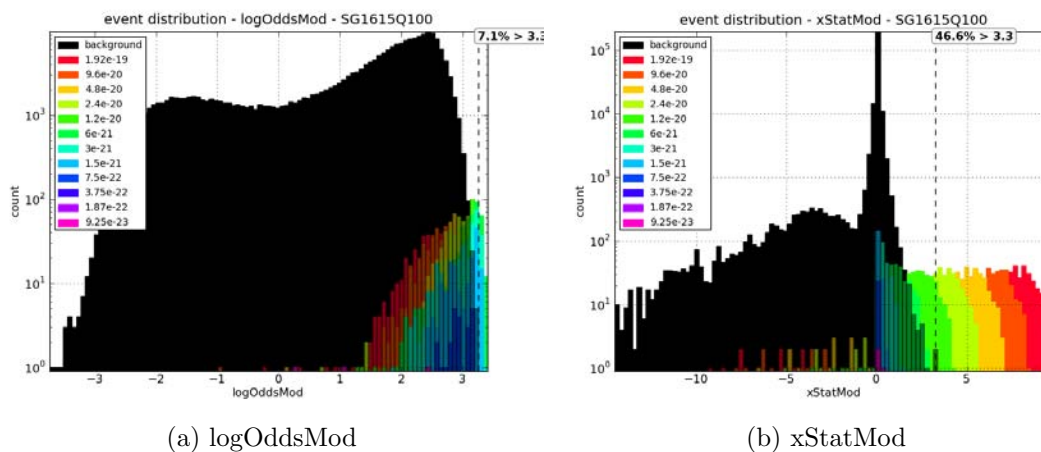


Figure A-80: SG1615Q100 injections histograms. Colors represent injection strain amplitude.

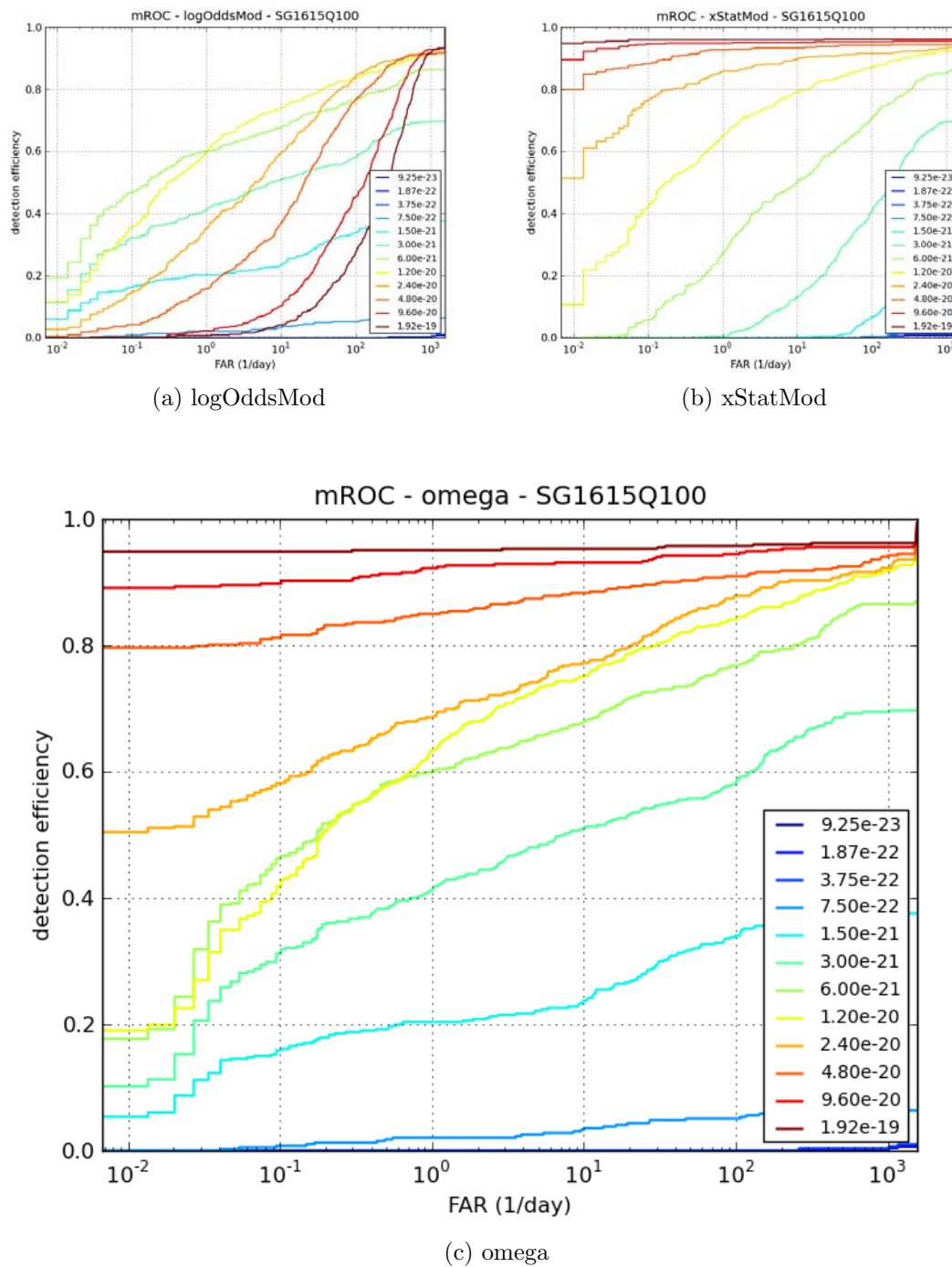


Figure A-81: SG1615Q100 ROC plots

A.5 White noise burst injections

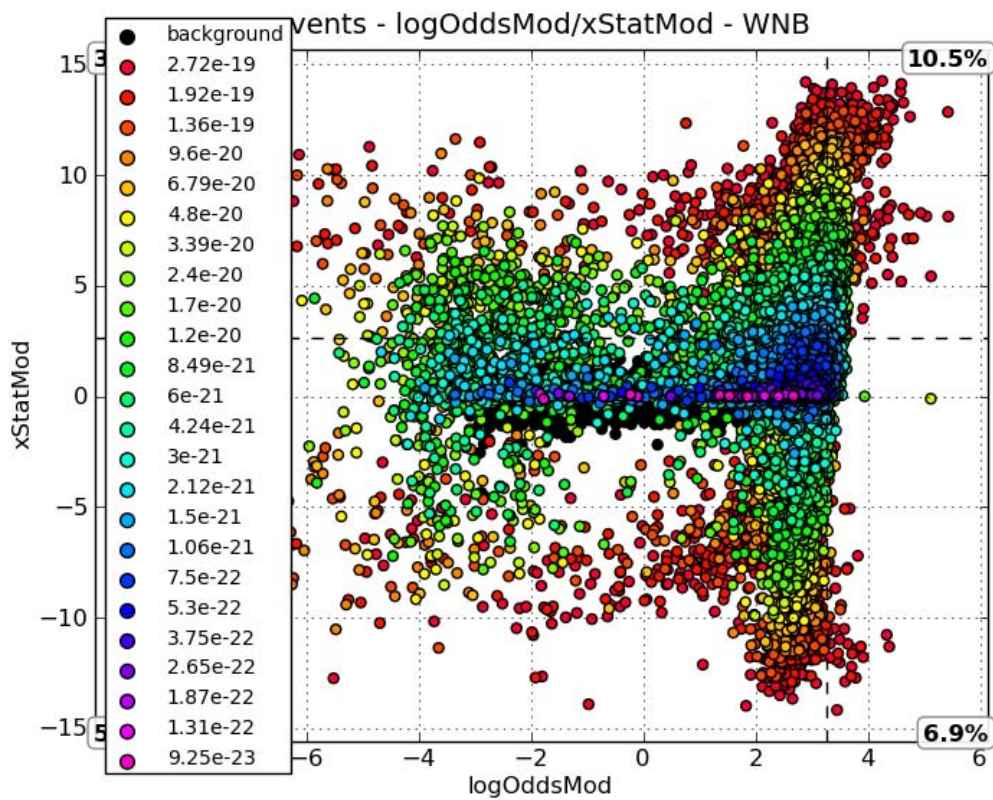


Figure A-82: WNB injections scatter plot. Colors represent injection strain amplitude.

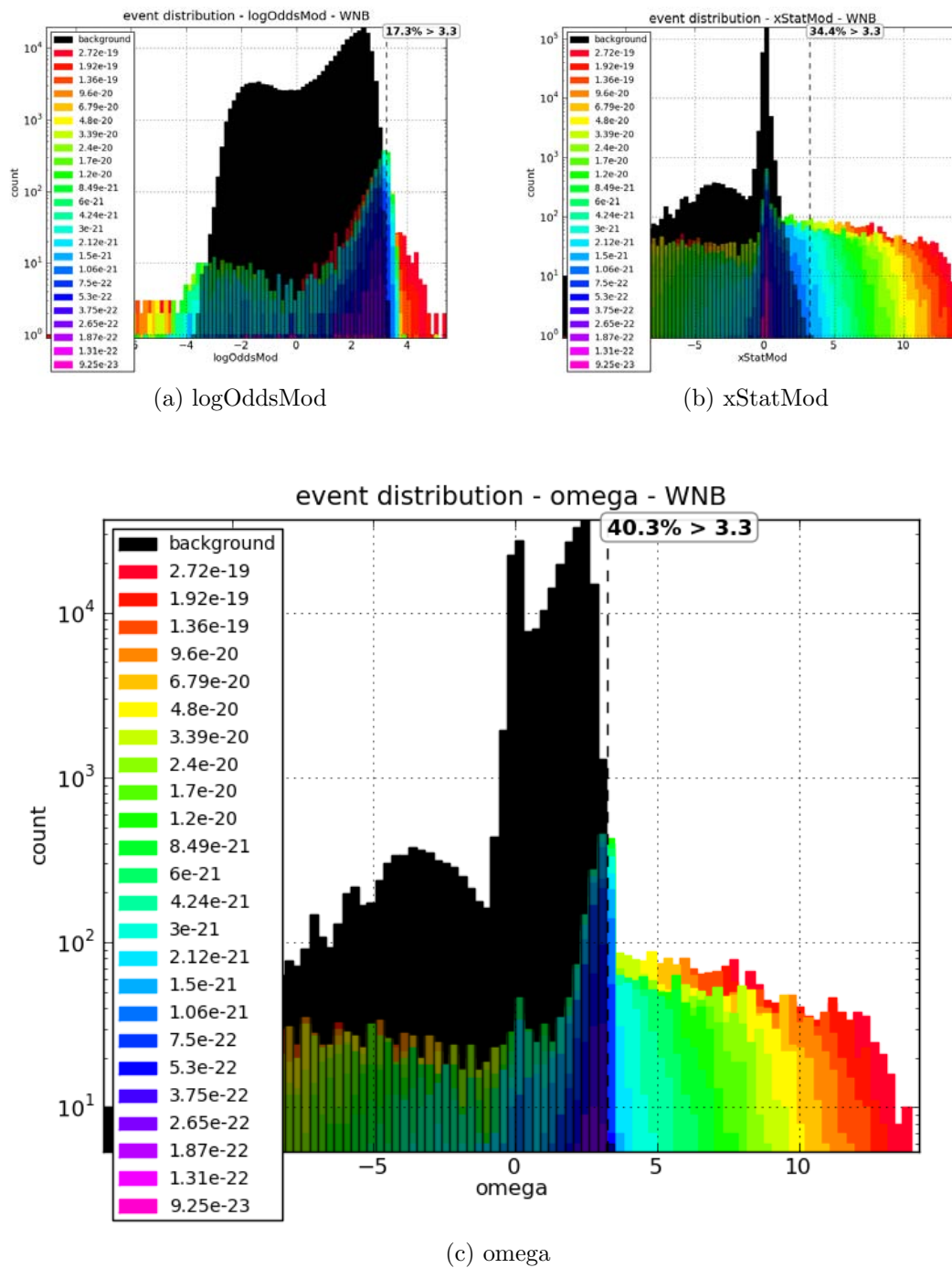


Figure A-83: WNB injections histograms. Colors represent injection strain amplitude.

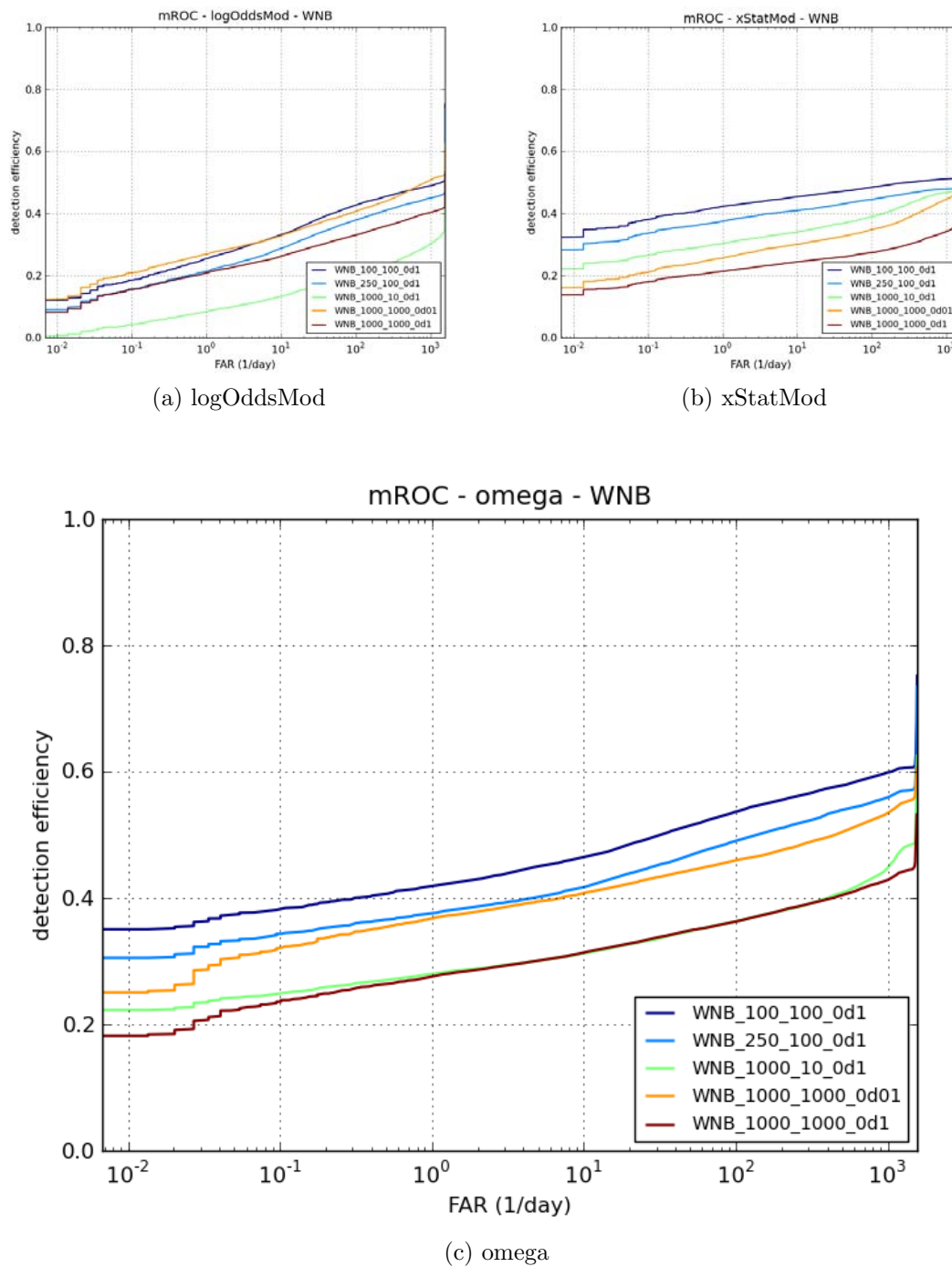


Figure A-84: WNB ROC plots

A.5.1 WNB_1000_1000_0d01 injections

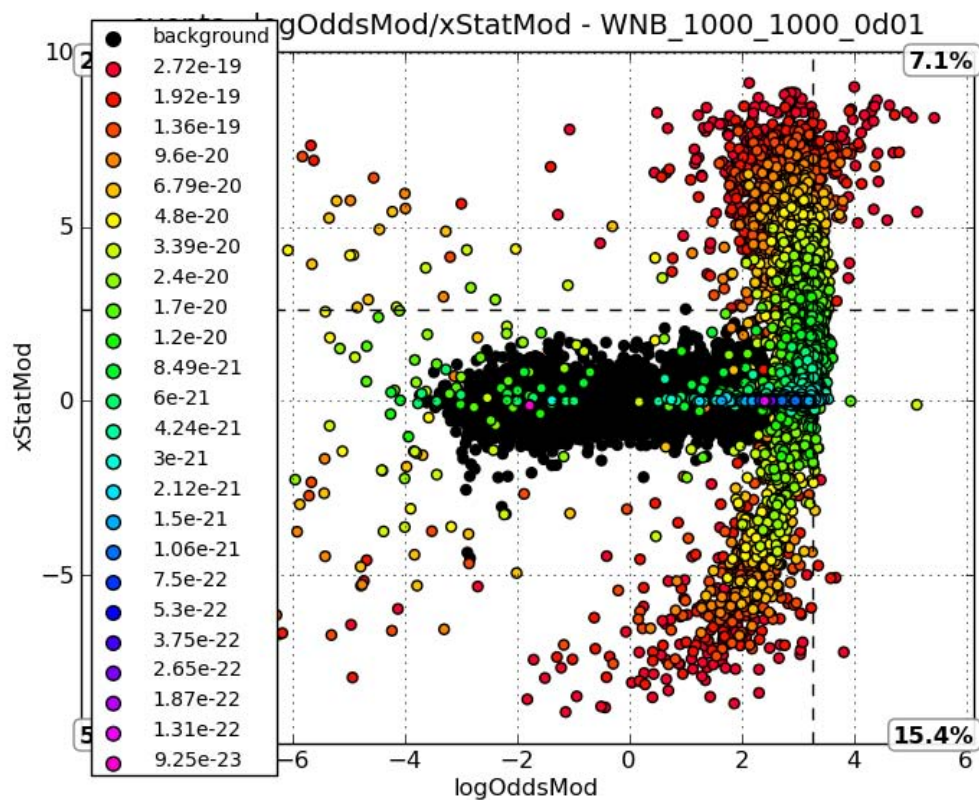


Figure A-85: WNB_1000_1000_0d01 injections scatter plot. Colors represent injection strain amplitude.

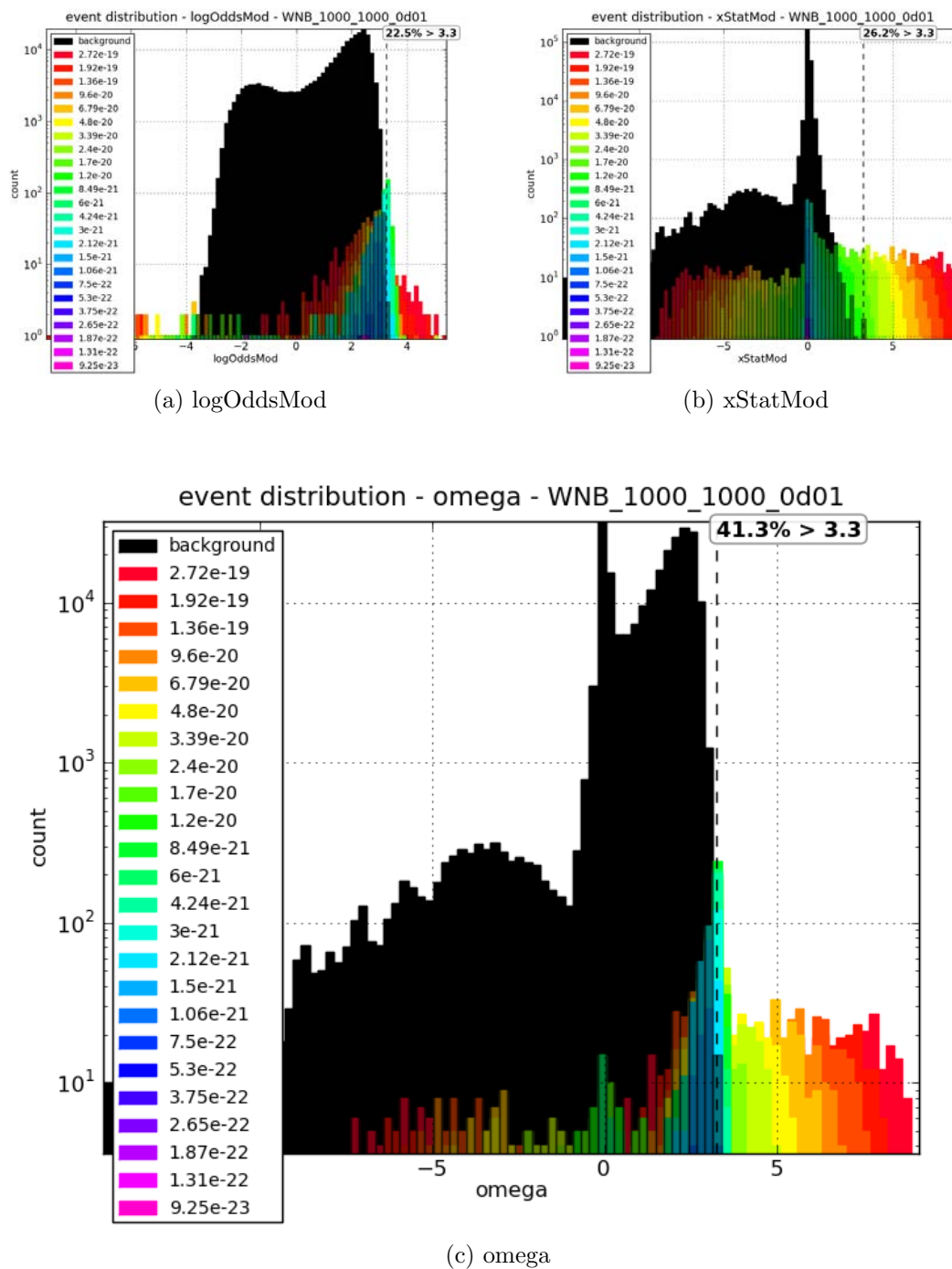
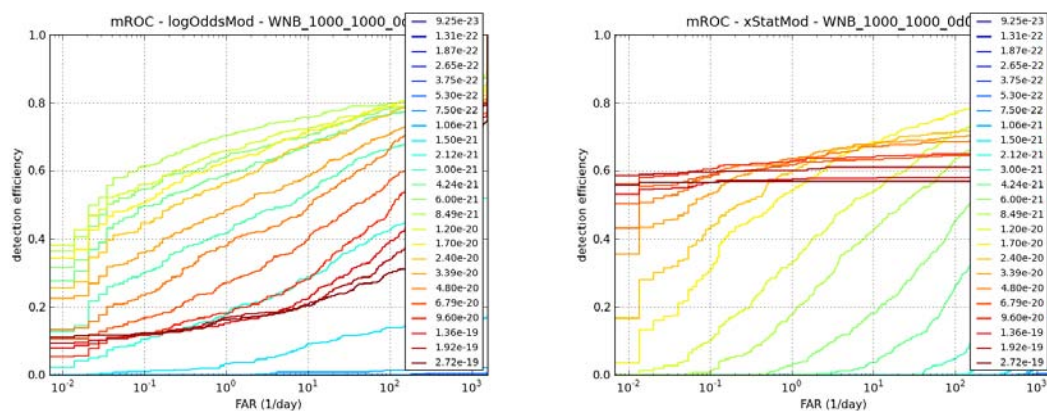
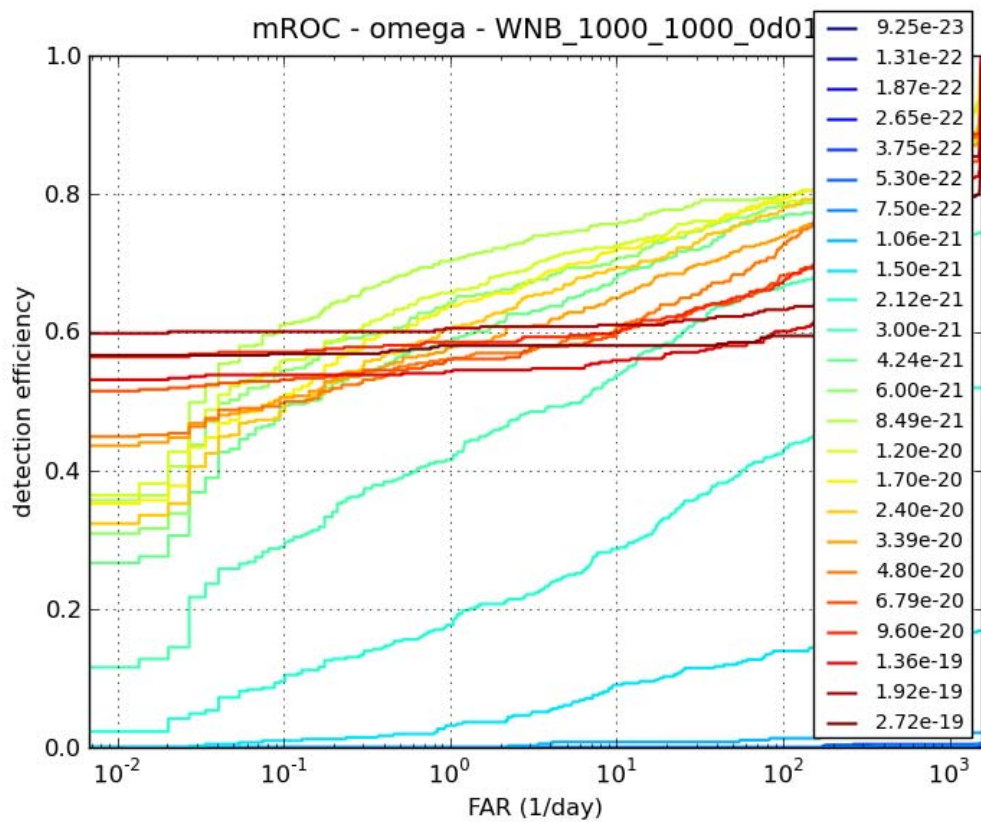


Figure A-86: WNB_1000_1000_0d01 injections histograms. Colors represent injection strain amplitude.



(a) logOddsMod

(b) xStatMod



(c) omega

Figure A-87: WNB_1000_1000_0d01 ROC plots

A.5.2 WNB_1000_1000_0d1 injections

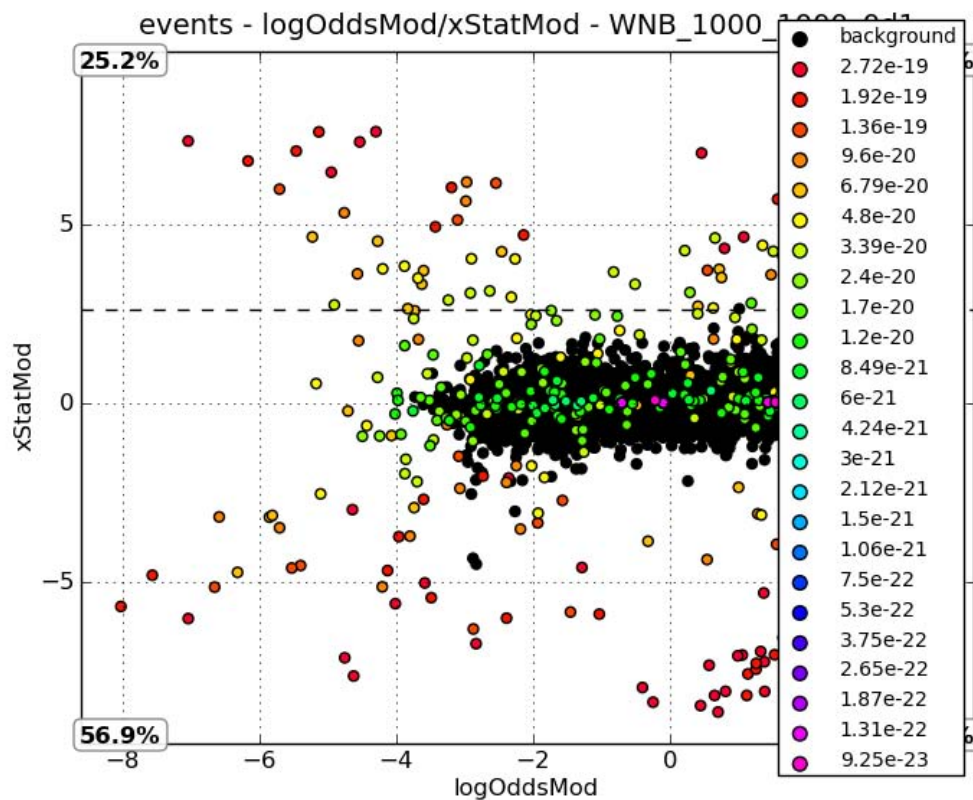


Figure A-88: WNB_1000_1000_0d1 injections scatter plot. Colors represent injection strain amplitude.

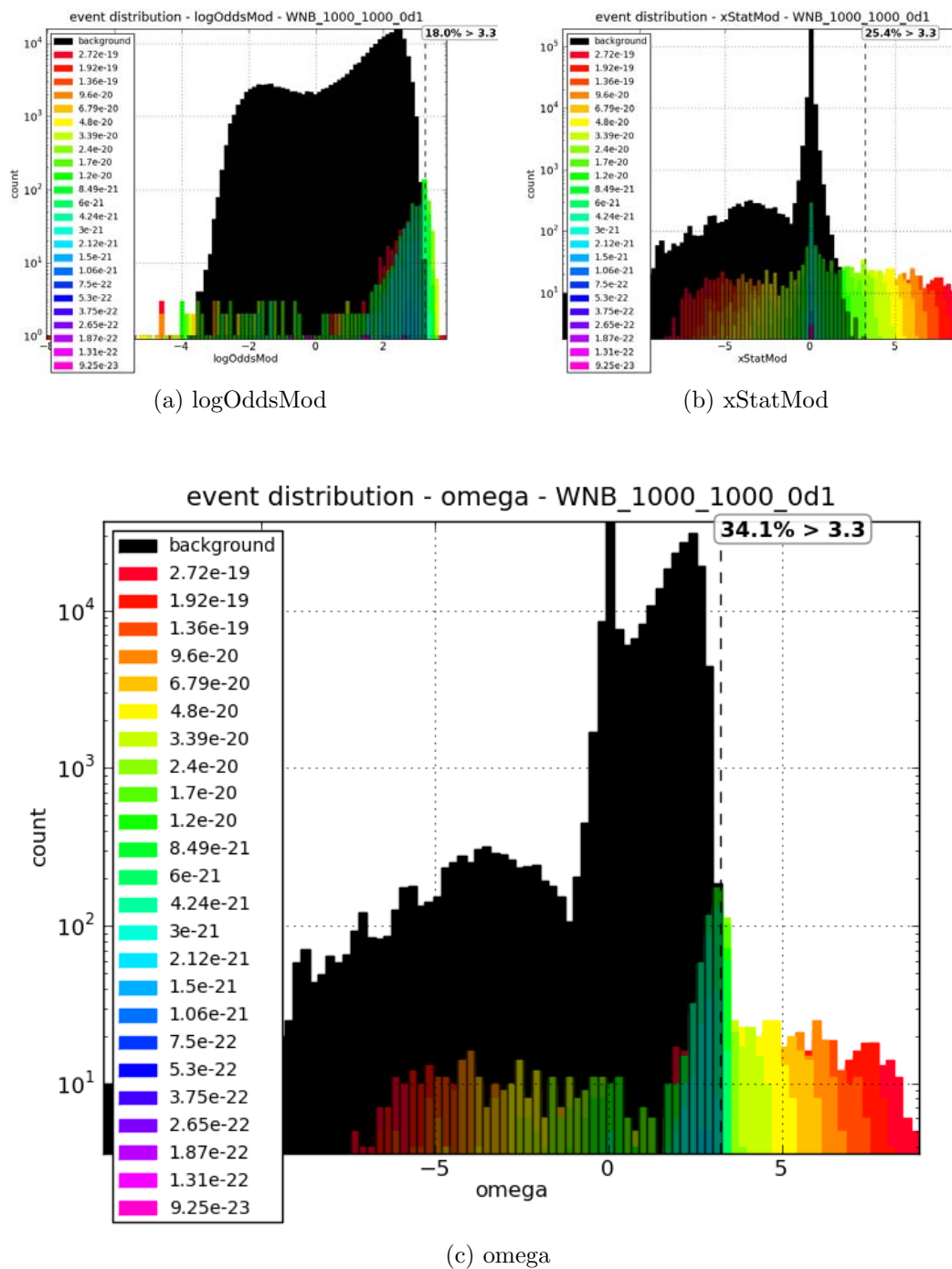
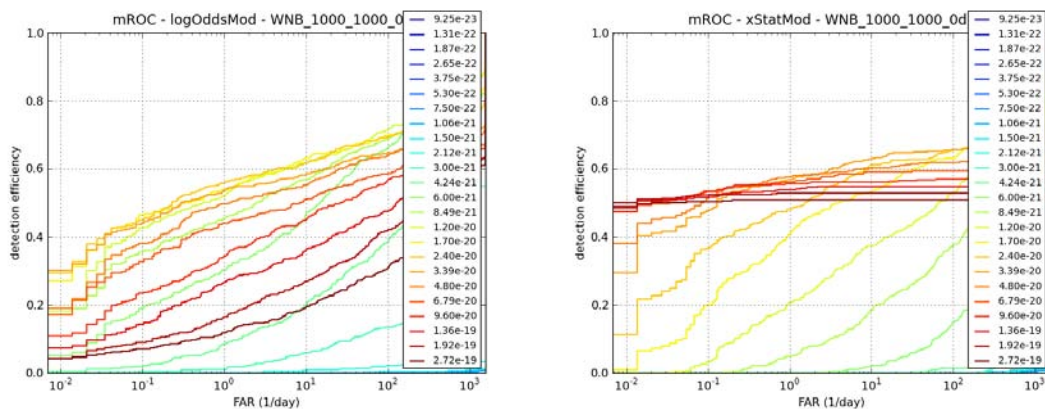
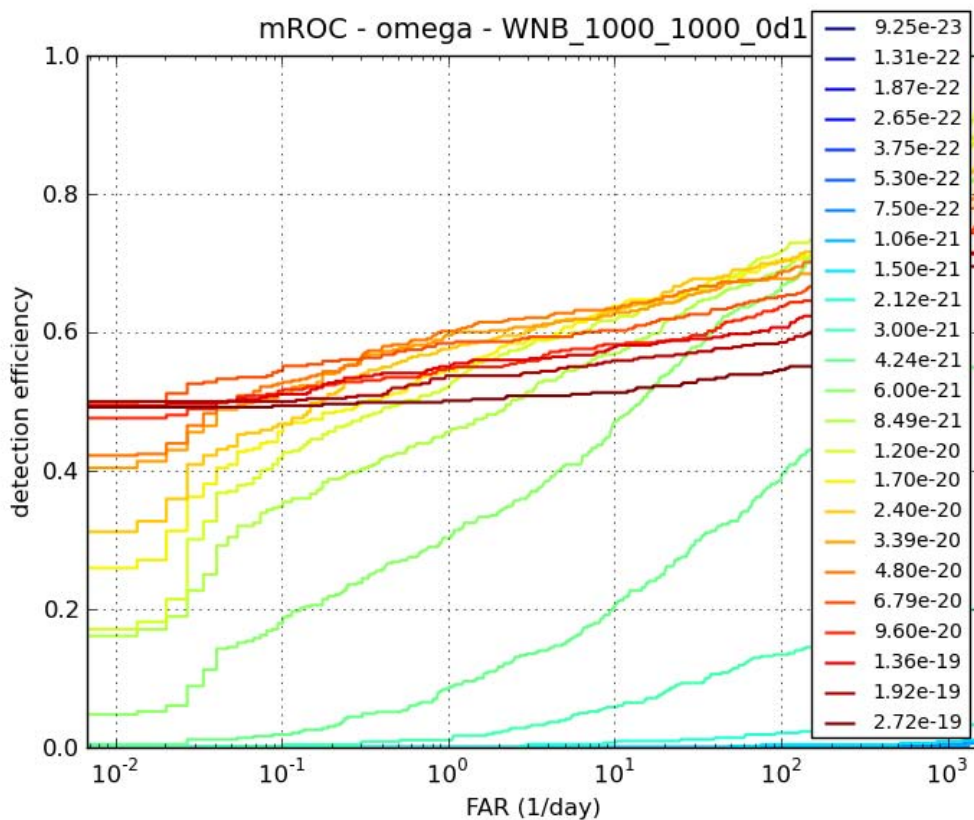


Figure A-89: WNB_1000_1000_0d1 injections histograms. Colors represent injection strain amplitude.



(a) logOddsMod

(b) xStatMod



(c) omega

Figure A-90: WNB_1000_1000_0d1 ROC plots

A.5.3 WNB_1000_10_0d1 injections

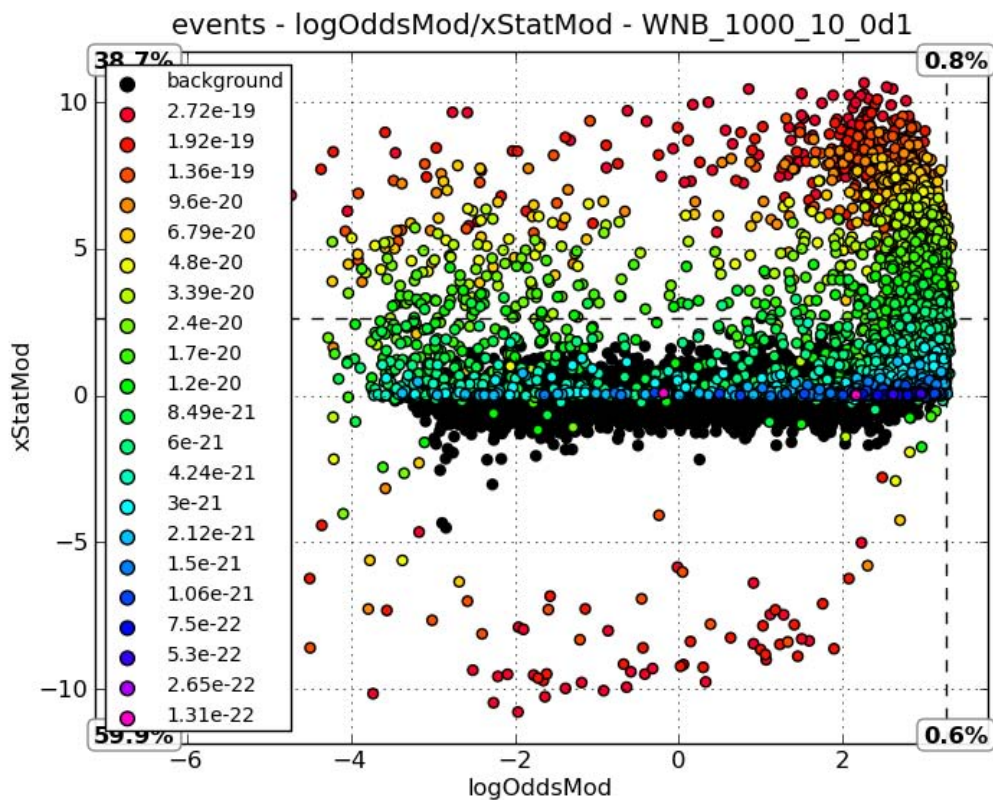
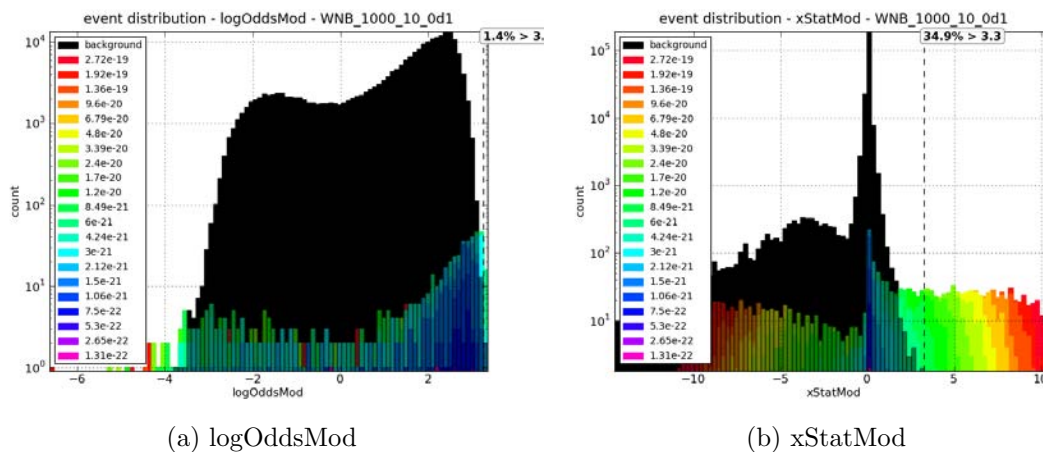
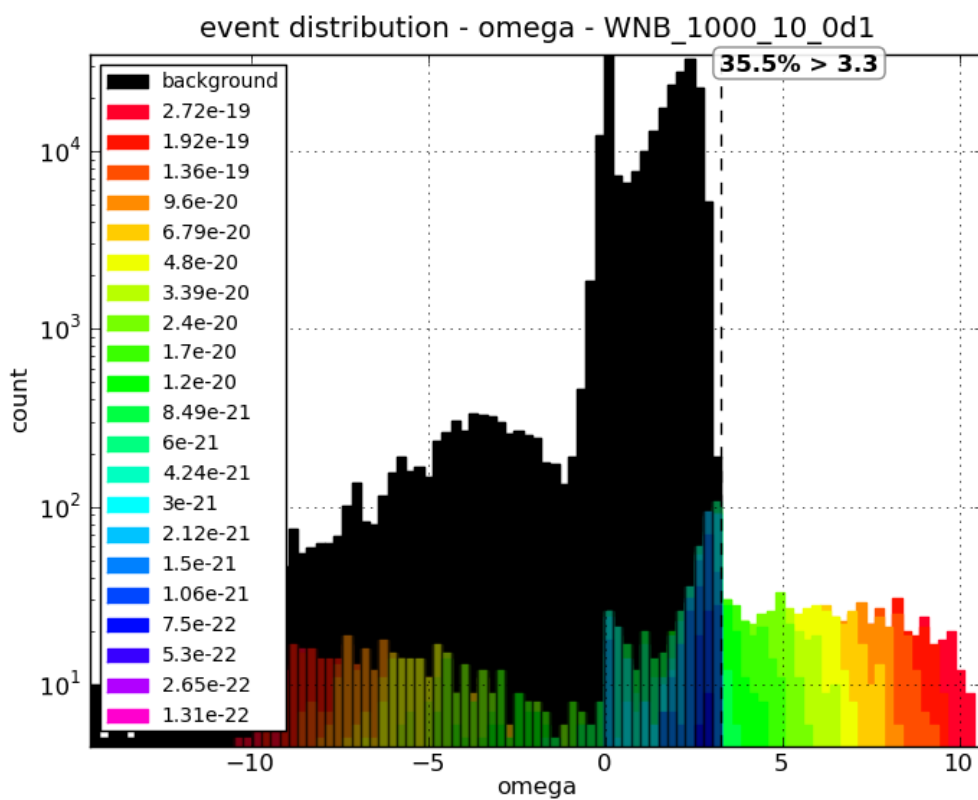


Figure A-91: WNB_1000_10_0d1 injections scatter plot. Colors represent injection strain amplitude.



(a) logOddsMod

(b) xStatMod



(c) omega

Figure A-92: WNB_1000_10_0d1 injections histograms. Colors represent injection strain amplitude.

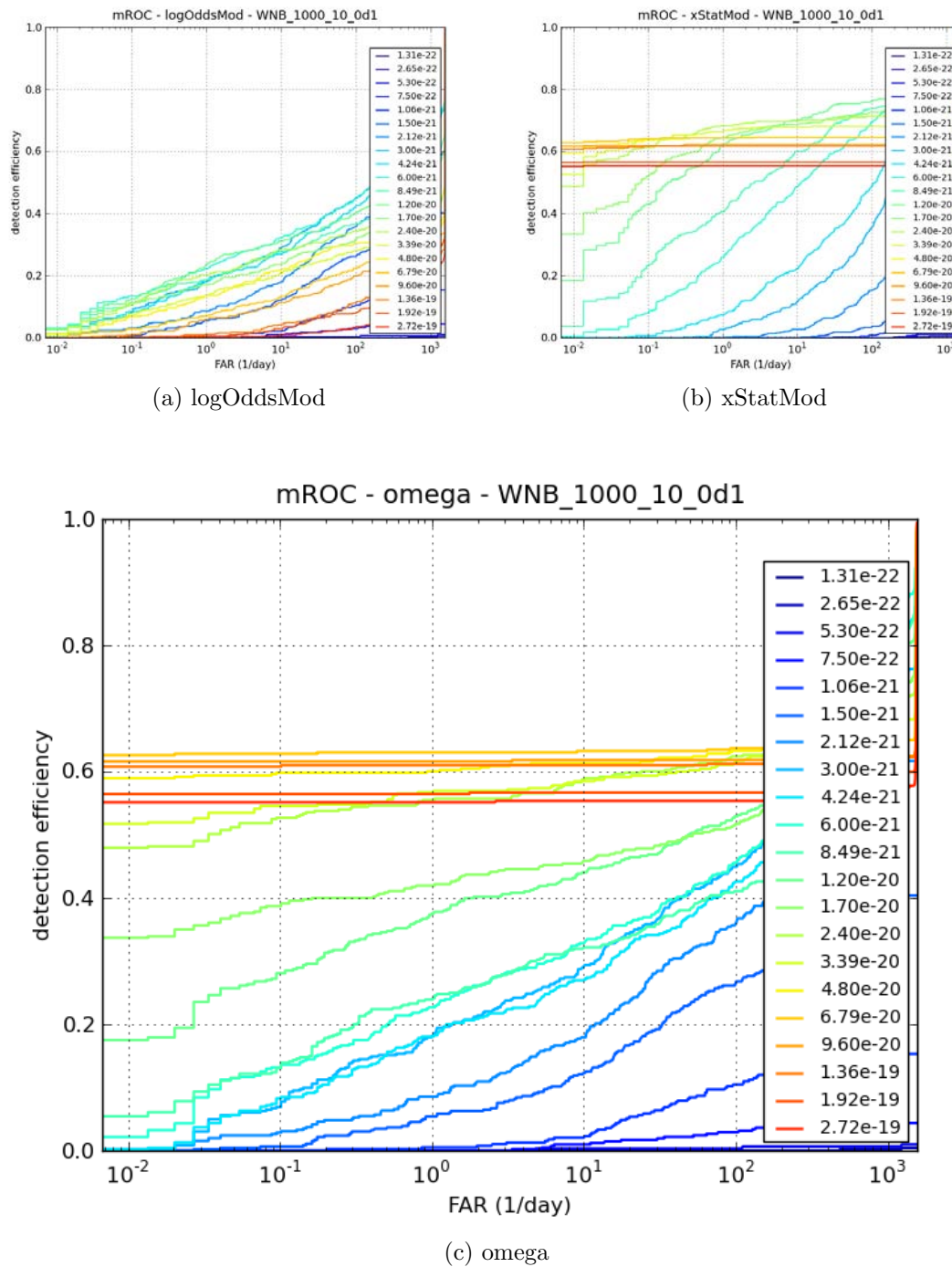


Figure A-93: WNB_1000_10_0d1 ROC plots

A.5.4 WNB_100_100_0d1 injections

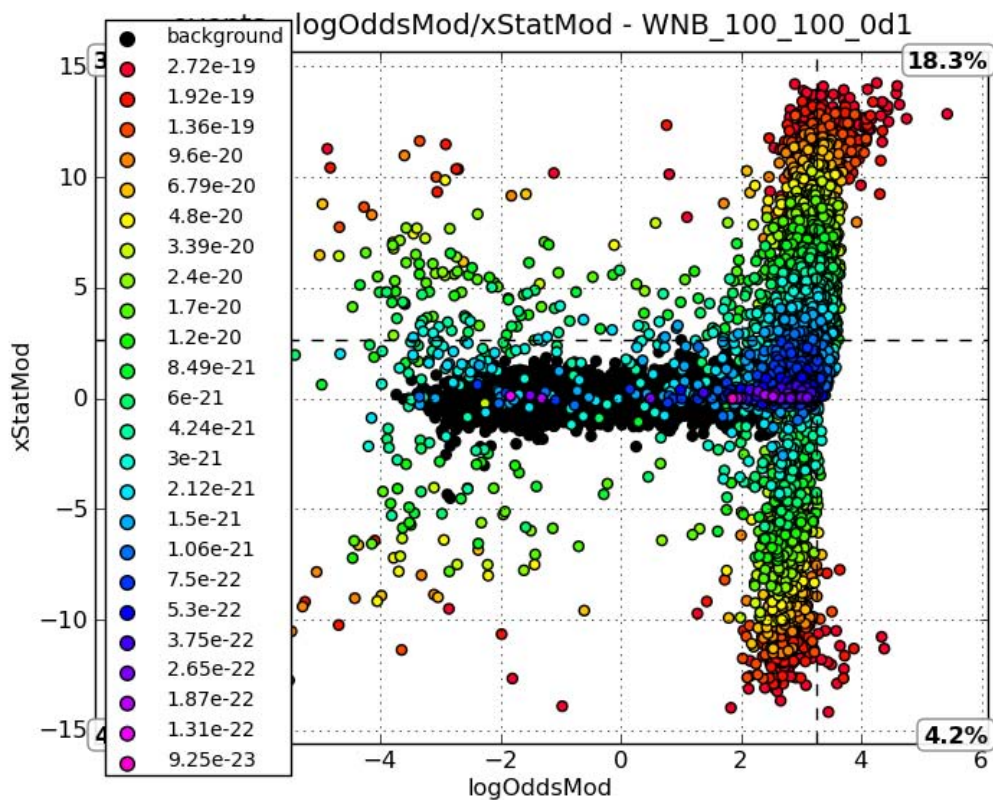


Figure A-94: WNB_100_100_0d1 injections scatter plot. Colors represent injection strain amplitude.

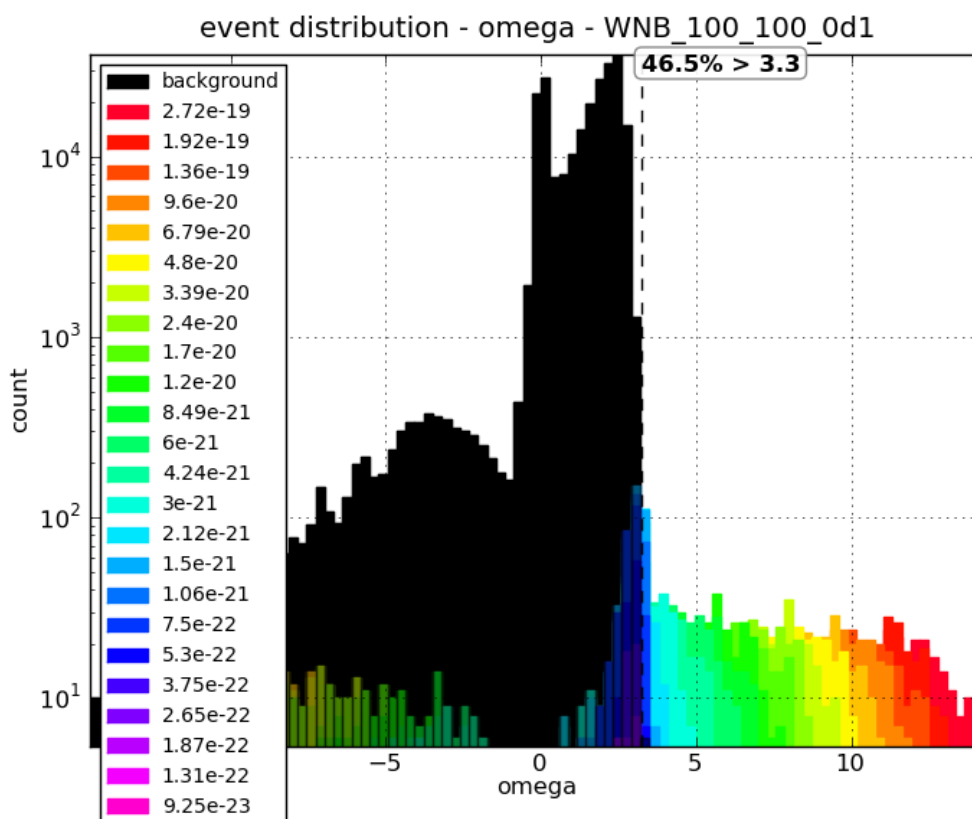
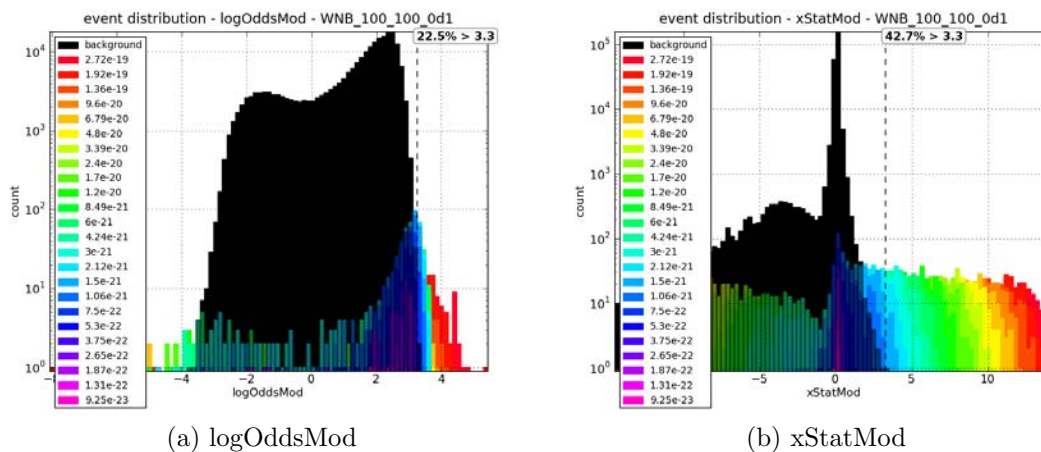
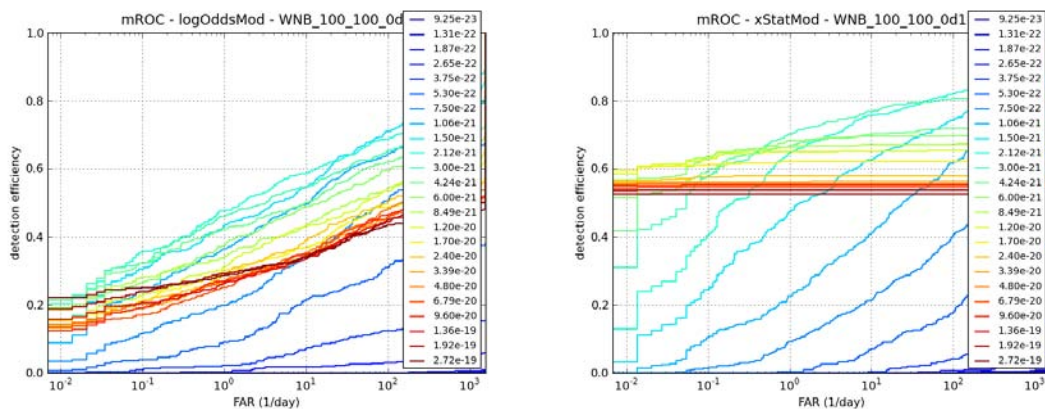
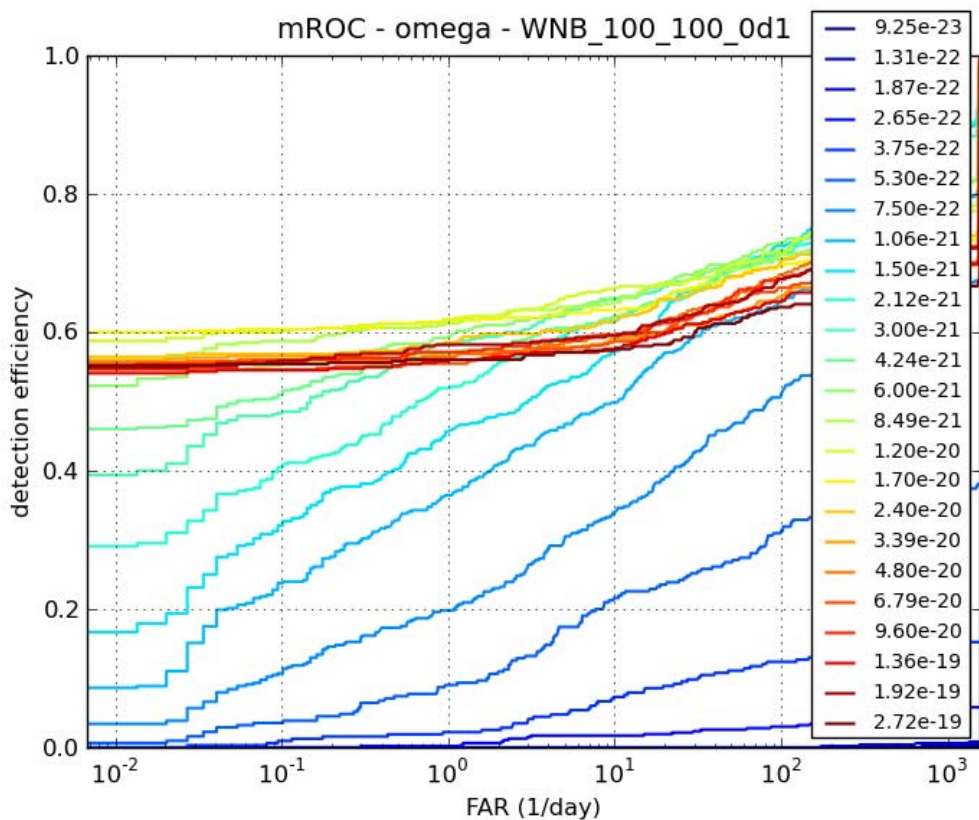


Figure A-95: WNB_100_100_0d1 injections histograms. Colors represent injection strain amplitude.



(a) logOddsMod

(b) xStatMod



(c) omega

Figure A-96: WNB_100_100_0d1 ROC plots

A.5.5 WNB_250_100_0d1 injections

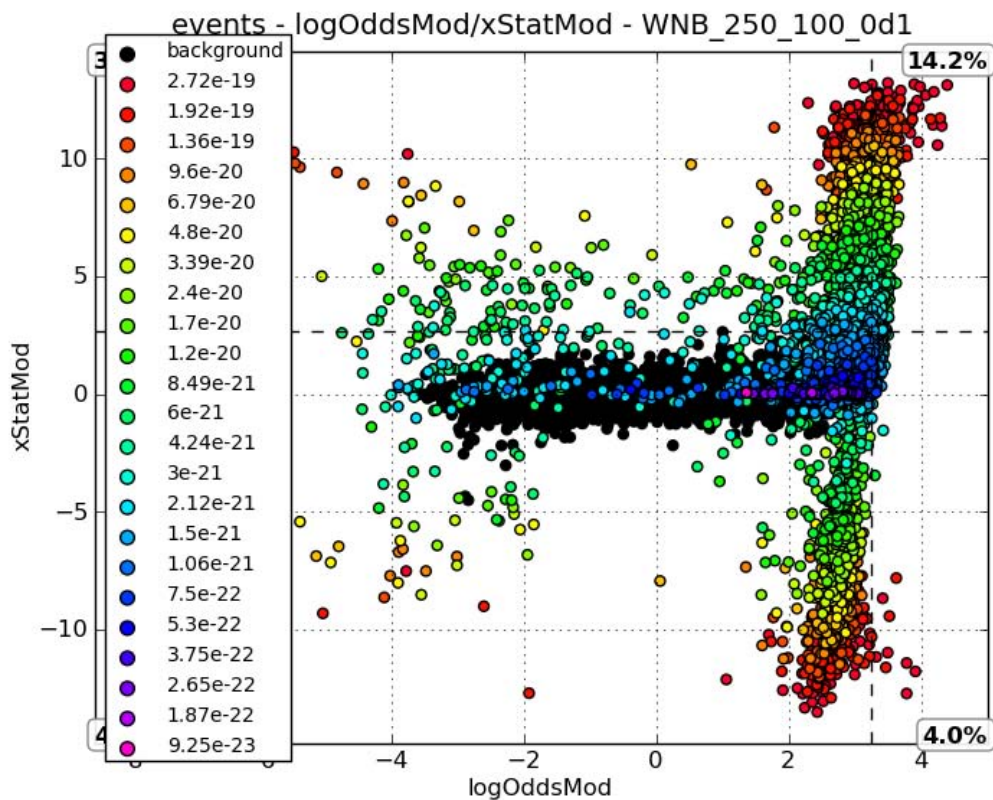
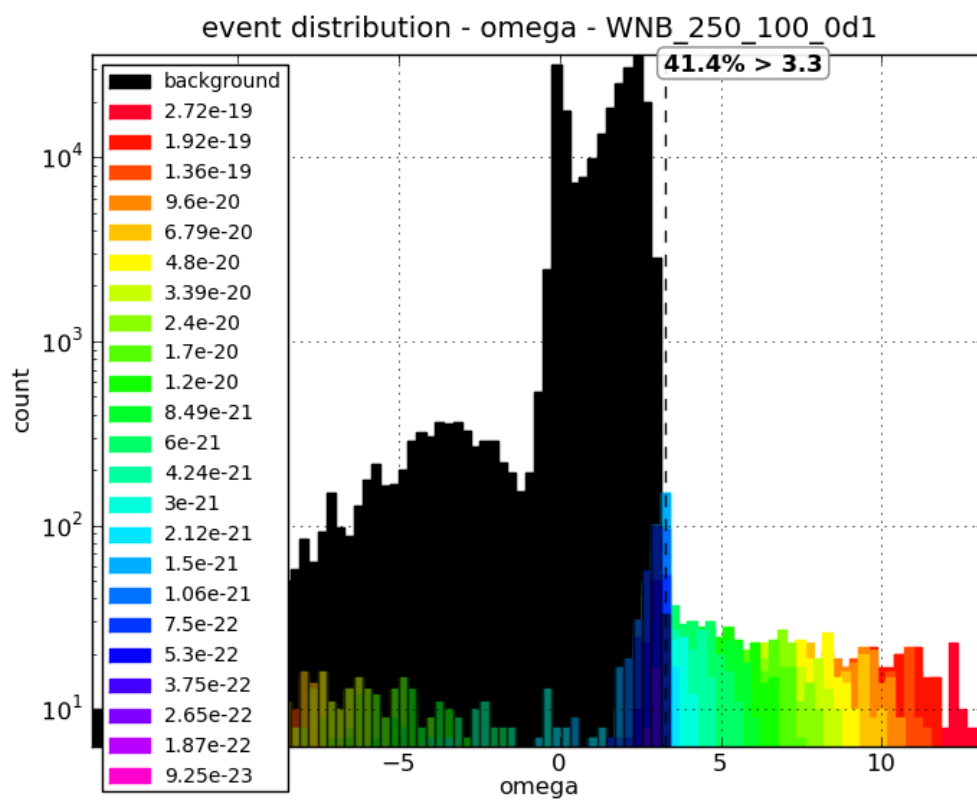
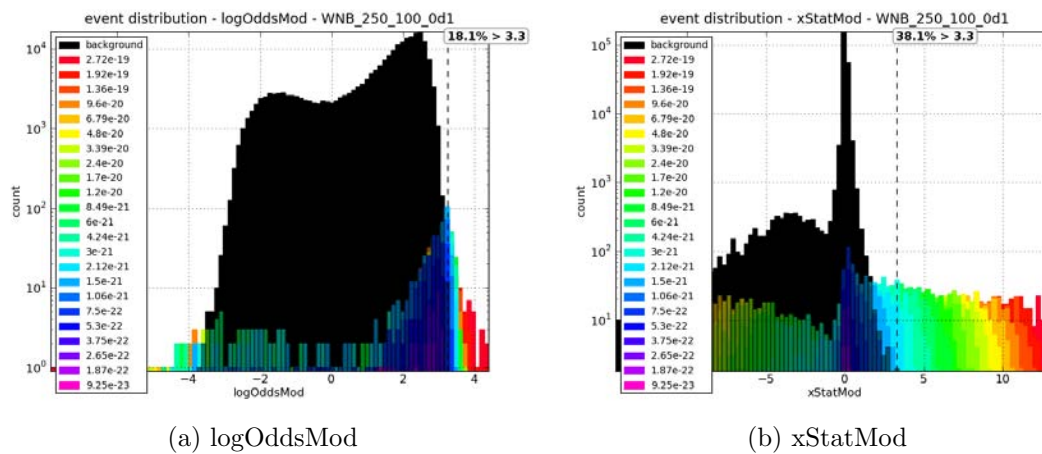
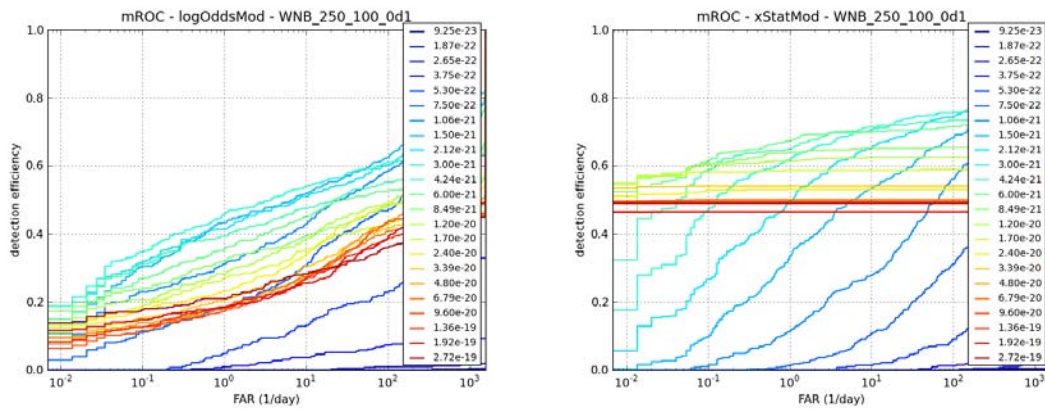


Figure A-97: WNB_250_100_0d1 injections scatter plot. Colors represent injection strain amplitude.



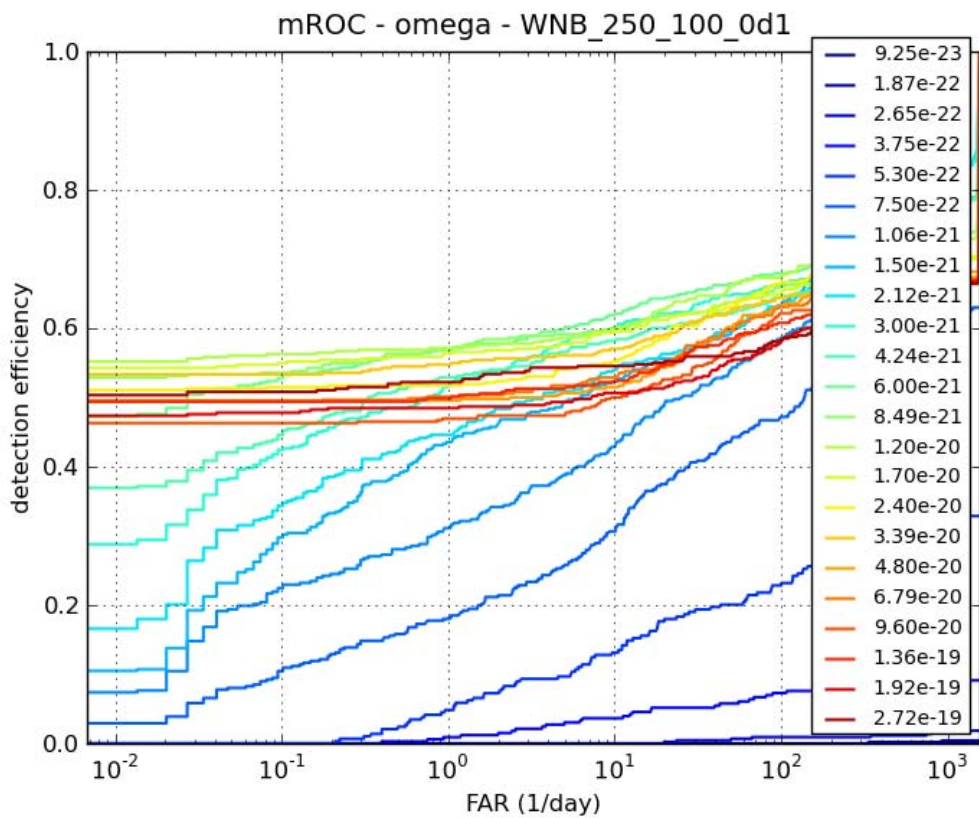
(c) omega

Figure A-98: WNB_250_100_0d1 injections histograms. Colors represent injection strain amplitude.



(a) logOddsMod

(b) xStatMod



(c) omega

Figure A-99: WNB.250.100.0d1 ROC plots

Appendix B

Sky Position Coordinate Transformation

The GW data analysis pipelines, such as Ω -Pipeline, use coordinates practically convenient to the detector network. Times are measured in GPS¹ seconds. Sky positions are measured in earth-fixed coordinates θ, ϕ , with the origin being the center of the earth. θ is the latitudinal angle measured down from the North Pole. ϕ is the longitudinal angle measured from the Prime Meridian ($0, 2\pi$). Conversion to right ascension (RA) and declination (DEC) are as follows:

$$\text{RA} = \phi + \text{GMST} \tag{B.1}$$

$$\text{DEC} = 90^\circ - \frac{180^\circ}{\pi}\theta, \tag{B.2}$$

where GMST is the *Greenwich mean sidereal time* of the event. The conversion from GPS to GMST is done with the following algorithm:

¹http://en.wikipedia.org/wiki/Global_Positioning_System

$$\begin{aligned}GPS_REF &= 630763213 \\LEAP_SECONDS &= 2 \\D &= \text{round}((GPS - GPS_REF)/(3600 * 24)) - 0.5 \\T &= D/36525 \\GMST_00 &= 6.697374558 + 2400.051336 * T + 0.000025862 * (T^2) \\GMST_00 &= \text{mod}(GMST_00, 24) \\UTC_SECONDS &= GPS - GPS_REF - 12 * 3600 - LEAP_SECONDS \\UTC_HOURS &= \text{mod}(UTC_SEC/3600, 24) \\GMST &= GMST_00 + (UTC_HOURS * 1.002737909) \\GMST &= \text{mod}(GMST, 24)\end{aligned}$$

Bibliography

- [1] Laser Interferometer Gravitational-wave Observatory (LIGO). <http://ligo.org>. 1, 21, 22
- [2] A. Abramovici, W. E. Althouse, R. W. P. Drever, Y. Gursel, S. Kawamura, F. J. Raab, D. Shoemaker, L. Sievers, R. E. Spero, and K. S. Thorne. LIGO - The Laser Interferometer Gravitational-Wave Observatory. *Science*, 256:325–333, April 1992. doi:10.1126/science.256.5055.325. 1
- [3] B. C. Barish and R. Weiss. LIGO and the detection of gravitational waves. *Physics Today*, 52:44–50, October 1999. doi:10.1063/1.882861. 1
- [4] B. P. Abbott, R. Abbott, R. Adhikari, P. Ajith, B. Allen, G. Allen, R. S. Amin, S. B. Anderson, W. G. Anderson, M. A. Arain, and et al. LIGO: the Laser Interferometer Gravitational-Wave Observatory. *Reports on Progress in Physics*, 72(7):076901–+, July 2009. arXiv:0711.3041, doi:10.1088/0034-4885/72/7/076901. 1, 25, 33, 36, 42, 43
- [5] E. Costa, F. Frontera, J. Heise, M. Feroci, J. in't Zand, F. Fiore, M. N. Cinti, D. Dal Fiume, L. Nicastro, M. Orlandini, E. Palazzi, M. Rapisarda#, G. Zavattini, R. Jager, A. Parmar, A. Owens, S. Molendi, G. Cusumano, M. C. Maccarone, S. Giarrusso, A. Coletta, L. A. Antonelli, P. Giommi, J. M. Muller, L. Piro, and R. C. Butler. Discovery of an X-ray afterglow associated

- with the γ -ray burst of 28 February 1997. *Nature*, 387:783–785, June 1997. [arXiv:arXiv:astro-ph/9706065](#), [doi:10.1038/42885](#). 3, 52
- [6] Sean M. Carroll. *Spacetime and Geometry*. Addison Wesley, 2004. 8, 16
- [7] Bernard F. Schutz. *A first course in general relativity*. Cambridge University Press, 1990. 9
- [8] Charles W. Misner, Kip S. Thorne, and John Archibald Wheeler. *Gravitation*. W. H. Freeman and Company, New York, 1973. 10
- [9] R. A. Hulse and H. J. Taylor. Discovery of a Pulsar in a Close Binary System. In *Bulletin of the American Astronomical Society*, volume 6 of *Bulletin of the American Astronomical Society*, pages 453–+, September 1974. 17
- [10] R. A. Hulse and J. H. Taylor. Discovery of a pulsar in a binary system. *ApJ*, 195:L51–L53, January 1975. [doi:10.1086/181708](#). 17
- [11] J. H. Taylor and J. M. Weisberg. Further experimental tests of relativistic gravity using the binary pulsar PSR 1913 + 16. *ApJ*, 345:434–450, October 1989. [doi:10.1086/167917](#). 17
- [12] J. H. Taylor, Jr. Binary pulsars and relativistic gravity. *Reviews of Modern Physics*, 66:711–719, July 1994. [doi:10.1103/RevModPhys.66.711](#). 17
- [13] J. M. Weisberg and J. H. Taylor. The Relativistic Binary Pulsar B1913+16: Thirty Years of Observations and Analysis. In F. A. Rasio & I. H. Stairs, editor, *Binary Radio Pulsars*, volume 328 of *Astronomical Society of the Pacific Conference Series*, pages 25–+, July 2005. [arXiv:arXiv:astro-ph/0407149](#). 18
- [14] K. S. Thorne. Gravitational radiation. In Stephen W. Hawking and W. Isreal, editors, *300 Years of Gravitation*. Cambridge University Press, 1989. 19

- [15] P. R. Saulson. If light waves are stretched by gravitational waves, how can we use light as a ruler to detect gravitational waves? *American Journal of Physics*, 65:501–505, June 1997. doi:10.1119/1.18578. 20
- [16] V. Faraoni. A common misconception about LIGO detectors of gravitational waves. *General Relativity and Gravitation*, 39:677–684, May 2007. doi:10.1007/s10714-007-0415-5. 20
- [17] Virgo. <http://www.ego-gw.it/>. 21, 22
- [18] GEO600. <http://www.geo600.org/>. 21, 22
- [19] TAMA. <http://tamago.mtk.nao.ac.jp/>. 21, 22
- [20] P. Barriga, D. G. Blair, D. Coward, J. Davidson, J.-C. Dumas, E. Howell, L. Ju, L. Wen, C. Zhao, D. E. McClelland, S. M. Scott, B. J. J. Slagmolen, R. Inta, J. Munch, D. J. Ottaway, P. Veitch, D. Hosken, A. Melatos, C. Chung, L. Sammut, D. K. Galloway, J. Marx, S. Whitcomb, D. Shoemaker, S. A. Hughes, D. H. Reitze, B. R. Iyer, S. V. Dhurandhar, T. Souradeep, C. S. Unnikrishnan, G. Rajalakshmi, C. N. Man, A. Heidmann, P.-F. Cohadon, T. Briant, H. Grote, K. Danzmann, H. Lück, B. Willke, K. A. Strain, B. S. Sathyaprakash, J. Cao, Y.-K. E. Cheung, and Y. Zhang. AIGO: a southern hemisphere detector for the worldwide array of ground-based interferometric gravitational wave detectors. *Classical and Quantum Gravity*, 27(8):084005–+, April 2010. doi:10.1088/0264-9381/27/8/084005. 22, 139
- [21] Large-scale Cryogenic Gravitational-wave Telescope (LCGT). <http://gw.icrr.u-tokyo.ac.jp/lcgt/>. 22, 44
- [22] Einstein Telescope. <http://www.et-gw.eu/>. 22, 44
- [23] Deci-hertz Interferometer Gravitational-wave Observatory (DECIGO). http://tamago.mtk.nao.ac.jp/decigo/index_E.html. 22, 44

- [24] Laser Interferometer Satellite Array (LISA). <http://www.et-gw.eu/>. 22, 44
- [25] R. W. P. Drever, J. L. Hall, F. V. Kowalski, J. Hough, G. M. Ford, A. J. Munley, and H. Ward. Laser phase and frequency stabilization using an optical resonator. *Applied Physics B: Lasers and Optics*, 31:97–105, June 1983. doi: 10.1007/BF00702605. 25, 26
- [26] Rana Adhikari. *Sensitivity and Noise Analysis of 4 km Laser Interferometric Gravitational Wave Antennae*. PhD thesis, Masechussets Institute of Technology, 2004. 27
- [27] F. Acernese, F. Antonucci, S. Aoudia, K. G. Arun, P. Astone, G. Ballardín, F. Barone, M. Barsuglia, T. S. Bauer, M. G. Beker, S. Bigotta, S. Birindelli, M. Bitossi, M. A. Bizouard, M. Blom, C. Boccara, F. Bondu, L. Bonelli, L. Bosi, S. Braccini, C. Bradaschia, A. Brillet, V. Brisson, R. Budzyński, T. Bulik, H. J. Bulten, D. Buskulic, G. Cagnoli, E. Calloni, E. Campagna, B. Canuel, F. Carbognani, F. Cavalier, R. Cavalieri, G. Cella, E. Cesarini, E. Chassande-Mottin, A. Chincarini, F. Cleva, E. Coccia, C. N. Colacino, J. Colas, A. Colla, M. Colombini, C. Corda, A. Corsi, J.-P. Coulon, E. Cuoco, S. D’Antonio, A. Dari, V. Dattilo, M. Davier, R. Day, R. de Rosa, M. Del Prete, L. di Fiore, A. di Lieto, M. di Paolo Emilio, A. di Virgilio, A. Dietz, M. Drago, V. Fafone, I. Ferrante, F. Fidecaro, I. Fiori, R. Flaminio, J.-D. Fournier, J. Franc, S. Frasca, F. Frasconi, A. Freise, L. Gammaitoni, F. Garufi, G. Gemme, E. Genin, A. Gennai, A. Giazotto, M. Granata, C. Greverie, G. Guidi, H. Heitmann, P. Hello, S. Hild, D. Huet, P. Jaranowski, I. Kowalska, A. Królak, P. La Penna, N. Leroy, N. Letendre, T. G. F. Li, M. Lorenzini, V. Loriette, G. Losurdo, J.-M. Mackowski, E. Majorana, N. Man, M. Manto-vani, F. Marchesoni, F. Marion, J. Marque, F. Martelli, A. Masserot, F. Menzinger, C. Michel, L. Milano, Y. Minenkov, M. Mohan, J. Moreau, N. Morgado, A. Morgia, S. Mosca, V. Moscatelli, B. Mours, I. Neri, F. Nocera, G. Pagliaroli,

- C. Palomba, F. Paoletti, S. Pardi, M. Parisi, A. Pasqualetti, R. Passaquieti, D. Passuello, G. Persichetti, M. Pichot, F. Piergiovanni, M. Pietka, L. Pinard, R. Poggiani, M. Prato, G. A. Prodi, M. Punturo, P. Puppo, O. Rabaste, D. S. Rabeling, P. Rapagnani, V. Re, T. Regimbau, F. Ricci, F. Robinet, A. Rocchi, L. Rolland, R. Romano, D. Rosińska, P. Ruggi, F. Salemi, B. Sassolas, D. Sentenac, R. Sturani, B. Swinkels, A. Toncelli, M. Tonelli, E. Tournefier, F. Travasso, J. Trummer, G. Vajente, J. F. J. van den Brand, S. van der Putten, M. Vavoulidis, G. Vedovato, D. Verkindt, F. Vetrano, A. Viceré, J.-Y. Vinet, H. Vocca, M. Was, and M. Yvert. Measurements of Superattenuator seismic isolation by Virgo interferometer. *Astroparticle Physics*, 33:182–189, April 2010. doi:10.1016/j.astropartphys.2010.01.006. 30
- [28] B. J. Meers. The frequency response of interferometric gravitational wave detectors. *Physics Letters A*, 142:465–470, December 1989. doi:10.1016/0375-9601(89)90515-X. 32
- [29] R. del Fabbro and V. Montelatici. Interferometric antenna response for gravitational-wave detection. *Appl. Opt.*, 34:4380–+, July 1995. 32
- [30] M. Rakhmanov, J. D. Romano, and J. T. Whelan. High-frequency corrections to the detector response and their effect on searches for gravitational waves. *Classical and Quantum Gravity*, 25(18):184017–+, September 2008. arXiv:0808.3805, doi:10.1088/0264-9381/25/18/184017. 32
- [31] H. B. Callen and T. A. Welton. Irreversibility and Generalized Noise. *Physical Review*, 83:34–40, July 1951. doi:10.1103/PhysRev.83.34. 37
- [32] P. R. Saulson. Thermal noise in mechanical experiments. *Phys. Rev. D*, 42:2437–2445, October 1990. doi:10.1103/PhysRevD.42.2437. 37
- [33] Y. Levin. Internal thermal noise in the LIGO test masses: A direct approach.

- Phys. Rev. D, 57:659–663, January 1998. arXiv:arXiv:gr-qc/9707013, doi:10.1103/PhysRevD.57.659. 37
- [34] Brian Thomas Lantz. *Quantum Limited Optical Phase Detection in a High Power Suspended Interferometer*. PhD thesis, Massachusetts Institute of Technology, 1999. 40
- [35] Advanced LIGO. <http://www.ligo.caltech.edu/advLIGO/>. 42
- [36] Advanced Virgo. <http://wwwcascina.virgo.infn.it/advirgo/>. 44
- [37] E. Chassande-Mottin, M. Hendry, P. J. Sutton, and S. Márka. Multi-messenger astronomy with the Einstein Telescope. *General Relativity and Gravitation*, pages 109–+, June 2010. arXiv:1004.1964, doi:10.1007/s10714-010-1019-z. 45
- [38] J. S. Bloom, D. E. Holz, S. A. Hughes, K. Menou, A. Adams, S. F. Anderson, A. Becker, G. C. Bower, N. Brandt, B. Cobb, K. Cook, A. Corsi, S. Covino, D. Fox, A. Fruchter, C. Fryer, J. Grindlay, D. Hartmann, Z. Haiman, B. Kocsis, L. Jones, A. Loeb, S. Marka, B. Metzger, E. Nakar, S. Nissanke, D. A. Perley, T. Piran, D. Poznanski, T. Prince, J. Schnittman, A. Soderberg, M. Strauss, P. S. Shawhan, D. H. Shoemaker, J. Sievers, C. Stubbs, G. Tagliaferri, P. Ubertini, and P. Wozniak. Astro2010 Decadal Survey Whitepaper: Coordinated Science in the Gravitational and Electromagnetic Skies. *ArXiv e-prints*, February 2009. arXiv:0902.1527. 45
- [39] B. Abbott, R. Abbott, R. Adhikari, P. Ajith, B. Allen, G. Allen, R. Amin, S. B. Anderson, W. G. Anderson, M. A. Arain, and et al. Astrophysically triggered searches for gravitational waves: status and prospects. *Classical and Quantum Gravity*, 25(11):114051–+, June 2008. arXiv:0802.4320, doi:10.1088/0264-9381/25/11/114051. 47

- [40] J. Pacione, S. Marka, P. S. Shawhan, J. Kanner, T. L. Huard, and D. C. Murphy. LOOC UP: Locating and Observing Optical Counterparts to Unmodeled Pulses in Gravitational Waves. In *Bulletin of the American Astronomical Society*, volume 38 of *Bulletin of the American Astronomical Society*, pages 910–+, December 2007. 47
- [41] Swift Gamma-Ray Burst Mission. <http://swift.gsfc.nasa.gov/>. 47, 121
- [42] Third Interplanetary Network (IPN 3). <http://www.ssl.berkeley.edu/ipn3/>. 47
- [43] B. Abbott, R. Abbott, R. Adhikari, A. Ageev, B. Allen, R. Amin, S. B. Anderson, W. G. Anderson, M. Araya, H. Armandula, and et al. Search for gravitational waves associated with the gamma ray burst GRB030329 using the LIGO detectors. *Phys. Rev. D*, 72(4):042002–+, August 2005. [arXiv:arXiv:gr-qc/0501068](https://arxiv.org/abs/gr-qc/0501068), [doi:10.1103/PhysRevD.72.042002](https://doi.org/10.1103/PhysRevD.72.042002). 47
- [44] B. Abbott, R. Abbott, R. Adhikari, J. Agresti, P. Ajith, B. Allen, R. Amin, S. B. Anderson, W. G. Anderson, M. Arain, and et al. Implications for the Origin of GRB 070201 from LIGO Observations. *ApJ*, 681:1419–1430, July 2008. [arXiv:0711.1163](https://arxiv.org/abs/0711.1163), [doi:10.1086/587954](https://doi.org/10.1086/587954). 47
- [45] B. Abbott, R. Abbott, R. Adhikari, J. Agresti, P. Ajith, B. Allen, R. Amin, S. B. Anderson, W. G. Anderson, M. Arain, and et al. Search for gravitational waves associated with 39 gamma-ray bursts using data from the second, third, and fourth LIGO runs. *Phys. Rev. D*, 77(6):062004–+, March 2008. [arXiv:0709.0766](https://arxiv.org/abs/0709.0766), [doi:10.1103/PhysRevD.77.062004](https://doi.org/10.1103/PhysRevD.77.062004). 47
- [46] B. P. Abbott, R. Abbott, F. Acernese, R. Adhikari, P. Ajith, B. Allen, G. Allen, M. Alshourbagy, R. S. Amin, S. B. Anderson, and et al. Search For Gravitational-wave Bursts Associated with Gamma-ray Bursts using Data

- from LIGO Science Run 5 and Virgo Science Run 1. *ApJ*, 715:1438–1452, June 2010. [arXiv:0908.3824](#), [doi:10.1088/0004-637X/715/2/1438](#). 47
- [47] J. Abadie, B. P. Abbott, R. Abbott, T. Accadia, F. Acernese, R. Adhikari, P. Ajith, B. Allen, G. Allen, E. Amador Ceron, and et al. Search for Gravitational-wave Inspiral Signals Associated with Short Gamma-ray Bursts During LIGO’s Fifth and Virgo’s First Science Run. *ApJ*, 715:1453–1461, June 2010. [arXiv:1001.0165](#), [doi:10.1088/0004-637X/715/2/1453](#). 47, 50
- [48] P. Kalmus, R. Khan, L. Matone, and S. Márka. Search method for unmodeled transient gravitational waves associated with SGR flares. *Classical and Quantum Gravity*, 24:659–+, October 2007. [doi:10.1088/0264-9381/24/19/S28](#). 48
- [49] B. Abbott, R. Abbott, R. Adhikari, P. Ajith, B. Allen, G. Allen, R. Amin, S. B. Anderson, W. G. Anderson, M. A. Arain, and et al. Search for Gravitational-Wave Bursts from Soft Gamma Repeaters. *Physical Review Letters*, 101(21):211102–+, November 2008. [arXiv:0808.2050](#), [doi:10.1103/PhysRevLett.101.211102](#). 48
- [50] B. P. Abbott, R. Abbott, R. Adhikari, P. Ajith, B. Allen, G. Allen, R. S. Amin, S. B. Anderson, W. G. Anderson, M. A. Arain, and et al. Stacked Search for Gravitational Waves from the 2006 SGR 1900+14 Storm. *ApJ*, 701:L68–L74, August 2009. [arXiv:0905.0005](#), [doi:10.1088/0004-637X/701/2/L68](#). 48
- [51] B. Abbott, R. Abbott, R. Adhikari, J. Agresti, P. Ajith, B. Allen, R. Amin, S. B. Anderson, W. G. Anderson, M. Arain, and et al. Search for gravitational wave radiation associated with the pulsating tail of the SGR 1806-20 hyperflare of 27 December 2004 using LIGO. *Phys. Rev. D*, 76(6):062003–+, September 2007. [arXiv:arXiv:astro-ph/0703419](#), [doi:10.1103/PhysRevD.76.062003](#). 48

- [52] ANTARES Collaboration. <http://antares.in2p3.fr/>. 48
- [53] IceCube Neutrino Observatory. <http://icecube.wisc.edu/>. 48
- [54] E. S. Phinney. The rate of neutron star binary mergers in the universe - Minimal predictions for gravity wave detectors. *ApJ*, 380:L17–L21, October 1991. doi:10.1086/186163. 50
- [55] V. Kalogera, R. Narayan, D. N. Spergel, and J. H. Taylor. The Coalescence Rate of Double Neutron Star Systems. *ApJ*, 556:340–356, July 2001. arXiv:arXiv:astro-ph/0012038, doi:10.1086/321583. 50, 56
- [56] K. Belczynski, V. Kalogera, and T. Bulik. A Comprehensive Study of Binary Compact Objects as Gravitational Wave Sources: Evolutionary Channels, Rates, and Physical Properties. *ApJ*, 572:407–431, June 2002. arXiv:arXiv:astro-ph/0111452, doi:10.1086/340304. 50
- [57] V. Kalogera, C. Kim, D. R. Lorimer, M. Burgay, N. D’Amico, A. Possenti, R. N. Manchester, A. G. Lyne, B. C. Joshi, M. A. McLaughlin, M. Kramer, J. M. Sarkissian, and F. Camilo. The Cosmic Coalescence Rates for Double Neutron Star Binaries. *ApJ*, 601:L179–L182, February 2004. doi:10.1086/382155. 50
- [58] J. A. de Freitas Pacheco, T. Regimbau, S. Vincent, and A. Spallicci. Expected Coalescence Rates of Ns-Ns Binaries for Laser Beam Interferometers. *International Journal of Modern Physics D*, 15:235–249, 2006. arXiv:arXiv:astro-ph/0510727, doi:10.1142/S0218271806007699. 50
- [59] J. Abadie, B. P. Abbott, R. Abbott, M. Abernathy, T. Accadia, F. Acernese, C. Adams, R. Adhikari, P. Ajith, B. Allen, and et al. TOPICAL REVIEW: Predictions for the rates of compact binary coalescences observable by ground-based gravitational-wave detectors. *Classical and Quantum Gravity*, 27(17):173001–+, September 2010. arXiv:1003.2480, doi:10.1088/0264-9381/27/17/173001. 50

- [60] E. Poisson. Gravitational radiation from a particle in circular orbit around a black hole. I. Analytical results for the nonrotating case. *Phys. Rev. D*, 47:1497–1510, February 1993. doi:10.1103/PhysRevD.47.1497. 50
- [61] L. Lindblom, B. J. Owen, and D. A. Brown. Model waveform accuracy standards for gravitational wave data analysis. *Phys. Rev. D*, 78(12):124020–+, December 2008. arXiv:0809.3844, doi:10.1103/PhysRevD.78.124020. 50
- [62] M. Tessmer and G. Schaefer. Full-analytic frequency-domain 1pN-accurate gravitational wave forms from eccentric compact binaries. *ArXiv e-prints*, June 2010. arXiv:1006.3714. 50
- [63] J. G. Baker, J. R. van Meter, S. T. McWilliams, J. Centrella, and B. J. Kelly. Consistency of Post-Newtonian Waveforms with Numerical Relativity. *Physical Review Letters*, 99(18):181101–+, November 2007. arXiv:arXiv:gr-qc/0612024, doi:10.1103/PhysRevLett.99.181101. 50
- [64] M. A. Scheel, M. Boyle, T. Chu, L. E. Kidder, K. D. Matthews, and H. P. Pfeiffer. High-accuracy waveforms for binary black hole inspiral, merger, and ringdown. *Phys. Rev. D*, 79(2):024003–+, January 2009. arXiv:0810.1767, doi:10.1103/PhysRevD.79.024003. 50
- [65] P. Ajith, M. Hannam, S. Husa, Y. Chen, B. Bruegmann, N. Dorband, D. Mueller, F. Ohme, D. Pollney, C. Reisswig, L. Santamaria, and J. Seiler. Inspiral-merger-ringdown waveforms for black-hole binaries with non-precessing spins. *ArXiv e-prints*, September 2009. arXiv:0909.2867. 50
- [66] B. Abbott, R. Abbott, R. Adhikari, A. Ageev, B. Allen, R. Amin, S. B. Anderson, W. G. Anderson, M. Araya, H. Armandula, and et al. Search for gravitational waves from primordial black hole binary coalescences in the galactic halo. *Phys. Rev. D*, 72(8):082002–+, October 2005. arXiv:arXiv:gr-qc/0505042, doi:10.1103/PhysRevD.72.082002. 50

- [67] S. Fairhurst, the LIGO Scientific Collaboration, H. Takahashi, and the TAMA Collaboration. Status of the joint LIGO TAMA300 inspiral analysis. *Classical and Quantum Gravity*, 22:1109–+, September 2005. [arXiv:arXiv:gr-qc/0504128](#), [doi:10.1088/0264-9381/22/18/S25](#). 50
- [68] B. Abbott, R. Abbott, R. Adhikari, A. Ageev, J. Agresti, P. Ajith, B. Allen, J. Allen, R. Amin, S. B. Anderson, and et al. Search for gravitational waves from binary black hole inspirals in LIGO data. *Phys. Rev. D*, 73(6):062001–+, March 2006. [arXiv:arXiv:gr-qc/0509129](#), [doi:10.1103/PhysRevD.73.062001](#). 50
- [69] B. Abbott, R. Abbott, R. Adhikari, A. Ageev, J. Agresti, P. Ajith, B. Allen, J. Allen, R. Amin, S. B. Anderson, and et al. Joint LIGO and TAMA300 search for gravitational waves from inspiralling neutron star binaries. *Phys. Rev. D*, 73(10):102002–+, May 2006. [arXiv:arXiv:gr-qc/0512078](#), [doi:10.1103/PhysRevD.73.102002](#). 50
- [70] A. Dietz and the LIGO Scientific Collaboration. Overview of LIGO Scientific Collaboration inspiral searches. *Classical and Quantum Gravity*, 23:705–+, October 2006. [doi:10.1088/0264-9381/23/19/S08](#). 50
- [71] L. M. Goggin and the LIGO Scientific Collaboration. Search for black hole ringdown signals in LIGO S4 data. *Classical and Quantum Gravity*, 23:709–+, October 2006. [doi:10.1088/0264-9381/23/19/S09](#). 50
- [72] B. Abbott, R. Abbott, R. Adhikari, J. Agresti, P. Ajith, B. Allen, R. Amin, S. B. Anderson, W. G. Anderson, M. Arain, and et al. Search for gravitational waves from binary inspirals in S3 and S4 LIGO data. *Phys. Rev. D*, 77(6):062002–+, March 2008. [arXiv:0704.3368](#), [doi:10.1103/PhysRevD.77.062002](#). 50
- [73] B. Abbott, R. Abbott, R. Adhikari, J. Agresti, P. Ajith, B. Allen, R. Amin, S. B. Anderson, W. G. Anderson, M. Arain, and et al. Search of S3 LIGO data for gravitational wave signals from spinning black hole and neutron star binary

- inspirals. *Phys. Rev. D*, 78(4):042002–+, August 2008. [arXiv:0712.2050](#), [doi:10.1103/PhysRevD.78.042002](#). 50
- [74] B. P. Abbott, R. Abbott, R. Adhikari, P. Ajith, B. Allen, G. Allen, R. S. Amin, S. B. Anderson, W. G. Anderson, M. A. Arain, and et al. Search for gravitational wave ringdowns from perturbed black holes in LIGO S4 data. *Phys. Rev. D*, 80(6):062001–+, September 2009. [arXiv:0905.1654](#), [doi:10.1103/PhysRevD.80.062001](#). 50
- [75] B. P. Abbott, R. Abbott, R. Adhikari, P. Ajith, B. Allen, G. Allen, R. S. Amin, S. B. Anderson, W. G. Anderson, M. A. Arain, and et al. Search for gravitational waves from low mass compact binary coalescence in 186 days of LIGO’s fifth science run. *Phys. Rev. D*, 80(4):047101–+, August 2009. [arXiv:0905.3710](#), [doi:10.1103/PhysRevD.80.047101](#). 50
- [76] D. Buskulic, Virgo Collaboration, and LIGO Scientific Collaboration. Very low latency search pipeline for low mass compact binary coalescences in the LIGO S6 and Virgo VSR2 data. *Classical and Quantum Gravity*, 27(19):194013–+, October 2010. [doi:10.1088/0264-9381/27/19/194013](#). 50
- [77] I. Horváth. A further study of the BATSE Gamma-Ray Burst duration distribution. *A&A*, 392:791–793, September 2002. [arXiv:arXiv:astro-ph/0205004](#), [doi:10.1051/0004-6361:20020808](#). 51
- [78] S. E. Woosley and J. S. Bloom. The Supernova Gamma-Ray Burst Connection. *ARA&A*, 44:507–556, September 2006. [arXiv:arXiv:astro-ph/0609142](#), [doi:10.1146/annurev.astro.43.072103.150558](#). 51, 59
- [79] K. Belczynski, R. Perna, T. Bulik, V. Kalogera, N. Ivanova, and D. Q. Lamb. A Study of Compact Object Mergers as Short Gamma-Ray Burst Progenitors. *ApJ*, 648:1110–1116, September 2006. [arXiv:arXiv:astro-ph/0601458](#), [doi:10.1086/505169](#). 51

- [80] E. Nakar. Short-hard gamma-ray bursts. *Phys. Rep.*, 442:166–236, April 2007. [arXiv:arXiv:astro-ph/0701748](#), [doi:10.1016/j.physrep.2007.02.005](#). 51, 52
- [81] W. H. Lee and E. Ramirez-Ruiz. The progenitors of short gamma-ray bursts. *New Journal of Physics*, 9:17–+, January 2007. [arXiv:arXiv:astro-ph/0701874](#), [doi:10.1088/1367-2630/9/1/017](#). 51, 52, 54
- [82] N. Gehrels, C. L. Sarazin, P. T. O’Brien, B. Zhang, L. Barbier, S. D. Barthelmy, A. Blustin, D. N. Burrows, J. Cannizzo, J. R. Cummings, M. Goad, S. T. Holland, C. P. Hurkett, J. A. Kennea, A. Levan, C. B. Markwardt, K. O. Mason, P. Meszaros, M. Page, D. M. Palmer, E. Rol, T. Sakamoto, R. Willingale, L. Angelini, A. Beardmore, P. T. Boyd, A. Breeveld, S. Campana, M. M. Chester, G. Chincarini, L. R. Cominsky, G. Cusumano, M. de Pasquale, E. E. Fenimore, P. Giommi, C. Gronwall, D. Grupe, J. E. Hill, D. Hinshaw, J. Hjorth, D. Hullinger, K. C. Hurley, S. Klose, S. Kobayashi, C. Kouveliotou, H. A. Krimm, V. Mangano, F. E. Marshall, K. McGowan, A. Moretti, R. F. Mushotzky, K. Nakazawa, J. P. Norris, J. A. Nousek, J. P. Osborne, K. Page, A. M. Parsons, S. Patel, M. Perri, T. Poole, P. Romano, P. W. A. Roming, S. Rosen, G. Sato, P. Schady, A. P. Smale, J. Sollerman, R. Starling, M. Still, M. Suzuki, G. Tagliaferri, T. Takahashi, M. Tashiro, J. Tueller, A. A. Wells, N. E. White, and R. A. M. J. Wijers. A short γ -ray burst apparently associated with an elliptical galaxy at redshift $z = 0.225$. *Nature*, 437:851–854, October 2005. [arXiv:arXiv:astro-ph/0505630](#), [doi:10.1038/nature04142](#). 52
- [83] W. H. Lee, E. Ramirez-Ruiz, and J. Granot. A Compact Binary Merger Model for the Short, Hard GRB 050509b. *ApJ*, 630:L165–L168, September 2005. [arXiv:arXiv:astro-ph/0506104](#), [doi:10.1086/496882](#). 52
- [84] D. B. Fox, D. A. Frail, P. A. Price, S. R. Kulkarni, E. Berger, T. Piran, A. M. Soderberg, S. B. Cenko, P. B. Cameron, A. Gal-Yam, M. M. Kasli-

- wal, D.-S. Moon, F. A. Harrison, E. Nakar, B. P. Schmidt, B. Penprase, R. A. Chevalier, P. Kumar, K. Roth, D. Watson, B. L. Lee, S. Shectman, M. M. Phillips, M. Roth, P. J. McCarthy, M. Rauch, L. Cowie, B. A. Peterson, J. Rich, N. Kawai, K. Aoki, G. Kosugi, T. Totani, H.-S. Park, A. MacFadyen, and K. C. Hurley. The afterglow of GRB 050709 and the nature of the short-hard γ -ray bursts. *Nature*, 437:845–850, October 2005. [arXiv:arXiv:astro-ph/0510110](#), [doi:10.1038/nature04189](#). 53
- [85] E. Berger, P. A. Price, S. B. Cenko, A. Gal-Yam, A. M. Soderberg, M. Kasliwal, D. C. Leonard, P. B. Cameron, D. A. Frail, S. R. Kulkarni, D. C. Murphy, W. Krzeminski, T. Piran, B. L. Lee, K. C. Roth, D.-S. Moon, D. B. Fox, F. A. Harrison, S. E. Persson, B. P. Schmidt, B. E. Penprase, J. Rich, B. A. Peterson, and L. L. Cowie. The afterglow and elliptical host galaxy of the short γ -ray burst GRB 050724. *Nature*, 438:988–990, December 2005. [arXiv:arXiv:astro-ph/0508115](#), [doi:10.1038/nature04238](#). 53
- [86] B. D. Metzger, G. Martínez-Pinedo, S. Darbha, E. Quataert, A. Arcones, D. Kasen, R. Thomas, P. Nugent, I. V. Panov, and N. T. Zinner. Electromagnetic counterparts of compact object mergers powered by the radioactive decay of r-process nuclei. *MNRAS*, 406:2650–2662, August 2010. [arXiv:1001.5029](#), [doi:10.1111/j.1365-2966.2010.16864.x](#). 53
- [87] V. V. Usov and J. I. Katz. Low frequency radio pulses from gamma-ray bursts? *A&A*, 364:655–659, December 2000. [arXiv:arXiv:astro-ph/0002278](#). 53
- [88] K. Belczynski, R. E. Taam, V. Kalogera, F. A. Rasio, and T. Bulik. On the Rarity of Double Black Hole Binaries: Consequences for Gravitational Wave Detection. *ApJ*, 662:504–511, June 2007. [arXiv:arXiv:astro-ph/0612032](#), [doi:10.1086/513562](#). 53

- [89] W. Baade and F. Zwicky. On Super-novae. *Proceedings of the National Academy of Science*, 20:254–259, May 1934. 56
- [90] F. Mannucci, R. Maiolino, G. Cresci, M. Della Valle, L. Vanzi, F. Ghinassi, V. D. Ivanov, N. M. Nagar, and A. Alonso-Herrero. The infrared supernova rate in starburst galaxies. *A&A*, 401:519–530, April 2003. [arXiv:arXiv:astro-ph/0302323](#), [doi:10.1051/0004-6361:20030198](#). 57
- [91] K. Hirata, T. Kajita, M. Koshiba, M. Nakahata, and Y. Oyama. Observation of a neutrino burst from the supernova SN1987A. *Physical Review Letters*, 58:1490–1493, April 1987. [doi:10.1103/PhysRevLett.58.1490](#). 56
- [92] K. S. Hirata, T. Kajita, M. Koshiba, M. Nakahata, Y. Oyama, N. Sato, A. Suzuki, M. Takita, Y. Totsuka, T. Kifune, T. Suda, K. Takahashi, T. Tanimori, K. Miyano, M. Yamada, E. W. Beier, L. R. Fieldscher, W. Frati, S. B. Kim, A. K. Mann, F. M. Newcomer, R. van Berg, W. Zhang, and B. G. Cortez. Observation in the Kamiokande-II detector of the neutrino burst from supernova SN1987A. *Phys. Rev. D*, 38:448–458, July 1988. [doi:10.1103/PhysRevD.38.448](#). 56
- [93] L. Ensmann and A. Burrows. Shock breakout in SN 1987A. *ApJ*, 393:742–755, July 1992. [doi:10.1086/171542](#). 56
- [94] J. Sylvestre. Prospects for the Detection of Electromagnetic Counterparts to Gravitational Wave Events. *ApJ*, 591:1152–1156, July 2003. [arXiv:arXiv:astro-ph/0303512](#), [doi:10.1086/375505](#). 56
- [95] H. A. Bethe. Supernova mechanisms. *Reviews of Modern Physics*, 62:801–866, October 1990. [doi:10.1103/RevModPhys.62.801](#). 58, 59
- [96] K. Kotake, K. Sato, and K. Takahashi. Explosion mechanism, neutrino burst and gravitational wave in core-collapse supernovae. *Reports on Progress in*

- Physics*, 69:971–1143, April 2006. arXiv:arXiv:astro-ph/0509456, doi:10.1088/0034-4885/69/4/R03. 58
- [97] C. D. Ott. TOPICAL REVIEW: The gravitational-wave signature of core-collapse supernovae. *Classical and Quantum Gravity*, 26(6):063001–+, March 2009. arXiv:0809.0695, doi:10.1088/0264-9381/26/6/063001. 58
- [98] H.-T. Janka, K. Langanke, A. Marek, G. Martínez-Pinedo, and B. Müller. Theory of core-collapse supernovae. *Phys. Rep.*, 442:38–74, April 2007. arXiv:arXiv:astro-ph/0612072, doi:10.1016/j.physrep.2007.02.002. 58, 59
- [99] C. D. Ott. Probing the core-collapse supernova mechanism with gravitational waves. *Classical and Quantum Gravity*, 26(20):204015–+, October 2009. arXiv:0905.2797, doi:10.1088/0264-9381/26/20/204015. 58
- [100] J. W. Murphy, C. D. Ott, and A. Burrows. A Model for Gravitational Wave Emission from Neutrino-Driven Core-Collapse Supernovae. *ApJ*, 707:1173–1190, December 2009. arXiv:0907.4762, doi:10.1088/0004-637X/707/2/1173. 58
- [101] H. Dimmelmeier, C. D. Ott, A. Marek, and H.-T. Janka. Gravitational wave burst signal from core collapse of rotating stars. *Phys. Rev. D*, 78(6):064056–+, September 2008. arXiv:0806.4953, doi:10.1103/PhysRevD.78.064056. 58
- [102] E. Müller, M. Rampp, R. Buras, H.-T. Janka, and D. H. Shoemaker. Toward Gravitational Wave Signals from Realistic Core-Collapse Supernova Models. *ApJ*, 603:221–230, March 2004. arXiv:arXiv:astro-ph/0309833, doi:10.1086/381360. 58
- [103] A. Burrows, L. Dessart, E. Livne, C. D. Ott, and J. Murphy. Simulations of Magnetically Driven Supernova and Hypernova Explosions in the Context of Rapid Rotation. *ApJ*, 664:416–434, July 2007. arXiv:arXiv:astro-ph/0702539, doi:10.1086/519161. 58

- [104] C. D. Ott, A. Burrows, L. Dessart, and E. Livne. A New Mechanism for Gravitational-Wave Emission in Core-Collapse Supernovae. *Physical Review Letters*, 96(20):201102–+, May 2006. [arXiv:arXiv:astro-ph/0605493](#), [doi:10.1103/PhysRevLett.96.201102](#). 58
- [105] T. A. Thompson, A. Burrows, and P. A. Pinto. Shock Breakout in Core-Collapse Supernovae and Its Neutrino Signature. *ApJ*, 592:434–456, July 2003. [arXiv:arXiv:astro-ph/0211194](#), [doi:10.1086/375701](#). 59
- [106] S. W. Falk and W. D. Arnett. Radiation Dynamics, Envelope Ejection, and Supernova Light Curves. *ApJS*, 33:515–+, April 1977. [doi:10.1086/190440](#). 59
- [107] R. I. Klein and R. A. Chevalier. X-ray bursts from Type II supernovae. *ApJ*, 223:L109–L112, August 1978. [doi:10.1086/182740](#). 59
- [108] S. Campana, V. Mangano, A. J. Blustin, P. Brown, D. N. Burrows, G. Chincarini, J. R. Cummings, G. Cusumano, M. Della Valle, D. Malesani, P. Mészáros, J. A. Nousek, M. Page, T. Sakamoto, E. Waxman, B. Zhang, Z. G. Dai, N. Gehrels, S. Immler, F. E. Marshall, K. O. Mason, A. Moretti, P. T. O’Brien, J. P. Osborne, K. L. Page, P. Romano, P. W. A. Roming, G. Tagliaferri, L. R. Cominsky, P. Giommi, O. Godet, J. A. Kennea, H. Krimm, L. Angelini, S. D. Barthelmy, P. T. Boyd, D. M. Palmer, A. A. Wells, and N. E. White. The association of GRB 060218 with a supernova and the evolution of the shock wave. *Nature*, 442:1008–1010, August 2006. [arXiv:arXiv:astro-ph/0603279](#), [doi:10.1038/nature04892](#). 59
- [109] L.-X. Li. Shock breakout in Type Ibc supernovae and application to GRB 060218/SN 2006aj. *MNRAS*, 375:240–256, February 2007. [arXiv:arXiv:astro-ph/0605387](#), [doi:10.1111/j.1365-2966.2006.11286.x](#). 59

- [110] G. Ghisellini, G. Ghirlanda, and F. Tavecchio. Did we observe the supernova shock breakout in GRB 060218? *MNRAS*, 382:L77–L81, November 2007. [arXiv:0707.0689](#), [doi:10.1111/j.1745-3933.2007.00396.x](#). 59
- [111] A. M. Soderberg, E. Berger, K. L. Page, P. Schady, J. Parrent, D. Pooley, X.-Y. Wang, E. O. Ofek, A. Cucchiara, A. Rau, E. Waxman, J. D. Simon, D. C.-J. Bock, P. A. Milne, M. J. Page, J. C. Barentine, S. D. Barthelmy, A. P. Beardmore, M. F. Bietenholz, P. Brown, A. Burrows, D. N. Burrows, G. Byrngelson, S. B. Cenko, P. Chandra, J. R. Cummings, D. B. Fox, A. Gal-Yam, N. Gehrels, S. Immler, M. Kasliwal, A. K. H. Kong, H. A. Krimm, S. R. Kulkarni, T. J. Maccarone, P. Mészáros, E. Nakar, P. T. O’Brien, R. A. Overzier, M. de Pasquale, J. Racusin, N. Rea, and D. G. York. An extremely luminous X-ray outburst at the birth of a supernova. *Nature*, 453:469–474, May 2008. [arXiv:0802.1712](#), [doi:10.1038/nature06997](#). 59
- [112] J. J. Eldridge and C. A. Tout. The progenitors of core-collapse supernovae. *MNRAS*, 353:87–97, September 2004. [arXiv:arXiv:astro-ph/0405408](#), [doi:10.1111/j.1365-2966.2004.08041.x](#). 59
- [113] A. I. MacFadyen and S. E. Woosley. Collapsars: Gamma-Ray Bursts and Explosions in “Failed Supernovae”. *ApJ*, 524:262–289, October 1999. [arXiv:arXiv:astro-ph/9810274](#), [doi:10.1086/307790](#). 59
- [114] D. N. Burrows, P. Romano, A. Falcone, S. Kobayashi, B. Zhang, A. Moretti, P. T. O’Brien, M. R. Goad, S. Campana, K. L. Page, L. Angelini, S. Barthelmy, A. P. Beardmore, M. Capalbi, G. Chincarini, J. Cummings, G. Cusumano, D. Fox, P. Giommi, J. E. Hill, J. A. Kennea, H. Krimm, V. Mangano, F. Marshall, P. Mészáros, D. C. Morris, J. A. Nousek, J. P. Osborne, C. Pagani, M. Perri, G. Tagliaferri, A. A. Wells, S. Woosley, and N. Gehrels. Bright X-ray Flares in Gamma-Ray Burst Afterglows. *Science*, 309:1833–1835, September 2005. [arXiv:arXiv:astro-ph/0506130](#), [doi:10.1126/science.1116168](#). 59

- [115] M. Vietri and L. Stella. A Gamma-Ray Burst Model with Small Baryon Contamination. *ApJ*, 507:L45–L48, November 1998. [arXiv:arXiv:astro-ph/9808355](#), [doi:10.1086/311674](#). 60
- [116] M. H. P. M. van Putten. Multi-messenger emissions from Kerr black holes. *ArXiv e-prints*, May 2009. [arXiv:0905.3367](#). 60
- [117] D. A. Kann, S. Klose, B. Zhang, D. Malesani, E. Nakar, A. Pozanenko, A. C. Wilson, N. R. Butler, P. Jakobsson, S. Schulze, M. Andreev, L. A. Antonelli, I. F. Bikmaev, V. Biryukov, M. Böttcher, R. A. Burenin, J. M. Castro Cerón, A. J. Castro-Tirado, G. Chincarini, B. E. Cobb, S. Covino, P. D’Avanzo, V. D’Elia, M. Della Valle, A. de Ugarte Postigo, Y. Efimov, P. Ferrero, D. Fugazza, J. P. U. Fynbo, M. Gålfalk, F. Grundahl, J. Gorosabel, S. Gupta, S. Guziy, B. Hafizov, J. Hjorth, K. Holhjem, M. Ibrahimov, M. Im, G. L. Israel, M. Jelinek, B. L. Jensen, R. Karimov, I. M. Khamitov, Ü. Kiziloğlu, E. Klunko, P. Kubánek, A. S. Kuttyrev, P. Laursen, A. J. Levan, F. Mannucci, C. M. Martin, A. Mescheryakov, N. Mirabal, J. P. Norris, J.-E. Ovaldsen, D. Paraficz, E. Pavlenko, S. Piranomonte, A. Rossi, V. Rumyantsev, R. Salinas, A. Sergeev, D. Sharapov, J. Sollerman, B. Stecklum, L. Stella, G. Tagliaferri, N. R. Tanvir, J. Telting, V. Testa, A. C. Updike, A. Volnova, D. Watson, K. Wiersema, and D. Xu. The Afterglows of Swift-era Gamma-ray Bursts. I. Comparing pre-Swift and Swift-era Long/Soft (Type II) GRB Optical Afterglows. *ApJ*, 720:1513–1558, September 2010. [arXiv:0712.2186](#), [doi:10.1088/0004-637X/720/2/1513](#). 60, 61
- [118] S. Horiuchi and S. Ando. High-energy neutrinos from reverse shocks in choked and successful relativistic jets. *Phys. Rev. D*, 77(6):063007–+, March 2008. [arXiv:0711.2580](#), [doi:10.1103/PhysRevD.77.063007](#). 60
- [119] R. C. Duncan and C. Thompson. Astrophysics of Very Strongly Magnetized Neutron Stars: A Model for the Soft Gamma Repeaters. In G. J. Fishman,

- editor, *Gamma-Ray Bursts*, volume 307 of *American Institute of Physics Conference Series*, pages 625–+, January 1994. 60
- [120] C. Thompson and R. C. Duncan. The soft gamma repeaters as very strongly magnetized neutron stars - I. Radiative mechanism for outbursts. *MNRAS*, 275:255–300, July 1995. 60
- [121] K. Hurley. The 4.5+/-0.5 soft gamma repeaters in review. In R. M. Kippen, R. S. Mallozzi, & G. J. Fishman, editor, *Gamma-ray Bursts, 5th Huntsville Symposium*, volume 526 of *American Institute of Physics Conference Series*, pages 763–770, September 2000. [arXiv:arXiv:astro-ph/9912061](#), [doi:10.1063/1.1361637](#). 60
- [122] C. Thompson, M. Lyutikov, and S. R. Kulkarni. Electrodynamics of Magnetars: Implications for the Persistent X-Ray Emission and Spin-down of the Soft Gamma Repeaters and Anomalous X-Ray Pulsars. *ApJ*, 574:332–355, July 2002. [arXiv:arXiv:astro-ph/0110677](#), [doi:10.1086/340586](#). 60, 63
- [123] P. M. Woods and C. Thompson. *Soft gamma repeaters and anomalous X-ray pulsars: magnetar candidates*, pages 547–586. April 2006. 60
- [124] S. Mereghetti. The strongest cosmic magnets: soft gamma-ray repeaters and anomalous X-ray pulsars. *A&A Rev.*, 15:225–287, July 2008. [arXiv:0804.0250](#), [doi:10.1007/s00159-008-0011-z](#). 60, 63
- [125] S. Rosswog. Last Moments in the Life of a Compact Binary System: Gravitational Waves, Gamma-Ray Bursts and Magnetar Formation. In *Revista Mexicana de Astronomia y Astrofisica*, vol. 27, volume 27 of *Revista Mexicana de Astronomia y Astrofisica*, vol. 27, pages 57–79, March 2007. [arXiv:arXiv:astro-ph/0612572](#). 60
- [126] K. Ioka. Magnetic deformation of magnetars for the giant flares of the soft

- gamma-ray repeaters. *MNRAS*, 327:639–662, October 2001. [arXiv:arXiv:astro-ph/0009327](#), [doi:10.1046/j.1365-8711.2001.04756.x](#). 60
- [127] J. A. de Freitas Pacheco. Do soft gamma repeaters emit gravitational waves? *A&A*, 336:397–401, August 1998. [arXiv:arXiv:astro-ph/9805321](#). 63
- [128] N. Andersson. TOPICAL REVIEW: Gravitational waves from instabilities in relativistic stars. *Classical and Quantum Gravity*, 20:105–+, April 2003. [arXiv:arXiv:astro-ph/0211057](#). 63
- [129] C. J. Horowitz and K. Kadau. Breaking Strain of Neutron Star Crust and Gravitational Waves. *Physical Review Letters*, 102(19):191102–+, May 2009. [arXiv:0904.1986](#), [doi:10.1103/PhysRevLett.102.191102](#). 63
- [130] G. L. Israel, T. Belloni, L. Stella, Y. Rephaeli, D. E. Gruber, P. Casella, S. Dall’Osso, N. Rea, M. Persic, and R. E. Rothschild. The Discovery of Rapid X-Ray Oscillations in the Tail of the SGR 1806-20 Hyperflare. *ApJ*, 628:L53–L56, July 2005. [arXiv:arXiv:astro-ph/0505255](#), [doi:10.1086/432615](#). 63
- [131] A. L. Watts and T. E. Strohmayer. Neutron star oscillations and QPOs during magnetar flares. *Advances in Space Research*, 40:1446–1452, 2007. [arXiv:arXiv:astro-ph/0612252](#), [doi:10.1016/j.asr.2006.12.021](#). 63
- [132] K. Hurley, S. E. Boggs, D. M. Smith, R. C. Duncan, R. Lin, A. Zoglauer, S. Krucker, G. Hurford, H. Hudson, C. Wigger, W. Hajdas, C. Thompson, I. Mitrofanov, A. Sanin, W. Boynton, C. Fellows, A. von Kienlin, G. Lichti, A. Rau, and T. Cline. An exceptionally bright flare from SGR 1806-20 and the origins of short-duration γ -ray bursts. *Nature*, 434:1098–1103, April 2005. [arXiv:arXiv:astro-ph/0502329](#), [doi:10.1038/nature03519](#). 63
- [133] D. M. Palmer, S. Barthelmy, N. Gehrels, R. M. Kippen, T. Cayton, C. Kouveliotou, D. Eichler, R. A. M. J. Wijers, P. M. Woods, J. Granot, Y. E. Lyubarsky,

- E. Ramirez-Ruiz, L. Barbier, M. Chester, J. Cummings, E. E. Fenimore, M. H. Finger, B. M. Gaensler, D. Hullinger, H. Krimm, C. B. Markwardt, J. A. Nousek, A. Parsons, S. Patel, T. Sakamoto, G. Sato, M. Suzuki, and J. Tueller. A giant γ -ray flare from the magnetar SGR 1806 - 20. *Nature*, 434:1107–1109, April 2005. [arXiv:arXiv:astro-ph/0503030](https://arxiv.org/abs/astro-ph/0503030), [doi:10.1038/nature03525](https://doi.org/10.1038/nature03525). 63
- [134] C. Thompson and R. C. Duncan. The Soft Gamma Repeaters as Very Strongly Magnetized Neutron Stars. II. Quiescent Neutrino, X-Ray, and Alfvén Wave Emission. *ApJ*, 473:322–+, December 1996. [doi:10.1086/178147](https://doi.org/10.1086/178147). 63
- [135] Y. Gürsel and M. Tinto. Near optimal solution to the inverse problem for gravitational-wave bursts. *Phys. Rev. D*, 40:3884–3938, December 1989. [doi:10.1103/PhysRevD.40.3884](https://doi.org/10.1103/PhysRevD.40.3884). 64, 68
- [136] S. Klimenko, S. Mohanty, M. Rakhmanov, and G. Mitselmakher. Constraint likelihood method: generalization for colored noise. *Journal of Physics Conference Series*, 32:12–17, March 2006. [doi:10.1088/1742-6596/32/1/003](https://doi.org/10.1088/1742-6596/32/1/003). 64
- [137] S. D. Mohanty, M. Rakhmanov, S. Klimenko, and G. Mitselmakher. Variability of signal-to-noise ratio and the network analysis of gravitational wave burst signals. *Classical and Quantum Gravity*, 23:4799–4809, August 2006. [arXiv:arXiv:gr-qc/0601076](https://arxiv.org/abs/gr-qc/0601076), [doi:10.1088/0264-9381/23/15/001](https://doi.org/10.1088/0264-9381/23/15/001). 64
- [138] S. Chatterji, A. Lazzarini, L. Stein, P. J. Sutton, A. Searle, and M. Tinto. Coherent network analysis technique for discriminating gravitational-wave bursts from instrumental noise. *Phys. Rev. D*, 74(8):082005–+, October 2006. [arXiv:arXiv:gr-qc/0605002](https://arxiv.org/abs/gr-qc/0605002), [doi:10.1103/PhysRevD.74.082005](https://doi.org/10.1103/PhysRevD.74.082005). 64, 69, 70
- [139] P. J. Sutton, G. Jones, S. Chatterji, P. Kalmus, I. Leonor, S. Poprocki, J. Rollins, A. Searle, L. Stein, M. Tinto, and M. Was. X-Pipeline: an analysis package for autonomous gravitational-wave burst searches. *New Jour-*

- nal of Physics*, 12(5):053034–+, May 2010. arXiv:0908.3665, doi:10.1088/1367-2630/12/5/053034. 65
- [140] E. T. Jaynes. *Probability Theory: The Logic of Science*. Cambridge University Press, 2003. 65
- [141] P. Gregory. *Bayesian Logical Data Analysis for the Physical Sciences*. Cambridge University Press, 2005. 65, 71
- [142] A. C. Searle, P. J. Sutton, M. Tinto, and G. Woan. Robust Bayesian detection of unmodelled bursts. *Classical and Quantum Gravity*, 25(11):114038–+, June 2008. arXiv:0712.0196, doi:10.1088/0264-9381/25/11/114038. 65
- [143] A. C. Searle, P. J. Sutton, and M. Tinto. Bayesian detection of unmodeled bursts of gravitational waves. *Classical and Quantum Gravity*, 26(15):155017–+, August 2009. arXiv:0809.2809, doi:10.1088/0264-9381/26/15/155017. 65
- [144] A. C. Searle. Monte-Carlo and Bayesian techniques in gravitational wave burst data analysis. *ArXiv e-prints*, April 2008. arXiv:0804.1161. 65
- [145] J. Clark, I. S. Heng, M. Pitkin, and G. Woan. Evidence-based search method for gravitational waves from neutron star ring-downs. *Phys. Rev. D*, 76(4):043003–+, August 2007. arXiv:arXiv:gr-qc/0703138, doi:10.1103/PhysRevD.76.043003. 65, 77
- [146] T. B. Littenberg and N. J. Cornish. Separating Gravitational Wave Signals from Instrument Artifacts. *ArXiv e-prints*, August 2010. arXiv:1008.1577. 65, 77
- [147] Shourov Keith Chatterji. *The search for gravitational-wave bursts in data from the second LIGO science run*. PhD thesis, Masseurhussets Institute of Technology, 2005. 82, 83

- [148] B. P. Abbott, R. Abbott, R. Adhikari, P. Ajith, B. Allen, G. Allen, R. S. Amin, S. B. Anderson, W. G. Anderson, M. A. Arain, and et al. Search for gravitational-wave bursts in the first year of the fifth LIGO science run. *Phys. Rev. D*, 80(10):102001–+, November 2009. [arXiv:0905.0020](#), [doi:10.1103/PhysRevD.80.102001](#). 82
- [149] J. Abadie, B. P. Abbott, R. Abbott, T. Accadia, F. Acernese, R. Adhikari, P. Ajith, B. Allen, G. Allen, E. Amador Ceron, and et al. All-sky search for gravitational-wave bursts in the first joint LIGO-GEO-Virgo run. *Phys. Rev. D*, 81(10):102001–+, May 2010. [arXiv:1002.1036](#), [doi:10.1103/PhysRevD.81.102001](#). 82
- [150] S. Chatterji, L. Blackburn, G. Martin, and E. Katsavounidis. Multiresolution techniques for the detection of gravitational-wave bursts. *Classical and Quantum Gravity*, 21:1809–+, October 2004. [arXiv:arXiv:gr-qc/0412119](#), [doi:10.1088/0264-9381/21/20/024](#). 83
- [151] B. Allen, W. G. Anderson, P. R. Brady, D. A. Brown, and J. D. E. Creighton. FINDCHIRP: an algorithm for detection of gravitational waves from inspiraling compact binaries. *ArXiv General Relativity and Quantum Cosmology e-prints*, September 2005. [arXiv:arXiv:gr-qc/0509116](#). 85
- [152] R. Khan and S. Chatterji. Enhancing the capabilities of LIGO time-frequency plane searches through clustering. *Classical and Quantum Gravity*, 26(15):155009–+, August 2009. [arXiv:0901.3762](#), [doi:10.1088/0264-9381/26/15/155009](#). 85
- [153] Liverpool Telescope. <http://telescope.livjm.ac.uk/>. 121
- [154] LOw Frequency ARray (LOFAR). <http://www.lofar.org/>. 121, 137
- [155] Palomar Transient Factory (PTF). <http://www.astro.caltech.edu/ptf/>. 121

- [156] Pi of the Sky Telescope. <http://grb.fuw.edu.pl/>. 121
- [157] QUasar Equatorial Survey Team (QUEST) variability survey. <http://hepwww.physics.yale.edu/lasillaquest/>. 121
- [158] Robotic Optical Transient Search Experiment (ROTSE). <http://www.rotse.net/>. 121
- [159] SkyMapper Telescope. <http://rsaa.anu.edu.au/skymapper/>. 121
- [160] TAROT Telescope. <http://www.eso.org/public/images/esopia-tarot-5395/>. 121
- [161] Zadko Telescope. <http://www.zt.science.uwa.edu.au/>. 121
- [162] B. Kocsis, Z. Frei, Z. Haiman, and K. Menou. Finding the Electromagnetic Counterparts of Cosmological Standard Sirens. *ApJ*, 637:27–37, January 2006. [arXiv:arXiv:astro-ph/0505394](https://arxiv.org/abs/0505394), [doi:10.1086/498236](https://doi.org/10.1086/498236). 136
- [163] Large Synoptic Survey Telescope (LSST). <http://www.lsst.org/lsst>. 137
- [164] Green Bank Telescope (GBT). <http://www.gb.nrao.edu/>. 137
- [165] Arecibo Observatory. <http://www.naic.edu/>. 137
- [166] SuperNova Early Warning System (SNEWS). <http://snews.bnl.gov/>. 137
- [167] The Gamma-ray bursts Coordinates Network (GCN). <http://gcn.gsfc.nasa.gov/>. 137
- [168] J. Abadie, B. P. Abbott, R. Abbott, M. Abernathy, C. Adams, R. Adhikari, P. Ajith, B. Allen, G. Allen, E. Amador Ceron, and et al. Calibration of the LIGO gravitational wave detectors in the fifth science run. *Nuclear Instruments and Methods in Physics Research A*, 624:223–240, December 2010. [arXiv:1007.3973](https://arxiv.org/abs/1007.3973), [doi:10.1016/j.nima.2010.07.089](https://doi.org/10.1016/j.nima.2010.07.089). 139